School Of Applied Science

Atmospheric Water Vapour Determination from Remotely Sensed Hyperspectral Data

Andrew P. Rodger

This thesis is presented as part of the requirements for
the award of the Degree of Doctor of Philosophy
of the Curtin University of Technology

February 2002

Abstract

The accurate estimation of atmospheric water vapour and the subsequent derivation of surface spectral reflectance from hyperspectral VNIR-SWIR remotely sensed data is important for many applications. A number of algorithms have been developed for estimating water vapour content from remotely sensed hyperspectral data that do not require in-situ measurements. Two algorithms, the Continuum Interpolated Band Ratio (CIBR) and the Atmospheric Precorrected Differential Absorption (APDA) have proven to be highly effective at estimating atmospheric water vapour. Although highly successful, the two methods still exhibit unwanted or spurious results when challenging conditions are encountered. Such conditions include the estimation of atmospheric water vapour over dark targets, when uncorrected atmospheric aerosols are present and over surfaces with complex spectral signatures.

A differential absorption method called the Transmittance Slope Ratio (TSR) has been developed that negates these problems. The TSR method is comprised of a weighted mean radiance that is defined between two atmospheric water absorption features which is divided by a reference channel radiance to produce a measurable ratio value. This, is turn, may be related to a reference curve, such that, the TSR value may be expressed as an atmospheric water vapour content. To test the TSR method over real terrains, AVIRIS and HyMap measured hyperspectral radiometric data were used. Three test sites were used in total with each site allowing different aspects of the water vapour estimation to be critically examined. The sites are, Jasper Ridge and Moffett Field in California and Brukunga in South Australia.

The TSR method is found to significantly improve estimated atmospheric water vapour over dark targets (with less than 3.5 % error for reflectances as low as 0.5 %), improvement over nonlinear surfaces, and finally, improvement in water vapour estimation when atmospheric aerosol conditions are not well known. In the final case the TSR method is found to estimate atmospheric water vapour with an error of less than 2 % when a 5 km visibility is assumed to be 25 km. The final result is at least an order of magnitude better than the CIBR and APDA methods.

Acknowledgements

Firstly, I would like to thank my beautiful wife Marie and daughter Siobhan for their support and never failing enthusiasm for my work (when mine has faltered from time to time). They have been there for the long haul and have stuck by me for the past three years while I carried this work out and have been my backbone for the duration. I can honestly say that Marie has more knowledge about remote sensing and the estimation of atmospheric water vapour from hyperspectral VNIR-SWIR sensors than any one else in the arts industry.

Secondly, I would like to acknowledge and thank my supervisors. Associate Professor Mervyn Lynch from the Remote Sensing and Satellite Research Group at Curtin University in Perth, Western Australia. Drove him around the twist with my edits Im sure. Dr Thomas Cudahy of the Exploration and Mining Division of CSIRO at the Leeuwin Centre in Floreat Park, Western Australia. I honestly would not have done half of what I have did without his available resources, financial and friendship support. Last but not least is Dr Peter Hick, also from Exploration and Mining. I am sure that I took time away from Peter enjoying his sailing, yet, he never complained just encouraged me. Many, many thanks to all three.

I would like to acknowledge my remote sensing friends from Curtin RSSRG who are also doing their thesis work. As well, I would like to thank my other personal friends who have seen my ups and downs yet still manage to keep me smiling and laughing. Many thanks to all.

Professionally I would like to acknowledge and thank the NASA Jet Propulsion Laboratory where AVIRIS originates from. They supply a number of free data sets which I consider as an excellent incentive and gesture for fostering research in the field of hyperspectral spectroscopy.

Foreword

The derivations in this report reference a number of authors and, as such, different authors tend to use different units. The adopted units for this report are SI units unless otherwise stated. Thus, derivations in this work may differ slightly to derivations of listed authors due to differences in units. This is usually apparent in the form of a π value in most cases. Also of note, the spelling throughout the thesis adopts British-English spelling. The typesetting package used to assemble the thesis was LaTeXwhich uses American dictionaries. A spell checking program that handles LaTeXdocuments was downloaded to cope with the British-English spelling (MicroSpell http://www.microspell.com/). This was found to be an excellent program and well worth the investment. Thus, the author has adopted this as the base dictionary used in the production of the thesis.

Contents

List of Figures

List of Tables

Chapter 1

Introduction

The advent of remote sensing, spaceborne and airborne, has opened the way for the examination of Earth's geophysical and biological properties at various levels of scientific investigation. Remote sensing instrumentation routinely collects data on a continuous basis over the Earth's surface and, as such, allows researchers to investigate a variety of issues, in various fields, on a variety of scales. The scales are both regional and global and the research derived from remotely sensed data is helping our understanding of the Earth itself, human impact on the Earth and the natural processes inherent with Earth. Spaceborne remote sensing is allowing investigations to be carried out on a global scale.

The information gathered by spaceborne remote sensing systems has allowed humans to view the Earth in unprecedented clarity for the first time in Human evolution. From the observations, and data collected, global maps of parameters, such as, vegetation, sea surface temperature, ozone content, sea-ice formation and various atmospheric properties, to name a few, have been derived. The use of remote sensing is allowing small scale or regional information to be examined on a time frame that is both economical and relevant to the researcher and third party alike. Like global studies, regional studies allow us to monitor and study a variety of different disciplines such as algae growth in coastal regions, oceanic dynamics, or seasonal changes in pasture production (de Hann *et al.*, 1991); all of which will have particular importance to various researchers. Both the global and regional studies are helping to improve our understanding of the environment around us and are allowing us to evaluate the impact of the human species on the Earth system.

1.0.1 Historical Perspective

The work carried out in this study is focused on examining the information content in remotely sensed data in the Visible Near-Infrared (VNIR) and Short Wave Infrared (SWIR) part of the electromagnetic spectrum. Remote sensing in this region of the electromagnetic spectrum typically uses reflected solar radiation for information estimation and derivation of the properties of the surface. The sensors typically used in this region of the spectrum are passive remote sensing instruments. The remote sensing community initially worked with broadband sensors which generally have few spectral channels, ranging from 5 to 30 in number, and with each channel encompassing a large spectral interval; see Chapter 2.4. Broadband sensors have proven invaluable to the remote sensing community and are a constant source of information and knowledge. Approximately ten years ago a new form of VNIR-SWIR sensor was developed, namely, the hyperspectral sensor. This sensor type has hundreds of spectral channels located in the VNIR-SWIR spectral region and is capable of producing near-laboratory quality spectra. With the advent of new sensors the need has emerged for new methods of data processing and information retrieval. Since the data are more complex, the algorithms required to derive useful information have also become more complex.

Through the study of the Radiative Transfer Equations (RTE) (see chapter 5) the signal received at the satellite (or airborne) sensor may be interpreted and solved for a given product, such as surface reflectance, Normalised Difference Vegetation Index (NDVI) or atmospheric aerosol optical depth for example. Multispectral sensors are robust and well proven in the field of remote sensing and have been used for countless applications over the years. The spectral and information content limitation imposed by the spectral bandwidth of multispectral sensors, however, has been a motivation for progressing hyperspectral remote sensing in the VNIR-SWIR. The demand and requirement for more spectral information, in the VNIR-SWIR spectral region, has seen the steady emergence of the hyperspectral sensor since the early 1980s. Hyperspectral sensors gather information at unprecedented spectral resolution as compared to the multispectral sensor (see Chapter 2.4) and have moved data analysis away from broad classifications of surface products to specific classification and have increased the need for accurate methods of retrieving the desired products from measured at-sensor radiances.

1.1 Description of the Problem

The passage of solar radiation through the Earth's atmosphere, and its reflection from the Earth's surface, may be calculated by considering the RTE. With the increased spectral resolution from hyperspectral remote sensing platforms the use of atmospheric modelling techniques for solving the RTE have become of great importance. With the sensor signal no longer restricted to atmospheric window regions, where reflected solar radiation is relatively unaffected by absorption and scattering, the RTE requires a complete solution for the entire VNIR-SWIR spectral region.

The increase in spectral data in the VNIR-SWIR region allows high spectral resolution products to be derived that require accurate atmospheric correction if the surface properties are to accurately retrieved. Desired properties include the surface spectral reflectance of vegetation which has known leaf water absorption features at 950 and 1150 nm (van den Bosch and Alley, 1991). The leaf water absorption features are not visible when multispectral broadband sensor data are examined. For hyperspectral and multispectral sensors operating within the VNIR-SWIR spectral region, the product of interest is primarily surface reflectance from which secondary products, such as leaf water absorption, mineralogical abundance maps, and atmospheric constituent information may be derived. The last point is of particular importance since it is the atmospheric properties that are required in order to solve for the apparent surface reflectance. Kindel *et al.* (2000) note that the largest source of error in the retrieval of apparent surface reflectance is an incomplete knowledge of the atmosphere at the time of measurement by a hyperspectral sensor.

A number of atmospheric gases are present in the VNIR-SWIR spectral region. These absorb and scatter the incoming and outgoing reflected solar irradiance

$E_0(\lambda)$. The compensation for the effect of the atmosphere is the basis of atmospheric correction. There are seven major absorbers in the VNIR-SWIR spectral range (Gao *et al.*, 1993) of which one is atmospheric column water vapour. Of the seven species only five produce appreciable absorption features. The interaction of solar radiation with temporal and spatially varying atmosphere causes significant alteration to the surface reflected radiance (Latorre and Dias, 2000). The composition of the five individual molecular species in the VNIR-SWIR spectral region are discussed in Section 3.2. Of the five absorbing species in the VNIR-SWIR region atmospheric water vapour is the largest absorber (Green *et al.*, 1991).

Water vapour varies on a spatial (Carrére and Conel, 1991; Gao *et al.*, 1991a) and temporal basis (Green, 1998) and leads to the requirement of a pixel-by-pixel derived estimate of atmospheric water vapour. Secondly, if in-situ atmospheric water vapour measurements are not available or acquired as ancillary data then an estimate of atmospheric water vapour is required from the in-scene measured at-sensor radiometric data. The high spectral resolution of hyperspectral sensors provides the required information for such estimates and allows the state of the atmosphere to be derived from the scene (Sommese *et al.*, 2000) in the absence of vicarious data. Deriving atmospheric column water vapour is of great importance, as pointed out by Carrére and Conel (1991, 1993), since water vapour is one of the key drivers to global atmospheric circulation and as such it is a product that is of great interest in studies involving weather, climate modelling and the hydrologic cycle.

1.2 Study Objectives & Outline

The goal of this study is to outline a method of estimating atmospheric column water vapour content from scene-based hyperspectral radiometric data in the VNIR-SWIR spectral region with a differential absorption technique. The differential absorption technique is termed the Transmittance Slope Ratio (TSR). The TSR method should allow the estimation of atmospheric column water vapour from at-sensor hyperspectral data on a per-pixel basis in the absence of vicarious data. It will be shown that the TSR method meets this requirement and is capable of estimating water vapour over varied topography and a range of reflecting surfaces. The study outlines the derivation of the TSR from the RTE, and the subsequent estimation of atmospheric column water vapour in terms of the TSR equation.

Firstly, a description of multispectral and hyperspectral sensors is presented, such that, the major differences existing between the two sensor types are established. As well, a description of the two hyperspectral airborne sensors used for the main thrust of the study are described. The two hyperspectral VNIR-SWIR airborne sensors used for this study are the NASA Jet Propulsion Laboratory (JPL) Airborne Visible Infrared Imaging Spectrometer (AVIRIS) and the Hyperspectral Mapper (HyMap).

Secondly, a description of the atmosphere and the major constituents active in the VNIR-SWIR spectral region are outlined; this encompasses the absorbing and scattering properties of the constituents in the VNIR-SWIR spectral region. Thus, the expected impact that the major constituents will have on remotely sensed hyperspectral radiometric data sensors are investigated. This chapter, more importantly, is relevant in establishing the extent and impact of the atmospheric column water vapour in the VNIR-SWIR. This is followed by a review of the current literature and methods used for estimating atmospheric column water vapour. The weaknesses and strengths from different methods are examined and flagged for areas of improvement.

Following this, the derivation of the RTE (describing radiance as a function of atmospheric water vapour) is outlined, initially for the case of small optical depth, and extended to encompass spectral regions of larger optical depths, such as, regions impacted by atmospheric absorption features. The derivations presented allow the RTE to be expressed in terms of atmospheric column water vapour for atmospheric window regions as well as atmospheric absorption regions and form the basis of the TSR method in terms of atmospheric column water vapour content.

This a followed by a description of the method for determining the surface spectral reflectance in the atmospheric window regions (see Chapter 7). The relevance of surface reflectance estimation in the atmospheric window regions is discussed in relation to the process of estimating atmospheric column water vapour. The derivation of surface reflectance in the window regions is extended to encompass larger spectral regions once an initial estimate of atmospheric column water vapour has been found. It is demonstrated how the extended reflectance retrieval leads to an improvement in atmospheric column water vapour estimation in the VNIR-SWIR.

An important component of this research is a sensitivity analysis of the TSR method and comparison against competitive approaches. The chapter (Chapter 8) describes the method used for analysis of the TSR and the results determined. In this chapter the robust nature of the TSR to changes in a number of variables is shown as well as significant improvement in areas found to be lacking in other competitive schemes. A brief chapter (Chapter 9) follows and describes the radiometric data sets used in the analysis of the TSR from measured hyperspectral VNIR-SWIR data. Lastly, the effectiveness and results of using the TSR with the AVIRIS and HyMap imagery are shown in Chapter 10. A number of different aspects are presented and include, topographical effects, surface effects and residual atmospheric effects observed in derived surface reflectance spectra.

This is finished with a discussion of the major findings and possible recommendations (Chapter 11) that may lead to further improvement of the TSR method, or alternatively, that may assist current water vapour estimation methods. In summary, this thesis outlines a differential absorption method, known as the TSR, for determining scene based atmospheric column water vapour from remotely sensed hyperspectral radiance measured at the sensor on a pixel-by-pixel basis in the VNIR-SWIR spectral region.

Chapter 2

VNIR-SWIR Hyperspectral and Multispectral Sensor Comparison

The ability to accurately determine scene-based water vapour estimates from a VNIR-SWIR sensor is, in the absence of in-situ data, in part a function of the sensor properties. The two sensors types predominantly used in the VNIR-SWIR are hyperspectral and multispectral sensors. This chapter compares the main differences and similarities between the two sensor types; in particular, spectral and spatial resolution, bandwidth and information content in the measured radiances. In some cases it is apparent that multispectral sensors have distinct advantages that hyperspectral sensors do not. However, it is also apparent that hyperspectral sensors are advantageous in other areas, such as, the determination of atmospheric column water vapour from scene based measurement are better suited to high spectral resolution sensors.

Following this is an examination of the two hyperspectral sensors used for this study, namely, AVIRIS and HyMap. The radiation received by hyperspectral VNIR-SWIR sensors is mainly of solar origin, while if used in a night time environment the sensor would receive lunar reflected radiation. The modification of the solar or lunar spectrum by the intervening atmosphere, and the subsequent surface interaction, determines what spectral radiance will be received at the sensor (Gao *et al.*, 1991b; Green *et al.*, 1998). An example of the modification of the solar spectrum in the VNIR-SWIR, due to the intervening atmosphere, is given by Figure 2.1.

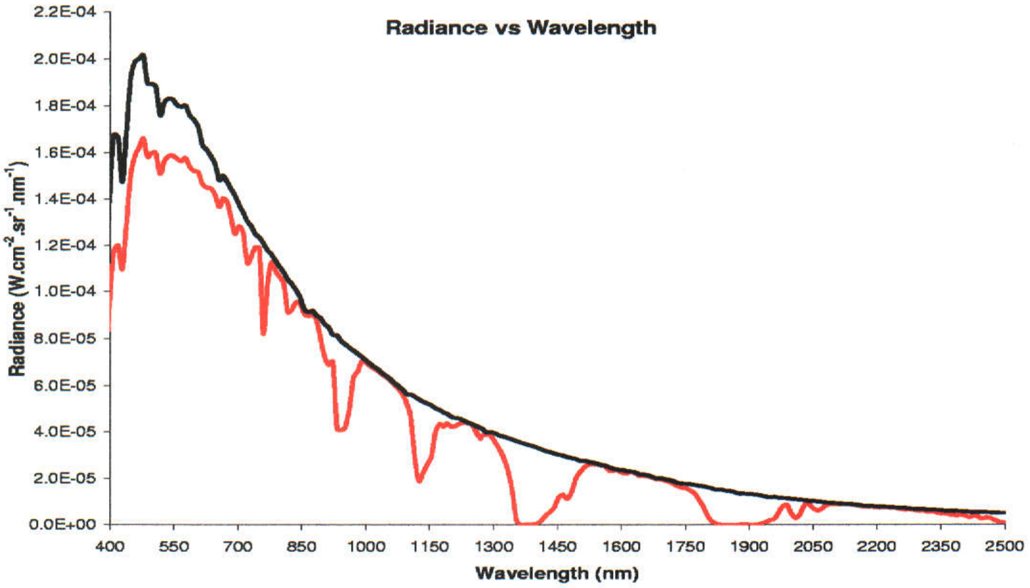

Figure 2.1: The solar spectrum (black) is modified as it passes through the atmosphere. Five important gaseous constituents, of the approximately 30 present in the atmosphere, produce absorption features seen in the modified radiance curve (red).

2.1 Spectral Resolution and Bandwidth

Multispectral and hyperspectral sensors are comprised of spectral channels in the VNIR-SWIR that measure spectral radiance at predetermined wavelengths. The radiance reflected from a surface into the sensor optics is measured by the sensor and is a function of the band-pass or spectral response filter function. Multispectral sensors are characterised by a limited number of spectral channels, in comparison to hyperspectral sensors, and generally have large channel bandwidth. It is not uncommon for multispectral sensors, such as the Landsat series (see Table 2.1) to have bandwidths on the order of 100 nm. The large bandwidth (in the case of Landsat) means physical information about the atmosphere or surface contained in spectral features smaller than 100 nm are not resolved, and hence, cannot be retrieved from the measured radiances. This is not to say that multispectral sensors always have large bandwidth; newer multispectral sensors, such as the Moderate Spectral Resolution Imaging Spectrometer (MODIS), have a greater number of spectral channels and smaller bandwidths. MODIS has 36 spectral channels covering the VNIR-SWIR spectral range with the spectral bandwidths ranging from approximately 10 nm to 537 nm (Barnes *et al.*, 1998).

MSS Bands		
Landsat 1-3	Landsats 4-5	Bandwidth
Band	Band	(nm)
4	1	500-600
5	2	600-700
6	3	700-800
7	4	800-1100
8	-	1041-1260

Table 2.1: The bandwidths of the Landsat MultiSpectral Scanner (MSS) are of the order of 100nm or larger. The bandwidth of such multispectral sensors can limit the spectral information in derived surface products. (http://landsat.gsfc.nasa.gov/project/Comparison.html)

Hyperspectral sensors, on the other hand have hundreds of spectral channels in the VNIR-SWIR spectral range. Examples are the AVIRIS instrument which has 224 spectral channels and the HyMap sensor with 128 spectral channels in the VNIR-SWIR. AVIRIS and HyMap spectral channels are narrow, with Full Width Half Maximums (FWHM) ranging from 10 nm for AVIRIS and 15 nm for HyMap. The spectral response for each channel of AVIRIS may be approximated by Gaussian curves (Green *et al.*, 1998), this is also the case with HyMap. Gaussian response functions typically allow the response modelling to be performed using only the centre wavelength and FWHM information for any given channel. This approach generally is not possible with multispectral filter functions due to the nontrivial shape of the response function.

Figure 2.2 shows a comparison between Landsat spectral filter functions and those of AVIRIS. The difference in spectral resolution and coverage between the two sensors in the VNIR-SWIR is observed to contrast markedly. While all of the VNIR-SWIR is seen by AVIRIS, including the atmospheric absorption features, Landsat has only limited coverage of the same spectral region, with almost all channels located in regions of reduced atmospheric absorption.

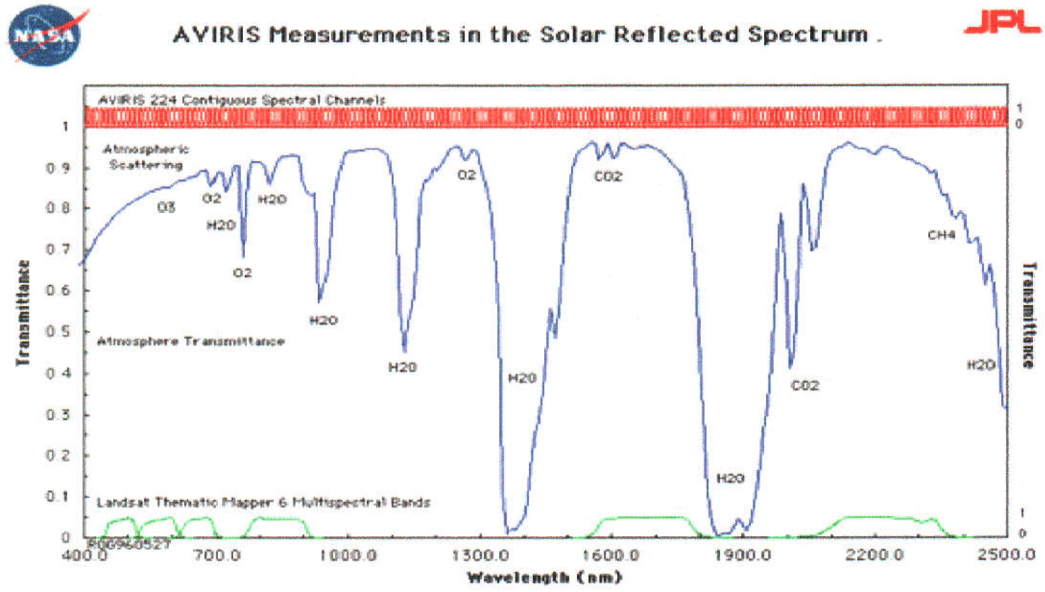

Figure 2.2: Spectral filters for the AVIRIS (red) and Landsat (green). AVIRIS has 224 spectral channels as opposed to the 6 Landsat channels. (Courtesy of Jet Propulsion Laboratory, California Institute of Technology, Pasadena, California).

2.2 Spatial Resolution

Multispectral sensors may have spatial resolutions ranging from tens of meters to kilometres. For example, the MODIS instrument has a spatial resolution ranging from 250 metres to 1 km (Barnes *et al.*, 1998). The large spatial resolution of multispectral sensors allows coverage of large areas of the globe and has, in combination with rapid repeat times, allowed surface monitoring at unprecedented levels. The spatial resolution though may be to coarse when detailed regional data is sought.

In combination with spectral and spatial resolution, multispectral data may limit the study of properties of interest. For example, multispectral data may not be of significant spatial resolution to determine accurate mineral or species distribution due to the surface targets of interest having subpixel distributions. Of course the need for high spatial resolution is not always a requirement. This may occur when the surface under consideration is relatively uniform, such as, ocean based measurements where large scale surface uniformity exists.

AVIRIS has a Field-Of-View (FOV) of 1.0 mrad giving a 20 metre spatial pixel when airborne at 20 kilometres (Green *et al.*, 1998). This is not to say that the pixel size of hyperspectral sensors cannot be increased. Spatial averaging of hyperspectral data can be performed if the effect is not detrimental to the data quality. The effect of spatial averaging has been shown, in studies by Adler-Golden *et al.* (1998) and Green and Boardman (2000), to increase the overall Signal-to-Noise Ratio (SNR).

Currently multispectral sensors have the benefit of being well established and tested in a spaceborne environment. Hyperspectral sensors, on the other hand, are still in the airborne phase with the only exception to this being the 220 channel TRW Hyperion sensor (see http://eo1.gsfc.nasa.gov/Technology/Hyperion.html). Unfortunately, a limiting factor in the success of hyperspectral sensors is the small swath width of the sensor. At present hyperspectral swath widths typically range from a few to tens of kilometres while multispectral sensors have swath widths of hundreds to thousands of kilometres. This imposes limitations on hyperspectral campaigns, such that, studies are essentially performed on a regional scale.

2.3 Information Content in Hyperspectral and Multispectral Sensors

A key question of importance for remote sensing studies is, What is the benefit of having so many spectral channels? Does it provide more information or does it simply create large data streams that must be stored for processing? A single AVIRIS scene contains around 140 Megabytes of data. The answer is entirely dependent on the user requirements for the data. If broad cover classification is required then the 224 spectral channels on the AVIRIS are not needed (Boardman and Green, 2000) and multispectral data should be sufficient. Yet, it turns out that a large number of spectral channels in the VNIR-SWIR spectral region are extremely advantageous to the field of imaging spectroscopy. Recent advances have provided the emphasis for hyperspectral spectral unmixing, nonlinear vegetation modelling and sub-pixel target detection algorithms. These forms have all been successfully demonstrated with remotely sensed hyperspectral radiance data (Boardman and Green, 2000). Recent studies, such as those by Boardman and Green (2000); Green and Boardman (2000), have demonstrated that all 224

AVIRIS channels provide useful spectral information.

Figure 2.3(a) shows an AVIRIS derived surface reflectance spectrum in the VNIR-SWIR and demonstrates the essentially continuous nature of the spectrum. The Landsat TM derived reflectance (Figure 2.3(b)), on the other hand, does not reveal spectral characteristics that would identify the pixel with mixed mineralogy. Therefore, only allow broad characterisation of the surface may be inferred from the Landsat spectrum. The AVIRIS spectrum in Figure 2.3(a) reveals the presence of three different mineral signatures. The high spectral resolution of AVIRIS provides a means of improving classification and diagnostic spectroscopy. In particular, Figure 2.3(a) shows that a hematite feature is located at 940 nm. The broad nature of the hematite feature is not resolved in the Landsat spectrum, as well, it is located in the 940 nm water vapour diagnostic feature and is therefore not seen by Landsat.

The increased spectral resolution of hyperspectral imaging spectroscopy allows direct measurement and examination of surface properties that are not discernible to multispectral sensors. The drive for accurate assessment of what is on the surface has led to an increasing number of scientists utilising the power of hyperspectral information as opposed to multispectral data. A broader view of the hyperspectral concept is shown in Figure 2.4 which demonstrates how the image or hyperspectral data for a given pixel is constructed. The combined spatial and spectral information gathered by the sensor is known as the hyperspectral data cube.

2.4 Sensor Description of AVIRIS and HyMap

The remaining chapters of this study are devoted to the estimation of atmospheric water vapour from hyperspectral sensors. The work builds on radiative transfer theory outlined in Chapter 5. Computationally, the assumption is that the remote sensing instrument response functions may be incorporated into the atmospheric modelling procedure. As well, it is assumed that radiative transfer modelling reflects radiative transfer in real atmospheres. In particular, all results presented to demonstrate the methodology developed are from two hyperspectral sensing platforms, HyMap and AVIRIS. The algorithms and methods outlined in

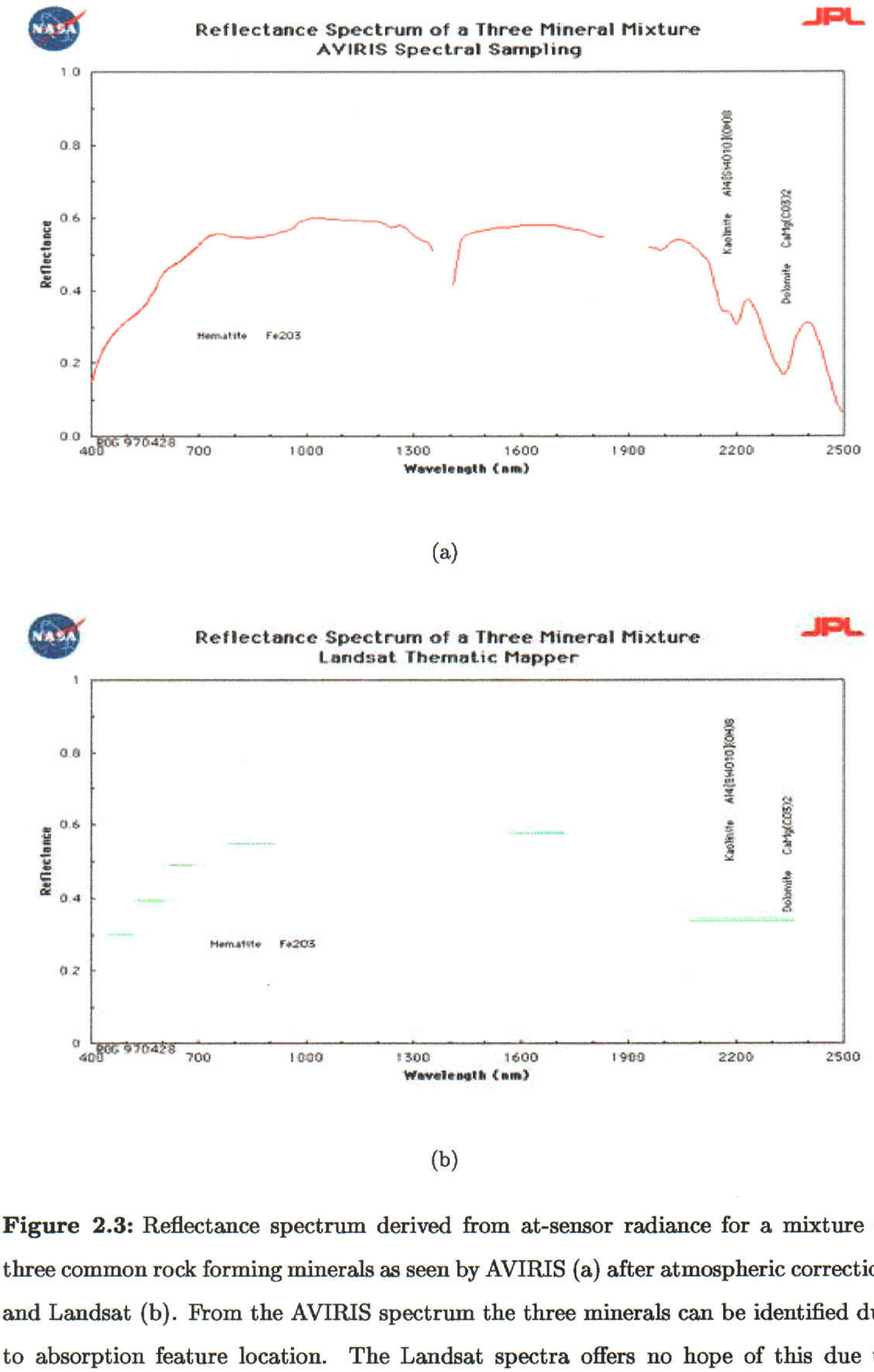

(a)

(b)

Figure 2.3: Reflectance spectrum derived from at-sensor radiance for a mixture of three common rock forming minerals as seen by AVIRIS (a) after atmospheric correction and Landsat (b). From the AVIRIS spectrum the three minerals can be identified due to absorption feature location. The Landsat spectra offers no hope of this due to the broad nature of its spectral channels. (Courtesy of Jet Propulsion Laboratory, California Institute of Technology, Pasadena, California).

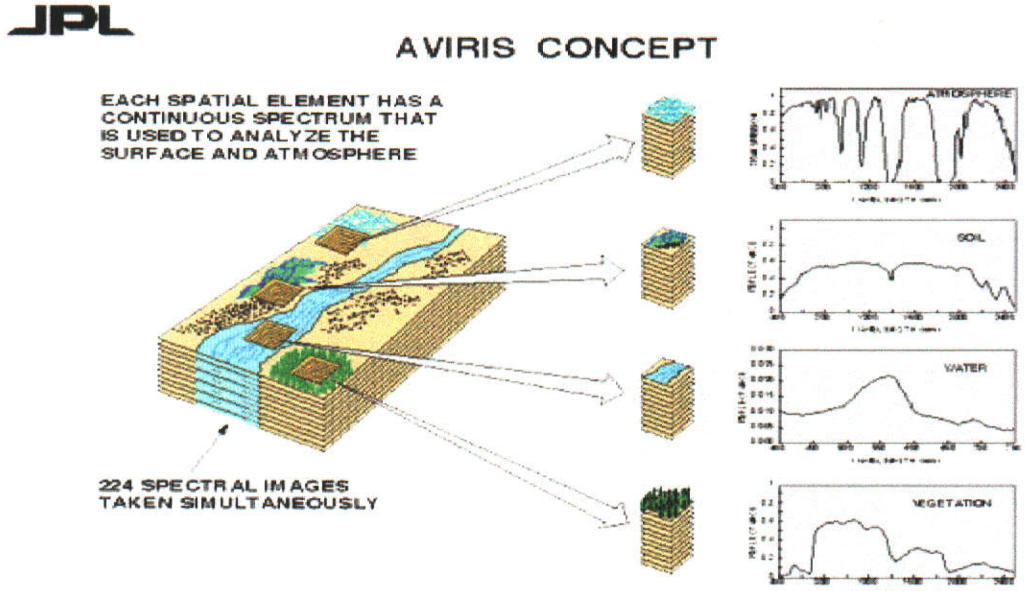

Figure 2.4: The concept of hyperspectral data and the hyperspectral data cube. Each spatial element contains spectral information from 224 channels located across 400–2500 nm. The at-sensor radiance data can be analysed in relation to the atmospheric properties at the time of data acquisition and the an estimate of surface spectral reflectance derived for a given spatial element or pixel. (Courtesy of Jet Propulsion Laboratory, California Institute of Technology, Pasadena, California).

this study are generalised methods and as such are applicable to any VNIR-SWIR hyperspectral sensor. Since the two sensors used in the study are AVIRIS and HyMap it is prudent to describe their characteristics and performance. Described first are the basic instrument characteristics, followed by a discussion of measurement and reference channels used for estimating atmospheric water vapour from AVIRIS and HyMap radiance data.

2.5 Airborne Visible/Infrared Imaging Spectrometer (AVIRIS)

The AVIRIS instrument operates in the VNIR-SWIR portion of the electromagnetic spectrum. The idea of designing and engineering an airborne imaging spectrometer for spectroscopic analysis was first instigated by JPL in 1983. AVIRIS first measured spectral images in 1987 and continues to do so on an operational basis. The measurement of spectral radiance is performed with 224 spectral channels located in the VNIR-SWIR. Each AVIRIS spectral channel has a nominal FWHM of 10 nm (Green *et al.*, 1998) and each channels spectral response function is approximated by a Gaussian distribution.

AVIRIS is flown in the Q-bay of a NASA ER-2 aircraft at an altitude of 20 km (Green *et al.*, 1998). This configuration produces an 11 km swath width and up to 800 km along track. The nominal spatial resolution of AVIRIS is 20 m, which in combination with the spectral resolution produces detailed imagery. The research performed with AVIRIS data has spanned such fields as atmospherics (Bruegge *et al.*, 1990; Green *et al.*, 1993, 1995; Moreno and Green, 1996), ecology and vegetation (Gao and Goetz, 1995; Green and Roberts, 1995; Roberts *et al.*, 1997), geology and soils (Green, 1990; Chabrillat and Goetz, 1999) and coastal and inland water studies (Davis, 1994; Bagheri and Dekker, 1999) to mention just a few. Rather than provide highly detailed information concerning AVIRIS, the remaining sensor characteristics are summarised in Tables 2.2 and 2.3 taken from Green *et al.* (1998). It is noted that AVIRIS also flies low altitude missions in a twin otter aircraft owned and operated by NOAA. All AVIRIS data considered in this study are high altitude measurements.

Imager Type	Whiskbroom scanner
Scan Rate	12 Hz
Dispersion	4 Grating spectrometers (A,B,C,D)
Detectors	224 detectors (32,64,64,64) Si and InSb
Digitisation	12 bits
Data Rate	20.4 Mbits/s
Spectrum Rate	7300 spectra/s
Data Capacity	>10 GB (>8000km^2)

Table 2.2: The main sensor characteristics of the JPL AVIRIS sensor (Green *et al.*, 1998).

Characteristics	**Value**
Spectral	
Wavelength range	400–2500 nm
Sampling	10 nm
Spectral response (FWHM)	10 nm
Calibration accuracy	<1 nm
Radiometric	
Radiometric range	0 to maximum Lambertian radiance
Sampling	1 DN noise RMS
Absolute calibration	≥96%
Inter flight stability	≥98%
Signal-to-noise	Exceeding 100:1 requirement
Polarisation sensitivity	≤1%
Spatial @ 20 km altitude	
Field of view	30 degrees (11 km)
Instantaneous FOV	1.0 mrad (20 m)
Calibration accuracy	≤0.1 mrad
Flight line length	800 km total

Table 2.3: The nominal data characteristics of the JPL AVIRIS sensor (Green *et al.*, 1998).

2.6 Hyperspectral Mapper (HyMap)

HyMap, like AVIRIS, is an airborne hyperspectral VNIR-SWIR sensor. HyMap was developed in Sydney Australia by Integrated Spectronics and is operated by the HyVista Corporation (Kruse *et al.*, 2000). HyMap operates in the VNIR-SWIR spectral region and uses a whiskbroom scanner and four spectral detector arrays. Each array comprises 32 element detectors, 1 Si and 3 liquid-nitrogen-cooled InSb, which provides a total of 126 spectral channels. As with AVIRIS, each channel in the HyMap sensor has a small FWHM allowing the instrument response characteristics to be modelled with a Gaussian function.

The bandwidth, or FWHM, of HyMap is variable unlike AVIRIS. The range of FWHM ranges from 10 to 20 nm (Kruse *et al.*, 2000). The AVIRIS concept shown in figure 2.4 is also directly applicable to the HyMap sensor. Unlike AVIRIS, HyMap operates at an altitude between 1.7 to 2.5 km. The variable operational altitude means that the spatial resolution of HyMap is also variable and can be tailored to a given campaign (3–10 m). HyMap has a larger scan angle (approx 61°) than AVIRIS which gives variable swath widths that depend on the altitude of HyMap.

The HyMap applications are as varied as AVIRIS as demonstrated in the 1999 AIG/HyVista Group Shoot. The HyMap applications listed by Kruse *et al.* (2000) include urban studies, littoral and near-shore marine studies, environment, minerals and geology and vegetation studies. Kruse *et al.* (2000) also note that HyMap has been sponsored by other interests such as military and intelligence applications, cross calibration missions and satellite system modelling. Table 2.4 lists the main instrument characteristics and configuration options for HyMap. The rapid installation time of 2 hours and the fact that it does not require modification of existing aircraft with aerial camera ports, makes HyMap an attractive commercial imaging spectrometer system.

2.7 Summary

By comparing multispectral and hyperspectral platforms it is found that each sensor has advantages and disadvantages. The nature of which is dependent

Instrument Characteristics and Configuration Options for HyMap
100-200 bands
bandwidths of 10–20 nm
high signal to noise, > 500:1
2–10 m spatial resolution
60–70 degrees swath width
on-board radiometric and spectral calibration
ground calibration facility with traceable standards
operates in aircraft equipped with standard aerial camera ports
rapid installation, typically 2 hours
3 axis gyro stabilised platform
interface to GPS or DGPS
data retrieval and pre-processing software
international airfreight in transport containers

Table 2.4: The operational and configuration characteristics of the HyMap sensor (http://www.intspec.com/).

on the form of study being undertaken. With multispectral remote sensors a distinct advantage is noted due to their spaceborne capabilities and large swath width. This allows spaceborne multispectral instruments to carry out large global coverage studies. The relatively small swath width, and lack of a spaceborne presence, of hyperspectral instrumentation has meant that only regional studies are performed at this point in time. With the inception and launch of Hyperion (approximately 1.5 years ago), as proof-of-concept, the spaceborne component may soon be accelerated for hyperspectral remote sensing. The spatial resolution of both multi and hyperspectral instruments is directly comparable and, as such, differences primarily lay in sensor spectral resolution.

A major advantage of using measured hyperspectral data is the ability of the sensors to resolve small spectral features within the VNIR-SWIR. The increased spectral resolution allows various surfaces to be analysed at near laboratory accuracy and has helped evolve scene based atmospheric correction techniques for determining atmospheric information from the measured atmospheric absorptions in the radiance data.

The increased spectral information in atmospheric water vapour absorption features makes the determination of column water vapour possible. It provides a means by which water vapour may be determined on a pixel-by-pixel basis and, as such, allows detailed water vapour maps to be generated. Thus, this study is focused on the use of hyperspectral sensors for the determination of atmospheric water vapour. The preceding chapters describe the theory and methodology required to estimate water vapour from a measured hyperspectral signal.

Chapter 3

The Atmosphere in the VNIR-SWIR Spectral Region

This chapter covers the wavelength-dependent nature of the major atmospheric constituents active in the VNIR-SWIR spectral region. For each constituent discussed the atmospheric transmittance as a function of wavelength is shown. As well, atmospheric profiles and the general properties of each species are examined. Each atmospheric profile is shown as a function of altitude and atmospheric model. All profile and transmittance plots are taken from MODTRAN4.0 (Adler-Golden *et al.*, 1999). In all cases the profiles are shown as concentration against altitude. No unit of measure is attached to the concentration variable since the overall atmospheric profile is of interest and not the constituent concentration in this case. Four models are considered, the mid-latitude summer (MLS) and winter (MLW), tropical and United States standard (USS 1977) atmosphere.

Even though the molecular species of interest for this study is atmospheric water vapour, other species are present in measured VNIR-SWIR radiance data and are therefore of interest. The understanding of the individual constituents is important for what is normally termed "atmospheric correction". Further, as part of the research undertaken, atmospheric transmittance models for various atmospheres are invoked as part of the procedure for estimating precipitable water vapour and surface spectral reflectance. Therefore, a knowledge of how the total transmittance may impact the estimation of water vapour and radiance-to-reflectance is required. It is shown in Chapter 10 that species other than water vapour leave residual atmospheric features in derived surface spectral reflectance. This suggests that total atmospheric correction in the VNIR-SWIR is only as accurate as the accuracy of the estimates and model transmittance parameterisations used for each species.

In the VNIR-SWIR, the dominant radiant source is solar illumination. It is the attenuation and scattering properties of the atmosphere that modify the ground reflected solar radiation (Gao *et al.*, 1991b; Green *et al.*, 1998). As solar radiation, between 400 and 2500 nm, commences its passage from space into Earths atmosphere it first encounters N_2 and O_2 at an altitude of approximately 60 km from the surface. O_2 and N_2 alone account for 99% of the total atmosphere with an almost constant volume ratio up to the 60 km level (Liou, 1980). Continuing its passage through the increasingly denser lower parts of the atmosphere, solar radiation encounters other species corresponding to the remaining 1% of the molecular species and is modified accordingly from the ensuing interactions. Since it is the modifications in angular distribution and intensity to the solar spectrum that is of interest, for atmospheric and surface studies and surface-atmosphere interaction studies, it is necessary to examine the atmosphere and its properties in the VNIR-SWIR spectral region.

3.1 The Molecular Species

With Earth's atmosphere containing approximately thirty gases, of which the majority do not produce observable absorption features in the VNIR-SWIR (Gao *et al.*, 1993), only seven require examination. These include water vapour (H_2O), methane (CH_4), carbon dioxide (CO_2), ozone (O_3), oxygen (O_2), carbon monoxide (CO) and nitrous oxide (N_2O). Of these seven gases two, namely, carbon monoxide and nitrous oxide, have only weakly absorbing bands between 2000 and 2500 nm. The peak absorption of these two species is approximately 1-2% (Gao *et al.*, 1993) and, as such, are considered negligible absorbers and not included in this discussion. Of the remaining five species, each has atmospheric absorption features that are, for the most part, spectrally independent from each of the remaining gases. This has important implications when attempting to estimate the amount of a particular species present in the sun-surface-sensor path based on atmospheric absorption feature structure. Some absorption features, such as CO_2 and H_2O, do overlap spectrally in the VNIR-SWIR, but the amount of overlap is minimal.

3.1.1 Ozone O_3

Ozone is an important trace gas in the atmosphere, yet it is well known that stratospheric ozone was significantly decreased in the 1980's and is continuing to decline with increasing human activity (Egorova *et al.*, 1999). The presence of O_3 in the terrestrial atmosphere is important for biological activities on the surface (Wang *et al.*, 1995) as well as its effect on radiation budget and climate (Wang *et al.*, 1995; Egorova *et al.*, 1999). O_3 has peak concentrations at two different altitudes, with the largest concentration found in the stratosphere (Liou, 1980). The first peak concentration (see Figure 3.1(b)) occurs at an altitude of approximately 35 to 40 km. The second peak concentration occurs in the thermosphere at an approximate altitude of 90 km. Figure 3.1(a) demonstrates the atmospheric transmittance of O_3 as a function of wavelength in the VNIR-SWIR. The absorption of solar radiation by atmospheric ozone occurs in the visible part of the spectrum and has an absorption band located near 600nm (Chappius band) (Gao *et al.*, 1993). Wang *et al.* (1995) note that sensitivity calculations indicate that land surface temperatures are most sensitive to O_3 concentration changes in the lower stratosphere and upper troposphere. The peak absorption of atmospheric O_3 is approximately 10%. The amount of ozone present between ground and space is known to change with latitude, longitude, season and with synoptic systems (Gao *et al.*, 1993) and, as such, is the focus of global distribution studies such as those carried out by Wang *et al.* (1995) and Egorova *et al.* (1999).

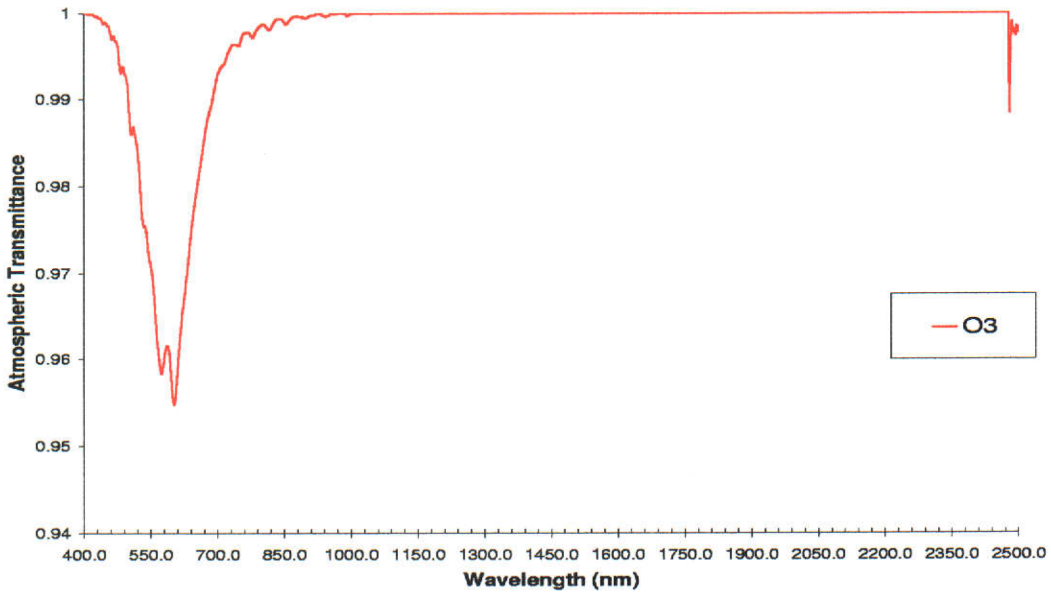

(a)

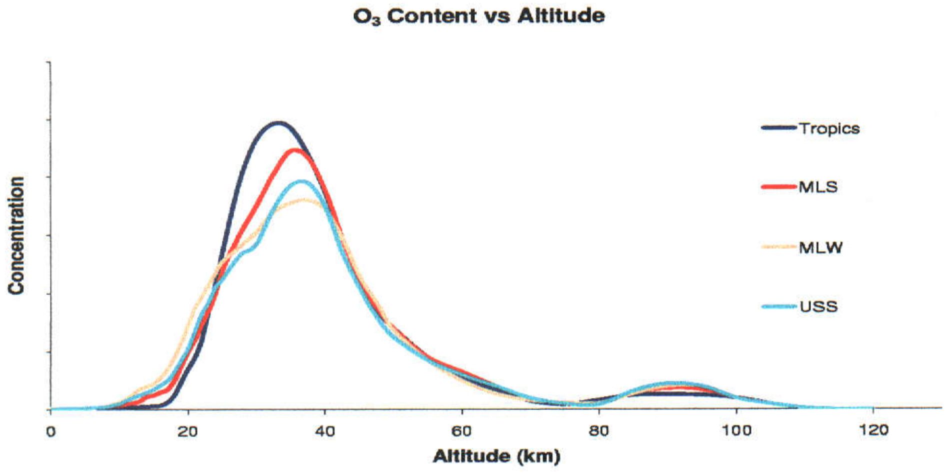

(b)

Figure 3.1: The transmittance (a) of atmospheric ozone as a function of wavelength and the concentration (b) of O_3 as a function of altitude. The peak concentration of atmospheric O_3 occurs in the stratosphere at an altitude of approximately 30 km. Significant variation is observed in O_3 concentrations as a function of atmospheric type.

3.1.2 Carbon Dioxide CO_2

Atmospheric carbon dioxide may be considered as a uniformly mixed atmospheric gas (Gao *et al.*, 1993), which is considered as well modelled (Burke *et al.*, 2000). Taylor and Orr (2000) has made note though that the estimates of CO_2 flux between atmosphere and ocean and the atmosphere and biosphere exhibit large inconsistencies . At present the effects of global warming on natural CO_2 sources and sinks are of great importance for the understanding of the global carbon cycle. Studies such as those by Taylor and Orr (2000) argue that, although poorly understood, the north-south distribution of the natural component of CO_2 offers essential information for improving our understanding of CO_2 exchange between atmosphere, oceans and the biosphere.

The transmittance of CO_2 in the VNIR-SWIR region is shown in Figure 3.2(a) and the atmospheric concentration profile of CO_2 in Figure 3.2(b). CO_2 absorption shows relatively strong absorption near 2000 nm and relatively weak absorption at 1600 and 1450 nm. Burke *et al.* (2000) notes that due to the partial spectral overlap with water vapour the effect of CO_2 absorption at 2000 nm is partially negated. The profile of CO_2 demonstrates that atmospheric CO_2, as a function of altitude, has a constant mixing ratio from the surface to the thermosphere.

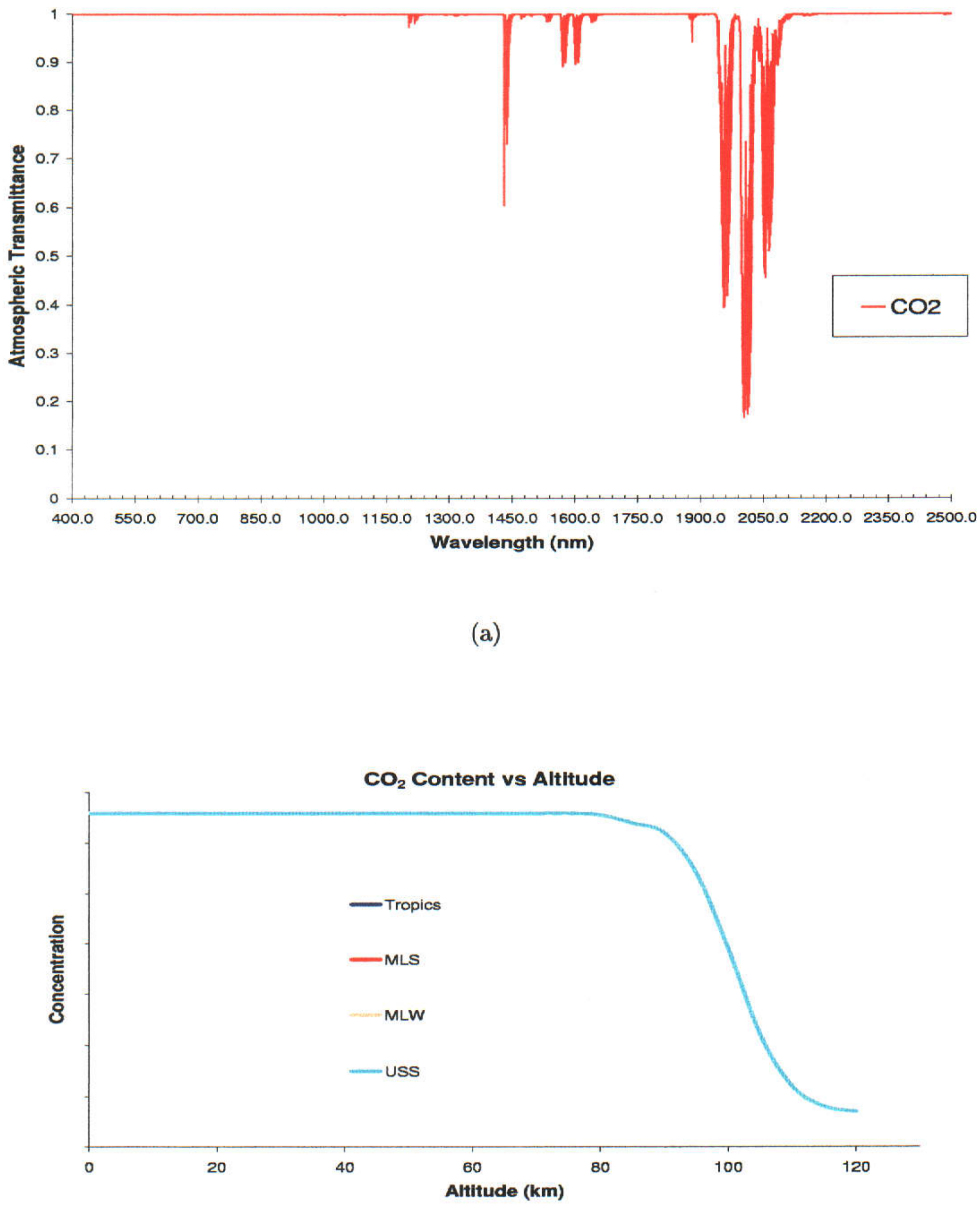

(a)

(b)

Figure 3.2: The transmittance (a) of carbon dioxide in the VNIR-SWIR is relatively small near 2000 nm. The absorption and subsequent transmittance calculation due to atmospheric carbon dioxide is thought to be well understood, yet residual CO_2 features are often observed in derived surface reflectance spectra. From (b) it is seen that the global distribution of atmospheric CO_2 is assumed to be uniformly distributed when using MODTRAN profiles.

3.1.3 Methane CH_4

Atmospheric methane levels have increased by a factor of 2.5 over the last 400 years with 80% of this increase having occurred this century and with 50% of the latter increase assigned to the last 50 years (Khalil and Rasmussen, 1994). Khalil and Rasmussen (1994) suggests that the reasons for change in the last century are predominantly due to changes in emission and perhaps small changes due to changes in the concentration of the OH radical which oxidises methane. Figure 3.3(b) shows the largest concentration of CH_4 is in the troposphere, which then rapidly declines through the stratosphere to an almost constant concentration in the mesosphere and thermosphere. Methane, which is also considered a well mixed gas (Burke *et al.*, 2000), has a transmittance spectrum such as that in Figure 3.3(a). Khalil and Rasmussen (1994) note that the current trend for CH_4 suggests that its concentration is decreasing with time most likely due to a slowdown in anthropogenic emissions.

3.1.4 Oxygen O_2

Atmospheric oxygen makes up approximately 21% of the Earth's atmosphere (Liou, 1980) and has several absorption bands located in the VNIR-SWIR. The absorption bands are narrow as observed in Figure 3.4(a). The O_2 absorption bands, although not broad, are strongly peaked at 760 nm. The 760 nm oxygen absorption band is known as the oxygen A band and led to the discovery of the isotopes ^{18}O and ^{17}O (Liou, 1980). Atmospheric oxygen is considered a well mixed gas (Burke *et al.*, 2000) which has a constant mixing ratio throughout the bulk of the atmosphere. This is seen in Figure 3.4(b) where the atmospheric profile of O_2 is essentially constant up to the thermosphere. Some O_2 modelling deficiencies occur and are generally seen as residual atmospheric features in atmospherically corrected data (see the derived surface spectra in Chapter 10). Matthew *et al.* (2000) note that this is due to the omission of certain collision induced absorption bands relating to atmospheric O_2.

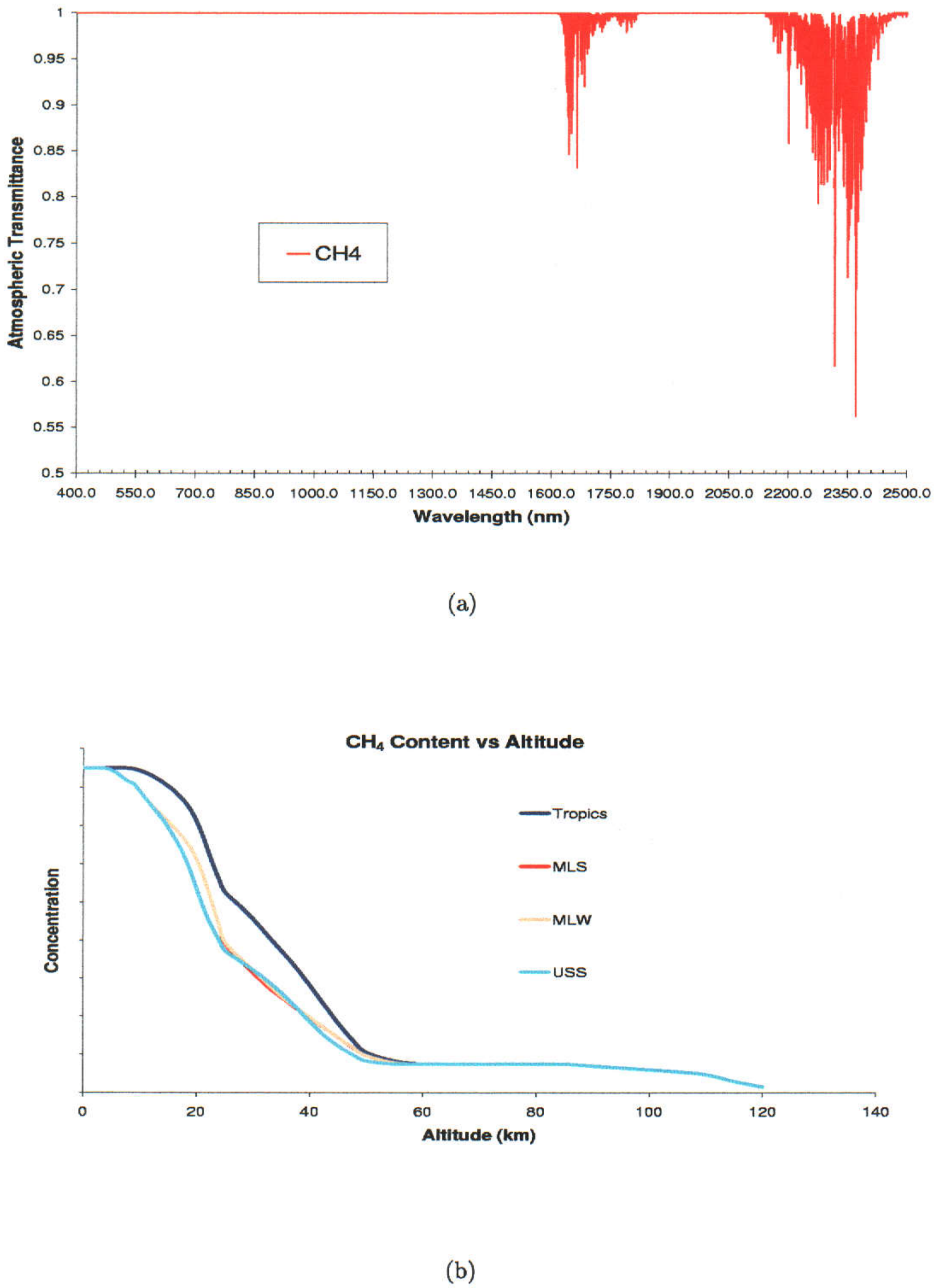

Figure 3.3: Methane, which is considered a well mixed gas has a profile (b) that is characterised by a uniform distribution up to approximately 5 km. The concentration of CH_4 is observed to rapidly decline as a function of altitude. The variation in CH_4 between atmospheric types is shown to occur between 5 and 60 km.

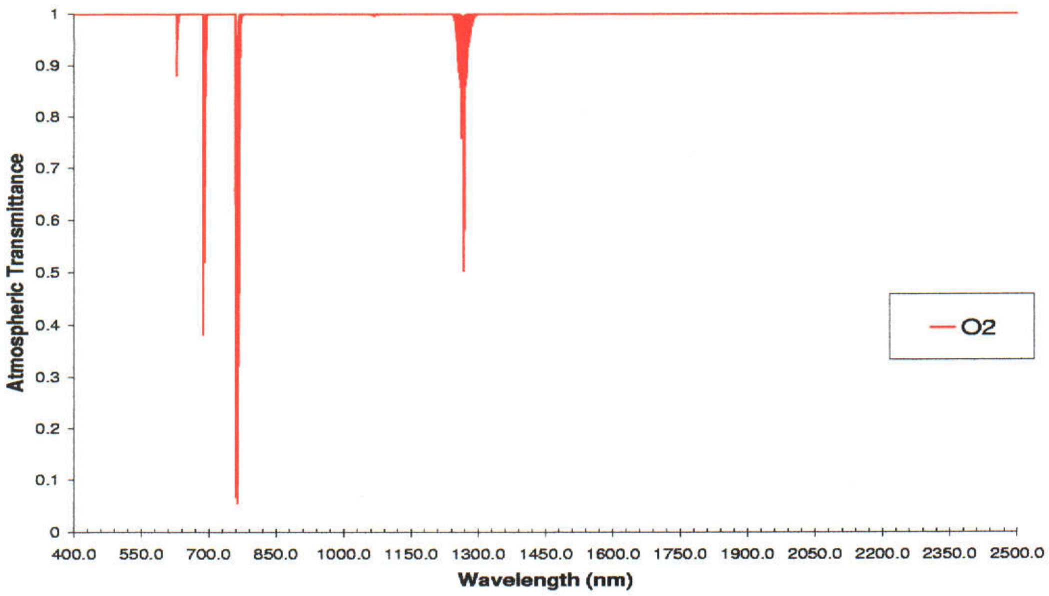

(a)

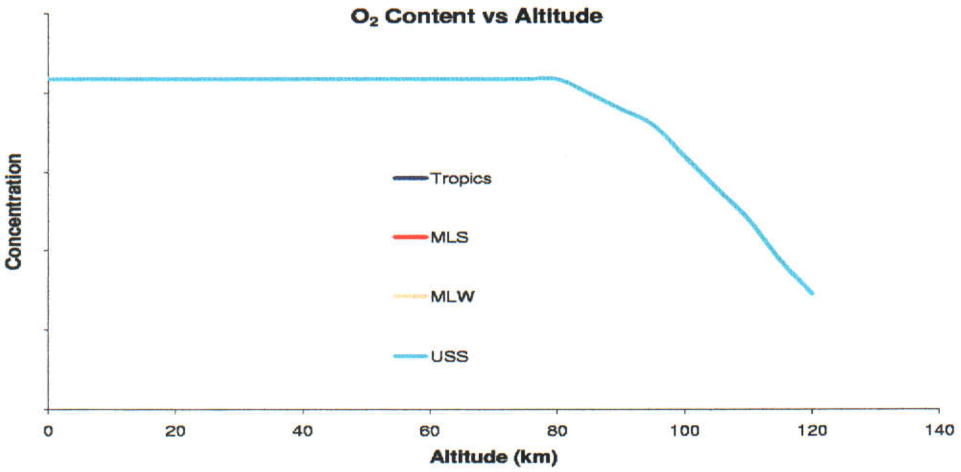

(b)

Figure 3.4: Atmospheric O_2 absorption is dominated by strong narrow band absorption (a). O_2 is considered well mixed and is, in most cases, well modelled. As (b) demonstrates the distribution of atmospheric O_2 is uniform through the atmosphere regardless of atmospheric type.

3.1.5 Water Vapour H_2O

Atmospheric water vapour plays an important role in the terrestrial system since it has a great impact on the climate of the Earth (Tahl and v. Shőnermark, 1998). Jacob (2001) notes that the vertical distribution of water vapour, with its regional and temporal variations, is not well observed nor fully understood. This same observation has also been made in other studies (Gao *et al.*, 1993; Green, 1998; Tahl and v. Shőnermark, 1998). Atmospheric water vapour is one of the principal elements in the thermodynamics of the atmosphere, and will therefore, strongly influence climate at various temporal and spatial scales (Jacob, 2001).

The atmospheric profile of water vapour is shown in Figure 3.5(b) for the four different atmospheric types considered. Figure 3.5(b) demonstrates that above 10 km, in the tropopause, the atmosphere is almost entirely devoid of atmospheric water vapour, while below 10 km the variation of different atmospheric models is markedly different. Approximately 80–90% of the water vapour in the tropopause is observed to lie below 4 km. Water vapour accounts for about 30^o C of atmospheric warming due to longwave radiation trapping (Jacob, 2001). In the VNIR-SWIR region, atmospheric water vapour is the most strongly expressed molecular absorber (Green *et al.*, 1991; Gao *et al.*, 1993) and is observed to have an effect over almost 60–70% of the VNIR-SWIR region as seen in Figure 3.5(a). Figure 3.5(a) demonstrates the H_2O one-way transmittance may range from approximately 0% to 100%. Atmospheric water vapour content changes as a function of scene elevation (Schläpfer *et al.*, 1996, 1998; Roberts *et al.*, 1997) and has been used to estimate properties of the bulk atmosphere by using relationships describing water vapour as a function of the surface elevation (Roberts *et al.*, 1997). Similar scene elevation investigations, as a function of water vapour, were carried out by Schläpfer *et al.* (1996, 1998).

The variability of atmospheric water vapour is demonstrated in Figure 3.6. Figure 3.6 shows Rogers Dry Lake (in the United States) in the visible portion of the spectrum (top series of images) as well as the corresponding estimated water vapour maps in the images below. Spatial variation is observed across the scene in any given image including temporal variation as the water vapour images are traversed from left to right. H_2O impact in the VNIR-SWIR leads to

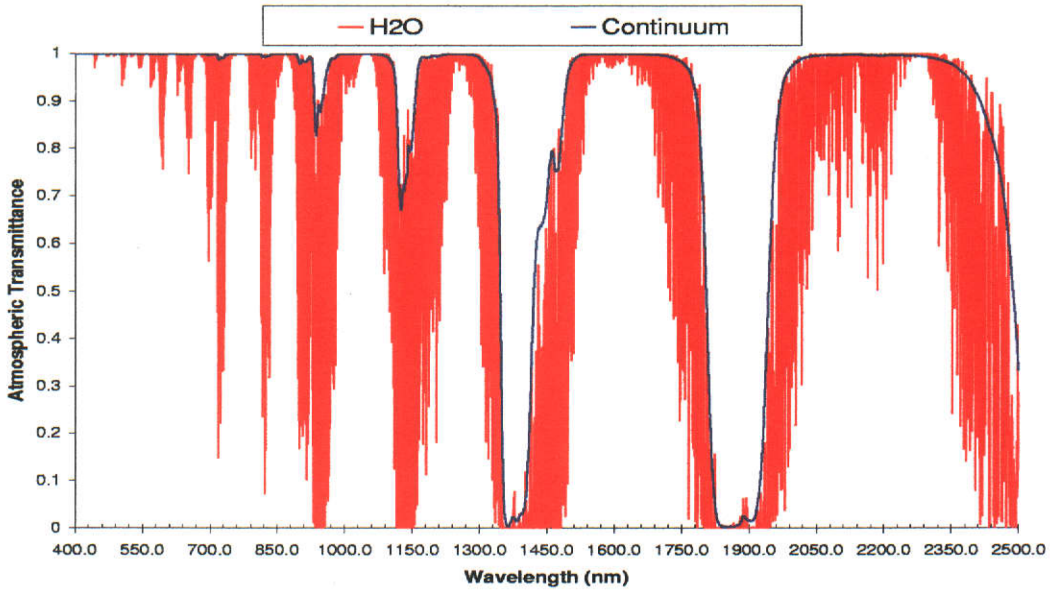

(a)

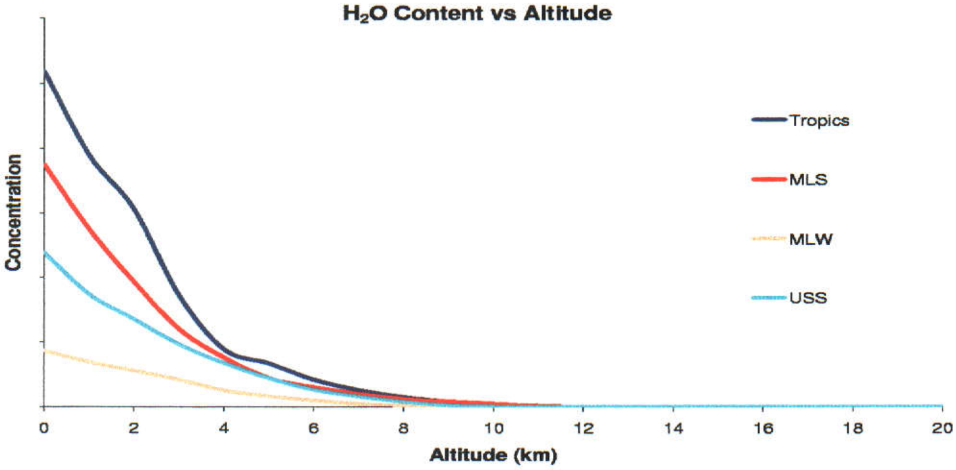

(b)

Figure 3.5: Atmospheric column water vapour is the strongest absorber present in the 400–2500 nm spectral region. The one-way transmittance of water vapour (a), shows the large impact on the VNIR-SWIR. While (b) shows the variation as a function of height, geographic location and season.

the requirement of accurate atmospheric water vapour estimation. Inaccuracies between a true and model transmittance of atmospheric water vapour causes residual features to appear in derived surface reflectance spectra. Since water vapour may change over small spatial domains (as demonstrated in Figure 3.6) a further requirement is estimation of water vapour on a per-pixel basis.

3.2 Molecular and Aerosol Scattering

The presence of atmospheric aerosols and molecules leads to scattering of solar radiation in the atmosphere. Molecular scattering is commonly known as Rayleigh scattering and was discovered by Lord Rayleigh in 1871 (Chandrasekhar, 1960). The scattering of solar radiation by molecules decreases as a function of wavelength (Chandrasekhar, 1960; Liou, 1980; Gao *et al.*, 1993) and is proportional to the wavelength raised to the negative fourth power ($\sim \lambda^{-4}$). When considering scattering regimes, two are viable depending on the spectral area under consideration. Single scattering theory describes the solutions to the RTE (see Chapter 5) in the NIR-SWIR, while multiple scattering theory is generally used in the visible portion of the spectrum.

The physics and descriptions of single and multiple scattering can be found in Chapter 5 and from Equations 5.26 to 5.33. Briefly, the effect of multiple scattering is to increase the radiation field in the visible portion of the spectrum. The transmittance effect of Rayleigh scattering at wavelengths greater than 1000 nm is negligible (Gao and Kaufman, 1998). This is demonstrated in Figure 3.7, where the molecular transmittance is observed to be close to unity from 1000 nm onward.

The spectral dependence of multiple molecular scattering is demonstrated in Figure 3.8. The increased radiance in the visible portion of the spectrum due to atmospheric molecular scatter is seen to rapidly decrease as the wavelength increases. Both signals in Figure 3.8 were generated synthetically for a MLS atmosphere with a constant surface reflectance.

Aerosol scattering also decreases with wavelength, yet not as rapidly as Rayleigh scattering (Gao *et al.*, 1993; Gao and Kaufman, 1998). This is demonstrated in studies such as those carried out by Kaufman *et al.* (1986) and Gao *et al.* (1993),

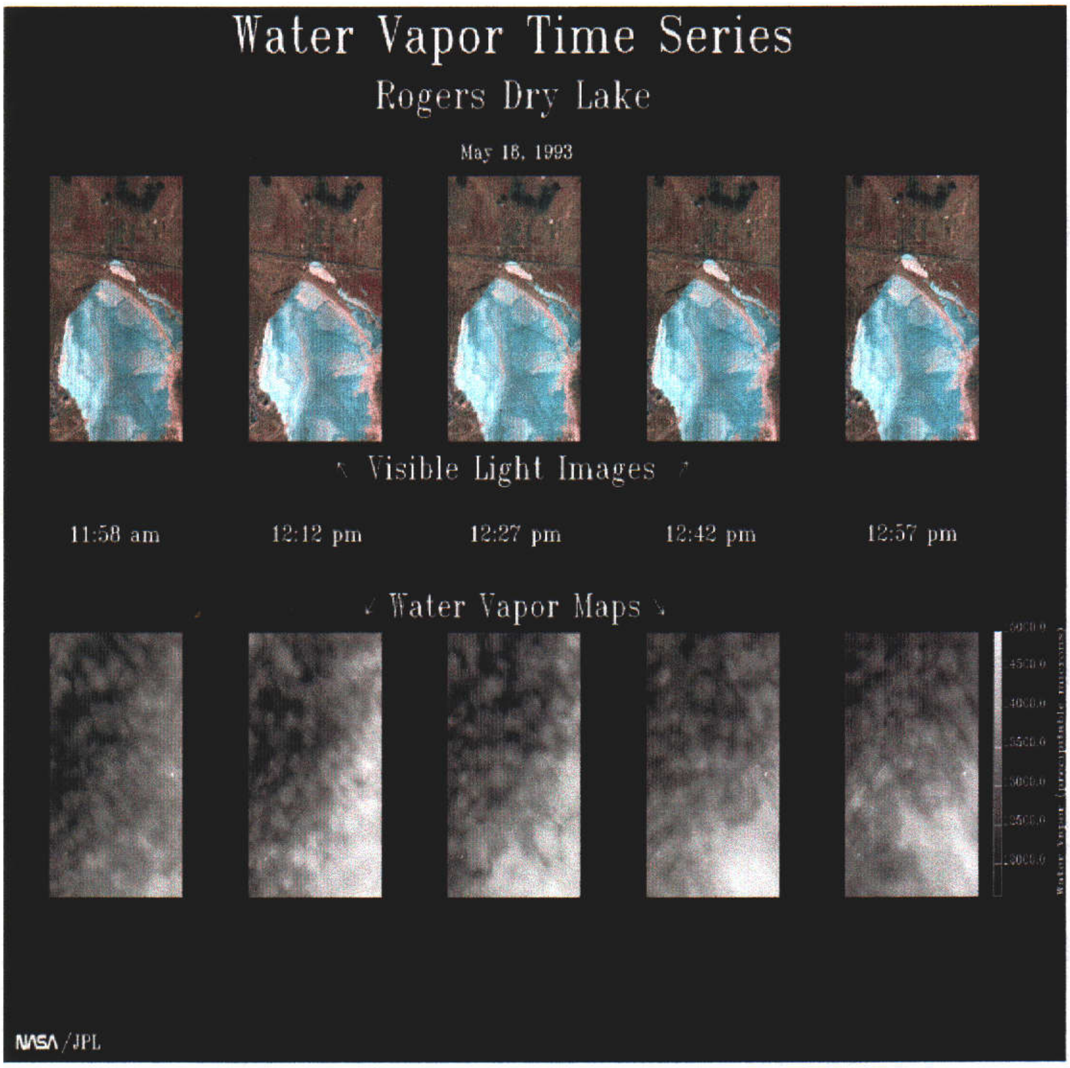

Figure 3.6: Rogers Dry Lake Time Series: The top series of images show Rogers Dry Lake in the visible part of the spectrum at five different times of the day. The lower set of images detail the corresponding atmospheric column water vapour images for the corresponding scene directly above. Spatial variability is observed as well as variability caused from the temporal aspect. (courtesy of Jet Propulsion Laboratory, California Institute of Technology, Pasadena, California.)

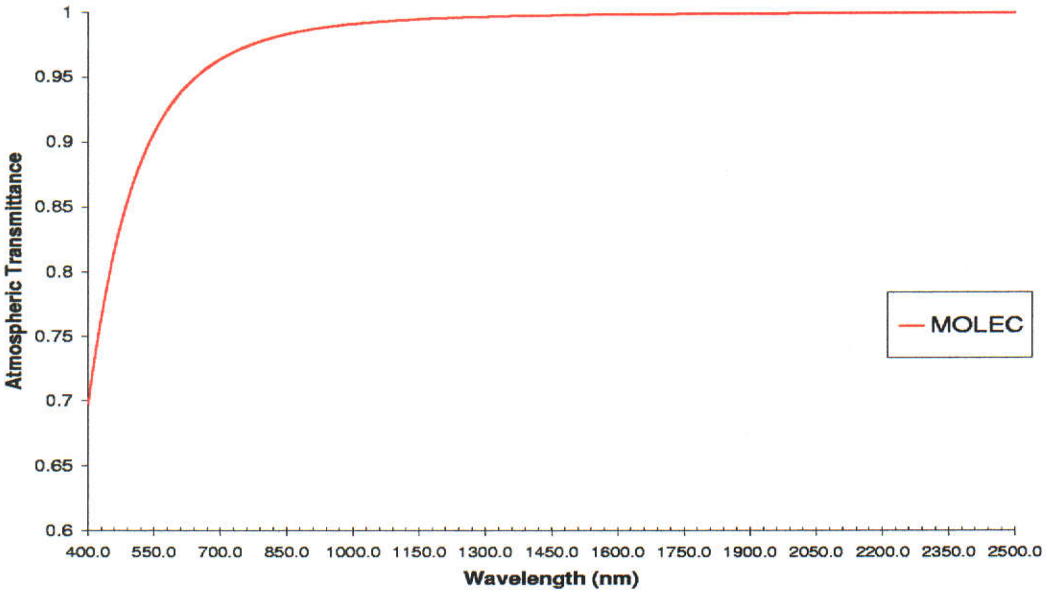

Figure 3.7: Atmospheric transmittance due to Rayleigh molecular scattering. Decreases rapidly with increasing wavelength, and is proportional to λ^{-4}. At wavelengths longer than 1000 nm the effects of molecular multiple scattering may be considered negligible.

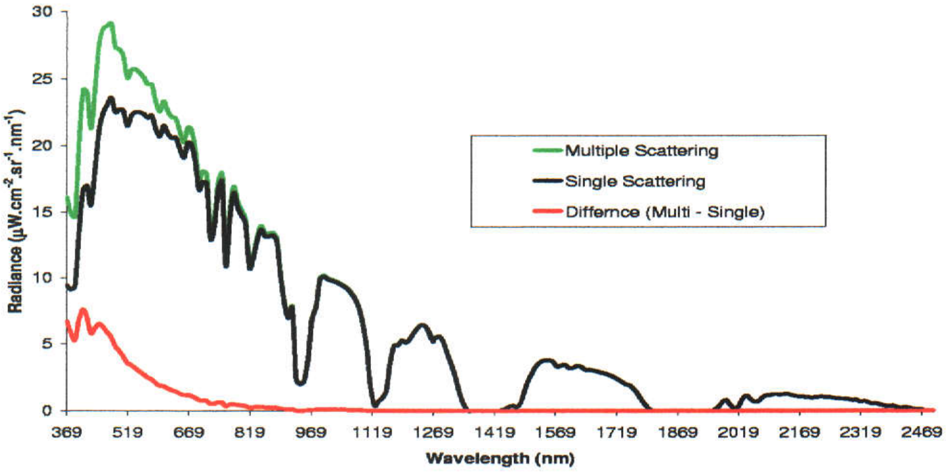

Figure 3.8: Radiance vs Wavelength: Multiple scattering effects (Rayleigh molecular scattering) is negligible beyond 1000 nm. The synthetically generated signals have a constant surface reflectance, equal to 1.0, in a mid-latitude-summer (MLS) atmosphere. The filter functions used are for AVIRIS with an 11° scan angle and solar zenith of 30° at sensor altitude of 21 km.

who states that aerosol scattering may contribute approximately 10% of the total radiance measured at-the-sensor near 1000 nm. Since the molecular scattered radiance at 1000 nm is negligible, the scattered radiance is almost entirely aerosol (Gao and Kaufman, 1998).

Shown in Figure 3.9 are synthetic radiance signals for three different aerosol visibilities (using an urban aerosol model). The absolute percentage differences highlight the magnitude differences between signals of non-equal aerosol loading. Figure 3.9(a) demonstrates the difference in radiance between a 23 km and 300 km visibility is approximately 6 to 1 % in the VNIR-SWIR.

Figure 3.9(b) shows the same as Figure 3.9(a) except the 23 km visibility is changed to 50 km. In Figure 3.9(b) the percentage difference between the two radiance signals ranges from 3% to $< 1\%$ with increasing wavelength. The difference at 2100 nm is less than 1% and the radiance, as noted by Stewart and Kaiser (2000), may be considered to be unaffected by aerosol. Therefore, for high visibility (>50 km) the aerosol effect may be ignored at little expense to reflectance retrieval, but for low visibility (less than 50 km) an estimate of the visibility should be used to increase the accuracy in any modelling process.

3.2.1 Total Transmittance

Combining the transmittance spectra (given in the previous figures) gives the total atmospheric transmittance. To perform atmospheric correction effectively the effect of each individual atmospheric transmittance spectrum requires compensation. The combination of the individual one-way transmittances are shown in Figure 3.10. The total transmittance in this case represents the transmittance of the solar irradiance from the sun to ground. As demonstrated by Figure 3.10, the impact of the total transmittance in the VNIR-SWIR is large with the largest effect, excluding aerosol, being caused by atmospheric water vapour.

3.3 Summary

This chapter demonstrated that only five, of the approximately thirty, atmospheric gases play any real part in the absorption and scattering of solar radiation.

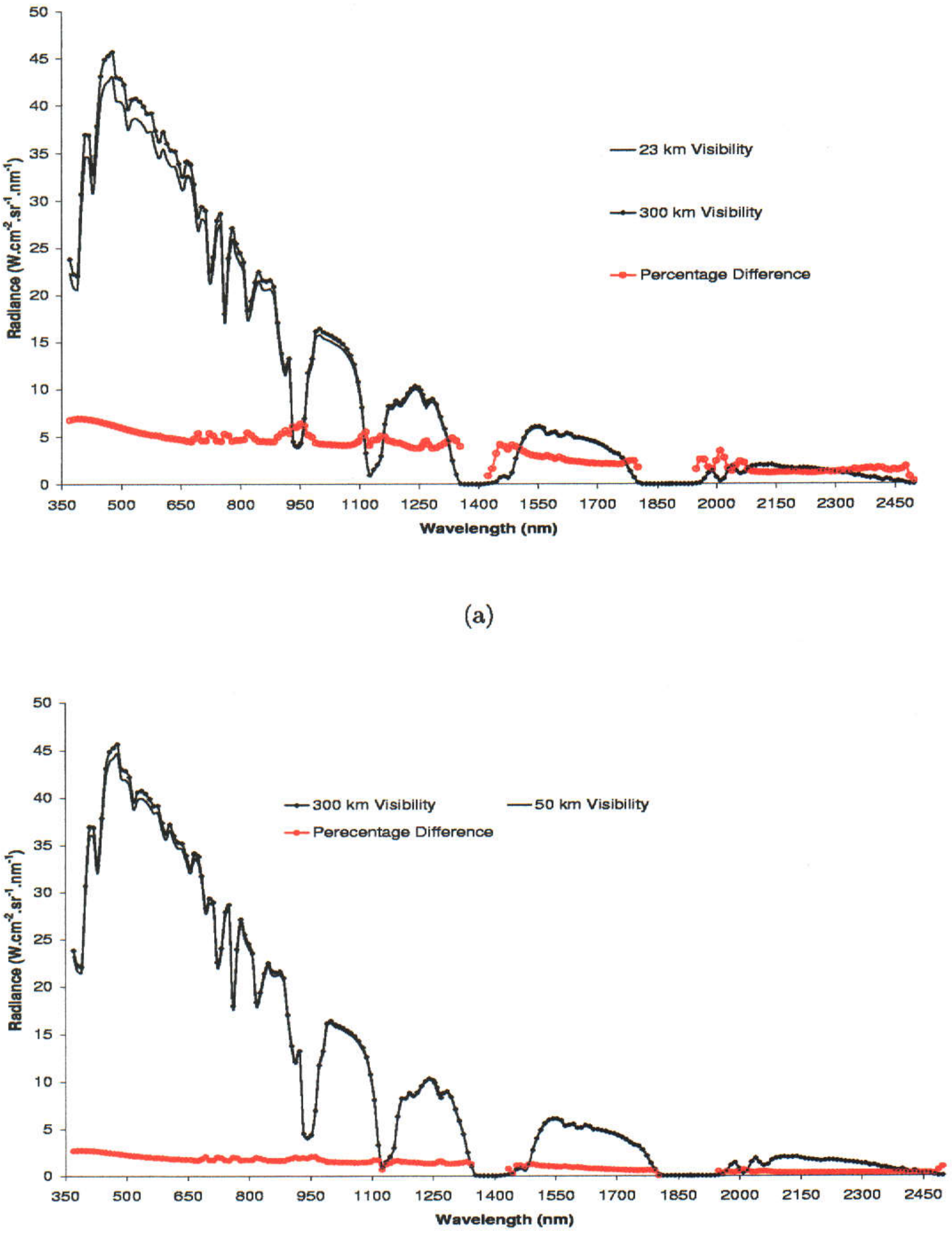

(a)

(b)

Figure 3.9: Radiance vs Wavelength: The effects of atmospheric aerosol decreases with increasing wavelength. The visibilities in (a) are set at 23 and 300 km respectively, while in (b) it is 50 and 300 km respectively.

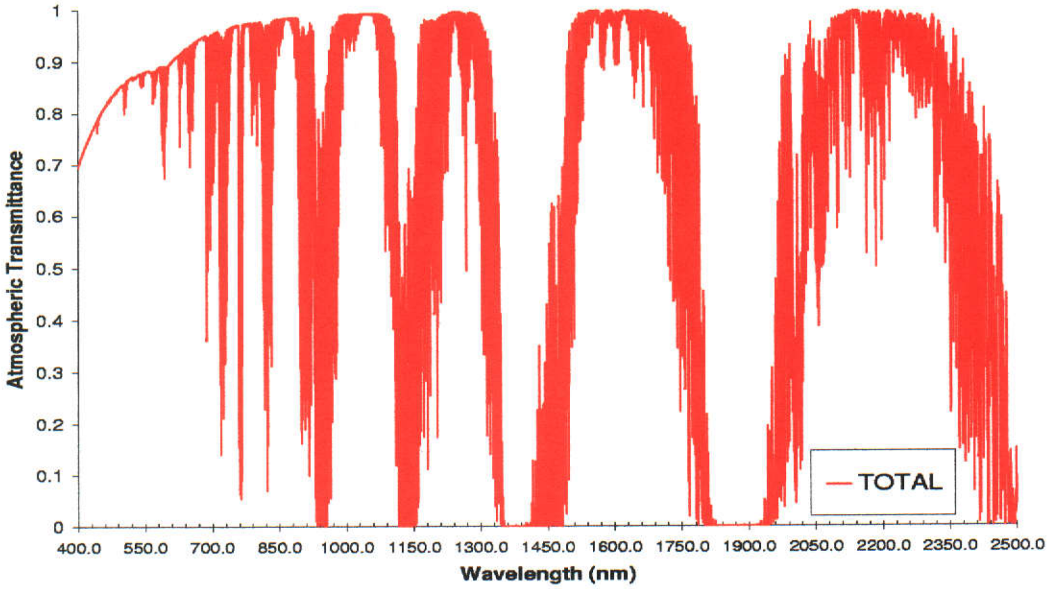

Figure 3.10: Total atmospheric transmittance versus wavelength. The impact of the total transmittance on the VNIR-SWIR spectral region is seen to be large. The species having the largest impact in the VNIR-SWIR is water vapour. Accurate atmospheric correction requires that the effects of the various atmospheric constituents be properly accounted for.

Their combined effect on the VNIR-SWIR though is found to be extensive. Of the five gases examined almost all are shown to play an important part in research areas ranging from global warming and distribution, heat exchange between surface and atmosphere, and the state of the general atmosphere in a particular location and time, as well as long and short term change detection studies.

The focus of this study however is primarily atmospheric water vapour and, as such, its impact on the VNIR-SWIR is of most interest. If hyperspectral VNIR-SWIR data are to be atmospherically corrected the effect of H_2O on the VNIR-SWIR spectral range requires accurately modelling not only as a function of wavelength, but as a function of spatial distribution. This leads to the requirement of per-pixel estimation of water vapour in the VNIR-SWIR. The estimation of water vapour on a per-pixel basis does not ensure that total atmospheric correction occurs but it does reduce the error. A study carried out by Green and Pavri (2000) shows that even if atmospheric water vapour, surface reflectance and all required geometries are known, error still occurs in synthetically generated at-sensor radiances when using programs such as MODTRAN. By this it is meant that, a ratio of the true at-sensor signal and the model at-sensor signal yields differences (most notably in the water vapour absorbing regions), which may be directly attributable to transmittance modelling error. Thus, radiance to reflectance conversion of measured at-sensor signals with model transmittance information may still produce atmospheric residual features in the derived spectra. More on this aspect is presented in Chapter 10.

The other gases, although of great importance, are not considered any further in this study. As noted though, derived surface reflectance spectra show residual features in the derived surface spectral reflectance due to inaccuracies and inconsistencies between the true and model atmosphere. Examples of residual atmospheric features, from established well mixed gases, are still observed in the derived surface spectra in Chapter 10. Most notable, excluding water vapour, are atmospheric O_2 and CO_2. Although not applicable to all molecular gases the method to be outlined, for the estimation of atmospheric water vapour, in its present form or a modified form, may possibly be used to estimate the column amounts of gases other than water vapour. This aspect though is not discussed further and the remaining chapters are focused on the derivation of column water vapour.

Chapter 4

Current Methods

Currently a number of methods exist for estimating atmospheric water vapour from remotely sensed hyperspectral data. Generally the methods fall into one of three categories. The first is based on differential absorption of atmospheric water vapour and includes the Atmospheric Precorrected Differential Absorption (APDA) technique (Borel and Schläpfer, 1996; Schläpfer *et al.*, 1996, 1998; Schläpfer, 1998), the Continuum Interpolated band Ratio (CIBR) (Carrére and Conel, 1991, 1993) and the Narrow/Wide (NW) method (Frouin *et al.*, 1990). A second method is to use curve fitting techniques (Gao and Goetz, 1990, 1995; Green *et al.*, 1991) and a third includes alternative methods of retrieval (Goetz *et al.*, 1998; Meidunas *et al.*, 2000; Sommese *et al.*, 2000).

Of the three categories, the most commonly used are differential absorption methods, also called band ratio methods. An examination of the current literature shows the CIBR and APDA are the favoured methods for the determination of atmospheric water vapour, a statement which is echoed by Hirsch *et al.* (2001). Reasons for this include, extensive use over the last ten years and creditable performance under a wide range of conditions as well as ease of implementation. The CIBR and APDA are flexible enough that they have been implemented in both hyperspectral and multispectral data. The multi-platform use of the two methods is well documented and demonstrated in a number of studies. Interested parties are directed to the following studies for further reading on use of the APDA and CIBR for determining atmospheric column water vapour; namely, Borel and Schläpfer (1996); Schläpfer *et al.* (1996, 1998); Schläpfer (1998); Hirsch *et al.*

(2001).

Since the TSR is also a differential absorption ratio method (see Chapter 6) it is prudent to examine the main properties and forms of the APDA and CIBR. This provides a reference point for performance testing and comparison of the TSR derived water vapour against two documented differential ratio methods. Before describing the APDA and CIBR the band ratio concept is first described to familiarise the reader with the basic concept of band ratio methodology. This is followed by a description and preliminary examination of the CIBR method and an examination of the APDA technique. As well, a summary of the most common issues associated with the two methods is presented. Lastly, a brief summary is provided that outlines the required improvements for improved water vapour retrieval methods, such as the TSR.

4.1 Basic Principle of Band Ratios

Before describing individual methods the basic premise of band ratio techniques is briefly outlined. The assumption is that a ratio R, of a measured channel radiance (in an atmospheric absorption feature), to a reference channel radiance outside the feature is proportional to the atmospheric transmittance $\gamma(W)$ (Schläpfer, 1998). This is represented as,

$$R(WV) = \frac{L_m(WV)}{L_r(W=0)} \propto \gamma(WV), \tag{4.1}$$

where, $L_m(WV)$ is the measured in-band radiance and $L_r(WV)$ is the measured out-of-band radiance or reference radiance, where it is assumed the atmospheric column water vapour WV is zero. The ratio R, found from applying equation 4.1, is related back to a calibration curve that provides WV as a function of R.

Schläpfer (1998) notes that this generalisation is correct only as long as the constraint of equal total transmittance is applicable to both back-scattered path radiance and the ground reflected radiance. The ratio defined by equation 4.1 is easily implemented but is also extremely sensitive to a varying background reflectance (Schläpfer, 1998). This aspect may often prove problematic over spectrally varying surfaces, which is the case for the majority of land surfaces. For this reason the need for techniques that encompass background surface reflectance are required.

Generally, the band ratio techniques are applied to the 940 and 1140 nm atmospheric water vapour features absorption features. The reason being, these two absorption features are the most sensitive to changes in the amount of atmospheric water vapour (Gao and Goetz, 1990). This is not strictly true yet the 940 and 1140 nm features are two VNIR-SWIR water vapour absorption features that display reasonable depth while not totally absorbing, as occurs at the 1380 and 1880 nm water vapour features (see Figure 3.10, Chapter 3).

4.2 CIBR

One of the first band ratio methods used for atmospheric water vapour estimation (and to partially account for background surface reflectance) was the CIBR. The CIBR uses an in-feature radiance measurement against a combination of reference channels. The in-feature channel is referred to as the measurement channel. The reference channels, which are located outside the water vapour absorption feature, are weighted such that a linear continuum curve is formed (Carrére and Conel, 1993; Schläpfer *et al.*, 1996). The CIBR is represented by,

$$CIBR(WV) = \frac{L_m(WV)}{W_1 L_{r1} + W_2 L_{r2}}, \tag{4.2}$$

where, $L_m(WV)$ is the measured radiance at wavelength λ_m in the water vapour absorption feature, WV is the atmopsheric water vapour L_{r1} and L_{r2} are the measured radiances at reference wavelengths λ_{r1} and λ_{r2} respectively and W_1 and W_2 are the weighting factors given by equation 4.3, namely,

$$W_1 = \frac{\lambda_{r2} - \lambda_m}{\lambda_{r2} - \lambda_{r1}}, \qquad W_2 = \frac{\lambda_m - \lambda_{r1}}{\lambda_{r2} - \lambda_{r1}}. \tag{4.3}$$

Figure 4.1 shows the graphical representation of the CIBR configuration. The construction of the continuum from λ_{r1} to λ_{r2} reconstructs the at-sensor radiance at wavelength λ_m as if no water vapour were present in the measurement channel. Therefore, a ratio of the measured radiance L_m and the continuum radiance at λ_m can be related to a predefined calibration curve that gives water vapour as a

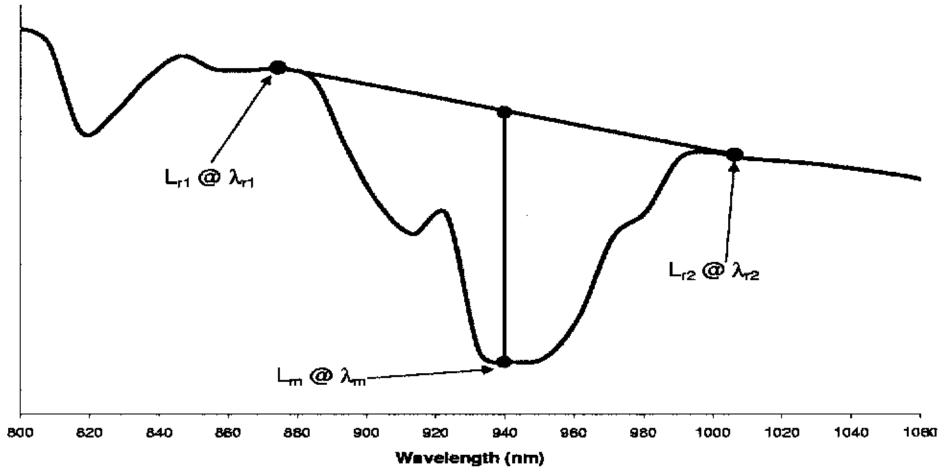

Figure 4.1: The CIBR concept. A continuum radiance is determined at two (or more) reference wavelengths. The ratio of radiance at the measurement wavelength is then made to the weighted continuum radiance and related to a calibration curve.

function of CIBR value.

This form ratio technique allows the slope of the background reflectance to be taken into account if it is assumed that the actual slope of the reflectance spectra is linear. The reader is pointed to the following study on the use of the CIBR over spectrally varying surfaces; Carrére and Conel (1993); Schläpfer *et al.* (1998). To construct the calibration curve requires that an atmospheric modelling program is applied for a series of varied water vapour values (using a predefined reference surface reflectance) and with atmospheric conditions that are appropriate to the time of data acquisition. Although the CIBR, and the APDA use a continuum slope to account for the surface reflectance across the water vapour feature of interest, it does raise issues concerning the linearity and the magnitude of the reference reflectance.

Issues such as non-linearity and deviation of the true surface reflectance from the reference reflectance has been examined by a number of authors (Gao and Goetz, 1990; Gao *et al.*, 1993; Carrére and Conel, 1993; Hirsch *et al.*, 2001) and is discussed further in section 4.4.

4.3 APDA

Although discussed further in section 4.4, one of the main issues concerning the CIBR is its failure to estimate water vapour content accurately over dark surface targets. A description of the problem of estimating water vapor over spectrally dark targets may be found in Borel and Schläpfer (1996); Schläpfer *et al.* (1998) and Hirsch *et al.* (2001). In particular, the Schläpfer *et al.* (1998) study describes the reason for the failing in the CIBR over such targets. The APDA represents a modified form of the CIBR technique that attempts to rectify this problem. The APDA form is essentially the same as the CIBR with the exception that the APDA removes an estimate of atmospheric path radiance, L_p, from all measurement and reference channels prior to forming the ratio. The form of the APDA equation is given by,

$$APDA(WV) = \frac{L_m(WV) - L_{mp}(WV)}{W_1(L_{r1} - L_{p1}) + W_2(L_{r2} - L_{p2})}. \tag{4.4}$$

Where the weights are the same as those given by equation 4.3 and $L_{mp}(WV)$, L_{p1} and L_{p2} are the path scattered radiances at wavelengths λ_m, λ_{r1} and λ_{r2} respectively. The removal of the path radiance term has been demonstrated by Schläpfer *et al.* (1996, 1998) to be effective in stabilising the ratio over surfaces of low reflectance. The reasoning is that over dark targets, of less than 10 % surface reflectance, the atmospheric component of the total measured radiance is now a major contributor (Schläpfer, 1998). Reduced surface reflectances produce higher ratio values in the CIBR, which in turn leads to lower estimates of column water vapour (Schläpfer, 1998; Hirsch *et al.*, 2001).

The reason for the increased CIBR value obtained when applying the CIBR over dark surfaces is that the CIBR is no longer proportional to the atmospheric transmittance (see equation 4.1) (Schläpfer *et al.*, 1996, 1998; Schläpfer, 1998). If unmodified this leads to underestimated atmospheric water vapour. The removal of a path radiance term prior to forming the APDA ratio helps ensure the depth of the water vapour feature is not reduced by the addition of atmospheric path added radiance and helps map the APDA to the correct water vapour content.

Because the APDA method has an estimate of path radiance removed from the total at-sensor radiance, it allows the APDA to be implemented in an iterative manner, which was first proposed by Borel and Schläpfer (1996). This is achieved by using the first estimate of column water vapour to recompute the atmospheric path radiance. The second estimate of path radiance is then employed using equation 4.4 again and a second estimate of atmospheric column water vapour calculated. This process is repeated until a preset convergence criterion level has been satisfied. Borel and Schläpfer (1996); Schläpfer (1998) and Schläpfer *et al.* (1998) provide a full description of the APDA implementation and show the implementation of the technique to real data sets.

4.4 Current Issues with Band Ratio Techniques

Although much faster to implement than curve fitting techniques (Schläpfer *et al.*, 1998), the APDA and CIBR schemes are still subject to areas of deficiency. As previously mentioned, known areas of deficiency exist in band ratio techniques when retrieving atmospheric column water vapour over dark surfaces. As well as dark surfaces, there exist issues in estimating atmospheric water vapour over surfaces exhibiting nonlinear reflectance in the 940 and 1140 nm spectral region (Gao *et al.*, 1993). Examples of nonlinear reflectances include vegetation and iron bearing minerals. Lastly, the band ratio techniques are still relatively sensitive to the effect of meteorological range, or visibility, and deviations away from an assumed aerosol visibility (Carrére and Conel, 1993).

4.4.1 Dark Target Issues

In its current form the CIBR technique does not perform well over dark terrain (Carrére and Conel, 1993; Borel and Schläpfer, 1996; Hirsch *et al.*, 2001). Since the CIBR does not account for the influence of path radiance it produces ratio values that are too large. This in turn leads to the atmospheric water vapour being underestimated (Schläpfer, 1998). A comprehensive sensitivity analysis carried out by Carrére and Conel (1993) note that CIBR vulnerability to background variation in surface reflectance is high for surface reflectance values that approach zero.

As mentioned, to reduce the magnitude of the error introduced by dark targets, the APDA removes an estimate of path radiance from all radiometric terms before calculating the value of the ratio. Borel and Schläpfer (1996); Schläpfer *et al.* (1996, 1998); Schläpfer (1998) have shown that improvement may be made to water vapour estimates if this process is implemented. This fact is also noted by Hirsch *et al.* (2001), although the study also notes that a good knowledge of aerosol optical depth and type is required when using the APDA.

An alternative approach is to account more accurately for the magnitude of the surface reflectance when using band ratio techniques. Hirsch *et al.* (2001) used a modified version of the CIBR to perform such an analysis. Rather than use a single look-up-table (LUT), several LUTs where generated with each LUT using a different surface reflectance. By using a nearest neighbour approach to estimate surface reflectance for each pixel in the image, the appropriate LUT is accessed. It was found that this improved the water vapour estimates over dark targets but still tended to produce lower than expected values.

Although not implemented in the Hirsch *et al.* (2001) study, the APDA method would most likely benefit from such a modification and, in all likelihood, should give an improvement over the modified CIBR technique.

4.4.2 Surface Reflectance Non-Linearity and Magnitude

A basic assumption of the APDA and CIBR methods is that surface spectral reflectance across the 940 and 1140 nm water vapour absorption features varies linearly (Gao and Goetz, 1990; Gao *et al.*, 1993). It is noted by Gao and Goetz (1990) that the linearity is dependent on the specific surface under consideration. The assumption of a linearly varying surface spectral reflectance will produce errors in the estimated column water vapour if the dependence is nonlinear across the 940 and 1140 nm water vapour absorption features, such as, snow and ice.

Examples of nonlinear surface reflectance in these regions are vegetation which is dominated by liquid water attenuation (Gao and Goetz, 1990), iron oxide bearing soils and soils containing gypsum (Carrére and Conel, 1993). For iron oxide bearing soils, both Gao and Goetz (1990) and Carrére and Conel (1993) note that the CIBR overestimated column water vapour by 10 % due to the broad absorption feature located between 780 and 1300 nm.

The presence of surface absorption features located in, or near, water vapour absorption features will continue to pose a problem until the CIBR and APDA methods incorporate the actual surface reflectance slopes. This may require extremely large LUTs that would prove impractical and be computationally demanding. Generally, the APDA and CIBR methods use a calibration curve that is generated with an assumed constant surface spectral reflectance. This raises the issue of departures of the actual surface reflectance away from the assumed constant reflectance form. Carrére and Conel (1993) found that the effect of using a reference surface reflectance can have dramatic effects on the estimated water vapour content.

Carrére and Conel (1993); Hirsch *et al.* (2001) also noted a detrimental effect in estimated water vapour when a departure from the reference reflectance, used in the formation of the calibration curve, is found. In an attempt to overcome the induced error in the estimated water vapour, Hirsch *et al.* (2001) modified the CIBR such that a series of LUTs were generated with different assumed constant surface reflectances. (Hirsch *et al.*, 2001), found that at the expense of increased computational time the accuracy of the surface reflectance dependent CIBR was an improvement over the APDA in all cases tested. However, as previously mentioned, there is no reason why the APDA should not also benefit from the same treatment.

4.4.3 Meteorological Range or Aerosol Visibility

The effect of aerosol visibility on the determination of atmospheric water vapour has been found to have large and sometimes dramatic results. Carrére and Conel (1993) found that a departure of the true visibility from an assumed visibility can cause, in some cases, water vapour to be overestimated by 35 % when using the CIBR. This large errors generally occurs when the model visibility is set higher than the true visibility. If the model visibility is set lower than the true visibility the error in derived water vapour tends toward lower values (although still in the 20 % range).

The comparison study of the CIBR and APDA carried by Hirsch *et al.* (2001) makes note of the vulnerability of the APDA to incorrect visibility and aerosol type but also states that the APDA is a better routine when the aerosol model and visibility are reasonably well known, as the APDA is prone to error when the aerosol type and visibility are incorrect. It was noted by Hirsch *et al.* (2001) as being sensitive to the detailed aerosol information.

4.5 Required Improvements

Any newly developed water vapour estimation method is required to address at least one or more of the issues raised in this chapter. Namely the effect of surface reflectance non-linearity and magnitude, dark target water vapour estimation and, lastly, the accurate estimation of water vapour in varied meteorological conditions.

If the estimation of atmospheric water vapour is to achieve a high level of accuracy over varied surfaces, it will be a general requirement that the identified method performs to a consistent level regardless of the surface type. This requirement means the retrieval method should be insensitive to changes in surface type, not be affected by surface reflectance non-linearity and be independent of surface reflectance magnitude.

In the case of water vapour estimation over dark targets the method should demonstrate the ability to accurately estimate the atmospheric column water vapour. This requirement is considered independent of the low signal-to-noise ratio (SNR) that is experienced over such targets (see Chapter 8, Figure 8.7). By this, it is meant that, if an instrument is noise free the water vapour will be estimated accurately. The presence of instrument noise is (as shown in Chapter 8) a limiting factor with regard to accuracy for the proposed atmospheric water vapour method (see Chapter 6) rather than the presence of a dark target.

Lastly, any new method should, if possible, be capable of accurately estimating water vapour even when the meteorological conditions are not well known. Thus, if an estimated aerosol visibility and type is used in the process and the true visibility and type is not identical, the method should still estimate water vapour to high accuracy. It is shown in later chapters that it is possible to address all three of these current issues. Further, it will be shown that a methodology may be developed that maintains high levels of estimation accuracy under extremely varied surface and atmospheric conditions.

Chapter 5

Radiative Transfer in Plane Parallel Atmospheres

To estimate atmospheric water vapour from a measured hyperspectral signal requires that the radiation received at the sensor is describable in terms of atmospheric water vapour. This chapter outlines the derivation of the radiative transfer equations (RTE) for plane parallel atmospheres. The RTE forms the basis of the TSR scheme (described in Chapter 6) and provides a means of expressing the TSR as a function of atmospheric column water vapour.

The derivations performed out in this chapter make the assumption that the dominant scattering regime is single scattering. In Chapter 3 it was demonstrated that, in the absence of atmospheric aerosol, the multiple scattering component beyond 1000 nm is negligible. With this said, all equations up to equation 5.32 are generalised equations that do not impose any constraints on the scattering regime. It will be shown that the derivations presented here may be extended to encompass regions of larger optical depth and therefore spectral regions where multiple scattering is predominant. The importance of this is that the VNIR-SWIR may be represented by a collection of polynomial expressions, where the order of the polynomials is dependent on the optical depth of the spectral region.

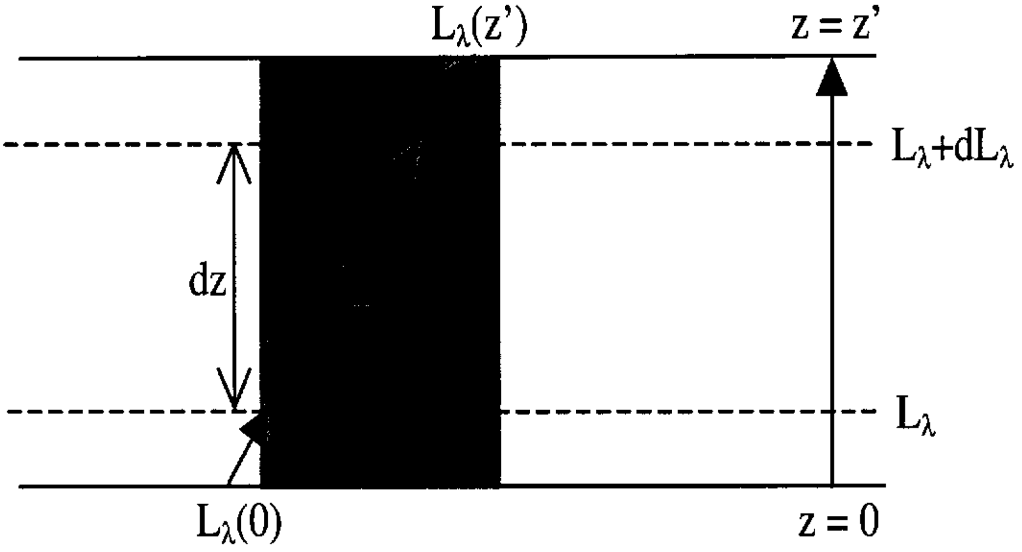

Figure 5.1: The propagation of radiation through an absorbing medium. The radiation is changed from L_λ to L_λ+dL_λ after traversing the medium.

5.1 Differential RTE

In the following derivations the atmosphere is assumed to be finite and bounded on two sides by an optical depth τ. The derivations to follow are based on the work of Chandrasekhar (1960), Liou (1980), Kaufman (1989) and are the basis for the representation of the at-sensor signals as a function of atmospheric column water vapour.

A beam of radiation passing through an absorbing and scattering medium is weakened because of its interaction with the medium. If the radiation has an initial radiance L that becomes $L + dL$, see Figure 5.1, after passing through a thickness ds in the direction of propagation we may write (Chandrasekhar, 1960),

$$dL = -\kappa\beta L ds, \tag{5.1}$$

where, κ is the mass absorption coefficient and β is the density of the absorbing medium. At this point no wavelength specifics are assumed. The medium itself may also contribute to the beam of radiation from scattering or emission events that occur within the medium. To represent this the emission is defined (Chandrasekhar, 1960),

$$dL = \beta j ds, \tag{5.2}$$

where, j is the emission coefficient. If equation 5.1 represents the loss term and equation 5.2 represents the gain term, then the total change in the radiance may be written as (Chandrasekhar, 1960),

$$dL = -\kappa\beta L ds + \beta j ds. \tag{5.3}$$

Further, the ratio of the emission coefficient j to the absorption coefficient κ is defined as the source function J. Therefore, the source function J has the units of radiance and is defined as (Chandrasekhar, 1960),

$$J = \frac{j}{\kappa}. \tag{5.4}$$

Dividing equation 5.3 by κ and β allows the equation of transfer to be written as,

$$\frac{dL}{\kappa\beta} = -L ds + J ds. \tag{5.5}$$

Further, in differential form the equation of transfer may be expressed as,

$$\frac{dL}{\kappa\beta ds} + L = J. \tag{5.6}$$

5.2 Derivation of the RTE

In plane parallel atmospheres it is convenient to measure normal to the plane of stratification (Chandrasekhar, 1960) and ds is modified to reflect this; namely,

$$ds = \frac{dz}{\cos\theta}, \tag{5.7}$$

where, ds is the path length of the radiation through the medium of layer thickness dz at an incident zenith angle θ and where dz is the path length normal to the plane of stratification (as shown in Figure 5.1). This allows equation 5.6 to be recast,

$$\cos\theta \frac{dL}{\kappa\beta dz} + L = J. \tag{5.8}$$

The dimensionless constant, the normal optical thickness τ, is defined as (Chandrasekhar, 1960),

$$\tau = \int_{z_1}^{z_2} \kappa\beta dz, \tag{5.9}$$

where the upper and lower limits of equation 5.9 are not yet defined since the limits are dependent on the direction of radiation propagation. The rate of change of equation 5.9 is given as,

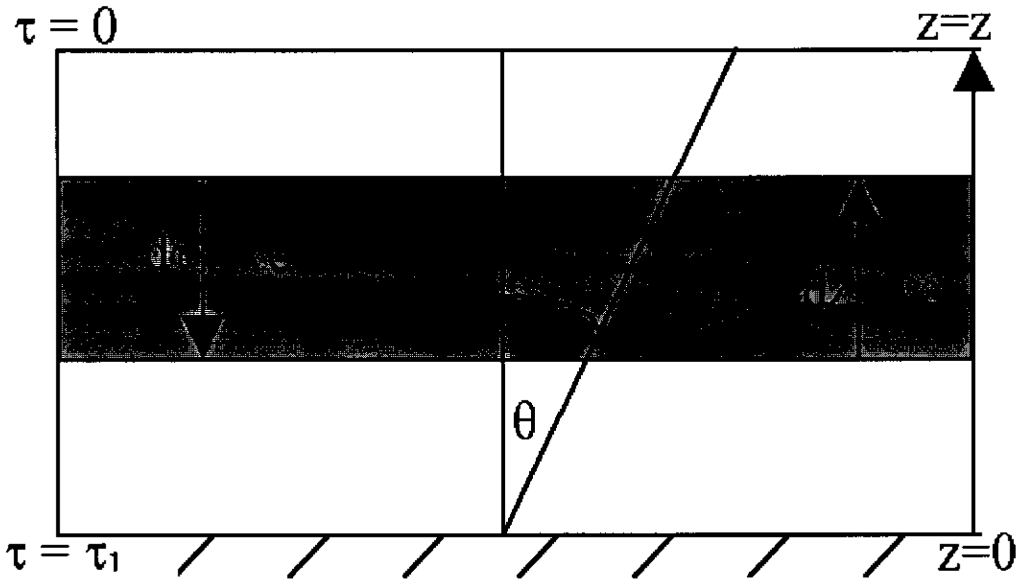

Figure 5.2: The geometry used for the definition of equation 5.10.

$$d\tau = -\kappa\beta dz, \tag{5.10}$$

and shown graphically in Figure 5.2. Equation 5.8 may now be recast as,

$$-\mu\frac{dL}{d\tau} + L = J, \tag{5.11}$$

where, $\mu = \cos\theta$ and $(1 \geq \mu > 0)$. Therefore the zenith angle ranges from 0° to 90°. The beam of radiation may also be defined in terms of its angular directionality by recasting equation 5.11 as (Chandrasekhar, 1960),

$$\mu\frac{dL(\tau,\mu,\phi)}{d\tau} - L(\tau,\mu,\phi) = -J(\tau,\mu,\phi), \tag{5.12}$$

where, ϕ is the azimuth angle between the incident radiation and the outgoing radiation. Figure 5.3 demonstrates the angular geometry defined for the RTE derivations. To solve equation 5.12, a linear first order differential equation, we first divide by μ to yield,

$$\frac{dL(\tau,\mu,\phi)}{d\tau} - \frac{1}{\mu}L(\tau,\mu,\phi) = -\frac{1}{\mu}J(\tau,\mu,\phi). \tag{5.13}$$

To solve equation 5.13 requires the use of an integrating factor F. The integrating factor used for the purpose of this analysis is given by equation 5.14,

$$F = e^{-\frac{\tau}{\mu}}, \tag{5.14}$$

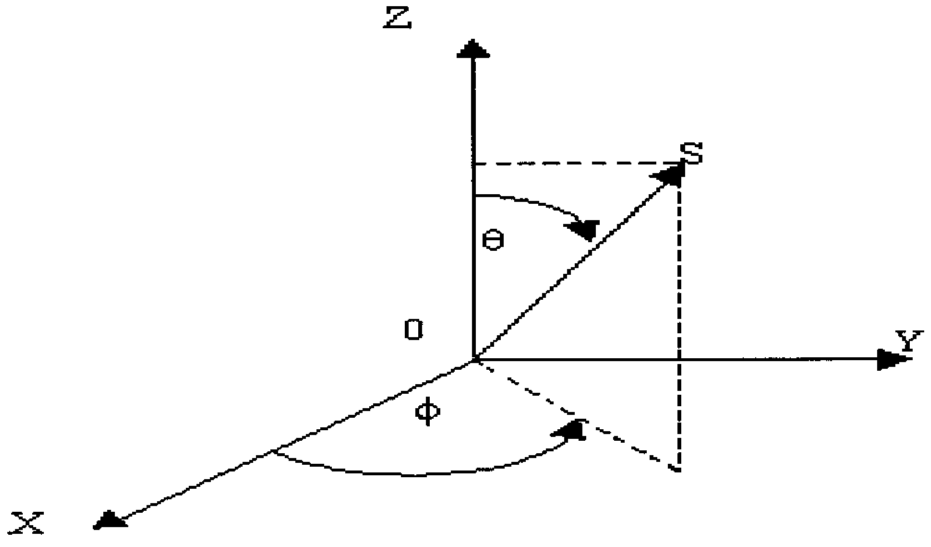

Figure 5.3: The geometry used for the derivation of the radiative transfer equation in plane parallel atmospheres.

For a finite atmosphere it is usual to have the boundary conditions such that $\tau = 0$ at the top of the atmosphere and $\tau = \tau_1$ at the bottom of the atmosphere (Chandrasekhar, 1960). Multiplying equation 5.13 by the integrating factor yields,

$$e^{-\frac{\tau}{\mu}} \frac{dL(\tau,\mu,\phi)}{d\tau} - e^{-\frac{\tau}{\mu}} \frac{1}{\mu} L(\tau,\mu,\phi) = -e^{-\frac{\tau}{\mu}} \frac{1}{\mu} J(\tau,\mu,\phi). \tag{5.15}$$

The solution we seek satisfies the following relationship,

$$\frac{d[e^{-\frac{\tau}{\mu}} L(\tau,\mu,\phi)]}{d\tau} = -e^{-\frac{\tau}{\mu}} \frac{1}{\mu} J(\tau,\mu,\phi). \tag{5.16}$$

Outward Radiance

To establish the outward (spacebound) radiance at level τ between τ_1 and τ we integrate,

$$\int_{\tau_1}^{\tau} d[e^{-\frac{\tau'}{\mu}} L(\tau',\mu,\phi)] d\tau' = -\int_{\tau_1}^{\tau} e^{-\frac{\tau'}{\mu}} \frac{1}{\mu} J(\tau',\mu,\phi) d\tau', \tag{5.17}$$

which proceeds as follows,

$$e^{-\frac{\tau}{\mu}} L(\tau,\mu,\phi) - e^{-\frac{\tau_1}{\mu}} L(\tau_1,\mu,\phi) = -\int_{\tau_1}^{\tau} e^{-\frac{\tau'}{\mu}} \frac{1}{\mu} J(\tau',\mu,\phi) d\tau'. \tag{5.18}$$

Dividing by $e^{-\frac{\tau}{\mu}}$, taking the $-e^{-\frac{\tau_1}{\mu}} L(\tau_1,\mu,\phi)$ term to the right hand side and interchanging the limits of integration on the $-\int_{\tau_1}^{\tau} e^{-\frac{\tau'}{\mu}} \frac{1}{\mu} J(\tau',\mu,\phi) d\tau'$ term yields

(Chandrasekhar, 1960),

$$L(\tau,\mu,\phi) = L(\tau_1,\mu,\phi)e^{-\frac{(\tau_1-\tau)}{\mu}} + \int_{\tau}^{\tau_1} e^{-\frac{(\tau'-\tau)}{\mu}}\frac{1}{\mu}J(\tau',\mu,\phi)d\tau'. \tag{5.19}$$

The emergent radiance at the top of the atmosphere (at $\tau = 0$) is seen to be (Chandrasekhar, 1960),

$$L(0,\mu,\phi) = L(\tau_1,\mu,\phi)e^{-\frac{\tau_1}{\mu}} + \int_{0}^{\tau_1} e^{-\frac{\tau'}{\mu}}\frac{1}{\mu}J(\tau',\mu,\phi)d\tau'. \tag{5.20}$$

Inward Radiance

To obtain the inward (earthbound) radiance at level τ between $\tau = 0$ and τ we integrate again and note that μ is between 0 and 1 but the direction is given as $-\mu$, where the negative indicates the inward direction. We have,

$$\int_0^{\tau} d[e^{-\frac{\tau'}{-\mu}}L(\tau',-\mu,\phi)]d\tau' = -\int_0^{\tau} e^{-\frac{\tau'}{-\mu}}\frac{1}{-\mu}J(\tau',-\mu,\phi)d\tau', \tag{5.21}$$

$$e^{-\frac{\tau}{-\mu}}L(\tau,-\mu,\phi) - e^{-\frac{0}{-\mu}}L(0,-\mu,\phi) = -\int_0^{\tau} e^{-\frac{\tau'}{-\mu}}\frac{1}{-\mu}J(\tau',-\mu,\phi)d\tau', \tag{5.22}$$

$$e^{\frac{\tau}{\mu}}L(\tau,-\mu,\phi) - L(0,-\mu,\phi) = \int_0^{\tau} e^{\frac{\tau'}{\mu}}\frac{1}{\mu}J(\tau',-\mu,\phi)d\tau'. \tag{5.23}$$

next, equation 5.23 is divided by $e^{\frac{\tau}{\mu}}$ and the $-L(0,-\mu,\phi)$ term is taken to the right hand side to yield (Chandrasekhar, 1960),

$$L(\tau,-\mu,\phi) = L(0,-\mu,\phi)e^{-\frac{\tau}{\mu}} + \int_0^{\tau} e^{-\frac{(\tau-\tau')}{\mu}}\frac{1}{\mu}J(\tau',-\mu,\phi)d\tau'. \tag{5.24}$$

The emergent radiance at $\tau = \tau_1$ impacting on the boundary is given as (Chandrasekhar, 1960),

$$L(\tau_1,-\mu,\phi) = L(0,-\mu,\phi)e^{-\frac{\tau_1}{\mu}} + \int_0^{\tau_1} e^{-\frac{(\tau_1-\tau')}{\mu}}\frac{1}{\mu}J(\tau',-\mu,\phi)d\tau'. \tag{5.25}$$

The Source Function

The source function $J(\tau;\theta,\phi)$ is now defined in the following manner (Chandrasekhar, 1960; Liou, 1980),

$$\begin{aligned} J(\tau;\theta,\phi) \;=\; & \int_0^{2\pi}\int_0^{\pi} \frac{P(\theta,\phi;\theta',\phi')}{4\pi}L(\tau;\theta',\phi')\sin\theta' d\theta' d\phi' \\ & + \frac{\omega_o}{4\pi}E_o e^{-\frac{\tau}{\cos\theta_0}}P(\theta,\phi;-\theta_0,\phi_0), \end{aligned} \tag{5.26}$$

where, θ_0 and ϕ_0 are the incident zenith and azimuth solar angles respectively. E_o is the solar irradiance, and ω_o is the single scattering albedo. The first term on the right hand side represents the diffuse radiation field while the second term represents the reduced radiation field that penetrates to a level τ after undergoing single scattering. Also, $P(\theta, \phi; -\theta_0, \phi_0)$ is the scattering phase function. The phase function is normalised such that,

$$\int_{4\pi} \frac{P(\Omega, \Omega')}{4\pi} d\Omega'' = 1, \tag{5.27}$$

where, Ω is the solid angle scattered into and Ω' is the solid angle from which the radiation is incident. $L(\tau; \theta', \phi')$ is the incident radiation from the direction θ' and ϕ'. Now $\sin\theta' d\theta'$ is expressed in terms of μ' such that,

$$\mu' = \cos\theta', \tag{5.28}$$

$$-d\mu' = \sin\theta' d\theta'. \tag{5.29}$$

Substituting equation 5.29 into equation 5.26 yields the following,

$$\begin{aligned} J(\tau; \mu, \phi) &= -\int_0^{2\pi} \int_1^{-1} \frac{P(\mu, \phi; \mu', \phi')}{4\pi} L(\tau; \mu', \phi') d\mu' d\phi' \\ &\quad + \frac{\omega_o}{4\pi} E_o e^{-\frac{\tau}{\mu_0}} P(\mu, \phi; -\mu_0, \phi_0). \end{aligned} \tag{5.30}$$

Interchanging the limits of integration of the variable μ in the integral in equation 5.30 leads to the following definition of the source function,

$$\begin{aligned} J(\tau; \mu, \phi) &= \int_0^{2\pi} \int_{-1}^{1} \frac{P(\mu, \phi; \mu', \phi')}{4\pi} L(\tau; \mu', \phi') d\mu' d\phi' \\ &\quad + \frac{\omega_o}{4\pi} E_o e^{-\frac{\tau}{\mu_0}} P(\mu, \phi; -\mu_0, \phi_0). \end{aligned} \tag{5.31}$$

Accordingly, the source function may be represented by,

$$J(\tau; \mu, \phi) = J_d(\tau; \mu, \phi) + J_r(\tau; \mu, \phi), \tag{5.32}$$

where, $J_d(\tau; \mu, \phi)$ is the source function from the diffuse radiation field and $J_r(\tau; \mu, \phi)$ is the source function from the reduced radiation field. If single scattering only is considered then the source function is represented by (Liou, 1980),

$$J_r(\tau; \mu, \phi) = \frac{\omega_o}{4\pi} E_o e^{-\frac{\tau}{\mu_0}} P(\mu, \phi; -\mu_0, \phi_0). \tag{5.33}$$

Equation 5.33 is used in the following section to derive the single scattering solution of the RTE.

5.3 The Single Scattering Solution to the Radiative Transfer Equation

If single scattering only is considered, equation 5.33 may be substituted into equation 5.13 to solve for the radiance,

$$\frac{dL(\tau,\mu,\phi)}{d\tau}-\frac{1}{\mu}L(\tau,\mu,\phi)=-\frac{1}{\mu}(J_r(\tau,\mu,\phi)). \tag{5.34}$$

Therefore, a solution to equation 5.35 is sought,

$$\frac{d[e^{-\frac{\tau}{\mu}}L(\tau,\Omega)]}{d\tau}=-e^{-\frac{\tau}{\mu}}\frac{1}{\mu}(\frac{\omega_o}{4\pi}E_oe^{-\frac{\tau}{\mu_0}}P(\Omega;-\Omega_o), \tag{5.35}$$

where the subscripts Ω and Ω_o have been used to represent solid angles defined by μ,ϕ and μ',ϕ' and μ_0,ϕ_0 respectively.

Single Scattered Outward Radiance

To determine the outward radiance between τ and τ_1, equation 5.35 is integrated,

$$\int_{\tau_1}^{\tau}d[e^{-\frac{\tau'}{\mu}}L(\tau',\Omega)]d\tau'=-\int_{\tau_1}^{\tau}(e^{-\frac{\tau'}{\mu}}\frac{1}{\mu}(\frac{\omega_o}{4\pi}E_oe^{-\frac{\tau'}{\mu_0}}P(\Omega;-\Omega_o)), \tag{5.36}$$

and,

$$\begin{aligned}L(\tau,\mu,\phi) &= L(\tau_1,\mu,\phi)e^{-\frac{(\tau_1-\tau)}{\mu}}\\ &+\int_{\tau}^{\tau_1}e^{-\frac{(\tau'-\tau)}{\mu}}\frac{1}{\mu}[\frac{\omega_oE_o}{4\pi}e^{-\frac{\tau'}{\mu_0}}P(\mu,\phi;-\mu_0,\phi_0)]d\tau'.\end{aligned} \tag{5.37}$$

Therefore, at optical depth $\tau=0$ the outward radiance is given by,

$$L(0,\mu,\phi)=L(\tau_1,\mu,\phi)e^{-\frac{\tau_1}{\mu}}+\frac{\omega_oE_o}{4\pi\mu}P(\mu,\phi;-\mu_0,\phi_0)\int_0^{\tau_1}e^{-[\frac{\tau'}{\mu}+\frac{\tau'}{\mu_0}]}d\tau'. \tag{5.38}$$

Single Scattered Inward Radiance

The inward radiance between optical depths $\tau=0$ and τ is stated, with details omitted, as,

$$\begin{aligned}L(\tau,-\mu,\phi) &= L(0,-\mu,\phi)e^{-\frac{\tau}{\mu}}\\ &+\int_{0}^{\tau}e^{-\frac{(\tau-\tau')}{\mu}}\frac{1}{\mu}[\frac{\omega_oE_o}{4\pi}e^{-\frac{\tau'}{\mu_0}}P(-\mu,\phi;-\mu_0,\phi_0)]d\tau'.\end{aligned} \tag{5.39}$$

Recasting equations 5.39 in terms of the atmospheric optical depth at $\tau=\tau_1$,

$$L(\tau_1,-\mu,\phi) = L(0,-\mu,\phi)e^{-\frac{\tau_1}{\mu}} + \frac{\omega_o E_o}{4\pi\mu}P(-\mu,\phi;-\mu_0,\phi_0)\int_0^{\tau_1} e^{-\left[\frac{(\tau_1-\tau')}{\mu}+\frac{\tau'}{\mu_0}\right]}d\tau'. \tag{5.40}$$

Equations 5.38 and 5.40 are equivalent to the upward and downward intensities derived by Liou (1980). If equation 5.38 is used in conjunction with instrument spectral response functions and for specific viewing conditions, solar geometry and atmospheric chemistry it will yield radiances detected by a sensor.

5.4 The RTE in Terms as a Function of Column Water Vapour

This section sets out the method of deriving the RTE for at-sensor spectral radiance as a function of the column water vapour W. Described first is the derivation of the atmospheric reflectance function $R(\mu,\phi;\mu_o,\phi_o)$ and the atmospheric transmission function $T(\mu,\phi;\mu_o,\phi_o)$. The derivation of $R(\mu,\phi;\mu_o,\phi_o)$ and $T(\mu,\phi;\mu_o,\phi_o)$ allows the spherical albedo $\bar{r}$ and the diffuse transmission $t(\mu)$ to be defined.

All derivations, at this point, assume a single scattering regime. A Lambertian reflecting surface ρ_s is introduced into the calculations and from this the RTE is derived to admit the inclusion of ρ_s. This approach allows the RTE to be expressed in terms of the optical depth τ_1, and ultimately the column water vapour W, where it is shown that a quadratic form of the RTE is representative for small optical depth. It is stated that the derivations up to this point are only valid for regions where τ_1 is considered small. This analysis is extended to regions of larger optical depth where it is shown that an approximating polynomial well represents the RTE and where the order is found to depend on the magnitude of the molecular optical depth τ_1. Therefore, making the derivation applicable in regions of larger optical depth and applicable to multiple scattering regimes.

5.4.1 Reflected and Transmitted Radiance

For a finite plane parallel atmosphere bounded on two sides at $\tau = 0$ and $\tau = \tau_1$, that doesn't contain atmospheric aerosols, and that scatters the incident radiation

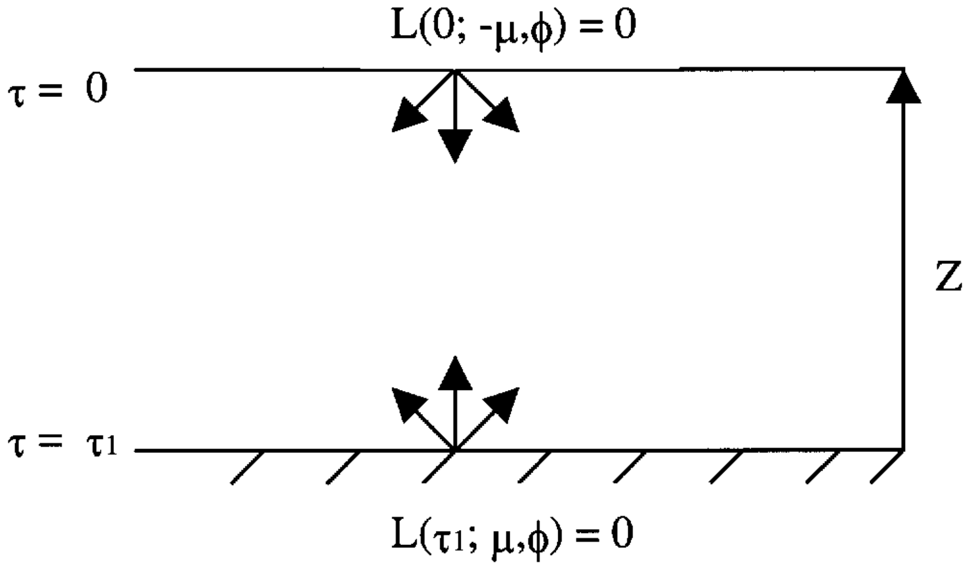

Figure 5.4: The Definition of the diffuse downward top-of-atmosphere radiance and the diffuse upward bottom-of-atmosphere radiance. The molecular thickness of the atmosphere is τ_1

only once, and where there is no diffuse upward and downward radiation at the base and top of the atmosphere, the following can be stated (Liou, 1980); see Figure 5.4,

$$L(0; -\mu, \phi) = 0, \tag{5.41}$$

and,

$$L(\tau_1; \mu, \phi) = 0. \tag{5.42}$$

where, $\mu = \cos(\theta)$ is the zenith angle and ϕ is the azimuth angle. A negative variable implies incoming radiation (space to Earth) and a positive value implies outgoing (Earth to space). It should be noted that no spectral dependencies are shown in 5.41 and 5.42 but they are implied.

Solving equations 5.38 and 5.40, with the boundary conditions given by equations 5.41 and 5.42, the reflected and transmitted radiances for a finite, single scattering atmosphere are given as (Liou, 1980; Kaufman, 1989),

$$L(0; \mu, \phi) = \frac{\omega_o \mu_o E_o}{4\pi(\mu + \mu_o)} P(\mu, \phi; -\mu_o, \phi_o) \left\{ 1 - \exp\left[-\tau_1 \left(\frac{1}{\mu} + \frac{1}{\mu_o} \right) \right] \right\}, \tag{5.43}$$

and,

$$L(\tau_1; -\mu, \phi) = \frac{\omega_o \mu_o E_o}{4\pi(\mu - \mu_o)} P(-\mu, \phi; -\mu_o, -\phi_o) \left(e^{\frac{-\tau_1}{\mu}} - e^{\frac{-\tau_1}{\mu_o}} \right), \tag{5.44}$$

Equation 5.43 represents the upward atmospheric reflected radiance and equation 5.44 represents the downward atmospheric transmitted radiance, where, ω_o is the single scattering albedo, μ_o is the solar zenith angle, μ is the scattered zenith angle, ϕ_o is the solar azimuth angle, ϕ is the scattered azimuth angle, E_o is the top-of-atmosphere (TOA) solar irradiance and τ_1 is the molecular optical depth of the atmosphere. $P(-\mu,\phi;-\mu_o,-\phi_o)$ and $P(\mu,\phi;-\mu_o,-\phi_o)$ are the molecular phase functions for the downward and upward propagated radiance. The following definition applies to the phase function. Unless stated otherwise, the first pair of angles in parentheses are the direction of the outgoing radiation after scattering while the second pair of angles are the direction of the incoming radiation before scattering.

5.4.2 The Transmittance and Reflectance Functions

Two functions are now defined, namely, the reflectance function $R(\mu,\phi;\mu_o,\phi_o)$ and the transmission function $T(\mu,\phi;\mu_o,\phi_o)$. The zenith angle μ_0 is inward but the negative sign is omitted for simplicity. The reflection function and the transmittance function are defined as,

$$L_r(0,\mu,\phi) = \frac{1}{\pi}\int_0^{2\pi}\int_0^1 R(\mu,\phi;\mu',\phi')L_0(-\mu',\phi')\mu' d\mu' d\phi', \tag{5.45}$$

and,

$$L_t(\tau_1,-\mu,\phi) = \frac{1}{\pi}\int_0^{2\pi}\int_0^1 T(\mu,\phi;\mu',\phi')L_0(-\mu',\phi')\mu' d\mu' d\phi'. \tag{5.46}$$

These definitions are analogous with those given by Chandrasekhar (1960) and Liou (1980). It is noted that the zenith angle μ in the transmission function is an arbitrary angle and does not necessarily represent the same angle that is in the reflectance function. The factor $(1/\pi)$ in equations 5.45 and 5.46 is a normalisation factor such that,

$$\frac{1}{\pi}\int_0^{2\pi}\int_0^1 R(\mu,\phi;\mu',\phi')\mu' d\mu' d\phi' = 1, \tag{5.47}$$

and,

$$\frac{1}{\pi}\int_0^{2\pi}\int_0^1 T(\mu,\phi;\mu',\phi')\mu' d\mu' d\phi' = 1. \tag{5.48}$$

In the terrestrial atmosphere $L_0(-\mu',\phi') = L_0(-\mu_0,\phi_0)$ and represents the incident solar radiance. For most practical problems, it can be approximated with the Dirac delta function (Chandrasekhar, 1960; Liou, 1980).

The Dirac Delta Function

The definition of the Dirac delta function $\delta(t-t_0)$ is given as (Boas, 1966),

$$\delta(t-t_0)=0,\ \text{for } t\neq t_0,\ \text{and }, \delta(t-t_0)=1,\ \text{for } t=t_0. \qquad (5.49)$$

This function is used in integral equations in the form (Boas, 1966),

$$\int \phi(t)\delta(t-t_0)dt=\phi(t_0). \qquad (5.50)$$

Accordingly, the incident solar radiance, which is approximated as monodirectional (Liou, 1980), has an angular distribution expressible in terms of the delta function,

$$L_0(-\mu,\phi)=\delta(\mu-\mu_0)\delta(\phi-\phi_0)E_0. \qquad (5.51)$$

Therefore, expressed in terms of the Dirac delta function, equations 5.45 and 5.46 are,

$$L_r(0,\mu,\phi)=\frac{1}{\pi}\int_0^{2\pi}\int_0^1 R(\mu,\phi;\mu_0,\phi_0)\delta(\mu'-\mu_0)\delta(\phi'-\phi_0)E_0\mu_0 d\mu' d\phi', \qquad (5.52)$$

and,

$$L_t(\tau_1,-\mu,\phi)=\frac{1}{\pi}\int_0^{2\pi}\int_0^1 T(\mu,\phi;\mu_0,\phi_0)\delta(\mu'-\mu_0)\delta(\phi'-\phi_0)E_0\mu_0 d\mu' d\phi'. \qquad (5.53)$$

Employing the definition of equation 5.50, equations 5.52 and 5.53 become,

$$L_r(0,\mu,\phi)=\frac{1}{\pi}\mu_0 E_0 R(\mu,\phi;\mu_0,\phi_0), \qquad (5.54)$$

and,

$$L_t(\tau_1,-\mu,\phi)=\frac{1}{\pi}\mu_0 E_0 T(\mu,\phi;\mu_0,\phi_0). \qquad (5.55)$$

The single scattering reflectance function $R(\mu,\phi;\mu_o,\phi_o)$ may be written as (Tanre *et al.*, 1986),

$$R(\mu,\phi;\mu_o,\phi_o)=\frac{L_r(0,\mu,\phi)\pi}{\mu_o E_o}, \qquad (5.56)$$

and is analogous with the definition given by Liou (1980), where $L_r(0,\mu,\phi)$ is the reflected radiance. The transmission function $T(\mu,\phi;\mu_o,\phi_o)$ is defined as (Liou, 1980)

$$T(\mu,\phi;\mu_o,\phi_o)=\frac{L_t(\tau_1,-\mu,\phi)\pi}{\mu_o E_o}, \qquad (5.57)$$

where, $L_t(\tau_1,-\mu,\phi)$ is the transmitted radiance. Substituting equation 5.43 into 5.56, the reflectance function $R(\mu,\phi;\mu_o,\phi_o)$ may be recast as,

$$R(\mu,\phi;\mu_o,\phi_o) = \frac{\omega_o P(\mu,\phi;-\mu_o,\phi_o)}{4(\mu+\mu_o)}\left\{1-\exp\left[-\tau_1\left(\frac{1}{\mu}+\frac{1}{\mu_o}\right)\right]\right\}. \qquad (5.58)$$

Substituting equation 5.44 into equation 5.57, recasts the transmission function $T(\mu,\phi;\mu_o,\phi_o)$ as,

$$T(\mu,\phi;\mu_o,\phi_o) = \frac{\omega_o P(-\mu,\phi;-\mu_o,\phi_o)}{4(\mu-\mu_o)}\left(e^{\frac{-\tau_1}{\mu}} - e^{\frac{-\tau_1}{\mu_o}}\right). \qquad (5.59)$$

It should be noted that $L_t(\tau_1,-\mu,\phi)$, the diffuse transmitted radiance, does not include the directly transmitted solar radiance $\frac{E_o}{\pi}e^{\frac{-\tau_1}{\mu_o}}$ (Liou, 1980). If the optical depth τ_1 is small, the following mathematical approximation is made (Kaufman, 1989),

$$e^{-\frac{\tau}{\mu'}} = 1 - \frac{\tau}{\mu'}. \qquad (5.60)$$

Equation 5.60 is used in conjunction with equations 5.58 and 5.59 to express $R(\mu,\phi;\mu_o,\phi_o)$ and $T(\mu,\phi;\mu_o,\phi_o)$ in terms of the molecular optical depth τ_1. The form of $R(\mu,\phi;\mu_o,\phi_o)$ shown is the same as that used by Tanre *et al.* (1986) in the 5S atmospheric modelling code, namely,

$$R(\mu,\phi;\mu_o,\phi_o) = \frac{\omega_o P(\mu,\phi;-\mu_o,\phi_o)}{4\mu\mu_o}\tau_1, \qquad (5.61)$$

and,

$$T(\mu,\phi;\mu_o,\phi_o) = \frac{\omega_o P(-\mu,\phi;-\mu_o,\phi_o)}{4\mu\mu_o}\tau_1. \qquad (5.62)$$

The Diffuse Transmittance Function

Equation 5.62 is used to define the downward diffuse transmission $t(\mu_0)$ over a hemispherical scattering atmosphere and is given by equation 5.63.

$$\begin{aligned} t(\mu_o) &= \frac{1}{\pi}\int_0^{2\pi}\int_0^1 T(\mu,\phi;\mu_o,\phi_o)\mu d\mu d\phi, \\ &= \int_0^{2\pi}\int_0^1 \frac{\omega_o P(-\mu,\phi;-\mu_o,\phi_o)}{4\pi\mu\mu_o}\tau_1 \mu d\mu d\phi, \\ &= \frac{\omega_o\tau_1}{4\pi\mu_o}\int_0^{2\pi}\int_0^1 P(-\mu,\phi;-\mu_o,\phi_o)d\mu d\phi, \\ &= \frac{\omega_o\tau_1}{4\pi\mu_o}P(-\mu_o,\phi_o), \qquad (5.63) \end{aligned}$$

where,

$$P(-\mu_o,\phi_o) = \int_0^{2\pi}\int_0^1 P(-\mu,\phi;-\mu_o,\phi_o)d\mu d\phi. \qquad (5.64)$$

Accordingly, the upward diffuse transmission $t(\mu)$ for a hemispherical scattering atmosphere may be defined as,

$$\begin{aligned} t(\mu) &= \frac{1}{\pi}\int_0^{2\pi}\int_0^1 T(\mu,\phi;\mu',\phi')\mu' d\mu' d\phi', \\ &= \int_0^{2\pi}\int_0^1 \frac{\omega_o P(\mu,\phi;\mu',\phi')}{4\pi\mu\mu'}\tau_1\mu' d\mu' d\phi', \\ &= \frac{\omega_o\tau_1}{4\pi\mu}\int_0^{2\pi}\int_0^1 P(\mu,\phi;\mu',\phi')d\mu' d\phi', \\ &= \frac{\omega_o\tau_1}{4\pi\mu}P(\mu,\phi), \end{aligned} \tag{5.65}$$

where, μ' and ω' are respectively the incoming zenith angle and azimuth angles before scattering and where,

$$P(\mu,\phi) = \int_0^{2\pi}\int_0^1 P(\mu,\phi;\mu',\phi')d\mu' d\phi'. \tag{5.66}$$

The Spherical Albedo

The local or planetary albedo is defined by Liou (1980) as,

$$r(\mu_0) = \frac{1}{\pi}\int_0^{2\pi}\int_0^1 R(\mu,\phi;\mu_0\phi_0)\mu d\mu d\phi. \tag{5.67}$$

Equation 5.67 is recast so that it is given as the spherical (or global) albedo. The ratio of the irradiance reflected by the entire planet to the irradiance incident upon the entire planet may be represented as (Liou, 1980),

$$\bar{r} = 2\int_0^1 r(\mu_o)\mu_o d\mu_o. \tag{5.68}$$

5.5 The Inclusion of the Surface Reflectance

For a Lambertian surface reflectance ρ_s the diffuse upward radiance in equation 5.42 may be written as (Liou, 1980),

$$L(\tau_1;\mu,\phi) = L_s = const, \tag{5.69}$$

and the source function, as defined by equation 5.31, is given as,

$$\begin{aligned} J(\tau;\mu,\phi) &= L_S\int_0^{2\pi}\int_{-1}^1 \frac{P(\mu,\phi;\mu',\phi')}{4\pi}d\mu' d\phi' \\ &\quad + \frac{\omega_o}{4\pi}E_o e^{-\frac{\tau}{\mu_0}}P(\mu,\phi;-\mu_0,\phi_0). \end{aligned} \tag{5.70}$$

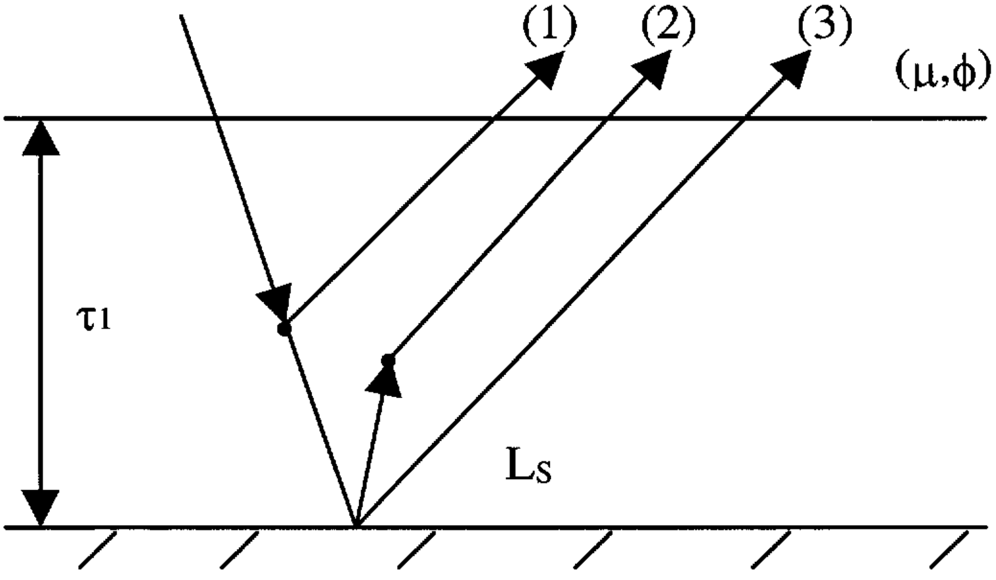

Figure 5.5: Upward diffuse radiance. (1) is the atmospheric reflected component, (2) is the diffuse transmitted surface reflected component and (3) is the directed transmitted surface reflected component. L_s represents the diffuse reflected radiance from the surface.

Substituting equations 5.69 and 5.70 into equation 5.20 and solving yields the solution of the upward at-sensor RTE for a Lambertian reflecting surface ρ_s. Equation 5.20 may now be recast, such that, the upward reflected radiance is given in terms of path, surface radiance and atmospheric transmittance. This is written as (Liou, 1980), (Figure 5.5 gives the definition of the radiative components (1), (2) and (3)),

$$L_S(0;\mu,\phi) = L(0;\mu,\phi) + L_s t(\mu) + L_s e^{-\frac{\tau_1}{\mu}}, \tag{5.71}$$

where, the first term ((1) in Figure 5.5) represents the atmospheric path radiance the second term ((2) in Figure 5.5) represents the upward diffuse radiance for L_s and the third term ((3) in Figure 5.5) represents the directly transmitted radiance for L_s. If the total transmission function $\gamma(\mu)$ is defined as (Chandrasekhar, 1960; Deschamps *et al.*, 1983; Liou, 1980),

$$\gamma(\mu) = e^{-\frac{\tau_1}{\mu}} + t(\mu), \tag{5.72}$$

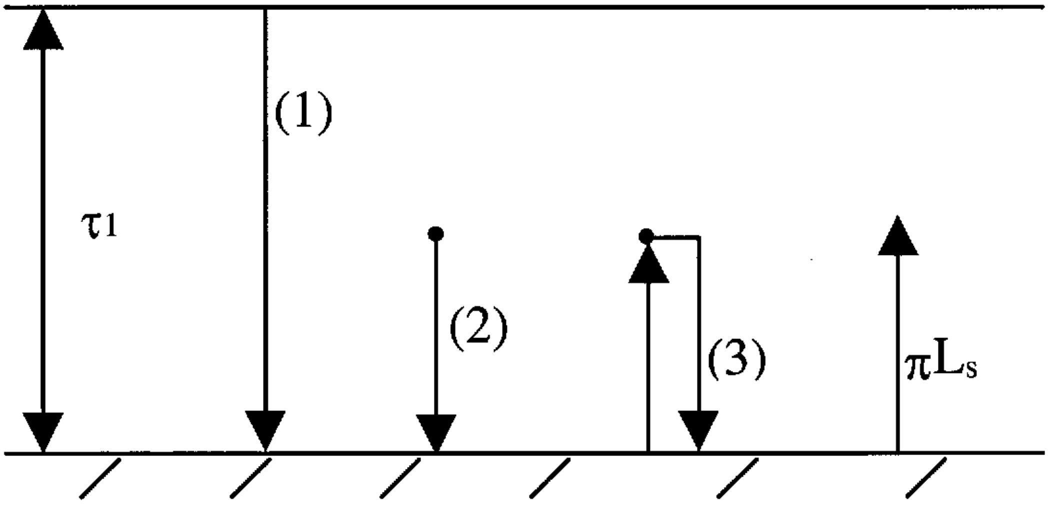

Figure 5.6: The downwelling irradiance is comprised of three parts. (1) The direct transmission component. (2) The diffuse transmission component. (3) The component of L_s reflected back down by the atmosphere.

and equation 5.61 is used for the representation of the path radiance, then equation 5.71 may be recast as,

$$L_S(0;\mu,\phi) = \frac{\mu_o E_o}{\pi} R(\mu,\phi;-\mu_o,\phi_o) + L_s\gamma(\mu). \tag{5.73}$$

5.6 The Derivation of the Diffuse Surface Radiance

To derive L_s, the upward irradiance has to equal the downward irradiance $F^{\downarrow}$ multiplied by the surface reflectance ρ_s (Chandrasekhar, 1960; Liou, 1980) (see figure 5.6 for the definition of the radiative components (1), (2) and (3)) therefore,

$$\pi L_s = \rho_s F^{\downarrow} \tag{5.74}$$

The downward irradiance is comprised of three components. These are,

- the direct transmitted solar irradiance. Given in Figure 5.6 as (1)

$$\mu_o E_o e^{-\frac{\tau_1}{\mu_o}} = \mu_o E_o \left(1 - \frac{\tau_1}{\mu_o}\right), \tag{5.75}$$

- the diffusely transmitted solar irradiance (photons that are scattered into the sensor view path). Given in Figure 5.6 as (2). It should be noted that these are not photons created in the atmosphere, merely scattered photons.

$$\int_0^{2\pi}\int_0^1 L(\tau_1;-\mu,\phi)\mu d\mu d\phi = \int_0^{2\pi}\int_0^1 E_o\mu_o T(\mu,\phi;\mu_o,\phi_o)\mu d\mu d\phi \tag{5.76}$$

$$= \frac{E_o\mu_o\omega_o\tau_1}{4\pi\mu_o}P(-\mu_o,\phi_o),$$

and,

- The component of L_s that is reflected back to the surface by the atmosphere. Given in Figure 5.6 as (3),

$$\int_0^{2\pi}\int_0^1 L_s r(\mu)\mu d\mu d\phi = 2\pi L_s\int_0^1 r(\mu)\mu d\mu, \tag{5.77}$$

$$= \pi L_s\bar{r}.$$

Adding equations 5.75, 5.76 and 5.77 and equating to the downward irradiance $F^{\downarrow}$ yields,

$$F^{\downarrow} = \left(\mu_o E_o\left(1-\frac{\tau_1}{\mu_o}\right) + \frac{E_o\mu_o\omega_o\tau_1}{4\pi\mu_o}P(-\mu_o,\phi_o) + \pi L_s\bar{r}\right) \tag{5.78}$$

Substituting equation 5.78 into equation 5.74 gives,

$$\pi L_s = \rho_s\left(\mu_o E_o\left(1-\frac{\tau_1}{\mu_o}\right) + \frac{E_o\mu_o\omega_o\tau_1}{4\pi\mu_o}P(-\mu_o,\phi_o) + \pi L_s\bar{r}\right). \tag{5.79}$$

Rearranging equation 5.79 to solve for L_s, yields (Liou, 1980),

$$L_s = \frac{\rho_s\mu_o E_o}{(1-\rho_s\bar{r})\pi}\left[1-\frac{\tau_1}{\mu_o}+\frac{\omega_o P(-\mu_o,\phi_o)}{4\pi\mu_o}\tau_1\right]. \tag{5.80}$$

Alternatively, equation 5.80 may be written as,

$$L_s = \frac{\rho_s\mu_o E_o}{(1-\rho_s\bar{r})\pi}\gamma(\mu_o), \tag{5.81}$$

where,

$$\gamma(\mu_o) = \left[1-\frac{\tau_1}{\mu_o}+\frac{\omega_o P(-\mu_o,\phi_o)}{4\pi\mu_o}\tau_1\right]. \tag{5.82}$$

Substituting equation 5.81 into equation 5.73 gives the total at-sensor radiance. This is expressed as (Liou, 1980),

$$L_S(0;\mu,\phi) = \frac{\mu_o E_o}{\pi}R(\mu,\phi;-\mu_o,\phi_o) + \frac{\rho_s\mu_o E_o}{(1-\rho_s\bar{r})\pi}\gamma(\mu_o)\gamma(\mu). \tag{5.83}$$

5.7 Expressing the Total Radiance in Terms of Optical Depth

The following derivations are defined by the author, and as such, are not cited. Equation 5.83 is now recast in terms of the optical depth τ_1. If the diffuse downward and diffuse upward transmission functions (defined in equation 5.82 with the appropriate geometry), $\gamma(\mu_o)$ and $\gamma(\mu)$ are multiplied together, we obtain

$$\begin{aligned}\gamma(\mu_o)\gamma(\mu) &= \left[1+\tau_1\left(\frac{\omega_o P(-\mu_o,\phi_o)}{4\pi\mu_o}-\frac{1}{\mu_o}\right)\right]\left[1+\tau_1\left(\frac{\omega_o P(\mu,\phi)}{4\pi\mu}-\frac{1}{\mu}\right)\right] \\ &= 1+\tau_1\left(\frac{\omega_o P(\mu,\phi)}{4\pi\mu}-\frac{1}{\mu}\right)+\tau_1\left(\frac{\omega_o P(-\mu_o,\phi_o)}{4\pi\mu_o}-\frac{1}{\mu_o}\right) \\ &\quad +\tau_1^2\left(\frac{\omega_o P(\mu,\phi)}{4\pi\mu}-\frac{1}{\mu}\right)\left(\frac{\omega_o P(-\mu_o,\phi_o)}{4\pi\mu_o}-\frac{1}{\mu_o}\right). \qquad (5.84)\end{aligned}$$

Let,

$$A_1=\left(\frac{\omega_o P(\mu,\phi)}{4\pi\mu}-\frac{1}{\mu}\right), \qquad (5.85)$$

$$A_2=\left(\frac{\omega_o P(-\mu_o,\phi_o)}{4\pi\mu_o}-\frac{1}{\mu_o}\right), \qquad (5.86)$$

and,

$$A_1A_2=A_3=\left(\frac{\omega_o P(\mu,\phi)}{4\pi\mu}-\frac{1}{\mu}\right)\left(\frac{\omega_o P(-\mu_o,\phi_o)}{4\pi\mu_o}-\frac{1}{\mu_o}\right). \qquad (5.87)$$

Equation 5.84 may be expressed as,

$$\gamma(\mu_o)\gamma(\mu)=1+(A_1+A_2)\tau_1+A_3\tau_1^2. \qquad (5.88)$$

Recasting equation 5.83, by substituting equations 5.88 for $\gamma(\mu_o)\gamma(\mu)$ and equation 5.61 for $R(\mu,\phi;-\mu_o,\phi_o)$, yields the following equation,

$$\begin{aligned}L_S(0;\mu,\phi) &= \frac{E_o\omega_o P(\mu,\phi;-\mu_o,\phi_o)}{4\pi\mu}\tau_1 \\ &\quad +\frac{\rho_s\mu_o E_o}{(1-\rho_s\bar{r})\pi}\left(1+(A_1+A_2)\tau_1+A_3\tau_1^2\right). \qquad (5.89)\end{aligned}$$

Further, if two more coefficients A_4 and A_5 are defined where,

$$A_4=\frac{E_o\omega_o P(\mu,\phi;-\mu_o,\phi_o)}{4\pi\mu}, \qquad (5.90)$$

and,

$$A_5=\frac{\rho_s\mu_o E_o}{(1-\rho_s\bar{r})\pi}, \qquad (5.91)$$

equation 5.89 is expressible as,

$$L_S(0;\mu,\phi) = A_4\tau_1 + A_5\left(1 + (A_1 + A_2)\tau_1 + A_3\tau_1^2\right) \tag{5.92}$$
$$= A_3A_5\tau_1^2 + \left[(A_1 + A_2)A_5 + A_4\right]\tau_1 + A_5.$$

Again, it is noted that the derivations that have been presented to this point are only valid for regions of small molecular optical depth.

5.8 Expressing the Total Radiance in Terms of the Atmospheric Water Vapour

To express equation 5.92 in terms of the column atmospheric water vapour W, the optical depth τ_1 requires definition in terms of W. It is assumed, for the purpose of this study, that atmospheric column water vapour is the strongest absorber in the VNIR-SWIR spectral region (Green *et al.*, 1991, 1993) and that it is the only absorber present in the region of interest. If the normal molecular optical depth is given as (Liou, 1980),

$$\tau_1 = \int_z^\infty \kappa\beta(z')dz', \tag{5.93}$$

where, κ is the absorption coefficient, β is the density of the absorbing medium and z is the normalised path distance. If κ is assumed to be constant for a given wavelength (i.e κ is independent of the normalised path distance z) (Liou, 1980), then τ_1 may be expressed in a plane parallel finite atmosphere as,

$$\tau_1 = \kappa \int_{z_1}^{z_2} \beta(z')dz', \tag{5.94}$$

where, the atmospheric water vapour content is described by,

$$W = \int_{z_1}^{z_2} \beta(z')dz'. \tag{5.95}$$

Therefore, τ_1 is recast as,

$$\tau_1 = \kappa W, \tag{5.96}$$

and equation 5.92 may be expressed in terms of the column atmospheric water vapour W as,

$$L_S(0;\mu,\phi) = A_3A_5\kappa^2W^2 + \left[(A_1 + A_2)A_5 + A_4\right]\kappa W + A_5. \tag{5.97}$$

With the following coefficients defined, namely,

$$A = A_3 A_5 \kappa^2, \tag{5.98}$$

$$B = [(A_1 + A_2)A_5 + A_4]\,\kappa, \tag{5.99}$$

and,

$$C = A_5, \tag{5.100}$$

equation 5.97 may now be recast in terms of the column atmospheric water vapour W. The form is shown to be quadratic and is,

$$L_S(0;\mu,\phi) = AW^2 + BW + C. \tag{5.101}$$

Using MODTRAN4 as a platform for the synthetic generation of an at-sensor spectral signal, equation 5.101 is found to hold true for total molecular optical depths ranging from approximately 0.025 to approximately 0.25. For this analysis, no atmospheric aerosol was used and the surface reflectance was set to unity. As well, the bandwidth of the MODTRAN output was 1 cm^{-1}, which was then convolved to AVIRIS bandpass. The two-stream radiative transfer method was used rather than the computationally expensive DISORT method. In regions where the total molecular optical depth is greater than approximately 0.01 and less than 0.025, equation 5.101 is reducible to a linear function of atmospheric water vapour W and under these conditions equation 5.101 may be expressed as,

$$L_S(0;\mu,\phi) = BW + C. \tag{5.102}$$

In regions where the molecular optical depth is less than 0.01, equation 5.102 may be further reduced and is accurately represented by a constant,

$$L_S(0;\mu,\phi) = C = \frac{\rho_s \mu_o E_o}{(1-\rho_s\bar{r})\pi}. \tag{5.103}$$

Equation 5.103 represents a region where the optical depth is zero and therefore the transmittance is unity. This type of spectral region is considered an atmospheric window region. Equations 5.103, 5.102 and 5.101 demonstrate that, as the optical depth decreases, the order required to represent the radiance as a function of atmospheric column water vapour decreases.

Figure 5.7 was generated with MODTRAN4.0 and with no aerosol present in the atmosphere. The figures show results from a tropical atmosphere and a MLW atmosphere with a surface reflectance of unity. The synthetic atmospheres were altered for a series of atmospheric column water vapour content and polynomial fits applied to a given spectral wavelength. Figure 5.7 shows the results of the analysis. The polynomial fits to the data, the order required and the r^2 values of the fits are shown for a particular wavelength. As the molecular optical depth increases the order of polynomial required to model the radiance also increases. It is noted that the magnitude of the first order coefficient for the 1047 nm fit is extremely small and may be neglected; therefore, the 1047 nm radiance values are well represented by equation 5.103.

5.8.1 Extension to Larger Optical Depths

The results of the previous section demonstrate that equations 5.103, 5.102 and 5.101 are only applicable in regions where the optical depth is relatively small, typically for $\tau_1(\lambda) < 0.25$, and therefore are not applicable in the band centre of atmospheric column water vapour absorption regions. As the molecular optical depth decreases the order required to model the at-sensor radiance was also seen to decrease until it was represented by a constant term. Therefore, if the optical depth increases, beyond those already tested, the order required to model the radiances should also increase beyond a second order polynomial. If a polynomial fit is used to model the atmospheric water vapour bands, then an nth degree polynomial, where n is greater than 2, should provide an accurate representation model of the at-sensor radiance for given geometries and surface spectral reflectance.

To test this hypothesis, three wavelengths in the water vapour absorption regions were used. Wavelengths at 942, 961 and 1124 nm are used in the analysis. The wavelengths at 1380 and 1870 nm regions are not used and are treated as totally absorbing in the VNIR-SWIR spectral region. MODTRAN4 was used to generate synthetic at-sensor spectral radiance for a given viewing and solar geometry and surface spectral reflectance $\rho_s(\lambda)$ and with ten values of W varying from 0.2 to 4.2 cm and 0.1 to 0.85 cm for the tropical and mid-latitude winter atmospheres respectively. Again, the analysis was performed in a no aerosol environment. This produces a series of spectral at-sensor radiance signals for a

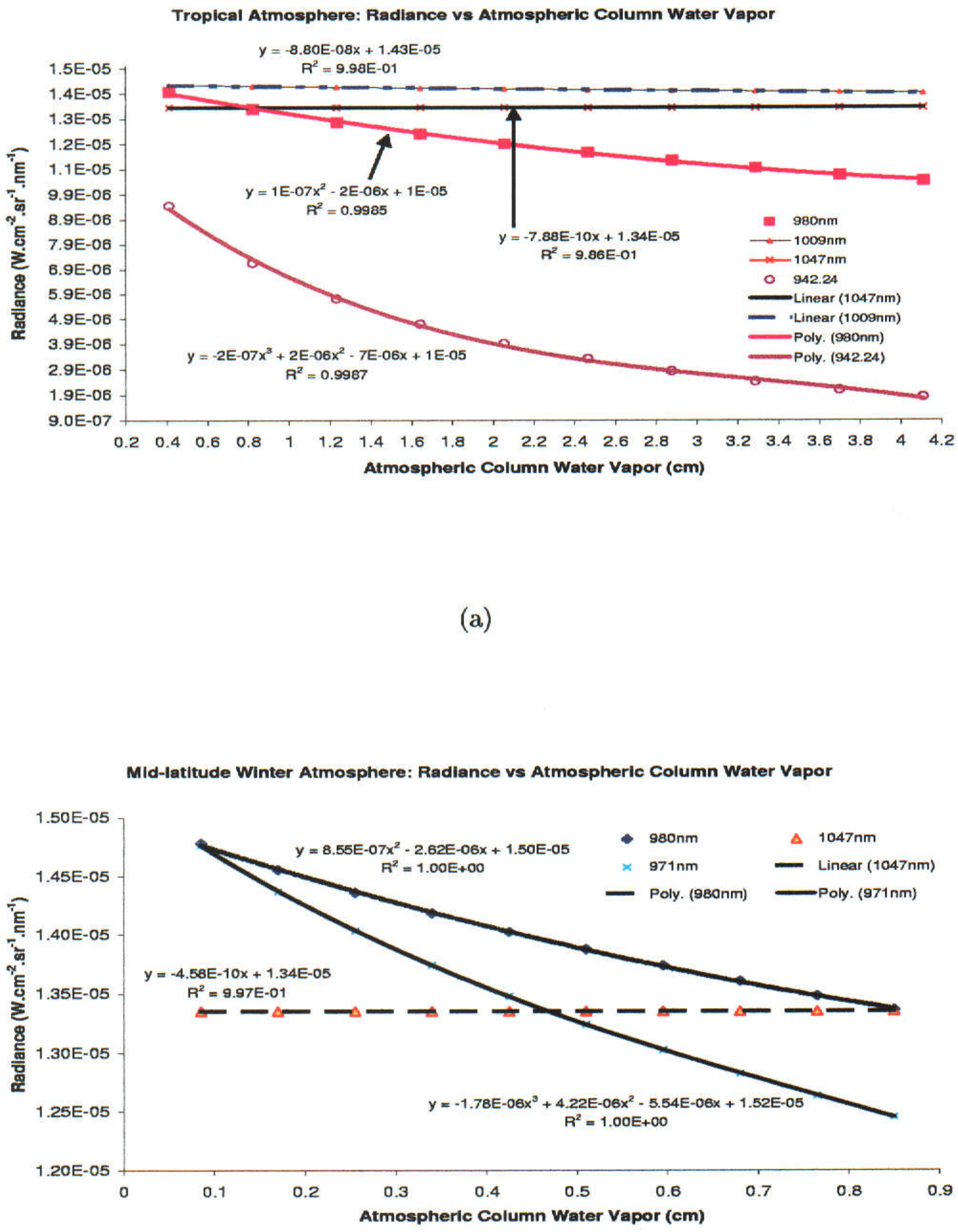

(a)

(b)

Figure 5.7: Radiance as a function of column water vapour for different wavelengths and two different atmospheric models (Tropics in 5.7(a) and Mid-latitude winter in 5.7(b)). As the optical depth increases the degree of the polynomial required to represent the radiance as a function of atmospheric column water vapour increases.

sequence of atmospheric column water vapour amounts which allows the validity of approximating with higher order polynomials to be investigated for larger molecular optical depths.

Figure 5.8 shows the results of the analysis for a tropical and MLW atmosphere where the solar zenith and scan angle were set to 30°. It is noted that, because of the smaller optical depth in the MLW atmosphere, the fourth order polynomial could be replaced by a cubic, if required. This conclusion is consistent with that found for decreasing optical depth. Therefore, to model at-sensor spectral radiance as a function of W for the 940 and 1140 nm water bands, a fourth order polynomial of the following form is required,

$$L_S(0;\mu,\phi) = a_4W^4 + a_3W^3 + a_2W^2 + a_1W + a_0, \qquad (5.104)$$

where, the coefficients a_4, a_3, a_2, a_1 and a_0 may be found from an empirical fit to the MODTRAN4.0 modelled data.

5.9 Summary

In this chapter the relevant radiative transfer theory has been reviewed and formulations developed that are appropriate to the thrust of the current research. Importantly, it is shown that the representation of the TOA radiance in the spectral regions of interest, in terms of atmospheric water vapour, has a sound theoretical basis.

This basis demonstrated that for given viewing and solar geometries and surface spectral reflectance $\rho(\lambda)$, the at-sensor radiance may be modelled with n^{th} order polynomials, where the order of the polynomial is determined by the optical depth of the spectral region under consideration. The importance of this is that the VNIR-SWIR spectrum may be modelled with spectrally dependent polynomials whose order is dependent on the spectral location under consideration.

Any polynomial established at a given wavelength, and for given surface reflectance, may be used to recreate the at-sensor radiance with differing water vapour contents. Figure 5.9 shows three such synthetic signals created by 224 spectrally dependent polynomials that are a function of atmospheric column water vapour. In this case, an AVIRIS signal for a mid-latitude summer is recreated

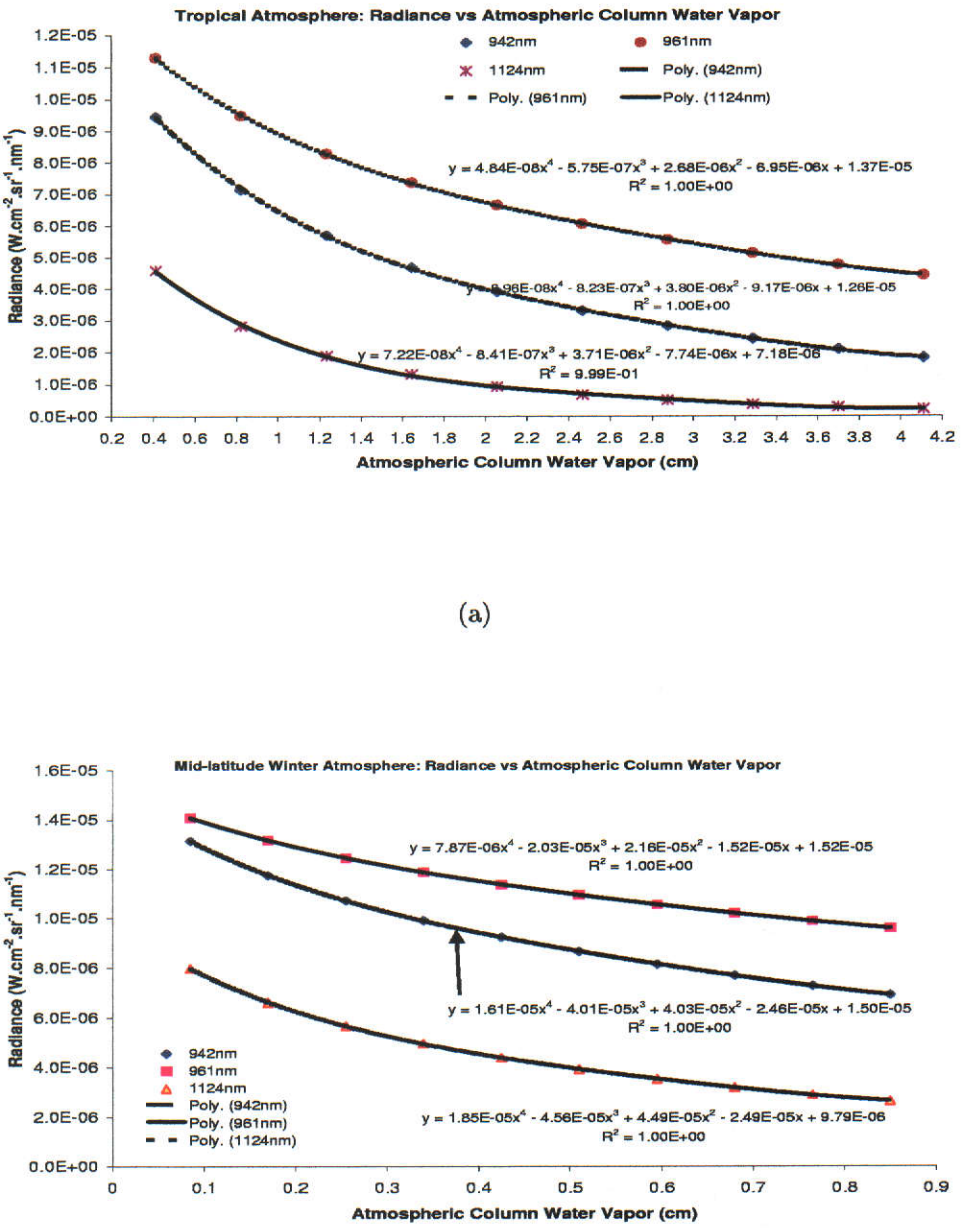

(a)

(b)

Figure 5.8: The changes in radiance for differing atmospheric column water vapour with a surface reflectance of unity. The wavelengths used are shown in the legend. Two of the fourth order fits to the MODTRAN modelled data are for the 942nm and 1124nm absorption feature. A fourth order polynomial fit is seen to represent the change in radiances exceptionally well.

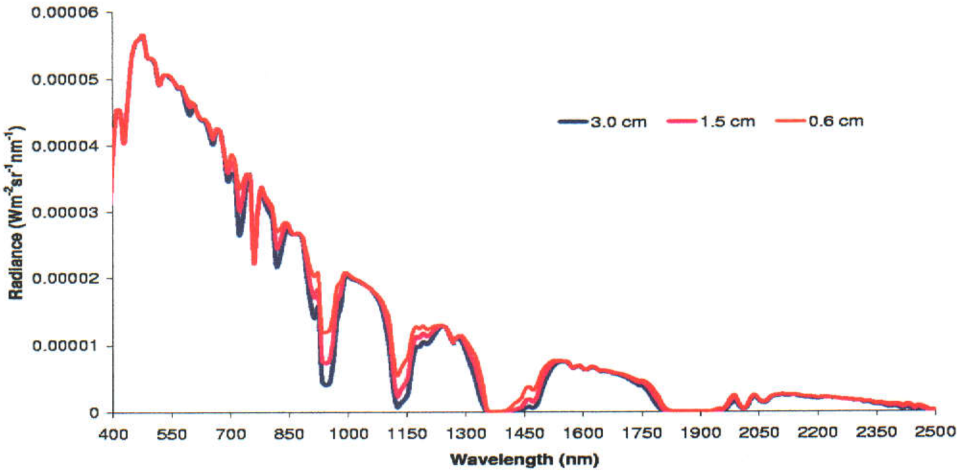

(a)

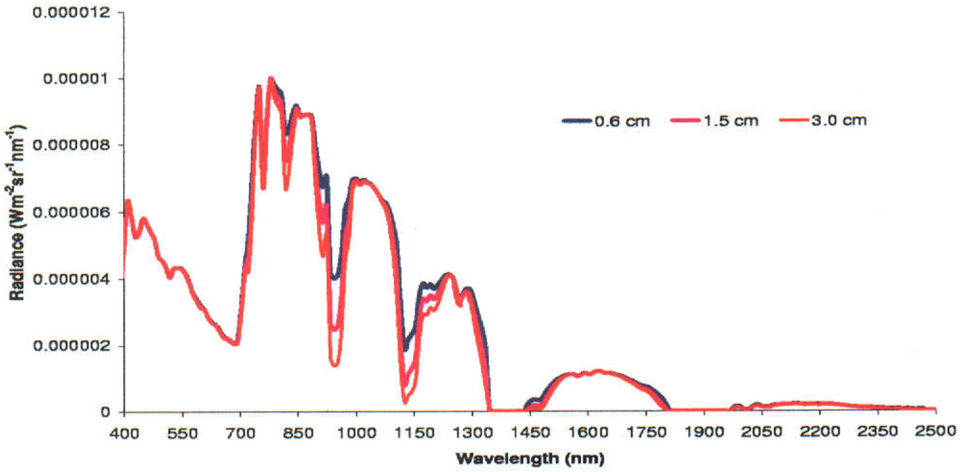

(b)

Figure 5.9: Shown in (a) are three synthetic generated signals for three different water vapour amounts. (b) shows the same signal scaled for a vegetation reflectance surface. Both (a) and (b) are created by a series (224 in this case) of spectrally dependent polynomials (fourth order) that are a function of water vapour.

with a surface reflectance of one. Using the same polynomials (created for total radiance and path radiance) the at-sensor signals are generated for a vegetated reflecting surface in 5.9(b).

For the plots in Figure 5.9 fourth order polynomials were used for the entire VNIR-SWIR. The following conclusion is made based on the MODTRAN4.0 trials. As the molecular optical depth τ_1 increases, the order of the polynomial required to model the at-sensor radiance, as a function of W, also increases. This is represented mathematically as,

$$L_S(\lambda, W) = \sum_{n=0}^{m} a_n(\lambda) W^n, \tag{5.105}$$

where, $L_S(\lambda)$ is the at-sensor spectral radiance for wavelength λ, $a_n(\lambda)$ is the n^{th} order coefficient at wavelength λ and W^n is the atmospheric column water vapour raised to the n^{th} power, where n ranges from 0 to m. The value of m has been found to range from 0 to 4 in the 400–2500 nm spectral region. The maximum value of m, equal to 4, is confined to the atmospheric absorption bands and the visible portion of the spectrum. The coefficients $a_n(\lambda)$ are found from an empirical fit to the synthetic MODTRAN computed at-sensor spectral radiance. Equation 5.105 may be thought of as an approximating polynomial for a spectrally dependent power series. The power series is defined as (Thomas and Finney, 1992),

$$\sum_{n=0}^{\infty} a_n(\lambda) W^n = a_0(\lambda) + a_1(\lambda) W + a_2(\lambda) W^2 + \ldots + a_n(\lambda) W^n + \ldots \tag{5.106}$$

A significant outcome from this chapter is that it provides the theoretical basis for the development of the core of the investigation which follows. Specifically, the TSR method, developed in the following chapter (and explored via application later in the study) stems from the conclusions and findings of this chapter.

Chapter 6

Transmittance Slope Ratio (TSR)

The chapter develops a method of estimating atmospheric water vapour from remotely sensed hyperspectral VNIR-SWIR data. The methodology is developed as a differential absorption method based on a measured hyperspectral radiance signal that may be related to a calibration or reference curve to provide an estimate of the water vapour.

One of the main aims of the method is to not only provide a physically robust method, but one that utilises a greater portion of the VNIR-SWIR for the estimation of column water vapour. By this it is meant that the use of the 940 and 1140 nm water vapour features is still applicable but that the method may be extended to encompass the 1380 and 1880 nm water features. It will be shown that the increased spectral range allows the method to employ rejection schemes that point to outlying water vapour results that may result from surface absorption features that may be located within the atmospheric water vapour features i.e. leaf water absorption features located in the 940 and 1140 nm water vapour features.

With the radiance at the sensor defined as a polynomial function of atmospheric column water vapour (see Chapter 5), the Transmittance Slope Ratio (TSR) may now be derived. It will be shown that a weighted mean radiance (based on measurement channels) may be defined (see section 6.4) and that it is a function of the reference wavelength. The weighted mean radiance is further expressed as a ratio against the reference radiance which in turn defines a TSR value. The TSR value is subsequently incorporated into a spectral calibration curve, allowing the TSR value to be expressed as an estimated water vapour content. The calibration curves are shown to be representable as a function of atmospheric water vapour, such that, a measured TSR value may be used to estimate atmospheric water vapour for the pixel of interest.

An estimate of surface reflectance is required, such that, it may be used in conjunction with the TSR method and spectral calibration curves. Chapter 7 outlines the methodology used to estimate surface reflectance, on a pixel-by-pixel basis, in the VNIR-SWIR spectral region. As such, all derivations in this chapter assume that an estimate of the surface reflectance has been made in accordance with the procedure to be described in Chapter 7.

6.1 The Weighted Mean Radiance

The TSR uses a weighted mean radiance value in the formation of the differential ratio, but rather than base the weighting on reference channels either side of a measurement channel, the weighting is given across consecutive water vapour absorption features. This produces a weighted radiance that is a function of the measurement channels rather than reference channels. The measurement channels are outlined in section 6.4.

The weighting of measurement channels across water vapour absorption bands is referred to in this document as the transmittance slope (TS) and is analogous with the continuum slope used by other methods. Figure 6.1 demonstrates the main difference between continuum slope weighting and TS weighting. The continuum slope, called the reflectance slope in Figure 6.1, may be termed by both names. It is equally true that the gradient across the absorption feature is indicative of the continuum as well as the underlying surface reflectance gradient. In the latter case the gradient is modified by the solar irradiance and atmospheric transmittance. In Figure 6.1, the TSR method weights the radiances between two consecutive water band absorption feature measurement channels rather than reference channels either side of the absorption feature. Shown in Figure 6.2 is an example of the weighted mean radiance as a function of wavelength λ for spectral region 1 (See Chapter 6.4 for the definition of a spectral region).

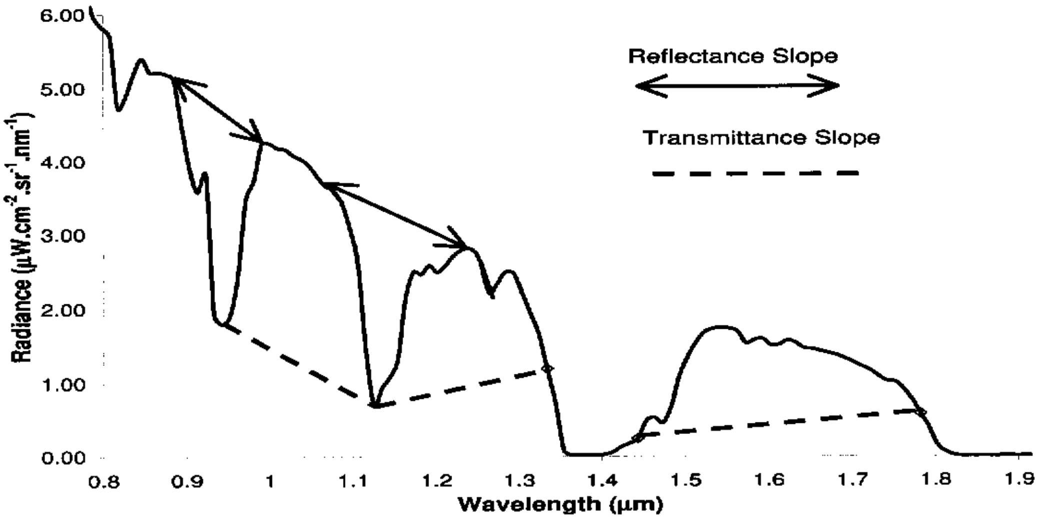

Figure 6.1: The Transmittance Slope (TS) is created between measurement channels that have their location in water vapour absorption features. The continuum slope (shown here as the reflectance slope: see text) used in other ratio methods spans an absorption feature instead. The use of a TS allows a larger part of the spectrum to be utilised. The last two transmittance slopes (far right and centre) do not use the band centre of the 1380 and 1880 nm water features due to the totally absorbing nature of these two features.

Definition of the Weighted Mean Radiance

The definition of weighted mean radiance, as a function of wavelength, is given as,

$$\bar{L}(W, \lambda_i) = X_1(\lambda_i) L_1(W, \lambda_1) + X_2(\lambda_i) L_2(W, \lambda_2), \tag{6.1}$$

where, $L_1(W, \lambda_1)$ is the radiance at measurement channel 1 with wavelength λ_1 with atmospheric column water vapour W, and $L_2(W, \lambda_2)$ is the radiance at measurement channel 2 with wavelength λ_2 with atmospheric column water vapour W and λ_i is the wavelength under consideration and where $\lambda_1 \le \lambda_i \le \lambda_2$. The weighting factors $X_1(\lambda_i)$ and $X_2(\lambda_i)$ are given as,

$$X_1(\lambda_i) = \frac{\lambda_2 - \lambda_i}{\lambda_2 - \lambda_1} \; and \; X_2(\lambda_i) = \frac{\lambda_i - \lambda_1}{\lambda_2 - \lambda_1}$$

6.2 Transmittance Slope Ratio

Producing a TSR value requires that the weighted mean radiance, defined by equation 6.1, is used in an appropriate ratio form. As with other ratio techniques,

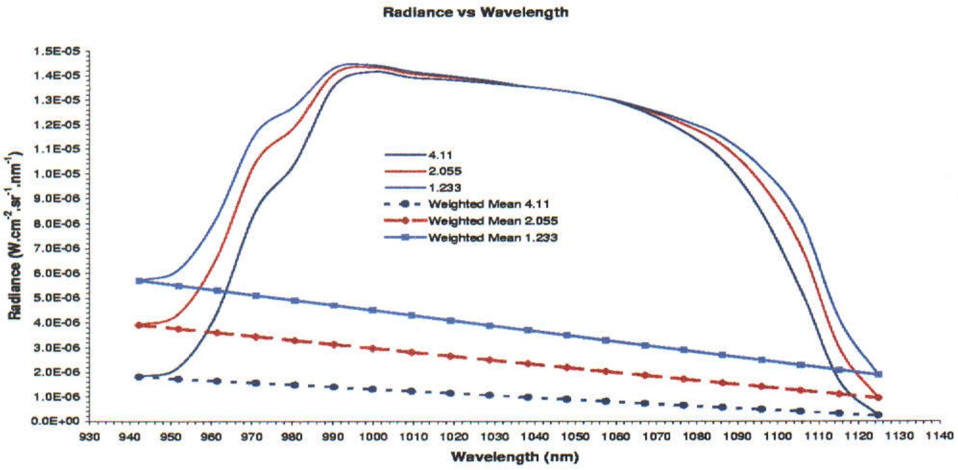

Figure 6.2: Three weighted mean radiance curves (linear curves) as a function of wavelength for spectral region 1 with three different water vapour content (in g cm^{-2}), see Tables 6.1 and 6.2. The wavelength position defines the amount of weighting. For example, as the 940 nm region is approached, heavier weighting is given to the 940 nm absorption feature rather than the 1140 nm feature.

the form of differential ratio is defined, and is given by, measurement channel radiance divided by reference channel radiance (see section 4). This process is similar to already established band ratio techniques, outlined in (Bruegge *et al.*, 1990); (Kaufman and Gao, 1992) and (Schläpfer, 1998), that are commonly used to evaluate atmospheric column water vapour. The measurement and reference channels, for HyMap and AVIRIS, are defined in section 6.4 and given by Tables 6.1 and 6.2 respectively. The configuration of reference and measurement channel used in the TSR method proves beneficial for a number of reasons and is discussed further in later chapters.

Definition of the TSR

The definition of the TSR proceeds in the following manner. The weighted mean radiance, given by equation 6.1, is divided by equation 5.105, which represents the at-sensor radiance, to produce equation 6.2,

$$TSR(W,\lambda_i) = \frac{\bar{L}(W,\lambda_i)}{L_s(W,\lambda_i)}, \tag{6.2}$$

where $TSR(W,\lambda_i)$ is the TSR value at wavelength λ_i with atmospheric column water vapour value W.

Figure 6.3 shows a series of TSR curves against wavelength, where the only parameter adjusted is the value of W used to generate the TSR curves. Accordingly, the measurement channels have a TSR value of unity with the remaining TSR values taking on values less than unity. It is also noted that regardless of the underlying surface reflectance, almost all the TSR curves have a similar appearance to those in Figure 6.3. As previously mentioned, to generate TSR curves requires that an estimate of surface reflectance is found using the water bands such that the radiance at the sensor may be modelled. How an estimate of surface reflectance is derived in the water bands is discussed in Chapter 7. At this point, it is assumed that such an estimate may be made.

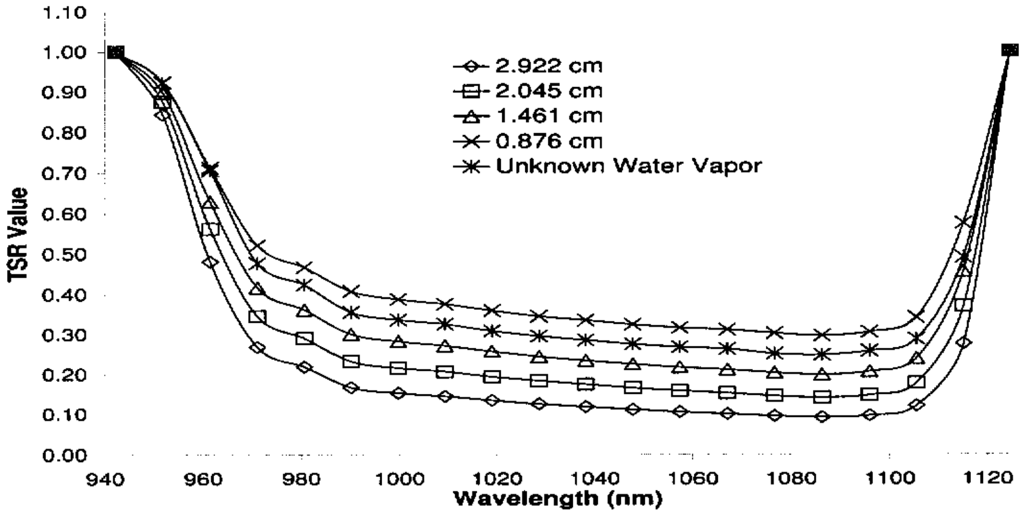

Figure 6.3: TSR value plotted against wavelength for four varying water vapour values. The TSR curves shown here are for spectral region one (see Tables 6.1 and 6.2 of section 6.4). Also shown is a measured signal, in TSR form, with unknown column water vapour. The water vapour of the measured signal is observed to have a value between 0.876 and 1.461 cm of precipitable water.

6.3 Expressing the TSR as A Function Of Atmospheric Water Vapour

To estimate atmospheric water vapour from a measured signal with an unknown column water vapour content requires that the TSR is expressible as a function of column water vapour. The resulting expression is found by considering the derivation of the at-sensor radiance as a function of atmospheric column water vapour W outlined in Chapter 5, section 5.8.1.

Writing equation 6.2 in power series form, as given by equation 5.105 for a given value of atmospheric column water vapour, yields the following equation,

$$TSR(W,\lambda_i) = \frac{X_1(\lambda_i)\sum_{k=0}^{\infty} b_k(\lambda_1)W^k + X_2(\lambda_i)\sum_{k=0}^{\infty} c_k(\lambda_2)W^k}{\sum_{k=0}^{\infty} B_k(\lambda_i)W^k}, \tag{6.3}$$

where, the numerator is the power series form of equation 6.1 and the denominator is given by equation 5.105. The numerator of equation 6.3 is recast as a single power series such that equation 6.3 is given as,

$$TSR(W,\lambda_i) = \frac{\sum_{k=0}^{\infty} C_k(\lambda_i)W^k}{\sum_{k=0}^{\infty} B_k(\lambda_i)W^k}. \tag{6.4}$$

From Thomas and Finney (1992), a convenient theorem is used to represent equation 6.4 as a single power series, if

$$A(x) = \sum_{n=0}^{\infty} a_n x^n, \tag{6.5}$$

and,

$$B(x) = \sum_{n=0}^{\infty} b_n x^n, \tag{6.6}$$

converge absolutely for $|x| < h$, where h is the radius of convergence, and,

$$c_n = a_0 b_n + a_1 b_{n-1} + a_2 b_{n-2} + \cdots + a_{n-1} b_1 + a_n b_0 = \sum_{k=0}^{n} a_k b_{n-k}, \tag{6.7}$$

then $\sum_{n=0}^{\infty} c_n x^n$ converges absolutely to $A(x)\ B(x)$ for $|x| < h$: That is,

$$(\sum_{n=0}^{\infty} a_n x^n) \cdot (\sum_{n=0}^{\infty} b_n x^n) = \sum_{n=0}^{\infty} c_n x^n. \tag{6.8}$$

It follows then that,

$$(\sum_{k=0}^{\infty} A_k(\lambda_i W^k) \cdot (\sum_{k=0}^{\infty} B_k(\lambda_i W^k) = \sum_{k=0}^{\infty} C_k(\lambda_i) W^k. \tag{6.9}$$

To confirm the left hand side of equation 6.9 is equal to the right hand side of equation 6.9, MODTRAN4 was used to produce synthetic signals from which the individual coefficients for each term in equation 6.9, were evaluated. The coefficients from the left hand side were multiplied according to equation 6.7 to produce coefficients that correspond to the right hand side of equation 6.9. The results of the equation 6.7 coefficients were compared to the MODTRAN based coefficients (corresponding to the right hand side of equation 6.9). In all cases, the relationship given by equation 6.9 was found to hold true and, as such, the following representation of equation 6.4 is used,

$$TSR(W, \lambda_i) = \sum_{k=0}^{\infty} A_k(\lambda_i) W^k = \frac{\sum_{k=0}^{\infty} C_k(\lambda_i) W^k}{\sum_{k=0}^{\infty} B_k(\lambda_i) W^k}, \tag{6.10}$$

where,

$$\begin{aligned} TSR(W, \lambda_i) &= \sum_{k=0}^{\infty} A_k(\lambda_i) W^k \\ &= A_0 + A_1 W + A_2 W^2 + \ldots + A_k W^k + \ldots, \end{aligned} \tag{6.11}$$

The coefficients $A_k(\lambda_i)$ of equation 6.11 are found by curve fitting to synthetically produced data, where $\rho_s(\lambda)$ has been retrieved in the atmospheric window regions and water bands as described in Chapter 7. Figure 6.4 shows a plot of TSR value against W for three different wavelengths.

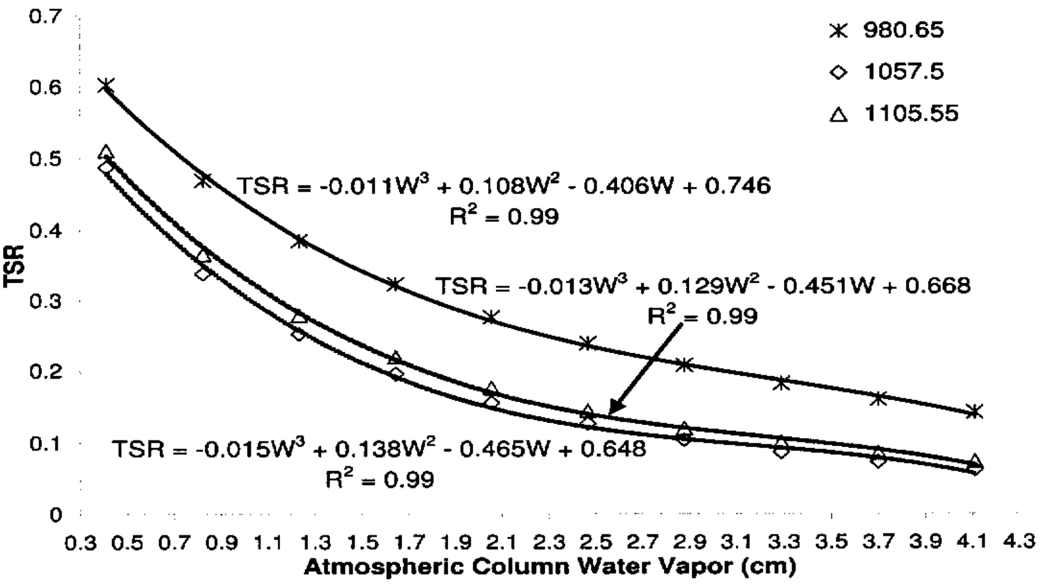

Figure 6.4: TSR versus column water vapour for three different wavelengths. All polynomials fitted to the data are cubic and are found to adequately describe the change in radiance as a function of atmospheric column water vapour W. The spectral region shown corresponds to section 1 as identified in Tables 6.1 and 6.2.

6.3.1 Polynomial Order and Representation

Using MODTRAN4 to model synthetic atmospheres allows the generation of TSR values which in turn provides a measure of the polynomial order required for equation 6.11. In all cases examined, it was found that a third order polynomial is sufficient when the range of column water vapour values used to generate equation 6.11 is large. Using equation 6.11, in the form of a third order polynomial, is not necessarily an easy task since it requires the polynomial to be solved for its characteristic roots. Rather, an alternative approach is to reflect the data in the $L_S = W$ plane. This has the effect of swapping the axes and allows equation 6.11 to be expressed in the following manner,

$$\begin{aligned} W &= \sum_{k=0}^{\infty} d_k(\lambda_i)[TSR(\lambda_i)]^k \\ &= d_0 + d_1[TSR(\lambda_i)] + d_2[TSR(\lambda_i)]^2 + \ldots \\ &\quad + d_k[TSR(\lambda_i)]^k + \ldots, \end{aligned} \tag{6.12}$$

where $TSR(\lambda_i)$ is the TSR value for a measured signal of unknown atmospheric column water vapour. Again, the coefficients of equation 6.12 may be found

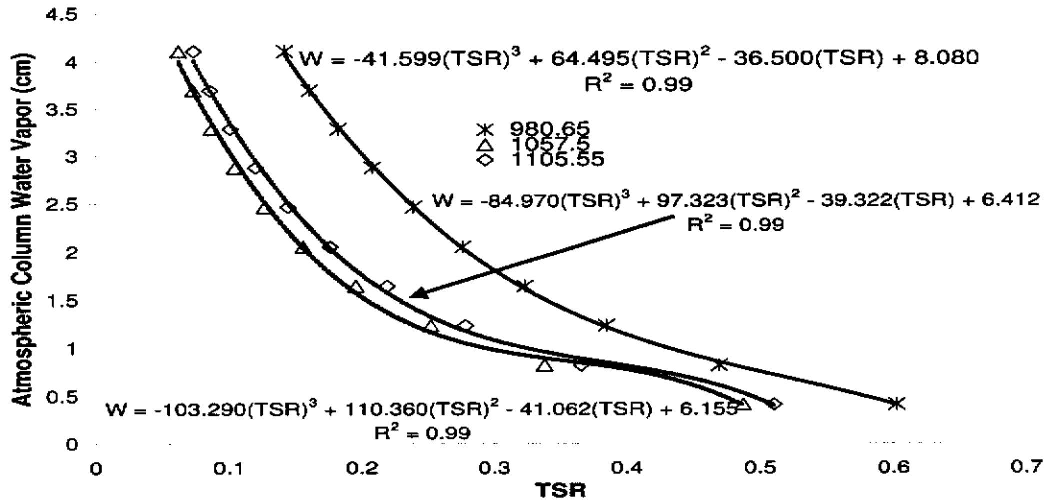

Figure 6.5: The three wavelengths (in nanometers) shown in the TSR vs Water Vapour curves of Fig. 6.4 are shown again here, the difference is that the axes have been swapped such that it is now water vapour vs TSR. In this form it is easier to solve for water vapour if a measured TSR value is known.

from a least squares fit to synthetically generated TSR values that have differing column water vapour content. Equation 6.12 may be evaluated to obtain an estimate of the minimum order required to accurately represent the atmospheric column water vapour as a function of $TSR(\lambda_i)$. As with the previous minimum order scheme, a third order polynomial was found to be sufficient, and in some cases, at the expense of accuracy (generally 3–4 %), a second order polynomial was found adequate.

An example of data corresponding to the swapped axes format is given in Figure 6.5. The form given by equation 6.12 is more practical since it does not involve the necessity to solve a third order polynomial in order to determine the atmospheric column water vapour W. The TSR value, from a measured radiance signal, is simply calculated and applied to a TSR calibration curve (e.g. Figure 6.5) given by equation 6.12 and a value of W estimated.

6.4 Measurement and Reference Channels

To produce TSR values requires a definition of measurement and reference channels used in the water vapour estimation process. Measurement and reference channels provide a means of establishing a measurable relationship between at-sensor radiance and atmospheric water vapour content. The channels are not assigned arbitrarily but are chosen to exploit desired properties of the channels in question. This section outlines the methodology for channel selection and defines the measurement and reference channels selected for use with AVIRIS and HyMap.

The reference channels used by the TSR method differ from those used by Carrére and Conel (1991, 1993), Borel and Schläpfer (1996) and Schläpfer *et al.* (1996) in two ways. Firstly, the TSR method requires two measurement channels that are used simultaneously as opposed to the one measurement channel traditionally used. Secondly, all reference channels are located between measurement channels rather than measurement channels being located between reference channels. The criterion that any given reference channel is free from absorption due to atmospheric gases is still upheld. Chapter 7 provides an example (see Figure 7.2) of this by showing surface reflectance derived in regions used as reference channels for varying water vapour amounts.

The choice of TSR reference channels means the requirement set by Schläpfer *et al.* (1996) of minimised wavelength separation of reference channels, with respect to the measurement channels, so as not to introduce errors due to surface nonlinearity does not require enforcement. Because of the manner in which the measurement and reference channels are used, three distinct spectral regions are defined in the VNIR-SWIR where the estimation of atmospheric water vapour may occur with the TSR method. Each spectral region contains two measurement channels and a number of reference channels. This section describes the selection of the measurement and reference channels, in terms of wavelength, and lists them in Tables 6.1 and 6.2 for the AVIRIS and HyMap sensors respectively

.

6.4.1 Measurement Channels

Shown in Table 6.1 are the wavelengths and corresponding channel numbers that are defined as measurement channels (M_1 and M_2) for the TSR method. Each wavelength pair defines the start and stop wavelength of a given region from

	AVIRIS		HyMap	
Region	M_1 nm (chan #)	M_2 nm (chan #)	M_1 (chan #)	M_2(chan #)
1	942 (62)	1124 (81)	(35)	(47)
2	1124 (81)	1334 (105)	(47)	(61)
3	1443 (116)	1782 (150)	(66)	(92)

Table 6.1: The selected measurement channels for AVIRIS and HyMap. M_1 and M_2 represent measurement channels 1 and 2 respectively for a given region. Shown in columns 2 and 3 are the wavelengths used by AVIRIS as well as the respective AVIRIS channels in brackets. Columns 4 and 5 are the HyMap channel numbers for the equivalent wavelength.

which the TSR may be calculated. Thus, three regions, in the context of the TSR method, are available in the VNIR-SWIR. The main criterion for a measurement channel is; it is located in a spectral region where only the active constituent of interest is present (i.e. water vapour) and that the region is sensitive to changes in the constituent content .

A subsidiary criterion is invoked if absorption due to constituent of interest is strong, such that, the band absorption centre is totally absorbing (as is the case with the 1380 and 1880 nm water vapour band centres). In the case of total absorption, in a band centre, the wings of the absorption feature are used to locate the measurement channel. If a measurement channel is set in the wings of an absorption feature it is set, such that, it still shows adequate sensitivity to constituent change and that the surface reflectance may still be estimated at the spectral location chosen.

Table 6.1 shows selected measurement channels for AVIRIS and HyMap. For both sensors two of the measurement channels are set in the band centre of water vapour absorption features (namely the 940 and the 1140 nm absorption features). The remaining three measurement channels are located off the band centre of the 1380 and 1880 nm water vapour bands. Since the transmittance of the 1380 nm and 1880 nm water vapour bands, at the band centres, is essentially opaque the measurement channels are located in the wings of the 1380 and 1880 nm water bands as per the criterion for such spectral regions. The spectral position of the measurement channels may be found by examining Figure 2.2. Even though the position of the three measurement channels are in the wings of the 1380 and 1880 nm features they are still sensitive to changes in atmospheric water vapour and therefore still provide water vapour content information when using the TSR scheme.

6.4.2 Reference Channels

In Chapter 7 it is shown that atmospheric window regions (see also Figure 7.2) are invariant to atmospheric water vapour. For the TSR scheme the criterion required of a reference channel is that it is not sensitive to changes in the constituent of interest. Thus if the at-sensor radiance for a given reference channel was modelled its value would not change if (and only if) the atmospheric water vapour content is altered. Therefore spectral channels located in atmospheric window regions are ideal reference channels since they are invariant to changes in water vapour.

Table 6.2 defines the spectral regions where suitable reference channels are found for the TSR method. In all cases the position of the reference channels are restricted such that they lie within atmospheric window regions. Since AVIRIS has a greater number of spectral channels in the window regions it also has a larger number of reference channels. If all three spectral regions are used for the estimation of water vapour a total of 32 reference channels are available for AVIRIS and 20 for HyMap. Due to the construction of the TSR method a TSR value may be estimated for each reference channel, and for each TSR value a spectral calibration curve may be defined. Therefore, an estimate of water vapor can be made for each TSR value that is determined at a given reference channel.

6.5 Procedure Outline

This section describes the methodology which when implemented, allows an estimate of column water vapour to be determined from measured hyperspectral data. Firstly, scattering definitions for use in the modelling process are discussed so as to avoid confusion about the scattering regimes. This is followed by a discussion

		AVIRIS	HyMap
Region	Wavelength (nm)	Channel Number	Channel Number
1	980-1086	66-77	40-46
2	1201-1274	89-99	54-59
3	1563-1642	128-136	77-83

Table 6.2: The reference channels for the 3 spectral regions used by the TSR method. All reference channels are located in atmospheric window regions. They are considered as stable points that are invariant to changes in atmospheric water vapour. As well as wavelength, the corresponding AVIRIS and HyMap spectral channel numbers are given.

of assumptions concerning the measured data. Following this is the procedure outline for implementing the atmospheric water vapour based on the TSR. Finally, a description of a rejection scheme used to identify outlying atmospheric water vapour results is presented.

6.5.1 Atmospheric Scattering Definitions

The derivations of the TSR are initially based on single scattering in a plane parallel, aerosol-free atmosphere. The derivation of surface reflectance on the other hand should be performed with multiple scattering models to ensure accuracy at wavelengths < 1000 nm. To use the TSR for entire spatial scenes (614 by 512 pixels per scene) required the method to be coded. To simplify the coding process all aspects of the TSR were performed under multiple scattering regimes. This does not affect the performance of the TSR method since the higher order polynomials used in the derivation ensure preservation of accuracy.

The contribution to at-sensor radiance from multiple and single scattering (SS) regimes is demonstrated in Figure 3.8, Chapter 3. The multiple scattering (MS) effect is seen to rapidly decrease ($\approx 1/\lambda^4$) and is negligible from 900 nm. The difference calculated in radiance at the sensor due to multiple and single scattering at 942 nm is approximately 1.3%.

6.5.2 TSR Procedure Assumptions

The following assumptions are made when using the TSR method for the retrieval of column water vapour on a per-pixel basis.

- All calculations carried out for the retrieval of $\rho_s(\lambda)$ use MS. Ensuring better accuracy in derived $\rho_s(\lambda)$ at shorter wavelengths ($<$ 900 nm).
- If an estimate of the meteorological range is available then it is used in the modelling process.
- The navigation data (for the flight line), including solar and viewing geometries, are known and are used as part of the modelling process.
- An accurate estimate of $\rho_s(\lambda)$ may be determined in spectral regions where $\tau_1(\lambda)$ is small, (i. e. in the atmospheric window regions), see Chapter 7.
- The terrain elevation is assumed at sea-level unless a mean scene elevation is known. Therefore any derivation of W is referenced to sea-level in the absence of terrain elevation information.

6.5.3 TSR procedure outline

To outline the procedure, such that, the TSR may be used in a coded format first requires that some of the main aspects of the coded method are discussed. Firstly, the TSR method requires that equations and concepts previously discussed are used. As well, concepts yet to be discussed (in the chapter following) are also required. The concepts and equations from the chapter following are not outlined in detail here but are shown or referred to if required.

The TSR in coded format has two main components, these are, the MODTRAN or synthetic modelling processes followed by the TSR component. MODTRAN is initially used to provide a basis set of reference synthetic at-sensor signals that vary in atmospheric water vapour content. Ancillary information, such as, latitude, longitude, day, time and sensor altitude are used to provide the basic input required by MODTRAN. It should be noted that this task is performed for the total at-sensor signal $L_S(\lambda)$ as well as the path scattered radiance $L_p(\lambda)$ signal. Any calculations and methods outlined from this point are applied to both components of the synthetic radiance signals. The synthetic radiances produced at this stage use an assumed surface reflectance of unity. So first,

(a) Using MODTRAN, generate a series of synthetic $L_S(\lambda)$ and $L_p(\lambda)$ signals that vary only in water vapour content and where the surface spectral reflectance is equal to one for five different water vapour contents.

(b) Using the output from above, and equation 5.105, curve fit to determine the required coefficients for each spectral channel, such that, each channel is represented by a unique fourth order polynomial.

$$L_{S\,\text{and}\,p}(\lambda, W) = \sum_{n=0}^{4} a_n(\lambda) W^n.$$

Since error due to scan angle effects may be significant (see Chapter 8 section 8.3.1) it is incorporated into the TSR to reduce error caused by neglecting scan angle effects.

(c) Run MODTRAN with the same initial ancillary input used in (a) for a preselected water vapour content (the highest water vapour content used in the previous step is generally used) for a range of varying sensor scan angles.

For each spectral channel the percentage change in radiance is modelled relative to the nadir viewing position as a function of scan angle i.e. if the percentage change is -4 %, for a given wavelength, then the signal percentage change scale factor (PC) will be 96 %.

(d) Using a polynomial expression, the percentage change in radiance as a function of sensor scan angle is given as,

$$PC(\lambda, \theta) = \sum_{n=0}^{m} e_n(\lambda) \theta^n, \tag{6.13}$$

where $PC(\lambda, \theta)$ is the percentage change scale factor for wavelength λ at scan angle θ.

This assumes that the PC is independent of water vapour amount and is only a function of sensor scan angle i.e. the PC is the same in a mid-latitude summer atmosphere with precipitable water vapour content of 2 cm as one with precipitable water vapour content of 1 cm. This provides a means of scaling the synthetic radiance at any water vapour to a given sensor scan angle such that,

$$L_{S\text{ and }p}(\lambda, W, \theta) = PC(\lambda, \theta)\sum_{n=0}^{4} a_n(\lambda)W^n. \tag{6.14}$$

This completes the MODTRAN component of the coded TSR scheme. Since the above equations (including 5.105) are based on an initial surface spectral reflectance of unity a method is required that allows the signals to be scaled to an arbitrary surface reflectance. To perform this task a simple process is employed. Once an estimate of surface spectral reflectance is calculated (to be discussed in Chapter 7) the synthetic at-sensor signals may be scaled to an arbitrary surface reflectance $\rho_s(\lambda)$ in the following manner,

$$L_S(\lambda, W, \theta, \rho) = \rho(\lambda)PC(\theta)\left(L_S(W) - L_p(W)\right) + PC(\theta)L_p(W). \tag{6.15}$$

From this point the process of estimating the atmospheric water vapour content is performed. Firstly,

1. Scale the $L_S(\lambda)$ and $L_p(\lambda)$ signals (established in **(b)**) to the appropriate scan angle with equation 6.14.

2. Using the PC scaled $L_S(\lambda)$ and $L_p(\lambda)$ from item 1, estimate the surface spectral reflectance (see Chapter 7) for the pixel of interest (POI).

3. Scale the PC $L_S(\lambda)$ and $L_p(\lambda)$ signals, given in item 1, to the derived surface reflectance (found in item 2) with equation 6.15, and where five different water vapour content values are used i.e. producing five at-sensor signals.

4. Calculate the appropriate TSR values for the five synthetic $L_S(\lambda)$ signals (from item 3) using equation 6.2.

5. Calculate the TSR values for the measured $L_S(\lambda)$ signals using equation 6.2.

6. Using the TSR values calculated in item 4 establish spectrally dependent fourth order polynomial reference curves of W against TSR using equation 6.12.

7. Using the measured TSR values (from item 5) with the appropriate spectral reference curve (established in item 6) estimate the water vapour content of the measured signal.
8. Scale the $L_S(\lambda)$ and $L_p(\lambda)$ signals from item 1 to the water vapour estimated from item 7.
9. Using the $L_S(\lambda)$ and $L_p(\lambda)$ from item 8 estimate enhanced surface reflectance.
10. Scale the $L_S(\lambda)$ and $L_p(\lambda)$ signals, given in item 1, to the enhanced derived surface reflectance (found in item 9) with equation 6.15 for the five selected water vapour content values.
11. Recalculate the appropriate TSR values for the five synthetic $L_S(\lambda)$ signals (from item 10) using equation 6.2.
12. Using the TSR values calculated in item 11 establish new spectrally dependent fourth order polynomial reference curves of W against TSR using equation 6.12.
13. Using the measured TSR values (from item 5) with the appropriate spectral reference curve (established in item 12) estimate the water vapour content of the measured signal.
14. Compare this result to the previous water vapour estimate. If an acceptable level of convergence is reached then stop. If convergence is not satisfactory then use the last estimate of water vapour and continue from item 8 to this point until an acceptable level of convergence is reached.

Figure 6.6 shows the procedure outline from item 2 to item 14 as a flow chart diagram.

Rejection Of Outlying column water vapour Results

Not all derived column water vapour results may be desirable. Some may be considered as outlying results. This may occur for a number of reasons and includes inaccurate $\rho_s(\lambda)$ retrieval, for a given section, which in turn leads to

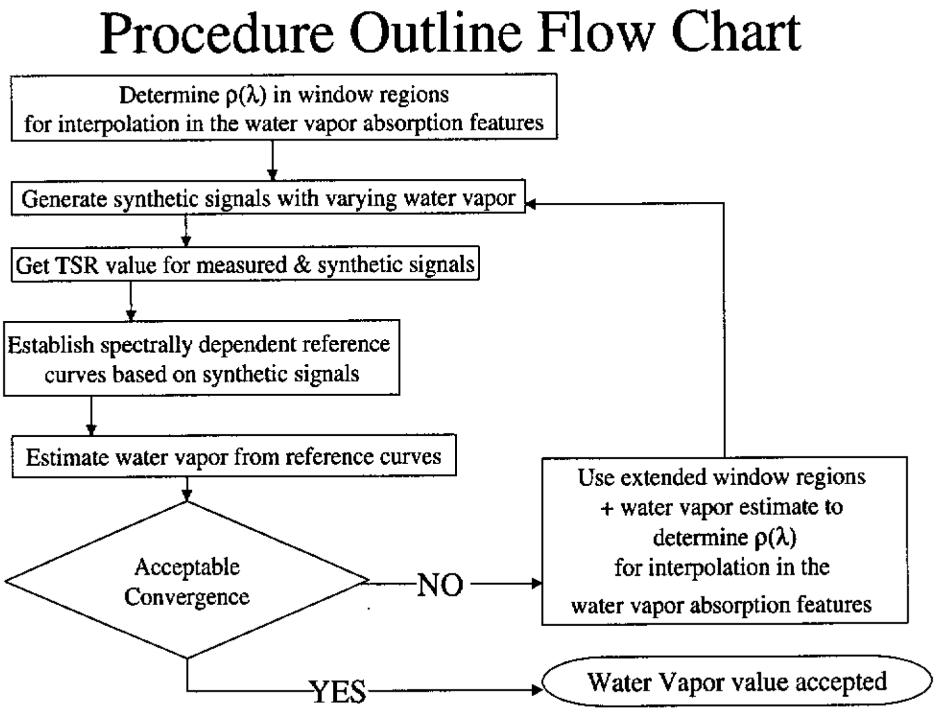

Figure 6.6: Flow diagram of the procedure implemented to estimate column water vapour from measured hyperspectral data using the TSR method once the MODTRAN component has been applied.

incorrect water vapour estimates. Alternatively, a surface absorption feature may be coincident with a water vapour band centre for a given section which in turn may lead to over or under estimation of water vapour.

The problem is to identify and remove outlying column water vapour results. The rejection scheme used in this study is implemented as follows,

1. For the n estimates that are derived for a given pixel, the mean column water vapour W is calculated.

   $$\bar{W} = \frac{\sum_{i=1}^{n} W_i}{n} \tag{6.16}$$

   where n is the number of channels (for AVIRIS n is initially equal to 32), and W_i is the derived water vapour for reference channel i.

2. Calculate the standard deviation s_w of the n derived estimates of W for the given pixel.

   $$s_w = \sqrt{\frac{\sum_{i=1}^{n} (W_i - \bar{W})^2}{n}} \tag{6.17}$$

3. Normalise each of the n derived W_i estimates given by Eq. (6.18).

   $$W_{iz} = \frac{W_i - \bar{W}}{s_w} \tag{6.18}$$

   where W_{iz} is the normalised W_i value at reference channel i.

4. Any W_{iz} value greater or less than ±1 is rejected.

5. Equations (6.16) to (6.18) are then applied to the channels that were not rejected from the previous step.

6. If the mean W result from step (5) is within 5% of that calculated in step (1) then it is accepted as the result for that pixel. Otherwise the process is repeated such that the results from selected channels are rejected until a final result is reached.

6.6 Summary

The main thrust of this chapter has been to demonstrate a means of estimating atmospheric water vapour from a method with its basis in the RTE. The methodology outlined in Chapter 5 was built upon to derive the forms necessary for estimating atmospheric water vapour loading in a top-of-atmosphere measurement of spectral radiance. The approach adopted is based on differential absorption methodology in the form of a ratio of measurement channels against reference channel. The ability to write the RTE in power series form (see Chapter 5) allows the defined ratio to be represented as a function of water vapour. In turn, this has provided a means of defining spectral calibration curves that are a function of atmospheric column water vapour.

An expression for the TSR as a function of atmospheric water vapour was derived (equation 6.11) and shown to have polynomial form. The polynomial order required to represent the TSR value as a function of water vapour loading, for a given wavelength, was found to be well represented by a third order polynomial. Finding a solution to a third order polynomial of the form given by equation 6.11 is not required if the independent and dependent variables are interchanged, such that, the TSR reference curves are in the form of equation 6.12. In this manner, a solution for the atmospheric water vapour W is found by substituting the calculated TSR, derived from radiometric measurements at top-of-atmosphere, into the appropriate reference curve.

In the derivations presented in this chapter it is assumed that an estimate of surface reflectance may be found in the required spectral regions and, as such, all derivations outlined in this chapter have assumed as much. The methodology used for estimating suitable surface spectral reflectance (for use in the TSR scheme) are discussed in Chapter 7.

Chapter 7

Surface Reflectance Determination in the Atmospheric Window Regions

To implement the TSR method requires that an estimate of surface spectral reflectance is used in the process. The equations outlined in Chapter 6 are constructed with this assumption in mind. As such, this chapter sets out to detail the methodology required, such that, an estimate of the surface reflectance may be found. If the surface spectral reflectance were exactly known, it should be a trivial matter to find the amount of water vapour present in a measured hyperspectral signal. Without water vapour content knowledge though, the surface spectral reflectance cannot be found exactly in water vapour absorption bands of an arbitrary radiance signal, but may be approximated.

From a measured hyperspectral scene a number of possible surfaces will be present. Therefore, a method is required, such that, an estimate of surface reflectance in the atmospheric window regions may be made from an arbitrary radiance signal. This in turn allows an estimate of surface spectral reflectance to be inferred in the water vapour absorption bands. Described first is the methodology used for a first pass estimate of surface spectral reflectance to be made in the VNIR-SWIR. This is expanded upon, such that, a second pass estimate of surface spectral reflectance may be derived. The improved second pass estimate is based on the premise that the first pass estimate allows the water vapour to be

Region	Start λ (nm)	End λ (nm)	Start Channel	End Channel
1	875	884	55	56
2	1009	1067	69	75
3	1230	1284	92	100
4	1543	1702	126	142
5	2078	2088	181	182

Table 7.1: The defined atmospheric window regions for the 400-2500 nm spectral region. Start and stop wavelengths for a given region (see Figure 7.1) are given as well as the equivalent AVIRIS channels. The last region, region 5, is not shown in Figure 7.1.

estimated with the TSR method to an improved level of accuracy and therefore leads to improved reflectance estimation.

The methodology describes how the derivation of surface reflectance is affected by differing atmospheric water vapour content and how the estimates of surface reflectance (in the window regions) are used to estimate surface reflectance in the atmospheric water vapour absorption bands.

7.1 Atmospheric Window Regions

To estimate surface reflectance in the water vapour absorption bands requires that surface reflectance is first estimated in the atmospheric window regions. The atmospheric window regions are defined in Table 7.1. Figure 7.1 shows the atmospheric window spectral regions outlined in Table 7.1. Shown in Figure 7.1 is the total atmospheric transmittance against wavelength for a mid-latitude summer atmosphere. In addition to the atmospheric windows (in regions of low absorption), regions of high absorption such as those centred at 940, 1140 and 1380 nm may be observed.

The extended window regions (as defined in Table 7.2) are used in conjunction with an initial TSR-estimated water vapour to further enhance iterative TSR water vapour estimates. The purpose of using extended spectral regions for surface reflectance estimation is discussed further in this chapter in relation to surface

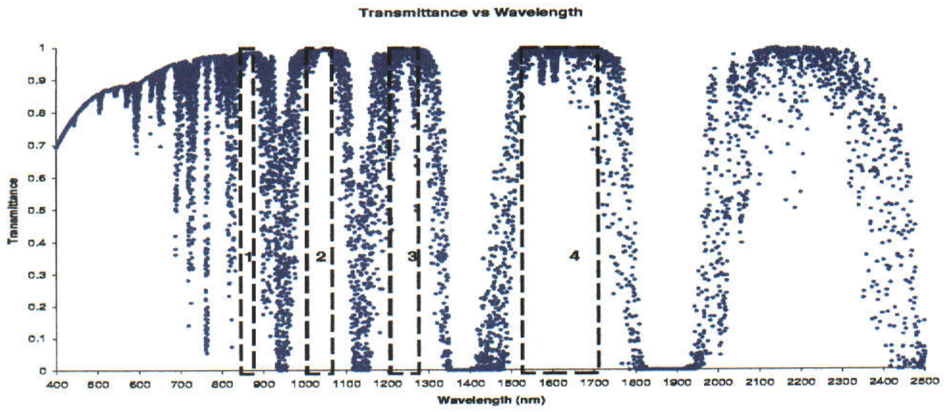

Figure 7.1: Total atmospheric transmittance versus wavelength for a mid-latitude summer atmosphere. The total transmittance is shown as a series of data points rather than continuous spectral curve. Shown in the bordered regions (labelled 1,2,3 and 4) are the areas that are deemed to be the atmospheric windows. These are regions of high atmospheric transmittance and hence regions where the molecular optical depth, τ_1, is small.

absorption features and nonlinearity of surface reflectance.

7.2 Reflectance Estimation Methodology

To implement the TSR equations, outlined in Chapter 6, the surface spectral reflectance $\rho_s(\lambda)$ is used, in either equation 6.11 or equation 6.12, to model synthetic versions of these equations based on the instrument ancillary data at the time of data acquisition. This allows the generation of synthetic at-sensor radiance signals that differ only in atmospheric water vapour.

The closer an estimated $\rho_s(\lambda)$ is to the true $\rho_s(\lambda)$, the better the TSR water vapour estimate will be. Initially a default water vapour content from a standard model, such as a mid-latitude summer atmosphere, is used to provide an initial $\rho_s(\lambda)$ estimate. The initial surface reflectance estimate in turn provides the means for determining the column water vapour with the TSR, such that, the first pass estimate of surface reflectance may be incorporated into the radiative transfer modelling process.

Region	Start λ (nm)	End λ (nm)	Start Channel	End Channel
1	875	913	55	59
2	961	1105	64	79
3	1163	1314	85	103
4	1463	1722	118	144
5	1978	2088	171	182

Table 7.2: The window regions defined as extended window regions. The extended regions are used to determine $\rho_S(\lambda)$ once an initial W estimate is made. The difference between the extended regions, and those of Table 7.1, is the extended regions encompass the extremities of the water vapour absorption features. The extended regions are used to provide a greater spectral range for subsequent derivations of $\rho_S(\lambda)$.

This allows a second, and improved, estimate of column water vapour to be made, which in turn leads to a second pass estimate of $\rho_s(\lambda)$. The second estimate of $\rho_s(\lambda)$ allows a third estimate of column water vapour to be made and so on. Since the second pass estimates of surface reflectance is assumed to be closer to the true form of $\rho_s(\lambda)$ than the first pass estimate of $\rho_s(\lambda)$, the unknowns in the RTE are reduced and the accuracy of the retrieval of water vapour increased. This process is repeated until the difference between estimated column water vapour iterations falls below a preset threshold.

The surface reflectance in the atmospheric window regions is derived with the following procedure. Firstly, commencing with equation 5.83 an estimate of the atmospheric path radiance $L_{mp}(\lambda)$ is removed from the measured at-sensor signal $L(\lambda)$ and a synthetic at-sensor signal $L_m(\lambda)$, as shown in equation 7.1 and equation 7.2,

$$L(\lambda) - L_{mp}(\lambda) = \frac{\rho_s(\lambda)\mu_0 E_0(\lambda)}{\pi(1-\rho_b\bar{r})}\gamma(\mu_0, \varphi_0)\gamma(\mu, \varphi), \tag{7.1}$$

and,

$$L_m(\lambda) - L_{mp}(\lambda) = \frac{\rho_m \mu_0 E_0(\lambda)}{\pi(1-\rho_m\bar{r}_m)}\gamma_m(\mu_0, \varphi_0)\gamma_m(\mu, \varphi). \tag{7.2}$$

The subscript m denotes a variable value that has been generated synthetically. $L_{mp}(\lambda)$ is initially generated with the value of column water vapour from a standard atmosphere such as a MLS or USS atmosphere. It is assumed for all derivations of $\rho_s(\lambda)$ that the solar zenith angle μ_0, the solar azimuth angle φ_0, the sensor zenith angle μ and the sensor azimuth angle φ are known or can be calculated. Further, it is assumed that the solar irradiance $E_0(\lambda)$, at wavelength λ, is the same in the synthetically generated spectra as the solar irradiance on the day of acquisition. In practice, the solar irradiance model may not be exactly the same and may produce residual features in derived surface reflectance spectra.

The synthetic surface reflectance ρ_m simply refers to a user supplied value. In most cases the value of ρ_m is set to 1 for simplicity. The constant reflectance ρ_m is given as,

$$\rho_m = constant. \tag{7.3}$$

Where ρ_m can take on all values greater than zero. All other terms in equation 7.1 and equation 7.2 have been previously described in Chapter 5 and may subsequently occur throughout remaining chapters (see Appendix A for a list of principle symbols). Equation 7.1 is divided by equation 7.2 and multiplied by equation 7.3 to yield,

$$[\frac{L(\lambda) - L_{mp}(\lambda)}{L_m(\lambda) - L_{mp}(\lambda)}]\rho_m = \frac{\frac{\rho_s(\lambda)\mu_0 E_0(\lambda)}{\pi(1-\rho_b \bar{r})}\gamma(\mu_0, \varphi_0)\gamma(\mu, \varphi)}{\frac{\rho_m \mu_0 E_0(\lambda)}{\pi(1-\rho_m \bar{r}_m)}\gamma_m(\mu_0, \varphi_0)\gamma_m(\mu, \varphi)}\rho_m. \tag{7.4}$$

Since the spectral regions of interest are within atmospheric window regions, the gaseous absorption, and therefore the optical depth $\tau_1(\lambda)$, is minimal (Kaufman, 1984, 1989), then the value of $\gamma(\mu_0, \varphi_0)\gamma(\mu, \varphi)$ divided by $\gamma_m(\mu_0, \varphi_0)\gamma_m(\mu, \varphi)$, is essentially unity. Further, the spherical albedo multiplied by the background surface reflectance is accepted as being smaller than 0.1 (Kaufman, 1989; Adler-Golden *et al.*, 1998) and for the purpose of this study is assumed to be zero. Therefore, equation 7.4 reduces to equation 7.5,

$$\rho_s(\lambda) = [\frac{L(\lambda) - L_{mp}(\lambda)}{L_m(\lambda) - L_{mp}(\lambda)}]\rho_m. \tag{7.5}$$

This form of reflectance determination has been used in previous studies (Green, 1990, 1991) and has the advantage, as noted by Green (1990, 1991), of being easily implemented with minimal modification of existing atmospheric transmittance codes.

The results of using equation 7.5 to estimate $\rho_s(\lambda)$ in the window regions (see Table 7.1) with varied amounts of atmospheric column water vapour is shown in Figure 7.2. Figure 7.2 demonstrates that $\rho_s(\lambda)$ is retrieved in the spectral

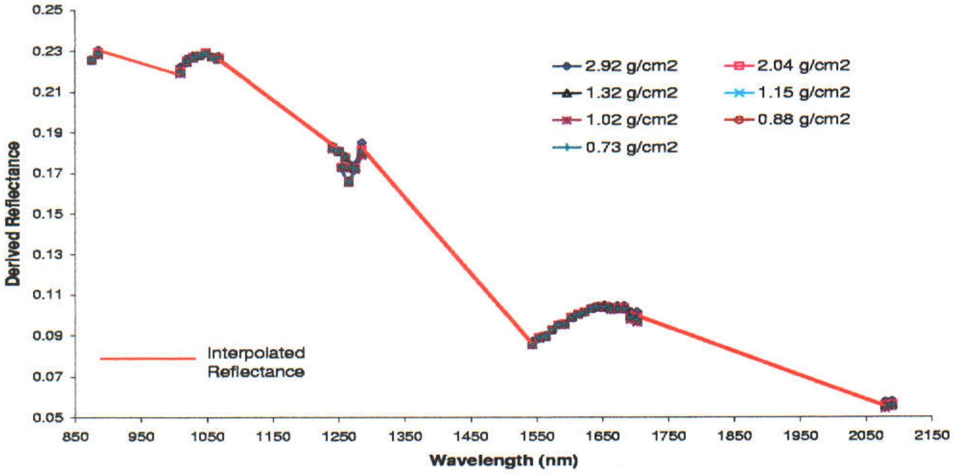

Figure 7.2: An example of surface reflectance derived using equation 7.5, in the atmospheric window regions (as defined by Table 7.1) for 7 different atmospheric total water vapour content amounts. The derived reflectance is invariant to water vapour in the window regions. The interpolated values, indicated by the straight line segments, provide an initial estimate of surface reflectance in the water vapour impacted spectral regions.

intervals outlined in Table 7.1 regardless of the amount of atmospheric water vapour present. Therefore equation 7.5 is considered invariant to atmospheric water vapour in the atmospheric window intervals outlined in Table 7.1 and fulfills the requirement of a reference channel as outlined in section 6.4.1.

The values of $\rho_s(\lambda)$ derived with equation 7.5 are used with an atmospheric modelling program (or a LUT) for the generation of synthetic at-sensor radiance values as a function of atmospheric column water vapour, as described by equation 5.105, for a given surface reflectance. To accurately model at-sensor-radiance for the entire VNIR-SWIR spectral region requires that an estimate of $\rho_s(\lambda)$ is found for the water vapour absorption bands as well as the window regions. To provide such an estimate the derived surface reflectance either side of an atmospheric water vapour absorption feature is interpolated (see Figure 7.2), such that, an estimate of surface reflectance is provided in the water absorption features.

This approach provides estimates of $\rho_s(\lambda)$ in the water absorption regions, as well as the window regions. The initial derivation of $\rho_s(\lambda)$is further enhanced by implementing the TSR method in an iterative procedure. This in turn, provides enhanced estimates of $\rho_s(\lambda)$ (see next section) from the absorption regions until a water vapour threshold is reached and the estimate of $\rho_s(\lambda)$ remains unchanging.

7.2.1 Enhanced $\rho_s(\lambda)$ Estimate

To improve the initial estimate of water vapour requires the surface spectral reflectance to be derived in the extremities of the water vapour regions so that unknowns, such as, surface reflectance features and magnitude errors in water vapour regions are reduced. To do this the initial water vapour estimate derived using the TSR (see Chapter 6), after first estimating the surface reflectance in the window and water regions, is incorporated back into the surface reflectance inversion process. The initial water vapour estimate is generally within 10 % of the true water vapour and provides enhanced modelling of the extremities of the water vapour regions.

The extension into the extremities of the water vapour regions (compare the spectral range of Tables 7.1 and 7.2) allows a greater portion of the spectral surface reflectance to be resolved and reduces the amount of interpolation required across water vapour regions. The following describes why a reasonable estimate of column water vapour (within 10%) allows the surface reflectance to be derived from the extremities of the water vapour regions.

Differences in estimated water vapour content, and true water vapour content, has more of an effect in the absorption band centre, where the optical depth is larger, than the extremities of the water feature where the optical depth is smaller. If the transmittance is thought of as being represented by a purely exponential function of optical depth, (ie Beer-Lambert law), then the ratio R of the true atmospheric transmittance to the assumed modelled transmittance may be represented as,

$$R = \frac{e^{-\tau}}{e^{-(\tau+\Delta\tau)}}, \tag{7.6}$$

where τ is the true optical depth in the extremities of the water feature and $\Delta\tau$ is the error in the estimated optical depth. Equation 7.6 may be reduced to equation 7.7, namely,

$$R = e^{\Delta\tau} = e^{k\Delta W} \approx 1 + k\Delta W, \tag{7.7}$$

where k is the mass absorption coefficient and ΔW is the error in column water vapour amount, that is, the difference between the true and modelled values. In the wings of the water vapour absorption feature, k (for a given W) is smaller than the absorption coefficients in the band centre (as witnessed by the smaller transmittance in the band centres) and, as such, the value of R, with a small ΔW, value has values close to 1. As the band centre of the water feature is approached, the absorption coefficient value is increased and the value of R is also increased.

The retrieval of $\rho_s(\lambda)$ in the extremities of the water vapour regions, once an initial estimate of column water vapour has been found using the TSR method, is shown in Figure 7.3. Figure 7.3 demonstrates that the initial linear interpolation across the water bands has been improved, as is evident by the now visible surface absorption features. The iterative process of re-estimating $\rho_s(\lambda)$ is not performed *ad-infinitum* since the iteratively derived water vapour converges and leads to unchanging estimates of $\rho_s(\lambda)$.

The linear interpolation procedure, although adequate does not work across all of the VNIR-SWIR spectrum such as the 1380 and 1890 nm water bands and, as such, linear extrapolation is used for part of the reflectance retrieval between

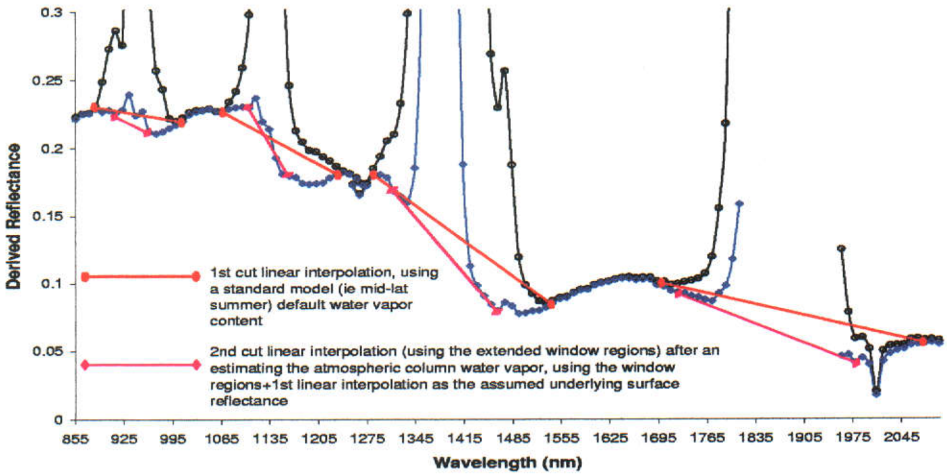

Figure 7.3: Derived reflectance versus wavelength: Using the default water vapour content for a given atmosphere (ie mid-latitude summer) allows the surface reflectance to be derived (black circles+line). To overcome the error in the water vapour regions a linear interpolation is used. Using the window+interpolated regions, as the underlying surface reflectance, the TSR is used to derive the column water vapour. Deriving again, the surface reflectance (with the 1st iteration water vapour) yields the blue curve. The extremities of the water bands are now resolved and the extended window regions used.

1400 and 1500 nm. In the case of AVIRIS, a linear curve is fitted through channels 126(1543 nm) and 128(1563 nm) and extrapolated to channel 118(1463 nm) when the first reflectance estimate is made. The interpolation is then carried out from channel 118(1463 nm) and across the 1380 nm water vapour band. After an initial estimate of the water vapour is calculated the linear curve is fitted through AVIRIS channels 123(1513 nm) and 124(1523 nm) and extrapolated to channel 118(1463 nm) again. The purpose of the extrapolation is an attempt to overcome the opaque nature of the water vapour band at 1380 nm. Without this approach surface water features, such as those in vegetation centred around the 1380 nm region (Conel *et al.*, 1993a,b; Gao and Goetz, 1995), will cause $\rho_s(\lambda)$ retrieval errors, and ultimately column water vapour retrieval errors.

7.3 Atmospheric Correction

When atmospheric water vapour content is estimated to an accepted level of convergence the measured radiance signal may be atmospherically corrected to yield surface spectral reflectance in the VNIR-SWIR. It is assumed that other trace gases and aerosols, when performing atmospheric correction, are known. If not, errors will be introduced into the derived surface spectra. To atmospherically correct a measured hyperspectral radiance signal in the VNIR-SWIR, once an estimate of atmospheric column water vapour is made, is achieved by applying equation 7.5 outlined in section 7.2. All calculations though, are now carried out for the entire 400–2500 nm spectral region and not restricted to specific spectral regions such as those used in section 7.1.

7.4 Summary

To derive atmospheric column water vapour, with the TSR method, requires that a reasonable estimate be made of the surface reflectance in the VNIR-SWIR. This chapter has described a method for estimating surface reflectance from the atmospheric window regions, as well as, the water affected spectral regions. It was demonstrated that surface reflectance estimation in the defined atmospheric window regions, of Table 7.1, is invariant to changes in column water vapour and therefore results in an accurate measure of the surface reflectance in such regions. This in turn provides a means of estimating surface reflectance in water vapour absorption affected regions. The process by which this is achieved is through the use of linear interpolation across a given water vapour absorption feature.

To further improve on the initial surface reflectance estimate the defined atmospheric windows (Table 7.1) are extended (Table 7.2). Using the initial derived surface reflectance in the TSR scheme allows an initial estimate of water vapour to be made. This, in turn, allows the second pass reflectance estimate to be extended into the wings of the water vapour absorption features. This may be thought of as extended window region enhancement. This form of secondary reflectance retrieval decreases the amount of interpolation required across the water vapour absorption bands and demonstrated that the surface reflectance slope, from the first pass estimate, is not necessarily the true slope (see Figure 7.3). This is especially true in the presence of surface absorption features that are present in atmospheric absorption features, such as those commonly found in vegetation.

The process outlined in this chapter for estimating surface spectral reflectance allows the TSR method of column water vapour derivation to be implemented in an iterative procedure. This in turn allows the estimate of surface reflectance to be updated and leads to convergence in the estimation of atmospheric column water vapour.

Chapter 8

Sensitivity Analysis

8.1 Introduction

With the TSR methodology established in Chapter 6, a sensitivity analysis of the TSR method to uncertain input parameters, such as atmospheric visibility, is required. The question of sensitivity is important for a number of reasons. These include providing an understanding of where the TSR method may encounter difficulties, as well as providing an estimate of the expected magnitude of error for any given derived water vapour value. The sensitivity analysis reveals, in some cases, that the approximation of certain input parameters does not significantly effect the derived water vapour result. This is important when modelling is required since the less complex the problem, in terms of unknown parameters, the simpler the problem of estimating water vapour with minimal ancillary information becomes.

Other methods of atmospheric water vapour retrieval have been subject to sensitivity analysis, such as the CIBR, APDA and Narrow/Wide method, and are of importance for comparison against the TSR method. The sensitivity of existing methods, to different variable input, allows a comparison of TSR robustness and accuracy to be established against existing water vapour retrieval techniques. This chapter describes the methodology used to perform the sensitivity analysis and is followed by an examination of the independent variables used to test the sensitivity of the TSR. This is followed by the results of the sensitivity analysis which are compared with published analysis results for existing water vapour retrieval methods.

8.2 Methodology

To examine the sensitivity of the TSR method to predefined input parameters, a number of variables were altered relative to their original values. Subsequently, each variable of interest was altered, one at a time, to generate a series of perturbed atmospheres with known water vapour content. Since the water vapour content in each of the perturbed atmospheres is known, the estimated water vapour may be compared to the true water vapour content in the perturbed model and a measure made of the sensitivity of the TSR with respect to that particular variable.

The derived water vapour is compared to the actual water vapour in a manner similar to that used by Carrére and Conel (1993) and presented as a fractional water difference $\Delta W/W$, where,

$$\frac{\Delta W}{W} = \frac{(W_x - W_{ref})}{W_{ref}}, \tag{8.1}$$

and W_{ref} is the true amount of water vapour in the altered atmospheric model and W_x is the water vapour derived with the TSR method from the altered atmospheric model.

8.2.1 Initial Input parameters

The TSR requires that an estimate of the ancillary data is provided prior to deriving water vapour from a given pixel or scene. The input parameters were chosen such that they could be perturbed to values greater than and less than the initial value.

Table 8.1 defines the input variables used to construct the reference atmosphere and sensor conditions. For the purpose of this study, the parameters used are typical of an AVIRIS flight as opposed to a HyMap flight. The main difference between AVIRIS and HyMap, is the sensor altitude, with HyMap having an operational altitude of 2.5 km, while AVIRIS has an operational altitude of 20 km. The variables used as input, (see Table 8.1) correspond to data taken from an AVIRIS flight over Jasper Ridge, California in 1997. The visibility was

Scan Angle (zenith)	nadir
Sensor Altitude	20 km
Surface Elevation	250 m
Aerosol Visibility	30 km
Sensor Latitude	37.43 degrees North
Sensor Longitude	122.26 degree West
Time (GMT)	20 hours 9 minutes
Julian Day	93
Precipitable Water Vapour Content(PWV)	1.55 cm
Path Azimuth	0 degree North
Surface Reflectance	0.5
Model	Mid-Latitude Summer (MLS)
Aerosol Model	Urban

Table 8.1: The initial parameters used for the sensitivity analysis of the TSR scheme. The values given are used to provide a reference atmosphere for water vapour retrieval when using the TSR.

Zenith (deg)	45	30	15	0	-15	-30	-45
Altitude (km)	5	4	3	0	-3	-4	-5
Elevation (m)	500	300	200	0	-200	-300	-500
Visibility (km)	30	20	10	0	-10	-20	-30
Latitude (deg)	3	2	1	0	-1	-2	-3
Longitude (deg)	3	2	1	0	-1	-2	-3
Time (min)	30	20	10	0	-10	-20	-30
Day (day)	3	2	1	0	-1	-2	-3
PWV (%)	30	20	10	0	-10	-20	-30
Azimuth(deg)	80	60	20	0	-20	-60	-80
Model	tropics	mls	mls	mlw	sas	saw	uss

Table 8.2: Each variable that was perturbed was changed from the initial value given in Table 8.1 by the amount shown.

decreased from an estimated 60 km, at the time of flight, to 30 km, so as to test the TSR under more rigid visibility conditions.

8.2.2 Perturbation Variables

Tables 8.2 and 8.3 list the variables used in the sensitivity analysis, as well as, the range of alteration applied to each variable. As seen in Table 8.2 each variable, excluding surface type, has a zero change applied. This allowed error due to curve fitting and the coding of the TSR method to be evaluated i.e. a zero error. In Table 8.2, zenith refers to the sensor scan angle, where nadir or 0, is vertical viewing. Azimuth refers to the sensor scan path azimuth where 0 is North, and PWV is the precipitable column water vapour. For the model type, MLS is the mid-latitude summer, MLW is the mid-latitude winter, SAS is the sub-arctic summer, SAW is the sub-arctic winter, USS is the United States standard and tropics is the tropical model.

When scene elevation is altered from sea-level, or the atmospheric type is altered, the amount of PWV present in the atmosphere is increased or decreased accordingly. Since scene elevation in the absence of accurate elevation-models, is

Elevation (m)	500	300	200	0	-200	-300	-500
PWV (cm)	1.211	1.339	1.408	1.553	1.712	1.795	1.973

Model	tropics	mls	mls	mlw	sas	saw	USS
PWV (cm)	2.199	1.553	1.553	0.461	1.119	0.231	0.765

Table 8.3: The amount of PWV contained in the elevation models and the different atmospheric models is presented here. The range of values is reasonably dynamic and has been chosen to represent the type of variation that might be found in an actual scene.

usually given as a mean value, the expected uncertainty in estimated water vapour when scene elevation is unknown is required. The water vapour content when the surface elevation (for a mid-latitude summer) and for differing atmospheric models are changed, is given in Table 8.3. The MLS atmosphere appears twice simply to complete the requirement of seven variable values.

8.2.3 Sensitivity Analysis Image Panel

MODTRAN4.0 was used to generate synthetic AVIRIS at-sensor signals with the perturbed variable values given by Table 8.2. The MODTRAN generated spectral data was incorporated into a single binary file, such that it is seven pixels wide by twelve lines long (i.e. 84 pixels in total with each pixel corresponding to an entry in Table 8.2) with 224 spectral channels per pixel. The 84 pixel file is called the sensitivity analysis panel. Except for the variable being modified all other inputs used to generate the panel are given by Table 8.1. The last row of the panel are altered surface types, this component is discussed in section 8.3.10. The TSR water vapour estimation method was applied to each pixel of the sensitivity panel and the water vapour for each pixel estimated with the TSR scheme. The estimated water vapour is used to assess the performance of the TSR method.

The fourth column has a constant value, which corresponds to no perturbation and is used to assess the TSR zero or model error when all variables are known exactly. If the TSR is used to estimate water vapour when all variables are known exactly the analysis, using the fourth column, found that the zero error for the coded version of the TSR is 1.29 %. By this it is meant that a value of 1.57 cm

Scan Angle (deg)	45	30	15	0	-15	-30	-45
Derived PWV (cm)	1.79	1.66	1.58	1.57	1.60	1.67	1.81
PWV Error (%)	14.01	5.73	0.64	0.00	1.91	6.37	15.29

Table 8.4: The error in estimated precipitable column water vapour (PWV) introduced into the TSR retrieval method if sensor scan angle is not accounted for in the retrieval scheme.

of precipitable column water vapour is retrieved rather than the 1.55 cm used for the default settings. This error is a combination of curve fit and coding error.

8.3 Results

The results of the sensitivity analysis are now presented for each of the variables shown in Table 8.2. For each variable a discussion and summary is included, as well as, a comparison, if available, with findings of previous studies that employ different water vapour estimation methods.

8.3.1 Scan Angle

To decrease computation time, when deriving column water vapour, the scan angle for sensors such as AVIRIS, which has small swath width (see Chapter 2, section 2.5), is often assumed at nadir for the entire scene. The error introduced into the derived water vapour by this assumption is therefore of reasonable importance. Table 8.4 shows the expected error in estimated water vapour if sensor scan angle is assumed to be at nadir, while in actuality it is at a scan angle other than nadir. The solar zenith and solar azimuth were 32.50° and 178.25° respectively. The solar geometry defines a forward scattered solar radiance for negative scan angles and a back scattered radiance for positive scan angles.

Since the scan angle for any given pixel may be calculated with a knowledge of sensor specifications and pixel location, the error is representative of the expected error if the TSR method does not incorporate scan angle into the estimation. However, the TSR model may be constructed to allow for scan angle and generally is. Table 8.4 demonstrates that, at maximum AVIRIS scan an-

Altitude difference (km)	5	4	3	0	-3	-4	-5
Derived PWV (cm)	1.56	1.57	1.57	1.57	1.57	1.57	1.57
PWV Error (%)	-0.64	0.00	0.00	0.00	0.00	0.00	0.00

Table 8.5: The error in estimated precipitable column water vapour, using the TSR scheme, for a sensor assumed to be at 20 km, if the operational altitude is ± that shown.

gles (± 15° off nadir) the PWV error is approximately 2.00 % maximum when viewing in the forward scattering direction and 1.00 % when viewing in the back scattered direction. For HyMap, which has maximum scan angles of ± 30°, the error introduced into the water vapour estimate is approximately 6 % in both directions. It is noted that, to minimise the effect of forward and back scattered solar radiation, airborne sensors are usually flown so as to have the sensor scan angle perpendicular to the relative solar back and forward scattering positions.

The results in Table 8.4 are of the same order of magnitude as those reported by Carrére and Conel (1993) who demonstrated errors of 0.4 and 3 % for typical AVIRIS conditions. With the TSR method, the water vapour is found to be overestimated while in the Carrére and Conel study, using the CIBR, the estimates were found to be less than the reference water vapour value.

8.3.2 Sensor Altitude

The error in water vapour, if sensor altitude is perturbed to within a maximum of plus or minus 5 km from its initial altitude, is presented in Table 8.5 . The range represents extreme altitude variation that would not be seen in an actual flight. This section is only applicable to airborne sensors and not to spaceborne sensors whose operational altitude does not change. Table 8.5 shows that the error in estimated water vapour is zero for all but the 5 km increase in altitude. The magnitude of the error in the derived water vapour is not unexpected since a sensor at an altitude of 20 km is essentially above all of the atmospheric water vapour (see Chapter 3 section 3.1.5), and any change in sensor altitude will not affect the total amount of atmospheric water vapour below the sensor.

HyMap does not have an operational altitude of 20 km but rather a mean

Elevation Difference (m)	500	300	200	0	-200	-300	-500
Derived PWV (cm)	1.16	1.31	1.38	1.57	1.75	1.83	2.01
PWV Error (%)	-5.20	-3.23	-3.04	0.00	1.17	0.86	0.81

Table 8.6: The error in precipitable column water vapour if the scene elevation is different to that of an assumed mean scene elevation of 250 m. The result given by the elevation difference of 500 m is comparable to that reported by Gao and Goetz (1990)

operational altitude of 2 km; see Chapter 2.4 section 2.6. A similar analysis, performed using HyMap operational altitudes, found that to introduce a one percent error in derived water vapour would require a maximum altitude uncertainty of ± 150 m. It is expected that the uncertainty in altitude of a low-altitude sensor, such as HyMap, will be significantly less than this. Based on the findings in Table 8.5, and with the assumption that most airborne sensing systems are relatively stable, it is concluded that the error introduced to derived water vapour due to uncertainty in operational altitude may be considered negligible.

8.3.3 Scene Elevation

Unless a digital elevation model (DEM) is available for the region under study, an estimate of scene elevation is required, such that, atmospheric mixing ratios may be adjusted accordingly. Therefore, a mean elevation is only a representative value of the true scene elevation of any field-of-view pixel within the scene. Knowledge of expected error in the derived water vapour from a scene that has varying topography is therefore required. The error, in derived water vapour, due to scene elevation uncertainty, is given in Table 8.6. The mean scene elevation (see Table 8.1) was defined as 250 m. The perturbation values of -300 and -500 m, in Table 8.6, correspond to areas that are below sea level relative to the mean scene elevation.

The results of the analysis are comparable to Gao and Goetz (1990) and Gao *et al.* (1993). Gao and Goetz (1990) reported that an error of 500 m in the scene elevation will give rise to an uncertainty of approximately 5 % in the derived column water vapour. The uncertainty of 5 % reported by Gao *et al.* (1993) is seen to be in good agreement with that presented in Table 8.6. Thus, to achieve

Visibility Difference (km)	30	20	10	0	-10	-20	-25
Derived PWV (cm)	1.56	1.58	1.57	1.57	1.56	1.58	1.60
PWV Error	-0.64	0.64	0.00	0.00	-0.64	0.64	1.91

Table 8.7: The error introduced into the TSR-estimated water vapour if the aerosol visibility estimate is incorrect. The true visibility was 5 km but assumed in the TSR retrieval to be 25 km visibility. The result is highly encouraging since, even with large uncertainties, the introduced error is still less than 2 %.

an accuracy of at least 3 % in derived water vapour, the scene elevation should be known to within 300 m. This result is also confirmed in the Gao and Goetz (1990) study. Of interest in Table 8.6 is the detail of the errors in derived water vapour. It is observed that the maximum error of -5.20 % occurs when the actual elevation is greater than that of the mean elevation, while the results for a scene elevation that is actually 500 m less than the mean elevation are of the 1 % order. Because of the asymmetry in the error field and since the true elevation in a field-of-view will vary about the mean elevation, as provided in a DEM, there would be a reduction in mean error if the elevation used in the TSR method was set higher than the mean elevation. This issue is not investigated any further in this study.

8.3.4 Aerosol Visibility

In the absence of meteorological data an estimate of the visibility, due to the presence of atmospheric aerosol, is required to account for scattering and absorption by the aerosol. The estimate of visibility is often subjective if instrumentation such as a transmissometer or solar photometer are not used to estimate visibility or aerosol loading, and hence optical depth, in the atmosphere. Therefore, the magnitude of error introduced into estimated water vapour due to incorrect aerosol visibility is required. For this study an urban aerosol model was used with an assumed visibility of 30 km. In Table 8.7, visibility differences of 30 and -25 km means the actual visibility was set to 60 and 5 km respectively.

The results show for extreme haze, where the visibility is only 5 km, the absolute error in TSR-estimated water vapour is approximately 2 % when the visibility was assumed to be 30 km. This is a promising result when compared to the results published by Carrére and Conel (1993) for the CIBR. Carrére and Conel (1993) showed that the error in derived water vapour was approximately 30 % when the actual visibility was 5km but assumed in their retrieval scheme to be 25 km.

The error in TSR derived water vapour when the visibility is actually 60 km (i.e. a + 30 km visibility difference), rather than the 25 km used, is significantly less than a percent. Carrére and Conel (1993) reported an error of 0 to 4% for similar visibility conditions. The result is extremely promising and suggests the TSR-estimated water vapour is relatively insensitive to visibility conditions. The importance of this finding is that a reasonable estimate of visibility (within 25 km) will not produce large error in the TSR-estimated water vapour.

Of note though is the effect of unknown visibility on derived surface reflectance. In the case where the actual visibility was 5 km but a 25 km visibility was used to estimate water vapour and surface spectral reflectance, the error in the derived surface reflectance is large. This is demonstrated in Figure 8.1, where the derived surface reflectance is shown. The actual spectral reflectance used in the synthetic data set was a constant value of 0.5 in the VNIR-SWIR as given in Table 8.1.

Figure 8.1 demonstrates that, even though the water vapour is within 3 %, as observed by the small residual water vapour features, the derived surface reflectance error is large and would require that an accurate estimate of aerosol visibility (Δvis= $\pm$10 km) be known if the surface reflectance is to be retrieved with acceptable accuracy.

8.3.5 Latitude and Longitude

The latitude and longitude of sensor flight lines are generally well known because of the use of global positioning satellites (GPS). To estimate water vapour from a scene, mean latitude and longitude for the flight plan are often used to decrease computational time. With this in mind, the latitude and longitude were altered so as to assess the effect that sensor location has on derived water vapour. The perturbations represent extreme errors in sensor latitude and longitude. Table

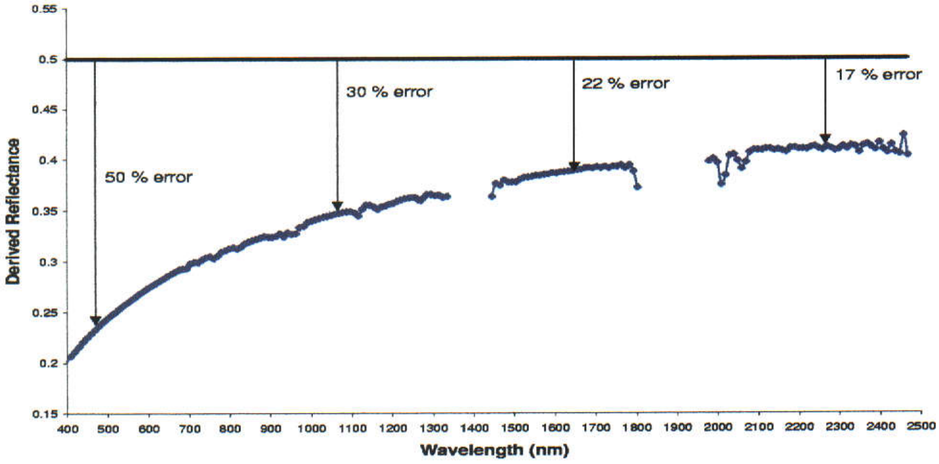

Figure 8.1: Derived surface reflectance versus wavelength. Even though the error in estimated water vapour is less than 2 % the error introduced into the derived reflectance, when the actual surface reflectance was 0.5 and when aerosol visibility is assumed to be 30 km, as opposed to the 5 km true value, is significant and demonstrates the need for accurate aerosol visibility estimates if surface reflectance is required.

Latitude Difference (deg)	3	2	1	0	-1	-2	-3
Derived PWV (cm)	1.59	1.58	1.58	1.57	1.55	1.54	1.53
PWV Error (%)	1.27	0.64	0.64	0.00	-1.27	-1.91	-2.55
Longitude Difference (deg)	3	2	1	0	-3	-2	-1
Derived PWV (cm)	1.57	1.57	1.56	1.57	1.57	1.57	1.56
PWV Error (%)	0.00	0.00	-0.64	0.00	0.00	0.00	-0.64

Table 8.8: The error introduced into the TSR derived water vapour when the sensor latitude and longitude is in error. Unless the latitude and longitude are unknown to within 2 degrees the error will be less than 2 %.

8.8 gives the combined results for the latitude and longitude sensitivity analysis. The sub-solar latitude and longitude, when using the input parameters defined in Table 8.1, are 37.43° North and 122.26° West respectively.

The error in derived water vapour, due to uncertainties in latitude and longitude, are essentially errors introduced from using incorrect solar zenith and azimuth angle information. As the sensor latitude is increased, in this case away from the sun, the maximum error in derived water vapour is less than 2 %, while the error introduced as the sub-sensor and sub-solar latitudes decreases has a maximum value of -3 %. Similarly, the effect of longitudinal uncertainty is observed to be less than 1 % and is best understood by considering that the solar zenith angle is not changing as rapidly as the solar zenith angle for the latitude analysis. These results indicate that a mean latitude and longitude will suffice when retrieving water vapour over a given geographic region providing the mean latitude and longitude are within ±2° of the respective means for the region.

8.3.6 Time and Day

As with the latitude and longitude investigations, the results for the time and day uncertainty are also small. Table 8.9 demonstrates that even with an error of plus or minus 30 minutes, relative to the true acquisition time, the error in derived water vapour is less than 1 %. In almost all cases, the time of data acquisition

Time Difference (min)	30	20	10	0	-10	-20	-30
Derived PWV (cm)	1.57	1.57	1.56	1.57	1.57	1.56	1.57
PWV Error (%)	0.00	0.00	-0.64	0.00	0.00	-0.64	0.00
Time Difference (day)	3	2	1	0	-1	-2	-3
Derived PWV (cm)	1.56	1.55	1.56	1.57	1.56	1.57	1.58
PWV Error (%)	-0.64	-1.27	-0.64	0.00	-0.64	0.00	0.64

Table 8.9: The error introduced into the estimated precipitable column water vapour when the assumed imaging time is different than the true imaging time, and when the assumed acquisition day differs from the true day. For time errors of ± 30 minutes, relative to the mean time, the error in estimated water vapour is found to be less than 1 %. While the error introduced for incorrect date acquisition is less than 2 %.

is well known due again to GPS and logged flight data. The error introduced by using a mean time for a particular flight line will introduce negligible error into the estimated water vapour result if the assumed time is within 30 minutes of the true mean acquisition time. The error introduced by using the incorrect day, shown in Table 8.9, is also shown to be minimal and is less than 2 %. Again, the knowledge of the acquisition date is absolute and so it is expected that such an uncertainty will not actually occur.

8.3.7 Water Vapour Amount

Since water vapour is variable both spatially and temporally (Green *et al.*, 1993; Roberts *et al.*, 1997; Jacob, 2001), knowledge of the uncertainty in estimated water vapour as a function of water vapour loading is required. The results of this analysis are provided in Table 8.10. Table 8.10 gives the actual amount of PWV used, as well as the TSR-estimated water vapour for each. The error introduced into the TSR-estimated water vapour is seen to range from -1.83 to 1.29 %. The extreme values of -1.48 and -1.83 % correspond to water vapour perturbations of ±30 % respectively about the mean value of 1.57 cm.

The derived water vapour errors given in Table 8.10 are comparable to results

Actual PWV (cm)	2.02	1.86	1.71	1.55	1.40	1.24	1.09
Derived Water Vapour (cm)	1.99	1.85	1.71	1.57	1.41	1.23	1.07
PWV Error (%)	-1.48	-0.54	0.00	1.29	0.71	-0.81	-1.83

Table 8.10: TSR-estimated column water vapour for a variety of column water vapour loading in a mid-latitude summer atmosphere. In all cases the absolute error in derived column water vapour is seen to be less than 2 % for the range considered.

Azimuth Difference (deg)	80	60	20	0	-20	-60	-80
Derived PWV (cm)	1.57	1.57	1.57	1.57	1.57	1.57	1.57
PWV Error	0.00	0.00	0.00	0.00	0.00	0.00	0.00

Table 8.11: The error introduced in estimated column water vapour due to incorrect solar azimuth angle. No error is noted since MODTRAN4.0 averages over azimuth angle. The error due to azimuth angle is assumed to be zero.

presented by Borel and Schläpfer (1996). The results of the Borel and Schläpfer (1996) study show the APDA scheme retrieved water vapour to an accuracy of approximately 3–5 %, while the CIBR has relative water vapour errors of 8–10 % for the water vapour range used in Table 8.10. Thus, the TSR water vapour results are a significant improvement on the CIBR and would also appear to be a valuable improvement on APDA derived water vapour.

8.3.8 Solar Azimuth Angle

Table 8.11 presents the results of the sensitivity analysis with respect to path azimuth. MODTRAN4.0, which is used for this analysis, averages the multiple scattering models over the azimuthal dependence (Berk *et al.*, 1998) and as such no variation due to changes in azimuth angle are seen. Berk *et al.* (1998) note that the incorporation into MODTRAN of a curved-Earth, refractive path DISORT routine, which models solar azimuth dependencies, is being pursued. Berk *et al.* (1998) also note that for nadir-viewing geometries, such as AVIRIS, solar azimuth effects are minimised.

Model	Tropics	MLS	MLW	SAS	SAW	USS
Derived PWV (cm)	2.11	1.57	0.51	1.132	0.25	0.78
Actual Water (cm)	2.20	1.57	0.46	1.12	0.23	0.77
PWV error (%)	-4.09	0.00	10.87	0.89	8.70	1.30

Table 8.12: Error in estimated precipitable column water vapour when using a mid-latitude summer model to retrieve column water vapour from the other five models. The worst case scenarios are when the MLS atmosphere is used to retrieve water vapour from winter atmospheres. The results are encouraging and show that beside the difficulty with winter models the retrieval method is relatively insensitive to model selection.

8.3.9 Atmospheric Models

Since six atmospheric models are available in MODTRAN4.0, the possibility of using an incorrect atmospheric model in a particular scenario may arise. The models used are a tropical model, MLS, MLW, SAS, SAW and the USS model. Obviously some models such as the SAW and SAS models are not appropriate for the majority of the globe but they are tested here because they do provide extremes with which to test TSR sensitivity.

Table 8.12 gives the results of the sensitivity analysis when using a MLS atmosphere to retrieve water vapour from different atmospheric models. The estimated water vapour, in cm of precipitable water vapour, is given as well as water vapour content in the atmospheric model used. Besides testing the TSR response to different water vapour models (similar to that in section 8.3.7), this analysis indirectly tests the TSR derived water vapour results when incorrect temperature, pressure and vertical mixing ratios (VMR) are used.

In all cases, with the exception of the MLW and SAW atmospheres, the retrieval is seen to have an accuracy better than 4 %. The MLS result show a zero error estimate of water vapour as expected. The largest errors, it is noted, are both for winter atmospheric models. The most likely cause for the retrieval errors are the differences between the pressure and temperature models used in the winter atmospheres as compared to the MLS atmosphere.

In reality, it is expected that if a data set was acquired in the winter then a winter atmospheric model would be used in processing the data. Conversely, if the data set was acquired in a tropical climate then a tropical model would be used. Results published by Gao and Goetz (1990) for data acquired by AVIRIS show similar results if a MLW atmosphere is used to retrieve water vapour rather than the correct MLS for the time of acquisition. The choice of atmospheric model is dictated by the time of year and geolocation of the data collect, thus the correct model or most appropriate model will in all likelihood be used.

8.3.10 Surface Reflectance

The derivation of column water vapour generally takes place over regions of varied spectral reflectance. This may include, vegetation, water, man made products and geological terrain. Thus far, the surface spectral reflectance has been set to a constant value of 50 %. This section of the analysis examines the sensitivity of the TSR water vapour method over different surface spectral reflectance types. A representative collection of spectra were chosen so as to test if the TSR method exhibited failings for any particular spectral cases.

Water Vapour Results

Table 8.13 gives the water vapour sensitivity results for the different surface reflectance analysis. The table is ordered into groups. The first group of four are considered dark targets with the darkest being the constant surface reflectance of 0.005 (or 0.5 %). The salt+water target used an actual AVIRIS derived reflectance over a salt evaporation pond at Moffett Field. The following two are vegetation targets which were used to evaluate the retrieval method over non-linear surfaces. Followed by two man made spectral targets and granite then sandy loam and the three mineral targets and finishes with a bright 80 % constant reflectance target. The mineral target reference spectra are from the ASTER spectral library (http://speclib.jpl.nasa.gov/). The vegetation, paint, granite and galvanised steel are MODTRAN4.0 supplied surface reflectances.

Dark Targets

Dark surface spectral targets often prove problematic when attempting to derive water vapour and it has been noted, that it is a remaining challenge to retrieve

Surface Type	PWV (cm)	Derived PWV (cm)	PWV Error (%)
0.005	1.55	1.60	3.23
0.01	1.55	1.60	3.23
0.02	1.55	1.57	1.29
Salt + Water	1.55	1.49	-3.87
Conifer	1.55	1.54	-0.65
Vegetation 2	1.55	1.56	0.65
Olive Paint	1.55	1.55	0.00
Granite	1.55	1.56	0.65
Galvanised Steel	1.55	1.56	0.65
Sandy Loam	1.55	1.56	0.65
Montmorillonite	1.55	1.56	0.65
Nontronite	1.55	1.55	0.00
alunite	1.55	1.55	0.00
0.8	1.55	1.56	0.65

Table 8.13: Fourteen different surfaces were used to test the TSR water vapour retrieval over. These ranged from constant reflectance values (low to high), water, vegetation, man made and mineral targets. All errors in the derived water vapour are below an absolute value of 4% regardless of spectral magnitude.

water vapour over dark and shadowed areas (Schläpfer *et al.*, 1998). Supposedly, the APDA algorithm does not underestimate atmospheric water vapour as dramatically over dark targets (Schläpfer *et al.*, 1998). Even so the Schläpfer *et al.* (1998) study still lists the estimation of water vapour over dark targets as only being possible by further improvements in the current methodology. The Carrére and Conel (1993) study showed that for surface reflectance in the 1–5 % range a 1 % departure of the true surface, from the assumed reflectance, can have an impact on the water vapour estimate ranging from 2–30 %. Carrére and Conel (1993) also showed that gross departures from an assumed 25 % reflectance produced under estimates of water vapour ranging from 1–20 % when the departure was toward lower reflectance.

The sensitivity results over the dark targets in Table 8.13 are, in light of the Carrére and Conel (1993) study, very encouraging. The magnitude of the under/over estimates is comparable with other sensitivity parameters already outlined in this chapter. The cause of the under/over estimates is due to the departure of the derived surface reflectance (used in the TSR method) away from the true reflectance. The process of incorporating an estimate of surface reflectance in the TSR method ensures that departures away from the true surface reflectance are kept to a minimum.

The TSR application results of water vapour estimation over dark targets and water targets is shown in Chapter 10. Although not discussed in detail here, the results show that the estimation of water vapour over such targets produces estimates that appear to be randomly distributed in terms of over and underestimation. It will be shown, in the case of AVIRIS, that the variation observed over dark targets, especially water, is due to low signal-to-noise. Figures 8.2(a) and 8.2(b) show derived reflectance for the first four entries of Table 8.13, after radiance-to-reflectance correction is performed using the TSR-estimated water vapour.

Vegetation

Vegetation has weak liquid water features located at approximately 980 and at 1200 nm (Gao *et al.*, 1993). This may lead to overestimates of water vapour if

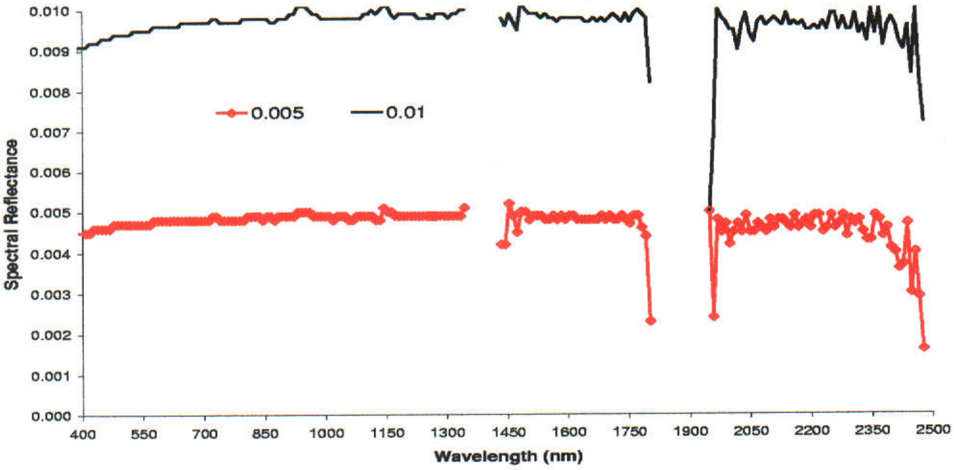

(a)

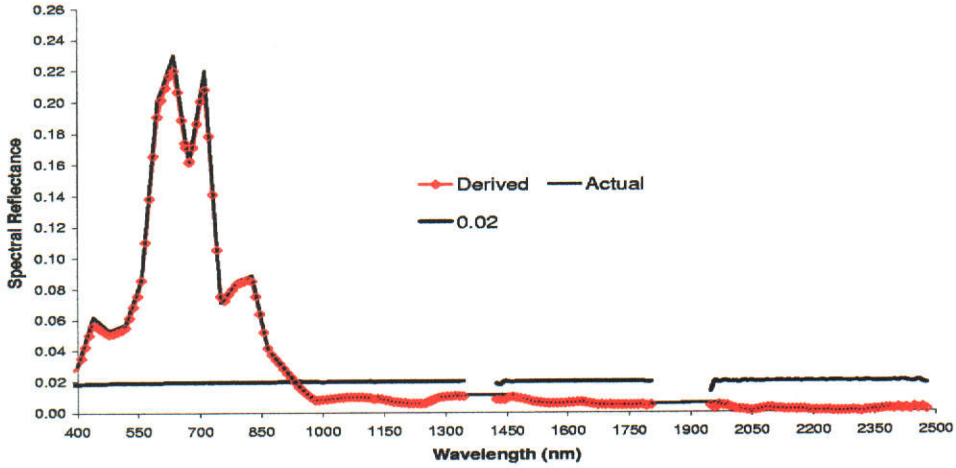

(b)

Figure 8.2: The derived reflectance over the first four dark targets of Table 8.13. Figure (a) shows the 0.5 and 1 % reflectance targets, while Figure (b) shows the 2 % and salt+water target. The absolute error in derived water vapour was less than 4 % for any of the targets. The success of the water vapour estimate is evident from the minimal water vapour absorption residual features observed in the spectra.

leaf water absorption feature is not accounted for. The results (Table 8.13) of the TSR water vapour estimation over vegetated spectra show the estimation error in water vapour is low (less than 1 %). The nonlinearity present in the vegetation spectrum will introduce systematic errors in derived water vapour using three-band ratios (Gao *et al.*, 1993) unless proper measurement and reference channel selection is made. The TSR on the other hand does not adjust the measurement or reference channels for different surface types since no prior knowledge of the surface is required.

(Gao *et al.*, 1993) showed that the error introduced into water vapour estimates with three band ratios is typically 5 % if the liquid water absorptions are ignored. A similar result was also noted by Carrére and Conel (1993) who found that the CIBR overestimated water vapour by 1–8 % and the narrow/wide method by 14 %, depending on the total water abundance present. Figures 8.3(a) and 8.3(b) show the derived reflectance for the two vegetation targets (Table 8.13). Figure 8.3(a), has a surface absorption feature located at approximately 1000 nm while Figure 8.3(b) has liquid water absorption features at 960 and 1200 nm. In both cases the derived reflectance compared with the actual reflectance is good. It is shown however in Chapter 10 that as the degree of nonlinearity in surface reflectance increases, the TSR method will introduce increased error into the water vapour estimates.

Man Made Products and Granite

The man made surfaces the TSR method was tested over were olive paint, galvanised steel and granite. The olive paint spectrum has a broad surface absorption feature at 880 nm while the granite is essentially linear in the VNIR-SWIR.

The error in water vapour estimate for the three surfaces is less than 1 %. The 880 nm feature in the olive paint spectrum has not hindered the estimation of water vapour. Figures 8.4(a),8.4(b) and 8.4(c) show the reflectance derived after the respective estimated water vapour content was applied in the atmospheric correction. The retrievals all show excellent agreement throughout the VNIR-SWIR, with some small discrepancy in Figures 8.4(b) and 8.4(c) in the visible part of the spectrum.

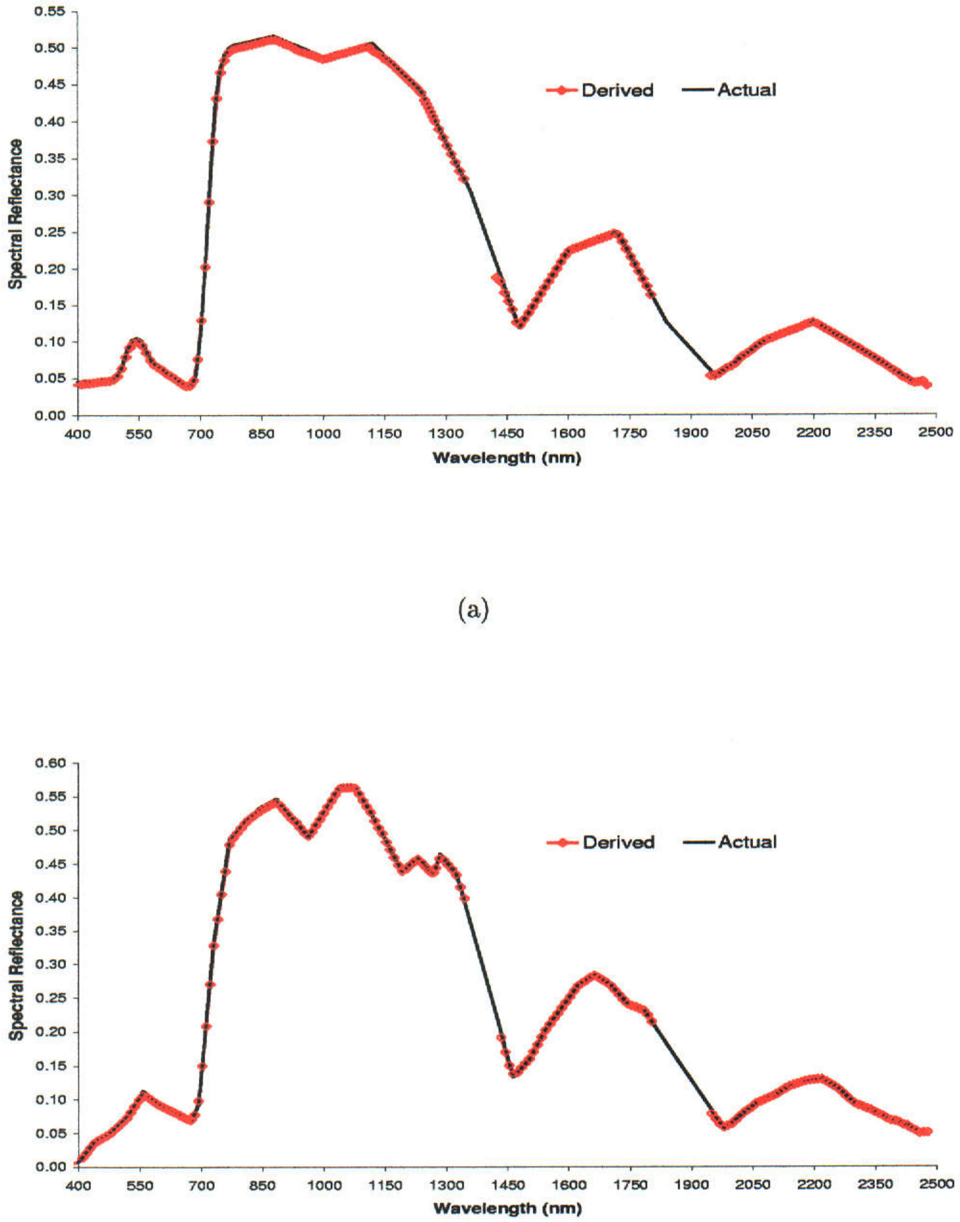

(a)

(b)

Figure 8.3: The derived reflectance over two vegetation targets. The first (a) has an absorption feature at approximately 1000 nm. The second (b) has a surface absorption feature at 960 and 1200 nm. The actual reflectance for each is also shown. The error in derived water vapour is less than 1 % in both cases.

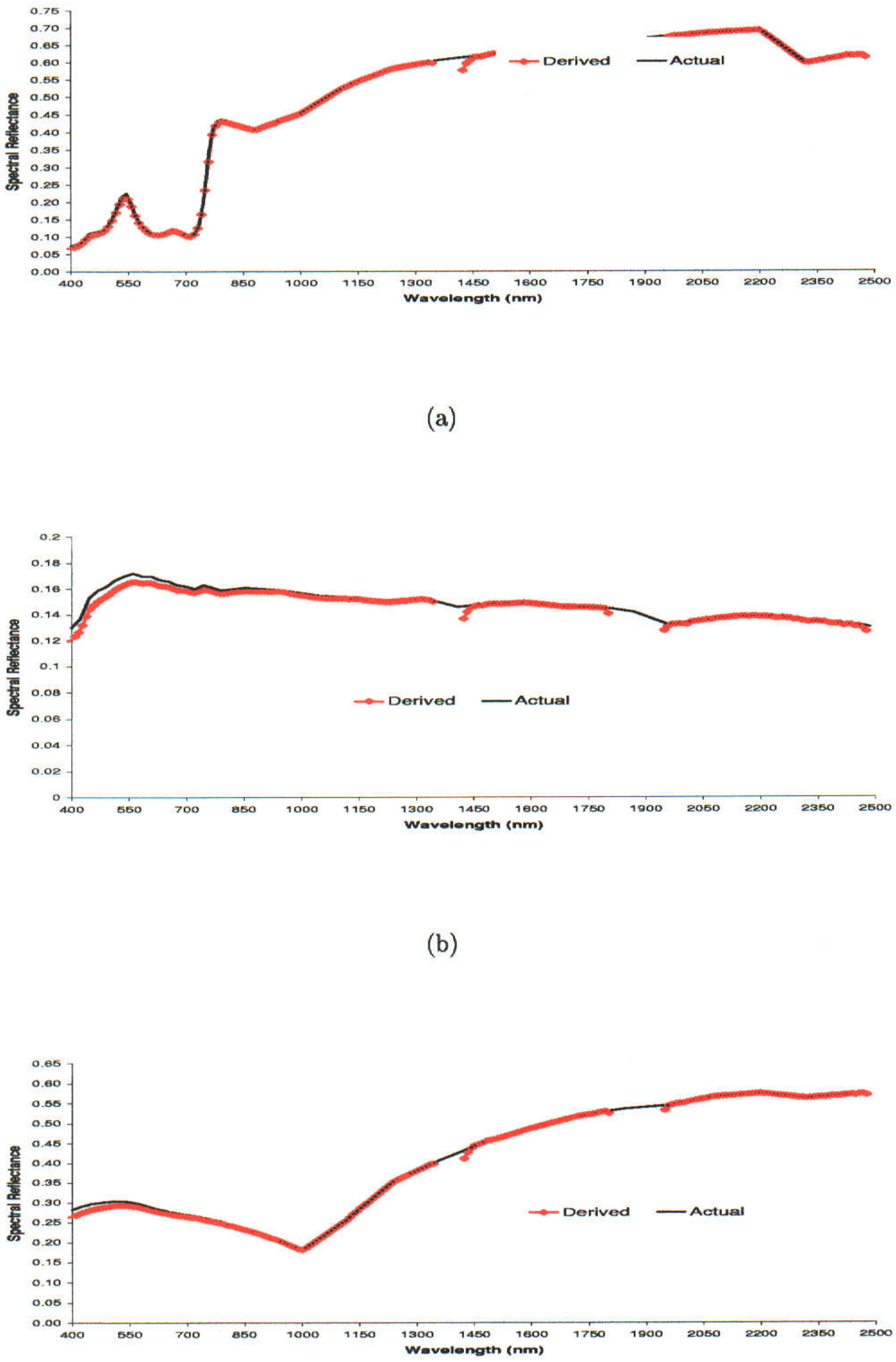

(c)

Figure 8.4: Retrieved spectral reflectance for Olive paint (a), granite (b) and galvanised steel (c).

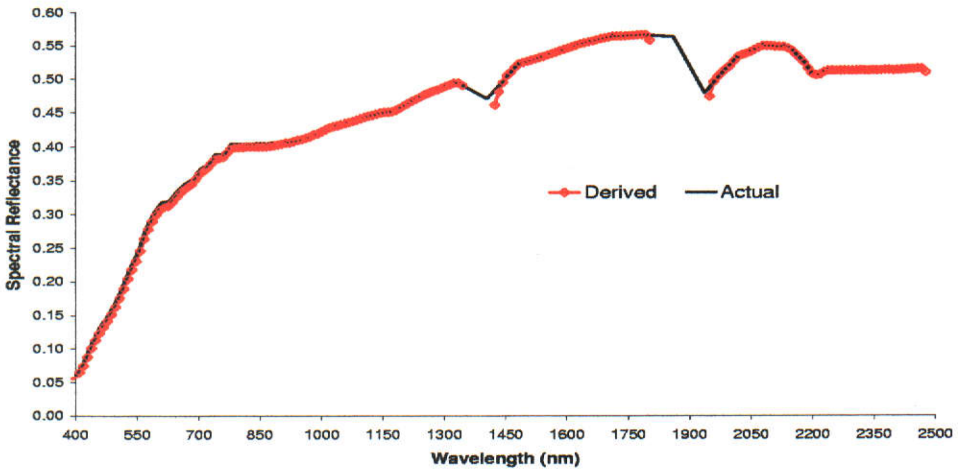

Figure 8.5: The derived and actual spectra for sandy loam. The error in derived water vapour over the sandy loam target is less than 1 %. The broad surface absorption feature centred at approximately 900 nm has not effected the estimate of water vapour and subsequently has lead to a good retrieval of surface reflectance.

Sandy Loam & Minerals

The broad surface absorption feature centred at 900 nm (see Figure 8.5) has not adversely effected the TSR water vapour estimate. The error in TSR-estimated water vapour (see Table 8.13) is less than 1 %. Figures 8.6(a),8.6(b) and 8.6(c) show the three mineral spectra used and derived. It is noted that the TSR does not use just the 940 and 1120 nm atmospheric water vapour absorption features but uses the majority of the spectrum from 800 to 2000 nm. Thus any absorption feature present in the interval could be considered as detrimental to the estimation of atmospheric water vapour if the surface reflectance is nonlinear. The presence of mineral surface absorption features was shown by Carrére and Conel (1993) to introduce error into CIBR or narrow/wide estimated water vapour ranging from 1 to 28 %.

Table 8.13 demonstrates that the absorption features located in or near the water vapour absorption features have negligible effect on the TSR derived water vapour. The error in estimated water vapour from any of the materials (montmorillonite, nontronite and alunite) is less than 1 %. This result is typical of the sensitivity analysis findings for other spectral types. Also, in Figure 8.6(a), is the retrieved reflectance for the constant reflectance target of 80 % with less than 1 % in estimated water vapour.

8.4 Summary

The sensitivity demonstrated the ability of the TSR method to estimate column atmospheric water vapour to high levels of accuracy. This has been shown to be hold true when reasonable levels of uncertainty exist in a number of input parameters. It was found the largest errors introduced into the TSR derived water vapour were caused by uncertainty in surface elevation, sensor scan angle and atmospheric model choice.

The errors for all three parameters was found to have maximum values ranging from 5 % to 8 %. All other factors, including aerosol visibility were found to have errors of less than 3 %. This shows the high stability and robust nature of the TSR method. In particular the small error introduced due to an incorrect knowledge of atmospheric aerosol visibility is a major step forward when compared to current methods.

The results of the analysis over differing surfaces is highly encouraging. It demonstrates that the TSR method is essentially independent of surface type. In practice though the derived water vapour is still a function of the remote sensing instrument used. If the instrument calibration is not 100 % characterised, or if the instrument drifts from its pre-flight configuration then error can be expected in the estimated atmospheric water vapour. As well, the analysis carried out was an analysis performed under ideal conditions, and as such, differences will exist between the model and true atmosphere. This will provide additional uncertainty to any water vapour estimate.

All though not analysed in this chapter, the SNR of any given instrument has an effect on the determination of column water vapour. If an instrument has low SNR the error in estimated water vapour can be expected to increase. If the surface reflectance is extremely small, as found over shaded and water targets, the decreased SNR introduce errors into the water vapour estimate. The SNR of AVIRIS, at a reference surface reflectance of 50 % has a mean value of

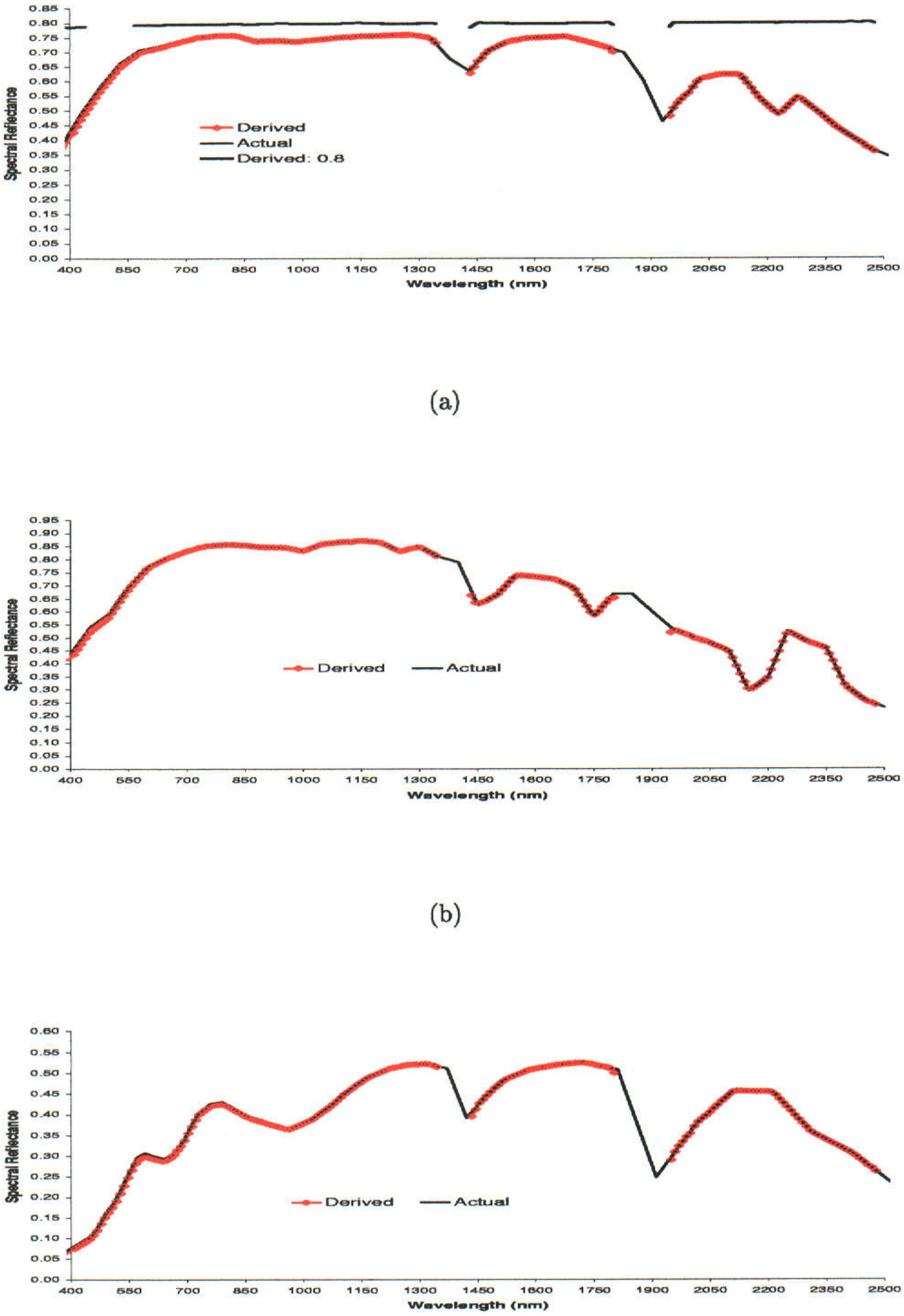

(a)

(b)

(c)

Figure 8.6: Retrieved spectral reflectance for montmorillonite and 0.8 reflectance target (a), nontronite (b) and alunite (c). The presence of surface absorption features in or near the water vapour absorption features has not hindered the retrieval of water vapour and the subsequent reflectance derivation.

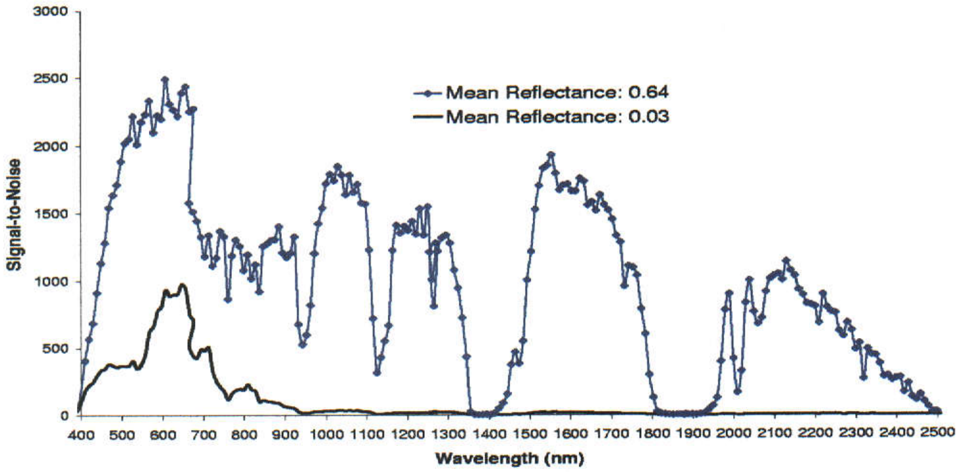

Figure 8.7: The derived SNR for a measured AVIRIS radiance signal from two different surfaces. The mean reflectance value produces an SNR that is directly comparable to published results (Green *et al.*, 1998). The mean reflectance of 0.03 shows how low the SNR can get over dark targets which in turn adds to the uncertainty of derived water vapour over dark targets.

approximately 700:1 - 800:1 (Green *et al.*, 1998). Using the 1999 noise equivalent radiance difference (NEDL) dark current values for AVIRIS (Green, 2000), a SNR was calculated using a measured AVIRIS radiance signal. The derived surface reflectance had a mean value of 0.65. The result is shown in Figure 8.7 and is comparable to the AVIRIS SNR Green *et al.* (1998) result. Also shown in Figure 8.7 is the calculated SNR of a water target with a mean reflectance of 0.03. The SNR at 940 nm is approximately 18:1 and 8:1 at 1120 nm. Thus at 940 nm almost 5 % of the signal is noise and at 1120 nm almost 13 % is noise. If the assumption that this noise will appear in the dark target water vapour estimates then an additional 5–13 % error can be expected in the derivations of water vapour over such targets. Chapter 10 shows the results of applying the TSR method over water and dark targets and demonstrates the effects of SNR over such targets.

As well, it will be shown (in Chapter 10) that in practice the linear interpolation method, used to estimate surface reflectance in the water absorption bands, begins to fail if the degree of nonlinearity in the true surface reflectance spectra is to large in the water vapour affected spectral areas.

Chapter 9

Geographic Sites used in the Analysis

To test and examine the TSR method three different hyperspectral data cubes were obtained. Two are AVIRIS measured, while the third is HyMap measured. The two AVIRIS data sets are from similar geographic areas, although the flight dates differ by approximately 3 months. Both of the AVIRIS data sets are considered as rugged terrain data sets. While the HyMap data set is a topographically flat region. The combination of the three data sets provides a means of testing the TSR scheme under varied conditions. This chapter outlines the three data sets and provides the main flight and navigation information for each area.

9.1 Jasper Ridge

Jasper Ridge (Figure 9.1) is located in San Mateo county in California at a latitude of 37.41° N and longitude 122.23° W. The AVIRIS flight occurred on the 03/04/1997. The flight line was labelled as *f970403t01p02_r03*. The mean coordinated universal time (UTC) of flight was 20 hours and 9 minutes. The mean scene elevation was 250 m. With the largest elevation in the scene being approximately 500 m, and the lowest elevation 150 m. Thus at the peak terrain elevations of 500 m a 2–3 % error may be expected in estimated water vapour. The mean sensor altitude was 21.5 km and a MLW atmospheric model was chosen according to the date of flight.

Jasper Ridge has mountains on one side of the image, with flat urban areas on the other. The presence of mountains and vegetation enable the TSR to be tested on non-linear spectral reflecting surfaces and topographically varying surfaces. The total flight line length shown is approximately 40 km. Figures 9.1(a), 9.1(c), 9.1(b) and 9.1(d) show the 4 subscenes that make up the total Jasper Ridge scene.

9.2 Moffett Field

AVIRIS data was collected over Moffett Field (see Figure 9.2) on the 20/06/1997 and labelled as *f970620t01p02_r03*. Moffett Field is located in the county of Santa Clara, California at a latitude of 37.42° N and longitude of 122.05° W. The mean UTC time for the time of over flight was 18 hours and 49 minutes. The mean scene elevation used in the processing was set to a value of 250 m. The highest elevation in the Moffett Field data is 800 m and the lowest elevation is 50 m. The mountainous regions in Moffett Field only occupy a small portion of the total scene though, and therefore the mean elevation used is weighted toward the predominant lower elevation. Referring to Chapter 8, the error in estimated water vapour at the higher elevations can be expected to reach 5 % due to the choice of mean surface elevation. The mean sensor altitude was set at 21.4 km with a MLS atmospheric model.

Moffett Field allows the testing of the TSR over both rugged terrain and dark targets. The dark targets include water and water+salt in the salt evaporation ponds located around San Francisco Bay. The total flight line is approximately 40 km.

9.3 Brukunga: South Australia

The Brukunga data was collected by HyMap on the 14/03/2001. Brukunga is located in South Australia at a latitude of 35.20° S and longitude of 138.56° E. The scene (Figure 9.3) has dimensions of 512 (pixels) by 1300 (lines) by 126 (spectral channels). The UTC time for the data acquisition was 3 hours 4 minutes and 38 seconds. The acquisition altitude was 1.71 km with an assumed mean scene

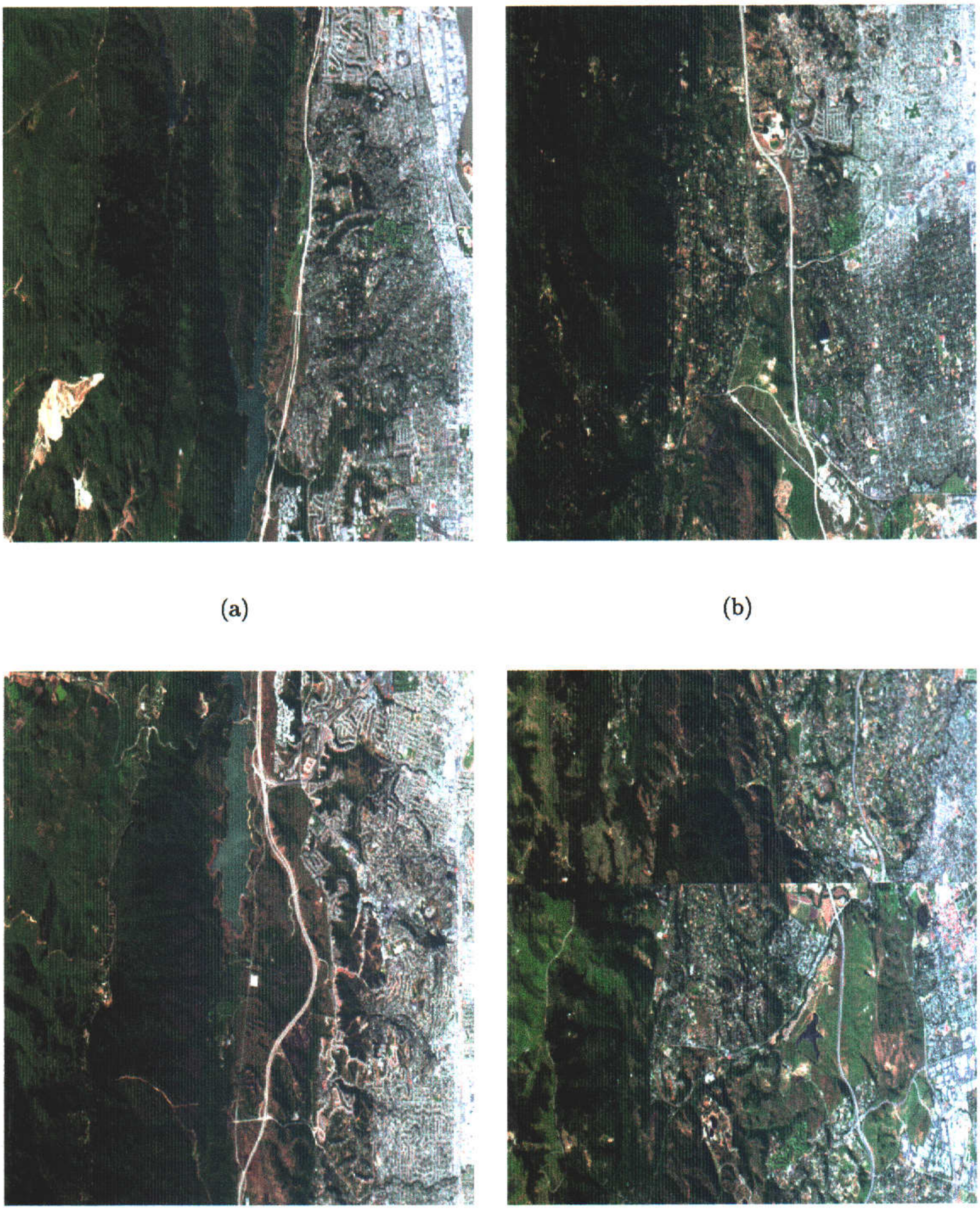

(a) (b)

(c) (d)

Figure 9.1: AVIRIS RGB images from the Jasper Ridge data set. The four separate scenes, 9.1(a), 9.1(c), 9.1(b) and 9.1(d) combine to produce the total AVIRIS scene for Jasper Ridge. Topographical variation is observed in scene with low lying urban areas as well as mountain regions. The most common surface type in the Jasper Ridge scenes is green vegetation. A mismatch in 9.1(d) is noted. This is not an instrument error but a processing error on the part of the author.

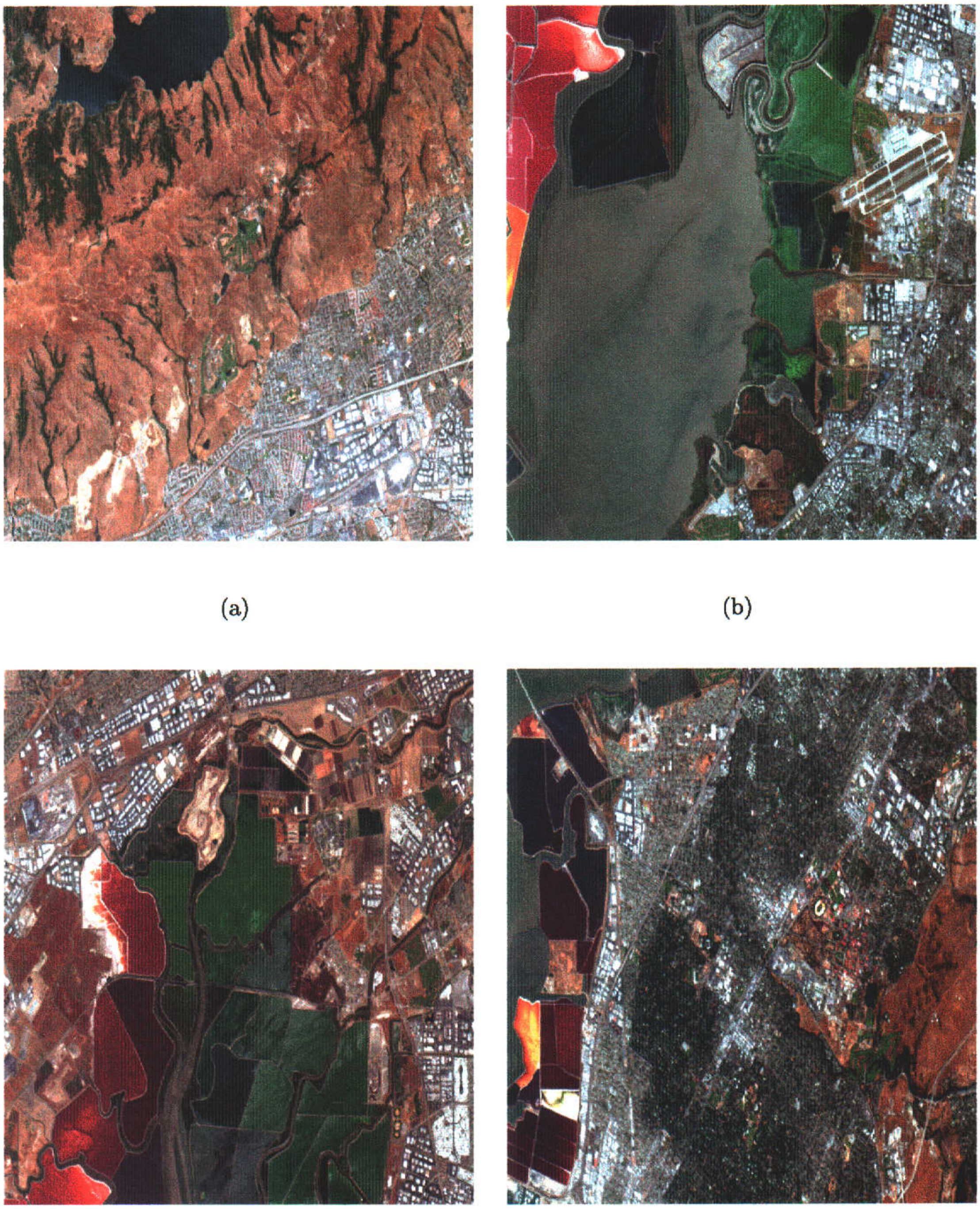

(a) (b)

(c) (d)

Figure 9.2: An AVIRIS RGB representation of Moffett Field. The four images, 9.2(a), 9.2(c), 9.2(b) and 9.2(d) combine to produce the total Moffett Field scene. The scene is observed to vary on a topographical basis as well as on surface type. The presence of the salt evaporators and the Bay area provide the opportunity to test the TSR over demanding surface targets.

elevation of 269 m. The aerosol visibility was set at 100 km. Figure 9.3 shows the HyMap RGB image of Brukunga. The Brukunga topography provides a flat surface for analysis. The atmospheric model selected to represent the Brukunga scenes was a MLS.

9.4 Summary

Three hyperspectral data sets were acquired for testing of the TSR water vapour estimation method. The combination of the three scenes provides the means for testing the TSR under a number of conditions. These include,

- topographically varied landscapes
  - rugged terrain (Jasper ridge and Moffett Field)
  - flat terrain (predominantly Brukunga. Also includes Jasper Ridge and Moffett Field)
- spectrally varied surfaces. That include,
  - vegetation (Moffett Field, Jasper Ridge and Brukunga)
  - man-made surfaces (Moffett Field, Jasper Ridge and Brukunga)
  - salt evaporators (Moffett Field)
  - water (Moffett Field and Jasper Ridge)
  - urban areas (Moffett Field and Jasper Ridge)

This combination provides a diverse range of conditions for which to test the TSR scheme. Unfortunately, no in-situ data was accessible for any of the test sites examined. To this end, established relationships were sought that described water vapour as a function of some other variable, such as surface elevation, and compared to the findings of other studies. As well, derived surface spectra were examined for the presence of atmospheric water vapour residual features. The latter indicating the degree of success in estimated water vapour for the pixel under consideration.

Figure 9.3: Brukunga Mine: Scenes 1 and 2. The RGB images show the open pit mine and the surrounding area. The images were acquired by HyMap on the 14/03/2001.

Chapter 10

Results

Presented in this chapter is an evaluation of the application of the TSR method on AVIRIS and HyMap radiometric data. The results form the end point of the scheme and are, in essence, the culmination of all methodologies and derivations outlined by previous chapters. They encompass three geographic regions which allows the method to be tested under a range of conditions. The physical characteristics of the regions range from flat to mountainous terrain and present a range of contrasting spectral surfaces exhibiting linearity and nonlinearity. The results are presented in five separate sections. Each section evaluates a particular aspect of the water vapour estimation scheme. In this manner the performance of the TSR scheme is evaluated in a piecewise manner.

Firstly, the water vapour results are presented for topographically varied surfaces. This allows the spatial distribution of estimated atmospheric water vapour to be examined. The second aspect examines the effect of contrasting spectral surfaces on the estimation of water vapour. Next the application of the TSR method to targets that are spectrally dark is investigated. The results show that the TSR method does not have difficulty with dark targets, but rather, the limitations are those imposed by instrument signal-to-noise. Next, the TSR method is presented in terms of the multiple water vapour estimates calculated for any given spatial element. It is demonstrated that the TSR method allows the detection of what may be surface absorption features located within atmospheric water absorption bands. Further, multiple water vapour estimates (per-pixel) provide a means of rejecting outlying results. Lastly, the TSR-estimated water vapour for

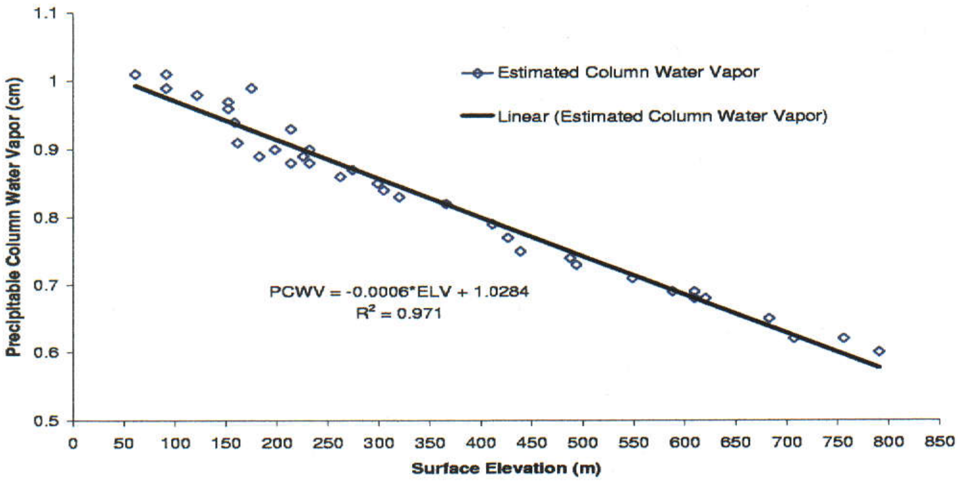

Figure 10.1: TSR-estimated precipitable water against DEM surface elevation. The relationship is strongly linear and agrees with the Roberts *et al.* (1993) study.

scene 1 of the Moffett Field site is compared to CIBR estimated water vapour of the same site. It will be shown that the CIBR is sensitive to changes in surface type.

10.1 Topographic and Spatial Effects

Roberts *et al.* (1993) and Schläpfer (1998) demonstrated that atmospheric water vapour exhibits a strong linear relationship with surface elevation. The Roberts *et al.* (1993) study used fifteen ground control points in conjunction with a DEM to create scatterplots of water vapour versus surface elevation. The result showed that atmospheric water vapour is highly correlated with terrain elevation.

To examine the results of the TSR-estimated water vapour over rugged terrain a similar approach was adopted. Scatterplots of known DEM surface elevation and TSR-estimated water vapour were determined for Moffett Field and Jasper Ridge data. Thirty-six ground points of known elevation were co-registered with TSR-estimated column water vapour image. The TSR-estimated water vapour with surface elevation results (Figure 10.1) show a strong linear relationship between atmospheric water vapour and surface elevation for Moffett Field. As noted

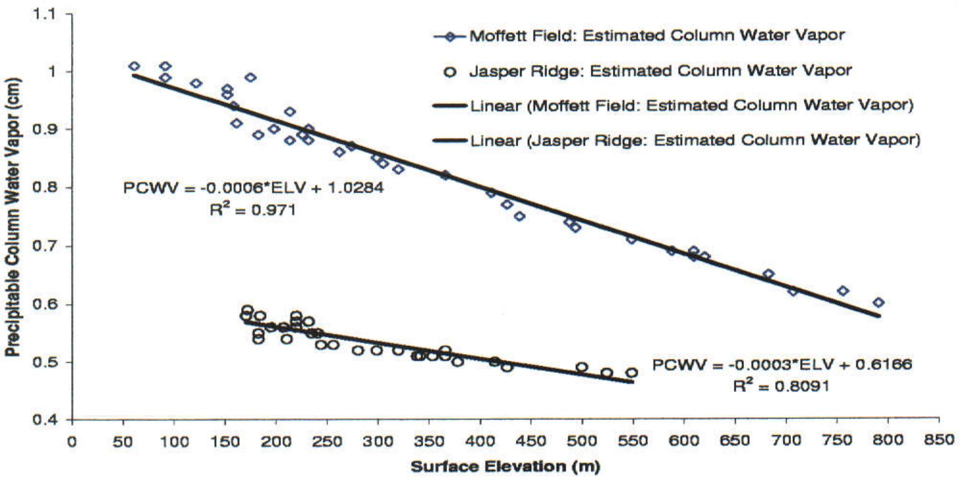

Figure 10.2: TSR-estimated precipitable water versus DEM surface elevation for Jasper Ridge and Moffett Field. Jasper Ridge shows less water vapour than Moffett Field and the lapse rate (0.0003 cm m^{-1}) is half that of Moffett Field. The relationship is strongly linear in both cases and is consistent with the Roberts *et al.* (1993) results.

by Roberts *et al.* (1993) the relationship between water vapour and elevation may also be represented by an exponential relationship which will be more suitable for increased surface elevation. Figure 10.2 presents the results for a similar analysis at Jasper Ridge. At Jasper Ridge the estimated water vapour is also highly correlated with surface elevation. The correlation at Jasper Ridge is not as strong as that of Moffett Field but still indicates high correlation. Figure 10.2 also shows the lapse rate (as determined from the gradients of the linear relationships) of precipitable water at Jasper Ridge is half that of Moffett Field, with Jasper Ridge having a water vapour lapse rate of 0.0003 cm per meter.

A comparison of the TSR-estimated water vapour imagery for Moffett Field, Jasper Ridge and Brukunga is shown in Figure 10.3. The same linear stretch is applied to all the water vapour maps in the Figure 10.3. The Moffett Field scene (Figure 10.3(a)) exhibits the largest range in precipitable water vapour and is followed by Jasper Ridge (Figure 10.3(b)), with the smaller elevation range, and finally the topographically flat Brukunga (Figure 10.3(c)). Moffett Field (Figure 10.3(a)) shows the mountainous areas (at the top of the image) as regions of low

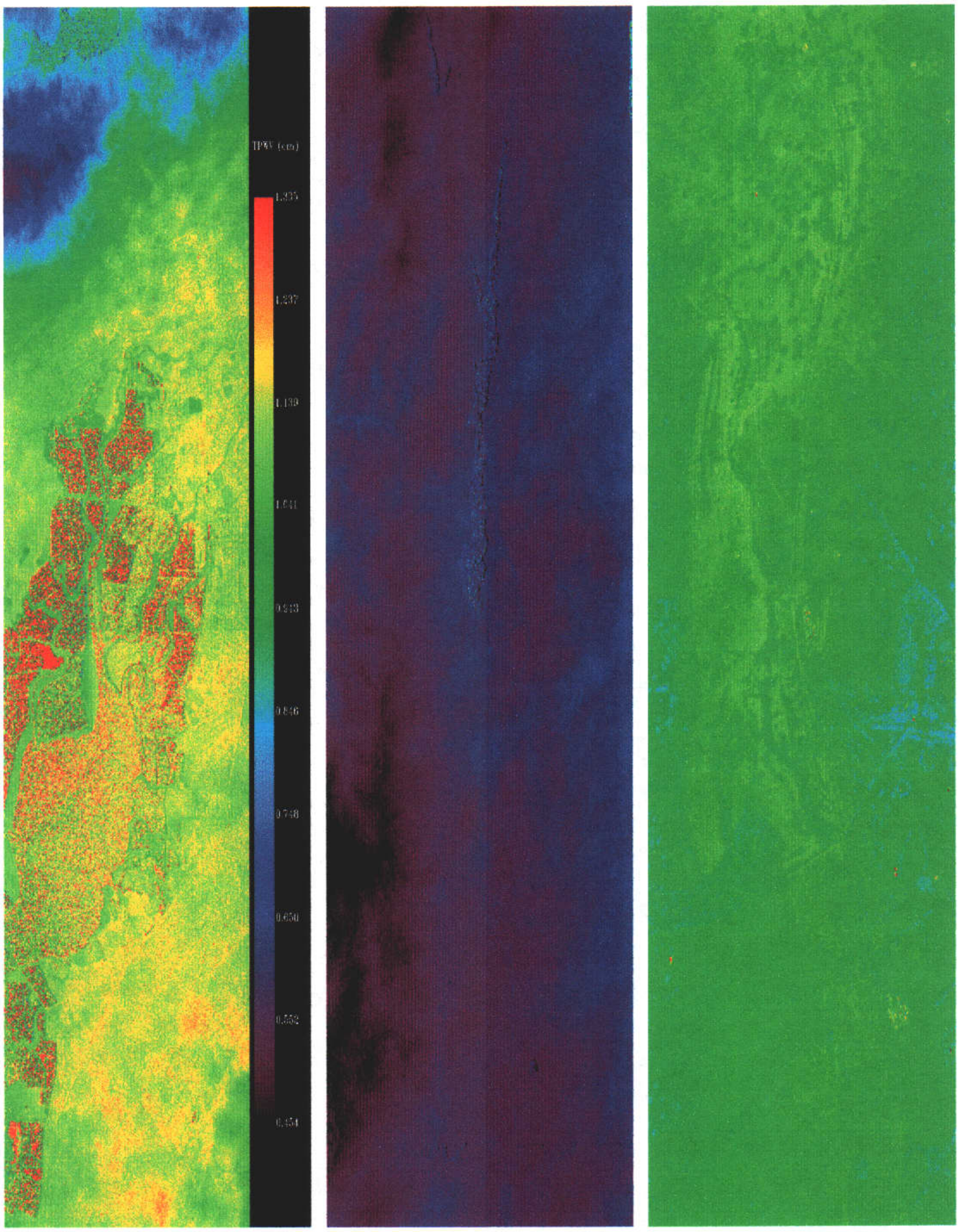

(a) (b) (c)

Figure 10.3: Estimated precipitable column water vapour imagery (in cm of precipitable water) for Moffett Field 10.3(a), Jasper Ridge 10.3(b) and Brukunga 10.3(c). The scale (in (a)) of precipitable water encompasses the range of TSR-estimated water vapour from all three scenes. Thus, the largest variation of water vapour is found at Moffett Field followed by Jasper and finally the topographically flat Brukunga has the smallest variation in estimated water vapour.

Region	Mean (cm)	Standard Deviation (cm)	% S.Dev from Mean
Moffett Field	1.081	0.481	45
Jasper Ridge	0.563	0.044	7.8
Brukunga	0.988	0.039	4

Table 10.1: Scene precipitable water vapour statistics for Moffett Field, Jasper Ridge and Brukunga. Interestingly, even though Moffett Field and Brukunga have approximately the same mean water vapour, they have vastly different ranges of water vapour for the scene. Likewise, Jasper Ridge and Brukunga have similar standard deviations yet Jasper Ridge has only 57 % of the water vapour content.

water vapour which increases as terrain elevation decreases. Jasper Ridge (Figure 10.3(b)) has a much smaller range of water vapour yet it still is evident in-scene topographic variation exists at this selected map stretch. The Brukunga water vapour map (Figure 10.3(c)) shows variation that are due to surface type rather than terrain elevation. The calculated water vapour variation for the Brukunga scene is approximately ±4 % about the mean. It is later demonstrated that the variation in estimated water vapour at Brukunga is approaching the noise level of the TSR scheme.

Table 10.1 gives calculated scene statistics for the three regions. Although Moffett Field and Brukunga have approximately the same mean precipitable water vapour, Brukunga only has a ±4 % standard deviation about the mean. Thus, the effect of the topography is apparent in the scene-derived statistics and shows that the flatter Brukunga scene displays vastly reduced variation in estimated water vapour. On the other hand, it is found that Jasper Ridge and Brukunga have standard deviations of similar order yet the higher terrain elevation of Jasper Ridge has a smaller mean column water vapour (almost half that of Brukunga).

Therefore, variation in atmospheric column water vapour is most dominant in regions exhibiting large topographical variation. In regions such as Brukunga, that are topographically flat, it requires reasonable differences in horizontal water vapour distribution to observe variation. With a 4 % variation across the entire scene (such as Brukunga) it would be possible to correct the entire scene for the effects of atmospheric water vapour (using a mean estimated water vapour value) at little sacrifice to accuracy of the derived surface reflectance.

As well, the linear relationship that exists between water vapour and scene elevation may provide a more efficient means of estimating column water vapour in regions having large topographical relief. Using a DEM of a given area and estimating column water vapour for a selection of high and low elevations, the linear (or exponential) relationship may be established. From this relation, the column water vapour may be estimated purely as a function of scene elevation. An example of the natural heterogeneity of atmospheric water vapour is shown in Figure 10.4 (Jasper Ridge rescaled to maximum and minimum water vapour). The right hand side of the water vapour map shows water vapour heterogeneity over a topographically flat region. It is possible that the increase in atmospheric water vapour over this area may be due to the presence of the ocean located just outside the sensor scan limit on the right hand side. It is observed that the distribution of water vapour in this area has its maximum values along the ocean-land border. The water vapour is observed to decrease and become more heterogeneous as the image is traversed from right to left.

10.2 Surface Effects and Results

This section examines the effects of varying spectral surfaces on TSR-estimated water vapour maps and derived surface reflectance spectra. Errors in presumed surface reflectance (estimated by the TSR modelling process) are revealed in the estimated water vapour images as pronounced demarkation between contrasting surface types. Conversely, errors in estimated water vapour are expressed as residual atmospheric water vapour features in the derived surface spectra (see Chapter 3 section 3.3). However, variation is also governed by other effects such as topography and the inherent background noise level in the TSR method. The water vapour images presented in this section have the bounding stretch limits set to the maximum and minimum estimated water vapour for the scene. This highlights differences in estimated water vapour that are attributable to surface effects.

It is noted that the presence of atmospheric residual features present in the derived surface reflectance do not always imply that the water vapour estimates

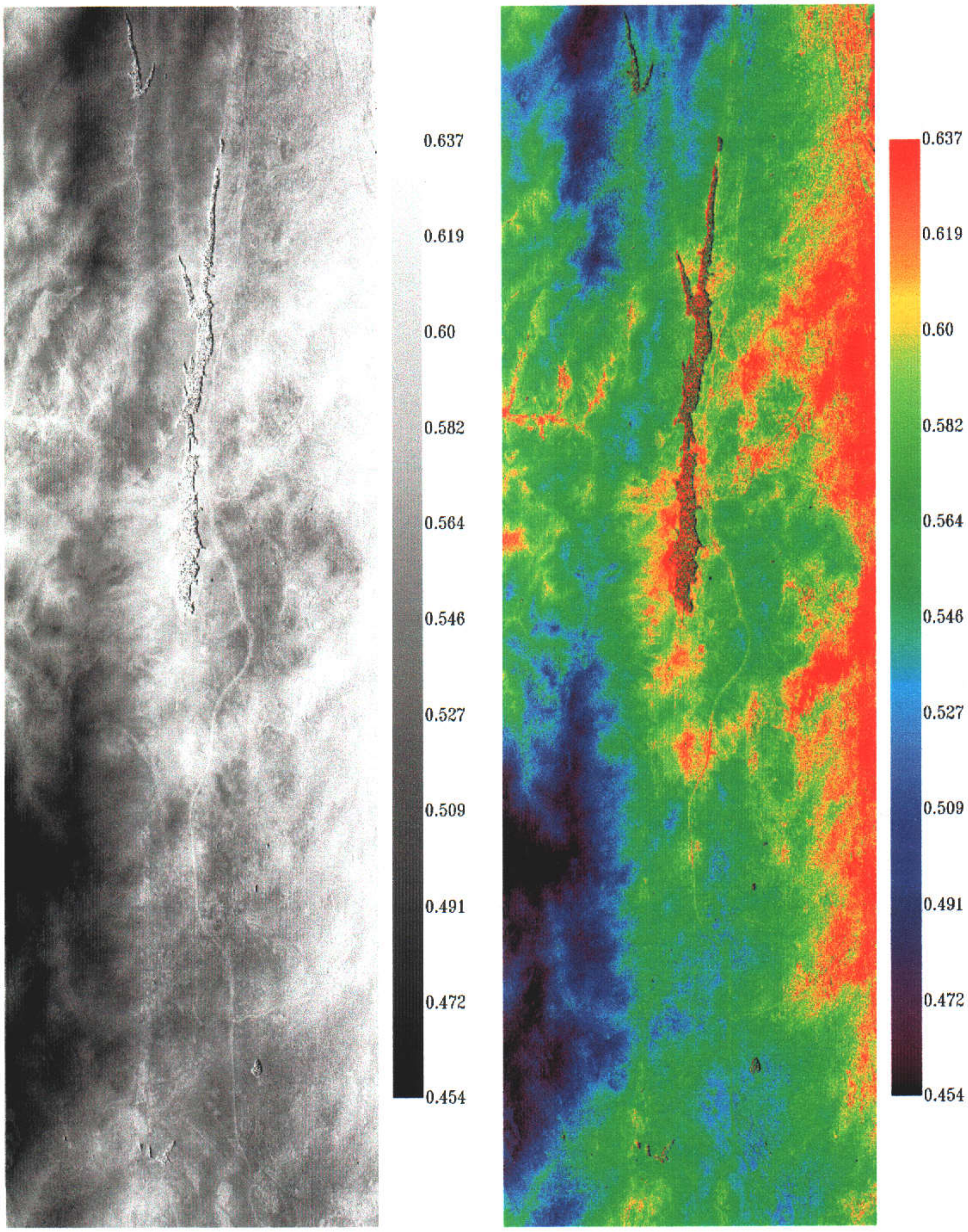

(a) (b)

Figure 10.4: TSR-estimated precipitable column water vapour (in cm of precipitable water) at Jasper Ridge. 10.4(a) is a grey scale water vapour image, shows while 10.4(b) is the colour scaled water vapour image of the same scene. Note the heterogeneous distribution of precipitable water vapour on the right of the water vapour image.

are in error. Green and Pavri (2000) show that, even when all possible measurements and in-situ data are collected, differences between MODTRAN-modelled and measured AVIRIS radiances may still occur. In the Green and Pavri (2000) study, the predominant errors occur in the atmospheric water vapour absorption bands. Other residual features are also observed for atmospheric CO_2 and O_2 (Adler-Golden *et al.*, 1999; Green and Pavri, 2000). It is conjectured by Adler-Golden *et al.* (1999) that the water vapour residual features, observed when using the MODTRAN transmittance model, may be due to water vapour continuum extrapolations that are based on mid-wave IR measurements. In both the Adler-Golden *et al.* (1999) and Green and Pavri (2000) study, examples of atmospheric residual features may be found in all surface reflectances determined.

No attempt has been made to spectrally smooth the derived surface reflectances presented in this chapter. As such, the surface reflectance spectra (from this point on) show almost all of the atmospheric residual features just discussed. As previously mentioned, no in-situ measurements were available for this study. This does not mean though that the method may not be evaluated. As noted by other researchers, namely (Adler-Golden *et al.*, 1999), in the absence of ground truth measurements, the success of the correction for atmospheric absorption bands may be assessed by examining the absorption band residuals in derived surface reflectances.

10.2.1 Moffett Field

Figure 10.5 shows the TSR-estimated precipitable column water vapour for Moffett Field. A number of regions are identified within the scene (namely, A, B, C, D, E, F and G) and represent regions of interest (ROI) selected to examine surface effects expressed in the estimated water vapour imagery. Table 10.2 gives the calculated mean and standard deviation of estimated water vapour for each ROI. All of the ROIs considered are in topographically flat areas of Moffett Field. The average percentage standard deviation of estimated water vapour for the seven ROIs was calculated as 2.4 %. This result is assumed to be the background noise level of the TSR method for the Moffett Field scene.

In the area listed as ROI A in Figure 10.5(b), surface structure is observed

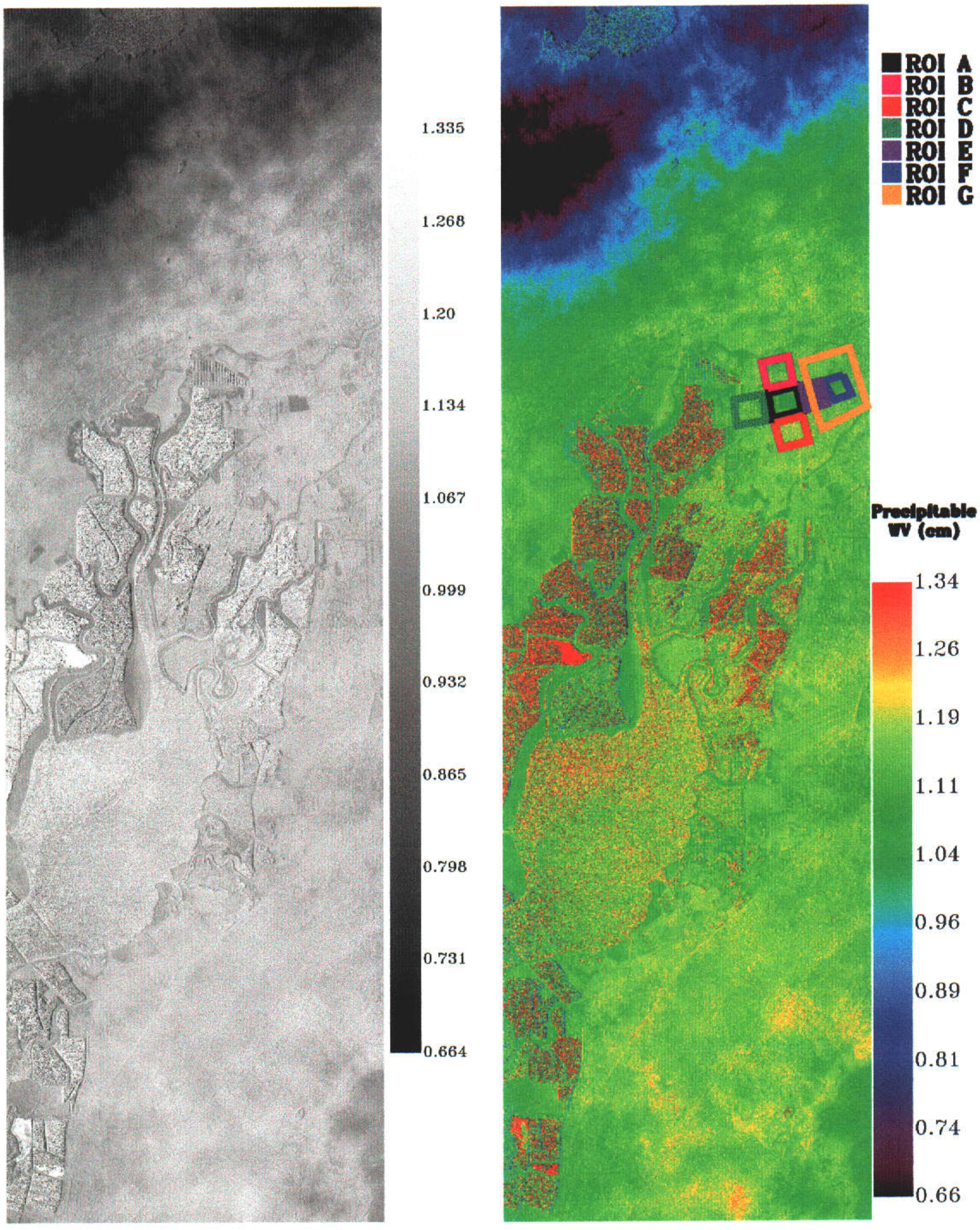

(a) (b)

Figure 10.5: Estimated TSR precipitable column water vapour (in cm for both images) from Moffett Field. Surface structure is observed in the water vapour image. The surface structure caused by the presence of the salt evaporators and the Bay area are discussed in section 10.3.

ROI	Mean Estimated Water Vapour (cm)	Standard Deviation (cm)
A	1.04	0.02
B	1.14	0.02
C	1.14	0.03
D	1.10	0.03
E	1.13	0.04
F	1.09	0.02
G	1.13	0.03

Table 10.2: Calculated mean estimated water vapour and standard deviation for the seven regions of interest (ROI) created in the Moffett Field scene. The average percentage standard deviation is 2.4 % and is assumed to be the background noise level for the TSR method at Moffett Field.

in the form of lower water vapour estimates. These may also be seen in the grey scale image Figure 10.5(a). From Table 10.2, the mean water vapour for ROI A is calculated as 1.04 cm of precipitable water vapour. This result shows that the water vapour in ROI A is approximately 8 % lower than for the surrounding ROIs (B, C, D and E). The cause of this difference in water vapour is attributed to errors in the surface reflectance knowledge being propagated through the TSR method.

An examination of the derived surface spectra from ROI A and the surrounding ROIs shows differences in spectral surface types for the ROIs. Figure 10.6 shows derived surface reflectance for pixels located within ROI A. The spectra are of green vegetation exhibiting heavy leaf water absorption. Differences in magnitude are observed in the derived spectra. The mean derived surface reflectance for ROI A is shown as the red spectra in Figure 10.6. In all cases, the derived spectra show indications of underestimated atmospheric water vapour.

An examination of the ROI A derived surface spectra shows that the surrounding surfaces differ spectrally from that of ROI A. Figure 10.7 shows the representative derived spectra from ROI B, C, D and E. In all cases, except ROI D, the surrounding area is dry grass. As noted at the start of this section, water vapour residual features may still appear in derived spectra due to inaccuracies in

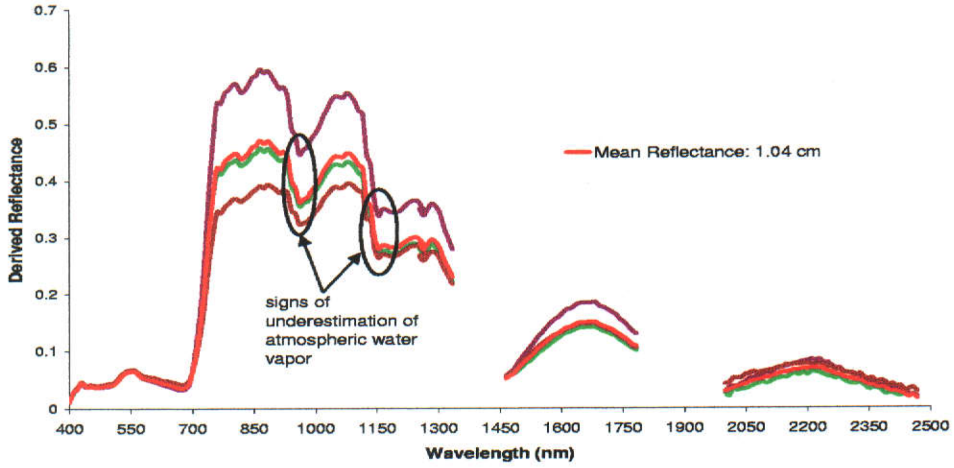

Figure 10.6: Derived surface reflectance for ROI A of Moffett Field. The ROI consists of green vegetation targets that exhibit strong leaf water absorption. The brightness of the spectra in the NIR is found to be strongly varied. The mean derived surface reflectance (red spectra) for the ROI is shown as well as the average estimated water vapour.

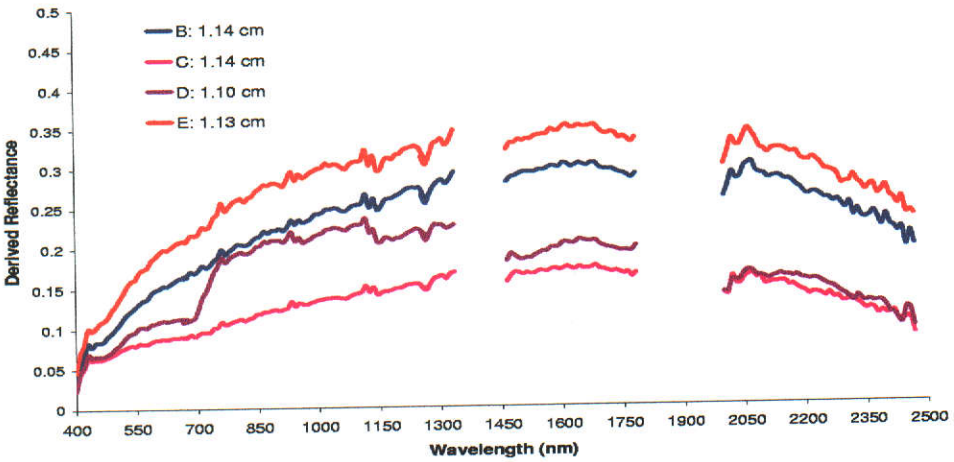

Figure 10.7: Derived surface reflectance for ROIs surrounding ROI A of Moffett Field. The spectra show dry grass and vegetation (D). Residual atmospheric features are observed but are considered as minimised with respect to atmospheric water vapour. The average precipitable water vapour for the surrounding ROIs was calculated to be 1.13 cm.

atmospheric modelling and instrument spectral and radiometric calibration. The residual features observed in Figure 10.7 are minimised (not spectrally smoothed) for the Moffett Field data. If the water vapour is lowered in an attempt to further reduce the water vapour residuals the derived surface spectra exhibit signs of underestimation of atmospheric water vapour.

The most notable difference between the surfaces surrounding ROI A are the surface absorption features located in, or near, the water bands. As noted in Chapter 7, the TSR method estimates surface reflectance in the water vapour bands via linear interpolation. This method, although highly effective, may still fail. The degree of surface reflectance nonlinearity in ROI A is large in the water vapour bands and, in this case, the relatively simple method of linear interpolation is beginning to fail. Essentially, the surface reflectance has been underestimated in the water bands, which in turn has caused the TSR method to under estimate the water vapour. An alternative approach to the linear interpolation method is discussed further in Chapter 11.

Table 10.2 lists the mean estimated water vapour for ROI F as 1.09 cm while a surrounding area (ROI G) is 1.13 cm; the latter value being consistent with the ROIs surrounding ROI A. The difference in estimated water vapour of 3.5 % between ROI F and G is again, attributed to surface reflectance modelling error. Of particular interest are the surface types representing ROI F and G as they demonstrate the effect that the degree of nonlinearity has on the water vapour estimates. Figures 10.8 show derived surface reflectances for the two ROIs. In this case both ROIs are comprised of vegetation targets. The difference between ROI F and G is the amount of leaf water present. ROI F spectra show greater leaf water absorption than the ROI G spectra.

As noted in the ROI A study, the estimated water vapour is lower in the ROI F results due to the degree of surface nonlinearity. This may be confirmed by examining the ROI F and G results in Table 10.2. Although ROI G contains vegetation, the amount of water vapour estimated in the ROI is consistent with the other ROIs (excluding ROI A). The estimated water vapour in ROI F is approximately 3.5 % smaller than that of the surrounding ROIs. It is suspected that the degree of nonlinearity in ROI F is less than that of ROI A, and thus, the ROI F estimated water vapour is closer to level in the surrounding areas.

Since the leaf water absorptions in ROI G are not causing the TSR method to retrieve incorrect atmospheric water vapour, it may be concluded that, the degree of nonlinearity in the ROI G spectra is not significantly large to cause failure in the linear interpolation scheme (outlined in Chapter 7). Again, the residual water vapour features cannot be minimised any further without having the derived reflectance show signs of water vapour underestimation.

10.2.2 Brukunga

Figure 10.9 shows the estimated precipitable water vapour for the Brukunga region. A contrast stretch has been applied, with the upper and lower bounds set to the maximum and minimum estimated water vapour respectively. This stretch, which represents 1.84 mm of water vapour, clearly shows surface-induced effects present in the water vapour imagery.

As with Moffett Field, a number of ROIs are selected to gauge the magnitude

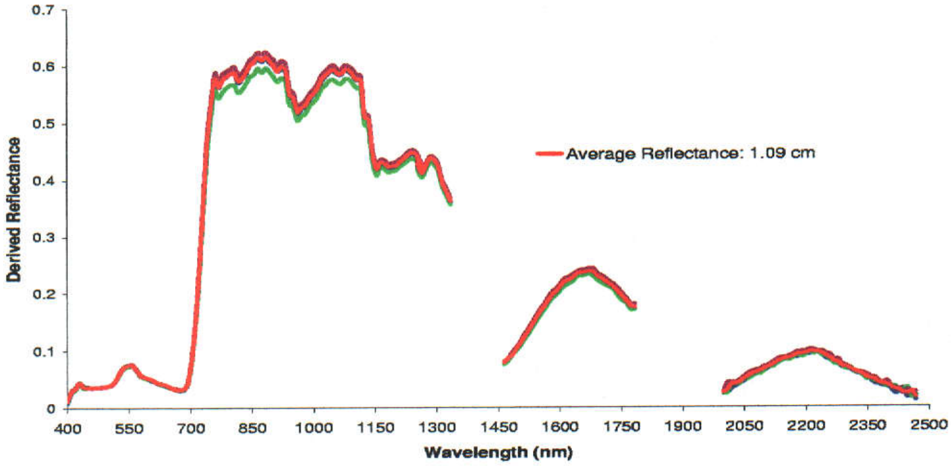

(a)

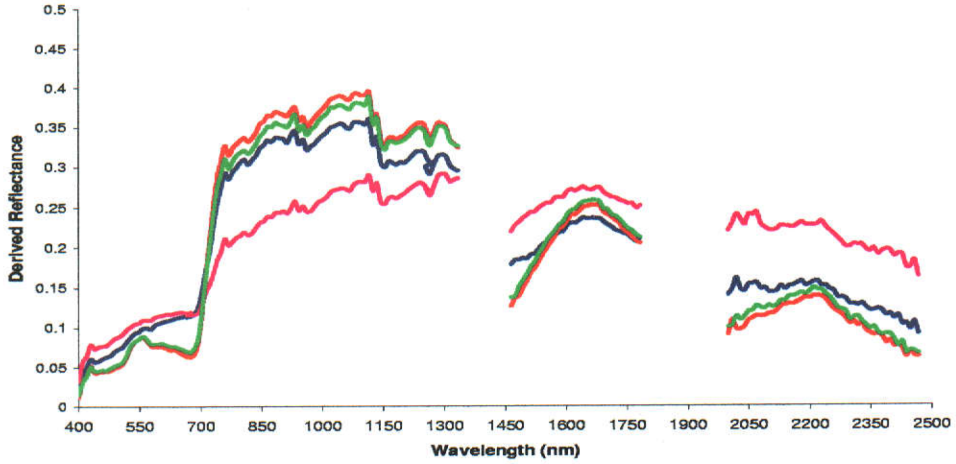

(b)

Figure 10.8: Derived surface reflectance at Moffett Field for green vegetation (10.8(a), ROI F) and drier vegetation (10.8(b), ROI G: 1.13 cm of precipitable water vapour). Although both show leaf water absorption features, the degree of leaf water absorption is higher for ROI F. The degree of nonlinearity in the Figure 10.8(a) spectra causes water vapour to be underestimated.

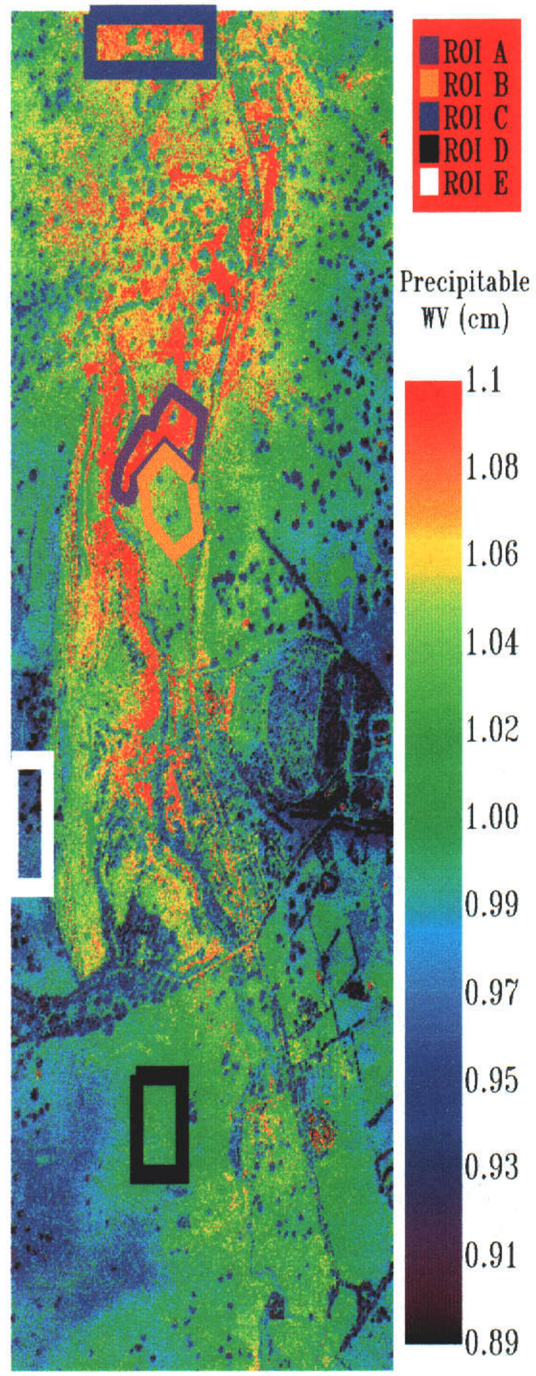

Figure 10.9: TSR-estimated precipitable water vapour for Brukunga. The estimated water vapour imagery shows extreme variation within the scene yet the standard deviation for the scene was found to be only 4 %.

ROI	Mean Estimated Water Vapour (cm)	Standard Deviation (cm)
A	1.05	0.02
B	1.02	0.02
C	1.04	0.03
D	0.99	0.01
E	0.92	0.02

Table 10.3: Brukunga regions of interest (ROI). The estimated precipitable water vapour, in cm, and the standard deviation for each of the selected regions is shown. The average deviation of water vapour over all 5 ROIs is approximately 2 %.

of the surface effect and to assess its relevance on the overall result. For each ROI the mean estimated precipitable water vapour and its standard deviation is calculated, the results of the analysis are given in Table 10.3. If the average deviation in estimated water vapour for all regions is calculated, an approximately ±2 % average deviation from the mean is found. The ±2 % variation is assumed to represent the background noise level present in the estimated water vapour at Brukunga.

Firstly ROI A and B are examined. In ROI A the water vapour is approximately 3 % higher than ROI B, with each region having 1.05 and 1.02 cm of precipitable water vapour respectively. The difference of 3 % between ROI A and B is attributed to errors in derived surface reflectance being propagated through the TSR method. An examination of the two surfaces in ROI A and B (Figure 10.10) show that the surface types are similar and represent dry grass surfaces. In the VNIR, the differences are minor, while in the SWIR reasonable differences are noted. The most notable difference (excluding magnitude) is the larger cellulose absorption feature in the ROI B spectra in Figure 10.10 at approximately 2100 nm The residual atmospheric water vapour features for both ROIs are of similar magnitude and indicate that the differences in estimated water vapour, due to inaccurate surface reflectance modelling, are small. The error in surface reflectance, in this case, should be minimal since the reflectance is essentially linear across the majority of the water vapour absorption features.

An examination of the results in Table 10.3 for ROI C, D and E show differing

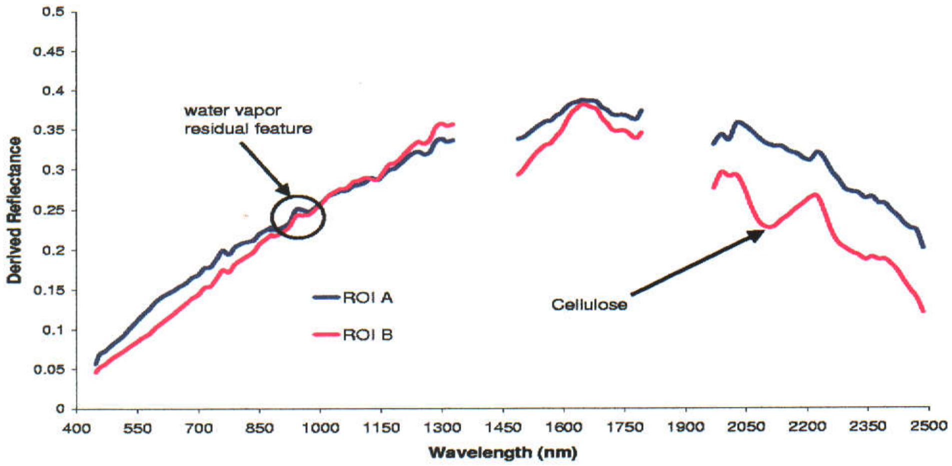

Figure 10.10: Derived surface reflectance for ROI A (dry grass) and B (dry grass) from Brukunga. A 3 % difference in water vapour was found for ROI A and B. The similar atmospheric water vapour residual features (at approximately 940 nm) indicate that water vapour has been well estimated in both regions.

amounts of water vapour for each ROI. In this case the surface type is found to be consistent for each of the three ROIs. Shown in Figure 10.11 are representative derived surface spectra for each of the three regions. Interestingly, the atmospheric water vapour residual features are approximately the same magnitude in all six spectra. Differences in estimated ROI water vapour are, to some extent, the product of surface modelling error propagation in the TSR method, but more importantly, are most likely due to the natural in-scene water vapour heterogeneity. The mean water vapour difference, between ROI C and E is approximately 11 %. If the difference is attributed to surface reflectance modelling error, rather than natural in-scene variation, the magnitude of the residual atmospheric water vapour features in one of the ROIs would be more heavily pronounced.

Lastly, two spectra from the Brukunga mine are shown in Figure 10.12 (labelled F and G). From Figure 10.9 it is seen that the two pixels are spatially close yet the magnitude of the reflectance for both targets is vastly different. The spectra marked F (blue spectra) has an estimated precipitable water vapour of 1.01 cm while that of G (pink spectra) is 1.07 cm. The difference in estimated

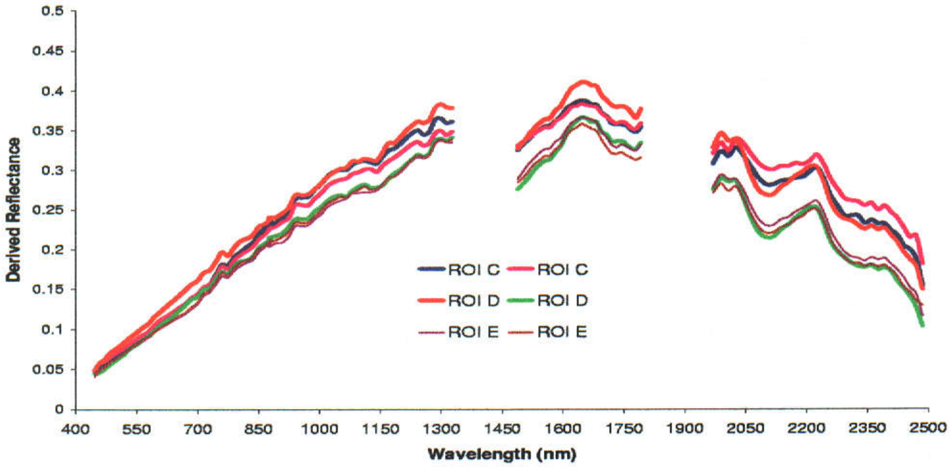

Figure 10.11: Brukunga derived surface reflectance of dry grass for ROI C, D and E. An 11 % difference in estimated water vapour was found between ROI C and E (see Table 10.3). This is attributed to in-scene heterogeneity and not surface reflectance modelling error. The similar atmospheric water vapour residual features (at approximately 940 nm) indicate that water vapour has been well estimated.

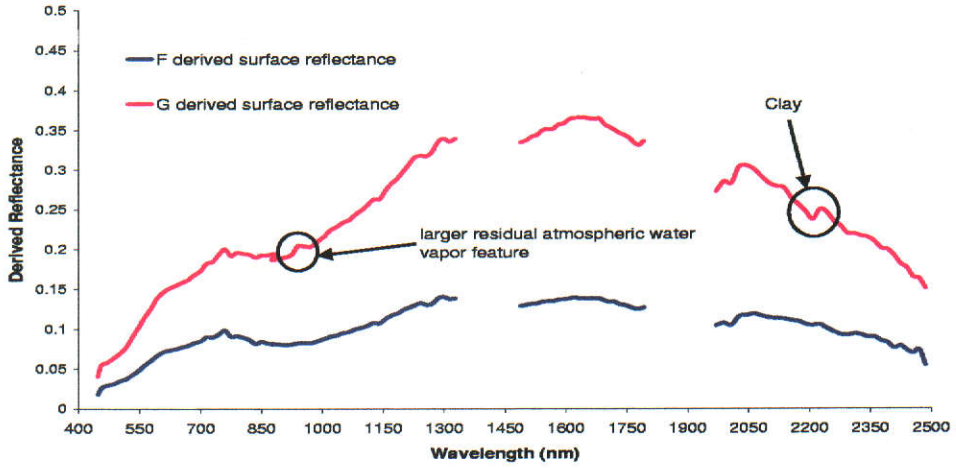

Figure 10.12: Derived surface reflectance for the Brukunga mine. A difference of 5.6 % in estimated water vapour was calculated for the two pixels (see Table 10.3). The difference is attributed to reflectance error propagation in the TSR method due to the iron absorption feature (760 - 1150 nm). This is highlighted by the larger atmospheric residual feature at approximately 940 nm (spectra G).

water vapour of 5.6 % is almost certainly due to inaccuracies in surface reflectance modelling. The larger residual feature, as well as the larger degree of nonlinearity (at approximately 940 nm) is the most likely cause for the increased estimated precipitable water vapour for G.

The cause of the error is almost certainly the same as that noted in the Moffett Field results. Namely, the magnitude or degree of nonlinearity present (in spectra G) is increasing, such that, the simple linear interpolation technique used to estimate surface reflectance in the water bands (see Chapter 7) is failing. In this case, the surface reflectance would have been overestimated in the water bands (namely the 940 and 1380 nm bands), which in turn lead to an overestimate of water vapour. Thus, the nonlinearity of the surface is not being preserved. A possible improvement on the current linear interpolation method is discussed in Chapter 11.

10.3 Dark Targets

The effect of dark surface targets on derived reflectance (after estimating the water vapour with the TSR) was examined for Jasper Ridge and Moffett Field. In both scenes a number of suitable dark targets were selected. These included lakes in both the Moffett Field and Jasper Ridge data, the Moffett Field salt evaporation ponds and waters of San Francisco Bay.

The salt evaporators at Moffett Field have an average surface reflectance of less then 2 % from approximately 800 nm onward and are extremely challenging targets from which to estimate water vapour content. The results of the sensitivity analysis (Chapter 8) demonstrated that in the absence of instrument noise the error in estimated water vapour over dark targets should be less than 3 %. It si noted that the 3 % error is for ideal scenarios where all inputs except surface reflectance are known.

Shown in Figure 10.13 is a transect of TSR-estimated water vapour from Jasper Ridge (see Figures 10.4(a) and 10.4(b)). The transect begins at the top of the scene and moves down through the lake area. The resultant water vapour estimated over the lake area shows significant scatter when compared to the neighbouring land surfaces. The average water vapour for the land on either side

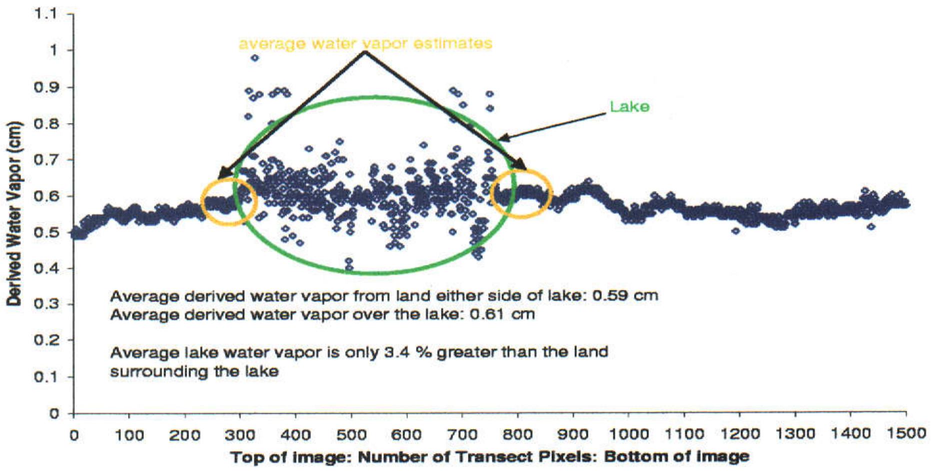

Figure 10.13: TSR-estimated precipitable water vapour from the Jasper Ridge Transect. The transect takes in the lake area and details the derived water vapour over the standing water target. The scatter is attributed to decreased SNR over the dark target.

of the lake (see Figure 10.13) was calculated as 0.59 cm while the average water vapour over the lake is 0.61 cm. That is, the average water vapour estimated over the lake is only 3.4 % higher than the water vapour either side of the lake. The scatter observed over the lake is the result of decreased SNR over the spectrally dark surface.

Though not assumed to be the case here, an increase in water vapour may be related to increased evaporation from the water boundary which leads to an increase in water vapour over the water-air interface. The average surface reflectance for the lake (Figure 10.14) shows that, even with the extreme variation in water vapour observed in Figure 10.13, the derived reflectance is essentially free from water vapour residual features.

A similar transect, as used for Jasper Ridge, was performed at Moffett Field (Figure 10.15). This transect spans high ground (left of Figure 10.15) to salt evaporators (large scatter left of centre) and the waters of San Francisco Bay (smaller scatter right of centre). The water vapour is observed to increase with decreasing scene elevation (as established in section 10.1) until it reaches the plateau at the base of the mountains, where it then remains essentially constant.

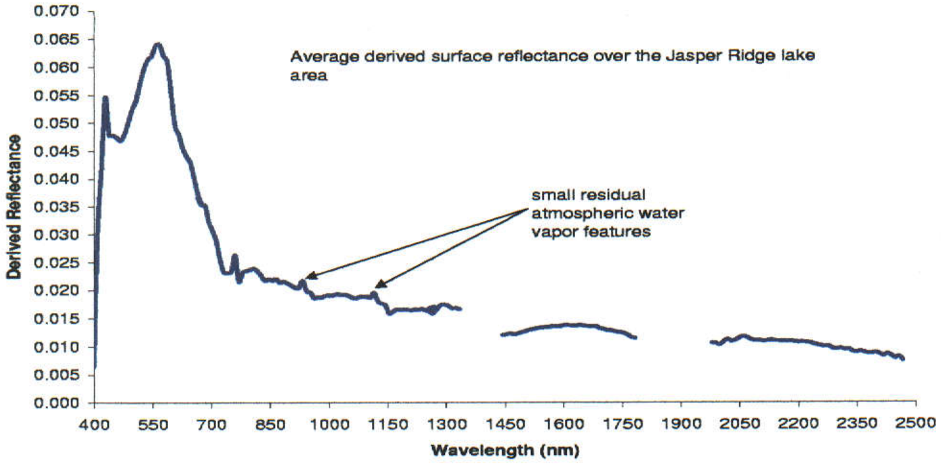

Figure 10.14: The average lake water surface reflectance derived from the Jasper Ridge radiometric data. The derived reflectance represents the water reflectance acceptably well and shows only small atmospheric column water vapour features.

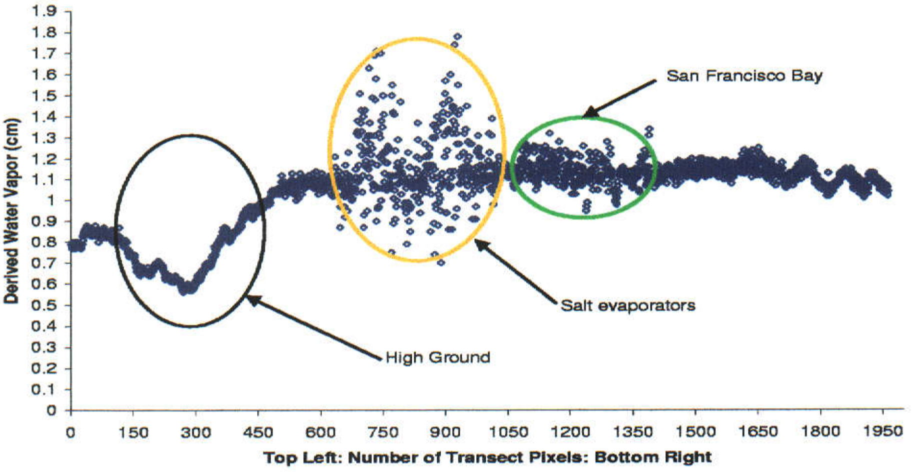

Figure 10.15: The transect of estimated water vapour for Moffett Field. The transect takes in the mountains, salt evaporators, Bay area and urban areas. Three distinct regions are seen, namely, the high ground, the salt evaporators (large variation) and the Bay area (smaller variation).

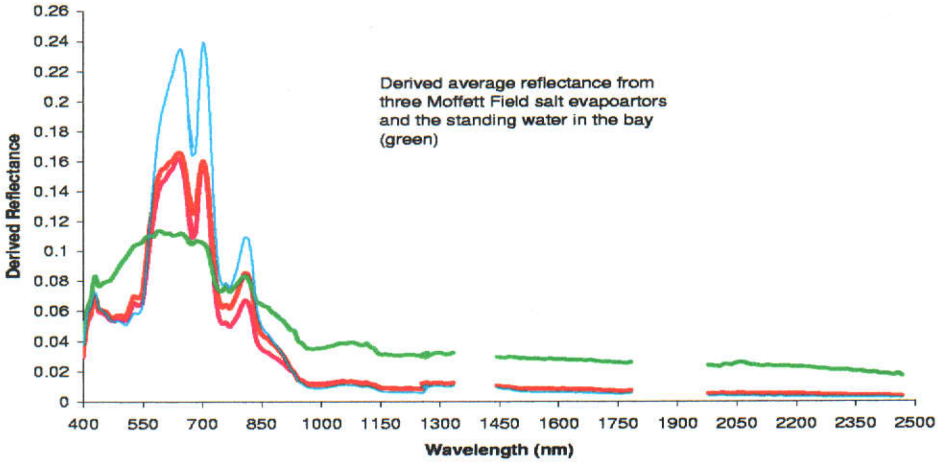

Figure 10.16: Derived surface reflectance from 3 salt evaporators and the Bay (green curve). No residual atmospheric water vapour features are observed in the spectra. The average estimated precipitable water vapour over the evaporators was found to be only 3.14 % higher than the surrounding area.

The mean estimated water vapour for the plateau region, excluding the Bay and salt evaporators, is 1.12 cm of water vapour. The average water vapour content over the salt evaporation pond region is 1.15 cm, which is 2.7 % higher than the neighbouring land surfaces. The average water vapour over San Francisco Bay is 1.14 cm, which is 1.8 % larger than the neighbouring land surfaces.

Of interest in Figure 10.15 is the magnitude of variation observed over the evaporators and the Bay. The variation between the two dark target areas is attributed to the difference in SNR for the two targets (see Chapter 8 for a discussion of dark target SNR). That is, the salt evaporation ponds have lower surface reflectance at longer wavelengths (> 850 nm) and therefore a smaller SNR than that of the Bay water (see Figure 10.16). The difference in surface reflectance is demonstrated in the derived surface spectra in Figure 10.16. Importantly, the surface derived spectra show no residual atmospheric water vapour features in either the salt evaporator or Bay spectra.

The lower spectral reflectance of the salt evaporators (> 850 nm) means a smaller SNR applies to the evaporator radiance signal as compared to the brighter

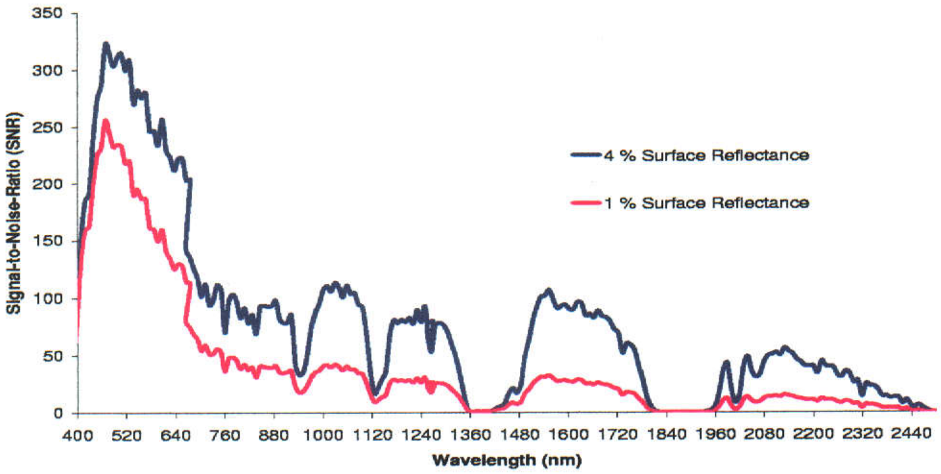

Figure 10.17: The signal-to-noise-ratio (SNR) for a 4 % and 1 % constant reflectance target, using the 1999 AVIRIS NEDL values. The 1 % target has an average SNR that is 60 % smaller than that of the 4 % target from 800 nm onward.

radiance signal from the Bay. Figure 10.17 presents the estimated SNR for a constant 4 % (i.e. Bay reflectance) and a 1 % (i.e. salt evaporator) reflectance. The SNR for the 1 % reflectance target is considerably less than that of the 4 % target (approximately 60 % smaller) from 800 nm onward. Thus, as the surface reflectance decreases, the SNR of the radiance signal decreases and consequently increases the amount of scatter present in the salt evaporation ponds estimated water vapour.

These results indicate that an estimate of the average water vapour over dark targets is achievable with the TSR method. To increase the SNR over large dark targets spatial averaging of the measured radiance may be performed prior to the estimation of water vapour. This has the effect of increasing SNR and therefore, reducing the associated error. If the SNR of the radiance measuring sensor is large enough, the scatter in the estimated water vapour should decrease over dark surfaces.

10.4 Multiple Water Vapour Estimate Benefits

In Chapter 6, section 6.5.3, it was noted that a rejection scheme is used with the TSR-estimated water vapour to remove possible outlying data. In the case of AVIRIS, approximately 30 estimates of water vapour are generated for any given pixel and 10-15 for a HyMap pixel. If the surface reflectance estimates used in the TSR scheme are significantly incorrect, it is reflected as error in the estimated water vapour. In the VNIR-SWIR spectral region, surface absorption features may be coincident with atmospheric water vapour absorption features. This can cause the TSR scheme to over/underestimate atmospheric water vapour because of apparently shallower/deeper water vapour bands (refer to Chapter 6 for a description of the TSR). Generally, the extended window regions (see Chapter 7) prevent this occurring by recreating the surface reflectance slope to a better approximation when compared with a simple interpolation from either side of a water band.

It is noted, however, that in some cases surface absorption features cannot be adequately separated from water vapour absorption features. The ability of the TSR scheme to provide multiple estimates of atmospheric water vapour for any given pixel, enables an alternative means of rejecting anomalous water vapour estimates on a pixel-by-pixel basis. This is not achievable using other band-ratio methods, such as CIBR and APDA, which only provide two estimates of water vapour per pixel.

This section examines TSR-estimated water vapour where the pixels spectrum has surface absorption features coincident with the atmospheric water vapour absorption features. The derived surface spectra are presented for each of the three TSR wavelength intervals (see Table 6.2, Chapter 6), together with their estimated water vapour. Figure 10.18 shows the derived spectra for a salt evaporator pixel from Moffett Field. In all cases, the TSR-estimated water vapour, for each of the three spectral intervals, is the average of approximately 10 separate water vapour estimates. The effect of the deep surface absorption centred at approximately 980 nm is found to erroneously increase the water vapour estimate for section one (2.13 cm of precipitable water vapour). This error produces a recognisable residual spike at 1140 nm, which is related to atmospheric water

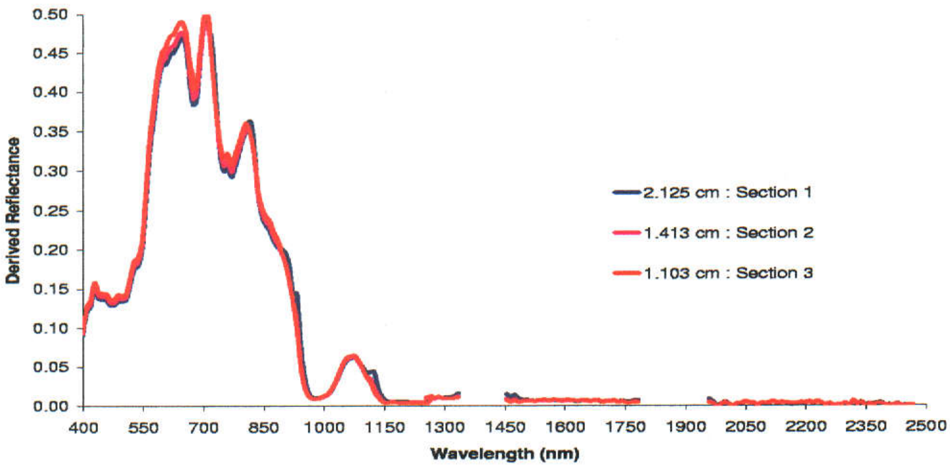

Figure 10.18: Derived surface reflectance from a salt evaporators from the Moffett Field data set. The derived surface spectra (using TSR-estimated water vapour) are shown for each of the 3 spectral intervals outlined in Table 6.2, Chapter 6.

vapour. However, the estimated water vapour from the other two TSR sections, are not affected by similar deep surface absorptions and so their estimates of water vapour are more consistent and do not produce the same residual error. In this case, the section one estimated water vapour would be rejected and the average of spectral sections two and three (1.26 cm) used as the pixel estimated water vapour. It is interesting to note that the average water vapour estimated over this dark target (at wavelengths > 1000 nm) is only 10 % higher than the 1.14 cm estimated for surrounding areas.

Figure 10.19 demonstrates the effectiveness of the TSR scheme to highlight possible surface absorption features that would not normally be resolved with other methods. The TSR-estimated water vapour from sections one and two are found to be consistent, while section three is high relative to the other two sections. The cause of the overestimated water vapour in section three is caused by a surface absorption feature located within the 1380 nm water vapour absorption band. Lastly, a typical result for the TSR scheme is shown in Figure 10.20. Here the TSR-estimated water vapour results for all three sections are consistent, largely because there are no overlapping surface absorption features. The results

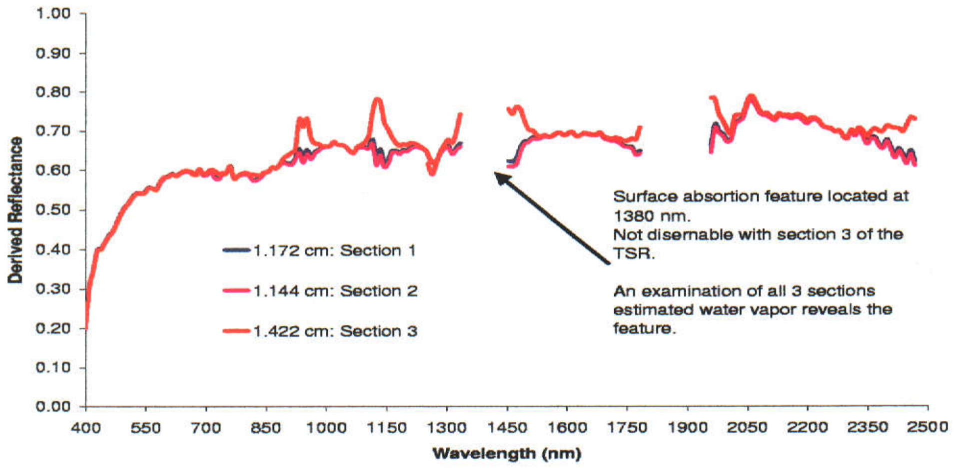

Surface absortion feature located at 1380 nm.
Not disernable with section 3 of the TSR.

An examination of all 3 sections estimated water vapor reveals the feature.

Figure 10.19: Derived surface reflectance from the Moffett Field data set. The three spectra derived from sections 1,2 and 3 (using TSR-estimated water vapour) are shown. Sections 1 and 2 (see Table 6.2, Chapter 6) are consistent while section 3 is not. This indicates the presence of a possible absorption feature at 1380 nm.

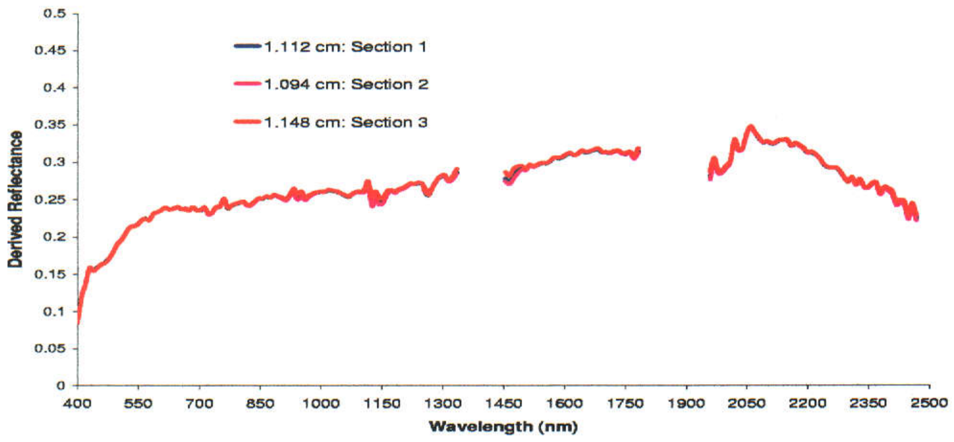

Figure 10.20: Derived surface reflectance from the Moffett Field data set. The three spectra derived from sections 1,2 and 3 (using TSR-estimated water vapour) are shown. See Chapter 6, Table 6.2 for the spectral section definitions. Consistent TSR-estimated water vapour is found for all three sections.

of the estimated water vapour for each spectral section are within approximately 3 % of the mean (1.12 cm). Generally, if the TSR results are not consistent between spectral sections, it is usually because one section contains surfaces that are comprised of overlapping absorption features.

10.5 TSR and the CIBR

The Moffett Field flight information was used to construct a CIBR calibration curve with an assumed surface reflectance of 25 % for the 940 nm water vapour feature. Equation 4.2 was applied to the measured AVIRIS radiances and a value calculated for each pixel. The calculated CIBR was applied to the calibration curve and the water vapour estimated for each pixel of Moffett Field, scene 1. The CIBR estimated water vapour (in cm of precipitable water) is shown in Figure 10.21(a) and the TSR-estimated water vapour in Figure 10.21(b). The general distribution of water vapour is similar in both the CIBR and the TSR maps with higher elevations showing less water vapour and increasing with decreasing surface elevation.

The CIBR result shows higher water vapour content when compared to the TSR result. This is confirmed by calculating the difference in estimated water vapour from both scenes. In this case, the CIBR water vapour was subtracted from the TSR estimate. The result is given in Figure 10.22. What is also apparent is the difference map does not show topographical effects due to terrain. To investigate the nature and type of surface where differences occur (or don't) six targets were selected and the spectra and estimated water vapour examined. The surfaces points selected are given in Figure 10.22 as A, B, C, D and E. The estimated water vapour for each point is given in Table 10.4 and the derived surface reflectance in Figure 10.23. The spectra shown are derived with TSR-estimated water vapour. No CIBR spectra are shown since the effect of using CIBR estimated water vapour may be inferred by comparing the results in Table 10.4 and examining the effect the CIBR water vapour content would have on residual water vapour features already existing in the TSR spectra.

The two targets listed in Figure 10.22 as A (grass) and D (road) both have linear reflectance slopes at 940 nm, and as such, they do not exhibit appreciable

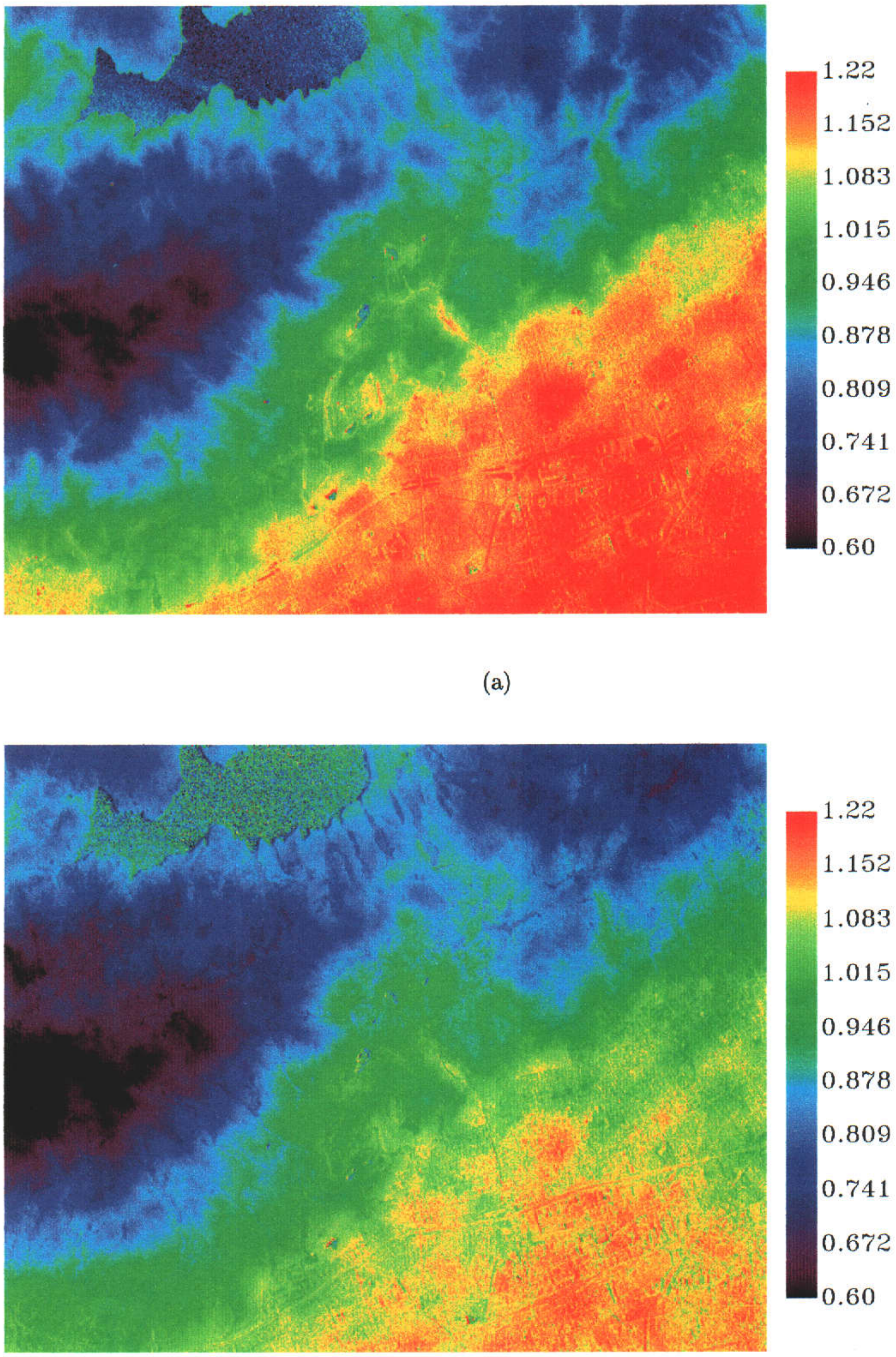

(a)

(b)

Figure 10.21: Estimated precipitable column water vapour (in cm) for Moffett Field using the CIBR 10.21(a) and TSR 10.21(b).

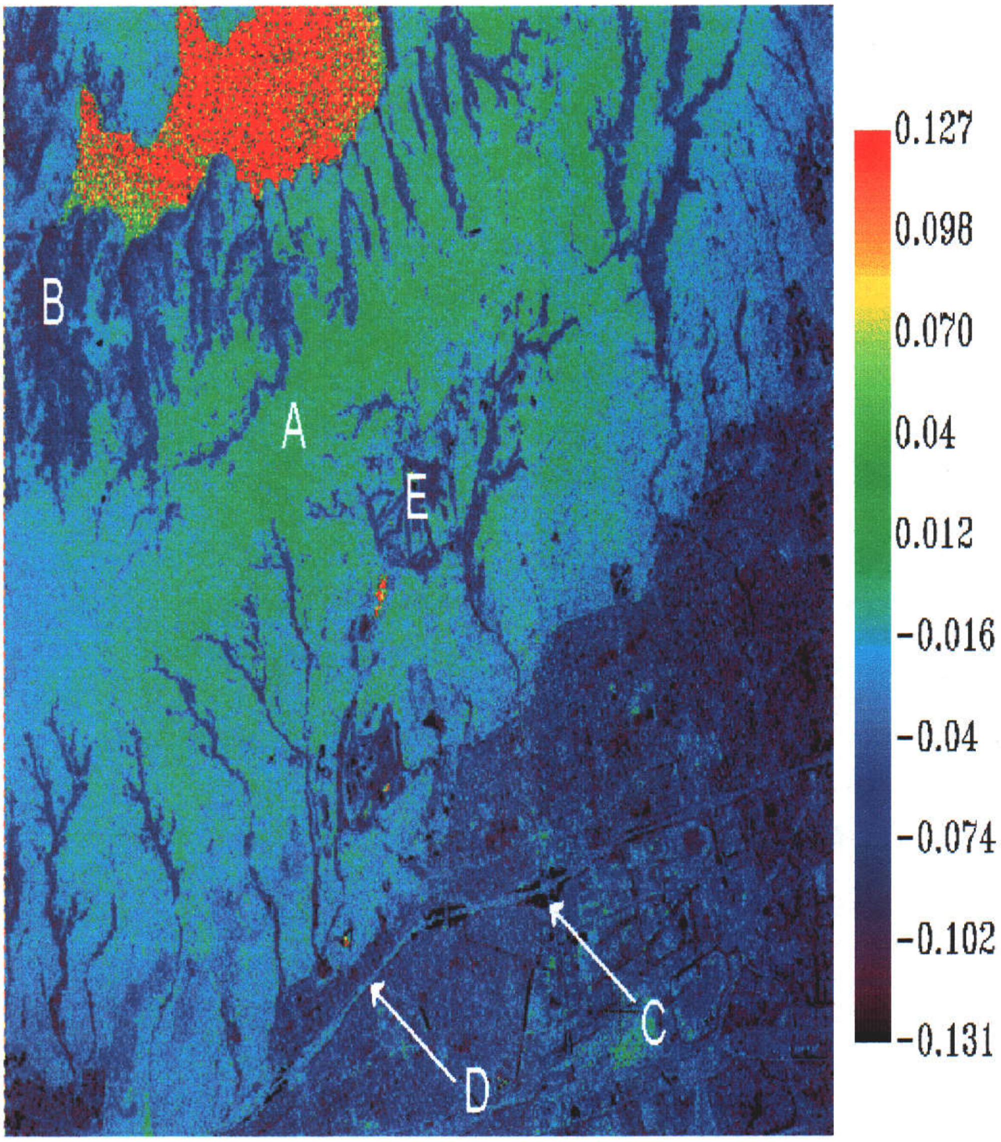

Figure 10.22: The calculated difference in estimated water vapour for the TSR and CIBR method. The scale is cm of precipitable water for TSR-estimated water vapour minus CIBR estimated water vapour. The dark regions correspond to vegetated areas exhibiting leaf water absorptions.

Target	CIBR (cm)	TSR (cm)	% difference from TSR		
A	0.71	0.72	-1.4	% Above Surroundings	
B	0.88	0.79	9.2	TSR/CIBR	Surroundings (cm)
C	1.28	1.02	25.5	-6.4/17.4	1.09
D	1.12	1.10	1.80	1.0/2.7	
E	0.88	0.80	10.0	-1.2/8.6	0.81

Table 10.4: A comparison of TSR and CIBR estimated water vapour for Scene 1 of Moffett Field. The CIBR always estimates higher water vapour over vegetation targets.

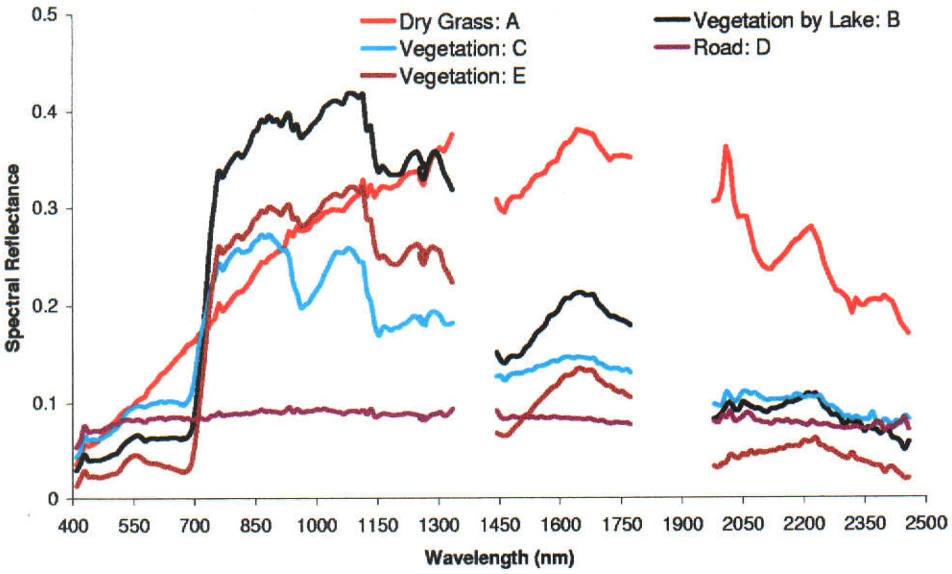

Figure 10.23: The surface reflectance derived at the points A to E in Figure 10.22. The spectra have used TSR-estimated water vapour when deriving from radiance to reflectance.

water vapour residual features. The result for both the CIBR and TSR is compatible in both cases as expected since linear reflectance slopes should not hinder either method. Table 10.4 and Figure 10.23 reveal that differences in estimated water vapour is occurring over specific surfaces, namely, vegetation. In all cases the CIBR estimates larger water vapour when compared to the TSR method. It may be seen that if the CIBR water vapour estimates were used to derive the vegetation targets, rather than the TSR estimates, then the magnitude of all residual water vapour features would increase.

The vegetation at C (in Figure 10.22) shows a high degree of nonlinearity, which in turn, has led to error in estimated water vapour for both the CIBR and TSR. The reason for the TSR underestimate (approximately -6.5 % smaller than the surroundings) was explained in section 10.2. The CIBR on the other hand has overestimated the water vapour by 17.5 %. This is due to a departure of the true reflectance slope from the reference reflectance slope used to construct the CIBR calibration curve.

Since the degree of nonlinearity is less in region E (compared to C) the error in estimated water vapour is less for the CIBR and TSR. In this case the CIBR is 8.6 % higher than the surroundings while the TSR is 1.2 % less than the surroundings (Table 10.4). Increasing the TSR-estimated water vapour to the CIBR estimate would only increase the magnitude of the water vapour residuals in the derived surface spectrum (see Figure 10.23) and would suggest that water vapour had been overestimated.

Error introduced in the estimated water vapour will change the appearance of its spatial distribution. The CIBR shows an almost uniform water vapour in the bottom left corner of Figure 10.21(a) as compared to the TSR distribution (Figure 10.21(b)). The change in surface absorption feature in such areas has effectively removed distribution structure information in the CIBR results. Ultimately, this could affect both atmospheric and surface studies. Thus it may be concluded that, the TSR produces the same general spatial distribution as an excepted water vapour estimation method, as well as, showing improvement in the overall result.

10.6 Summary

The results presented in this chapter have demonstrated the ability of the TSR to perform under a number of conditions. These include the estimation of precipitable water vapour,

- over rugged terrain that exhibits large topographical variation (such as Moffett Field and Jasper Ridge)
- over regions considered as topographically flat (such as Brukunga)
- over spectrally dark surface targets (such as water targets)
- over surface targets that have absorption features coincident with atmospheric water vapour bands.

From the results examined and for each of the points listed, a number of conclusions may be drawn. Firstly, the TSR estimation of precipitable water vapour over varied terrain height was found to be consistent with previously published results, namely Roberts *et al.* (1993). In regions where topographic variation is small, it was concluded that the observed variation in the estimated water vapour image was primarily a function of the surface reflectance error. By this, it is meant that the surface was observed to express its characteristics on the water vapour product. However, an examination of ROIs over topographically flat areas found that this form of variation was generally confined to surfaces that exhibit a large degree of reflectance nonlinearity. The reasonably small variation in observed water vapour, in such regions, is promising as it suggests the TSR scheme is working to optimal levels. It was established that a background noise level was inherent in all of the scenes and that the magnitude of the noise level was <3 % in most cases. As well as inherent noise, some of the spatial variation is attributable to the non-homogeneous distribution of water vapour.

In all cases, atmospheric water vapour residual features in derived surface spectra were found to be small in magnitude. The success of the TSR method over surfaces with nonlinear surface absorption features was demonstrated by examining the surface reflectance over such surfaces. These included, vegetated surfaces, surfaces containing iron bearing materials and surfaces where absorption features are coincident with atmospheric water vapour bands. This is an important result since it does not require the TSR method to account for differing surface types when estimating water vapour. It was found, however, that as the degree of nonlinearity in surface reflectance increases the interpolation scheme used to estimate reflectance in the water bands may fail. A possible solution is discussed in Chapter 11.

In this study the dark targets examined were water targets (from Jasper Ridge and Moffett Field) and salt evaporator targets (Moffett Field). The salt evaporator surfaces are considered as extremely dark targets (approximately 1 % or less reflectance from 940 nm onward) and are therefore an ideal test case for the ability of the TSR method in relation to dark surfaces. It was shown in Chapter 8 that the TSR estimation of water vapour from spectrally dark surfaces produces small error (less than 3 %), in the absence of instrument noise. It was found that TSR-estimated water vapour over such surfaces is heavily influenced by instrument noise. As the surface becomes spectrally darker, the SNR is decreased and the error in the estimated water vapour increased. An examination of Moffett Field (Figure 10.5) showed estimated water vapour (over salt evaporation ponds and the Bay area) displayed random fluctuations that were a direct consequence of the scheme working at the instrument noise level. Even so, the results for the dark target areas showed that reasonable estimates of water vapour, relative to brighter surrounding areas, may be made with the TSR method.

Lastly, the nature of the TSR method was such that multiple estimates of water vapour were generated for each pixel. This allows the TSR to use rejection schemes in an attempt to overcome problems such as coincident surface absorption and atmospheric water absorption bands. The importance of this result is twofold. Firstly, it means that such features, which may cause overestimates of water vapour, do not hinder the scheme. Secondly, it provides a means of identifying surface absorption features in water bands. In the case of the spectra in Figure 10.19, a possible surface absorption feature was located in the 1380 nm water band. In this opaque region, where one would not normally be able to resolve such information, the TSR (through its use of multiple estimates) allows the feature to be identified (as a possible outlier) and would allow a measure of the depth of the feature by comparing the difference in estimated water vapour for each section. The large increase in estimates of water vapour from the TSR scheme is therefore of great benefit for not only reducing outlying results but also for studying surface features that would not normally be detected by other methods.

Chapter 11

Conclusions

11.1 Review of Major Conclusions

The work presented in this thesis has covered a number of important results and conclusions relating to the estimation of atmospheric column water vapour from VNIR-SWIR hyperspectral radiance. This has guided the direction of the study and contributed toward a more comprehensive view of the problem. This final chapter draws together the major conclusions and findings and outlines possible recommendations that will benefit further work or studies involving the TSR method.

Firstly, in Chapter 3 it was shown that the effects of atmospheric column water vapour on a radiance signal in the VNIR-SWIR are extensive. By this it is meant that, atmospheric column water vapour is the major absorbing species in the VNIR-SWIR region and, as such, its impact upon this portion of the spectrum will greatly modify any measured signal. This has a profound impact on the resultant ground reflected solar irradiance if absorption by water vapour is not properly accounted. It was shown that the absorption of solar radiation by atmospheric water vapour in the VNIR-SWIR occurs almost exclusively of other absorbing species. Exceptions to this are noted with overlaps of atmospheric CO_2 and H_2O at approximately 1400 and 2000 nm. The exclusive nature of water vapour absorption is of importance when attempting to estimate its content from a measured radiometric signal. The reason being that absorption features such as the 940 and 1140 nm water bands, are free of other absorbing gases and therefore the other absorbing atmospheric species may be ignored in such regions. With this said, it was noted in Chapters 3 and 10 that, even when all input variables are known, differences in modelled and measured signals may still occur and, as such, atmospheric residual features will still be noted and primarily are due to atmospheric column water vapour, carbon dioxide and atmospheric oxygen.

In Chapter 2 a comparison of broadband and hyperband sensors demonstrated that the information content in broadband radiometric spectrometers does not always contain the necessary spectral resolution required to estimate water vapour content from a measured signal. It was concluded that hyperspectral sensors measure radiance at sufficient spectral resolution, such that, information content is adequate for estimating the parameter of interest. To extract the desired information requires that the physical processes governing the parameter of interest are explained, in this case solar radiation interactions with atmospheric water vapour, in terms of a known physical basis.

Chapter 5 set out the foundation and basis for explaining in terms of the RTE how solar radiation interacts with atmospheric water vapour. The derivations outlined and presented in Chapter 5 show how the measured radiance at the sensor can be described in terms of atmospheric column water vapour. The form of RTE found to adequately describe the at-sensor radiance, as a function of atmospheric water vapour, was found to be an n^{th} order polynomial. This result established a foundation by which the water vapour could be estimated if it is assumed to be the only unknown.

The Chapter 5 results provided a means for establishing the differential absorption ratio that relates the absorption of atmospheric water vapour to measured radiances. The ratio equation, known as the TSR value, is describable in two different polynomial formats. In the first, the TSR value is given as a function of atmospheric water vapour. The second, a more convenient form, is where atmospheric water vapour is given as a function of the calculated TSR value. The polynomial form allowed reference curves, that are a function of TSR value, to be described which in turn may be applied on a pixel-by-pixel basis. As well, the form of ratio defined by the TSR was found to be applicable to a number of spectral regions in the VNIR-SWIR and allowed multiple estimates of atmospheric water vapour, for a given spatial unit (or pixel), to be made. This is an advancement on current differential ratio techniques as previous methods have generally only provided two estimates of water vapour per-pixel.

The results from Chapter 8 demonstrated that the TSR method shows superior performance in relation to three areas identified as requiring water vapour estimation improvement (see Chapter 4). The three areas were (a) the estimation of water vapour over spectrally varied surface targets, that may also exhibit spectral nonlinearity, as well as, (b) the estimation of water vapour in the presence of atmospheric aerosol when the content of the aerosol is not well known and (c) the ability to estimate water vapour over spectrally dark surfaces. It was demonstrated that the TSR method was extremely robust in all cases. Thus, the error dependence in estimated water vapour is reduced to just a few key parameters.

11.1.1 Surface Reflectance Improvements

To establish spectrally dependent water vapour reference curves required a means of estimating surface reflectance in the atmospheric water vapour bands. The method of providing such reflectances was described in Chapter 7. Other methods such as the CIBR and APDA, as described in Chapter 4, have assumed surfaces to generate the necessary reference curves required to estimate water vapour. This means the CIBR and APDA must rely on the surface under examination having the same surface reflectance as that of the reference reflectance. Previous studies (see Chapter 8) have shown that such assumptions may lead to erroneous estimates of water vapour over surfaces differing from the reference reflectance.

As well, the reflectance estimate method established in Chapter 7 allowed the effects of surface reflectance nonlinearity to be taken into account. Thus, surfaces, such as vegetation targets, which exhibit nonlinearity in the atmospheric water vapour bands, will have less of an effect on the final estimate of water vapour as compared to those outlined in Chapter 4. Even so, the method was shown to fail when the degree of nonlinearity present in the surface reflectance becomes too large. This is due to the form of interpolation that is employed. Rather than use the linear interpolation method employed in this study, it is recommended that a polynomial interpolation scheme be used. This will ensure the preservation of curvature in nonlinear features and should decrease the amount of over/under estimation of atmospheric water vapour when such surfaces are encountered. The reflectance estimation method (Chapter 7) has the advantage of making the TSR method essentially independent of surface type. This same principle may also be applied to methods such as the CIBR and APDA, such that, the methods more accurately account for the true surface reflectance slope.

11.1.2 Aerosol Visibility Improvements

The sensitivity results for unknown aerosol visibility presented in Chapter 8 are at least an order of magnitude better than previous studies. It may be concluded from this finding that the accurate estimation of water vapour in the presence of unknown aerosol visibility is achievable with the TSR method. It is noted though, the sensitivity analysis was carried out in an ideal environment and would greatly benefit from coincident airborne and in-situ measurements. It was also shown that the error in assumed visibility leads to inaccurate surface reflectances. Although not examined here, the error in derived surface reflectance, when aerosol loading is not well known, may be of use for estimating aerosol visibility if the derived surface reflectance can be identified and compared to library spectra.

11.1.3 Dark Target Improvements

The results in Chapters 8 and 10 demonstrated that dark targets do not essentially pose a problem for the TSR method. It was shown that the error introduced into the TSR-estimated water vapour over dark targets (with surface reflectance as low as 0.5 %) was as little as 3 % in the absence of instrument noise. Chapter 10 demonstrated that when radiometric signal decreases over dark targets, the error in estimated water vapour is increased. This was well demonstrated in the Moffett Field results for the salt evaporation ponds as compared to the spectrally brighter waters of San Francisco Bay. However, the average estimated water vapour (over the ponds and Bay) showed the result was only a few percent higher than for surrounding land surfaces. This is an important finding since it has been identified by many studies (see Chapters 4 and 8) as an area that is problematic for differential absorption methods of water vapour estimation.

The results successfully demonstrated that the presence of spectrally dark targets is not the primary cause of error in TSR water vapour estimates for these targets, but rather, it is the limitations imposed by instrument response over such targets. The estimated water vapour over such targets (lakes, salt evaporation ponds and Bay water), showed strong evidence for being noise dominated. This implies that if the radiometric SNR is increased beyond its current capacity the error introduced into the TSR-estimated water vapour will decrease. This is an extremely important finding since current methods of water vapour estimation will generally overestimate water vapour over spectrally dark targets, and as such, are usually not included in a final analysis.

11.2 General

The results presented in Chapter 10 demonstrated the ability of the TSR method to function under a range of surface and atmospheric conditions. The three hyperspectral scenes used in the case studies were appropriate for a number of reasons. The first advantage being that two of the scenes, Moffett Field and Jasper ridge, provided a means of testing the method over rugged terrain. The results of the analysis over the mountainous regions of Moffett Field and Jasper Ridge were found to be consistent with previously published results (see Chapter 10) and demonstrated the dominating effects of terrain elevation on the spatial distribution of atmospheric water vapour content. The water vapour was found to vary considerably between Jasper Ridge and Moffett Field, yet, the distribution was found to have the same expected linear relationship over elevated terrain.

The second benefit was that, both of the scenes (Moffett Field and Jasper Ridge) had a variety of surface types ranging from linear to nonlinear surface reflectances (thus testing and evaluating the method outlined in Chapter 7) and spectrally dark surface targets. The latter established the effect of instrument SNR on the TSR water vapour product. The effect of nonlinearity was best demonstrated in the Moffett Field scene where it was confirmed that errors introduced into the estimated water vapour, due to nonlinearity, was directly related to the degree of nonlinearity. Again, this result suggests and supports the recommendation of moving to a polynomial interpolation method rather than the linear interpolation method used here.

Thirdly, the Brukunga scene afforded the means by which to test the TSR method over topographically flat terrain that, for the most part, can be considered as exhibiting small spectral reflectance variation. The Brukunga scene demonstrated that the water vapour distribution over topographically flat terrain was a product of natural heterogeneity, and error introduced into the TSR method via derived surface reflectance error. In all three scenes, a background noise level of approximately ±3 % was estimated. This modest value confirms the ability of the TSR method to estimate water vapour to high accuracy regardless of the terrain type or topography.

Lastly, the ability of the TSR method to estimate multiple water vapour estimates from a given spectral signal is a distinct improvement over current methods. This has been shown to improve pixel-based estimates of atmospheric water vapour by allowing rejection schemes to be utilised, such that, outlying estimates may be removed to reduce the overall error in the final water vapour product. Statistically this allows a higher confidence level to be placed on the final estimated water vapour for any given pixel. As well, it was shown that the resulting erroneously higher water vapour estimates can in some cases be used to identify possible surface absorption features present in the opaque water bands. This may allow a comparison of the overestimated water vapour result with the accepted result, such that, a depth measure of the feature may be inferred. This is an outcome not achievable with the current methods and represents a major accomplishment for differential absorption methodology.

In conclusion, an alternative method of estimating atmospheric column water vapour from remotely sensed hyperspectral platforms has been defined with the TSR method. This study has demonstrated that the TSR method of water vapour estimation is both a robust and accurate method while still maintaining the advantages of differential absorption band ratio methodology. As noted in Chapter 4, any new or proposed method of column water vapour retrieval from hyperspectral data should aim to improve upon problems that exist with band ratio techniques. The TSR has demonstrated this ability for a number of circumstances and has proven to overcome or reduce the error associated with the water vapour product for most, if not all, of the issues noted in Chapter 4.

The main improvements made by the TSR method are evident in the following three areas,

- Improved water vapour estimation accuracy in the absence of accurate aerosol visibility information,
- Improved accuracy over surface targets that exhibit nonlinear spectral reflectance behaviour in or near the atmospheric water vapour features,
- Increasing the accuracy of water vapour estimation over dark targets and reducing the problem to one of instrument SNR limitations.

Certain aspects of the TSR method provides a means of improving the current water vapour estimation methods. Firstly, the use of iterative methods of estimating water vapour has been shown to improve the derived water vapour results (Schläpfer, 1998; Schläpfer *et al.*, 1996, 1998). This, in turn, may be further improved upon by implementing aspects inherent to the TSR method. Namely, an approach that estimates surface spectral reflectance in certain spectral regions prior to water vapour estimation. As noted in Chapter 4 this, to some extent, has been touched upon by other studies such as those carried out by Hirsch *et al.* (2001).

To code the TSR into a working algorithm, such that, water vapour and surface reflectance may be estimated, required that forward modelling as well as inverse modelling was possible. This was achieved by using the MODTRAN generated LUT database (used in the TSR method) in a two-way format rather than just the inverse format usually employed by other methods. This aspect is one that has not been taken advantage of by LUT-based water vapour retrieval methods to date.

The study carried out by Hirsch *et al.* (2001) noted that to implement the CIBR with multiple LUTs (that are a function of surface spectral reflectance and water vapour) proved time consuming and computationally expensive. If though, a single LUT is defined and used for both forward and inverse modelling, CIBR and APDA could be used as a function of surface spectral reflectance and column water vapour allowing the dependence on surface spectral reflectance to be adequately accounted for. Thus, one of the major obstacles of the CIBR and

APDA could be significantly overcome by using a simpler scheme employed by the TSR.

Future work would include trials of the TSR with in-situ atmospheric and surface data. This proposal is recommended so as to explore further the performance and stability of the TSR method. Even though this is essentially a proof-of-concept study, due to the lack of ground truth, this research has shown that the TSR method appears very sound. Lastly it is recommended that the TSR method be incorporated into full LUT procedures (pseudo-LUTs were used in this study). This would allow the TSR to be applied to hyperspectral spatial scenes on a much faster time-frame than is currently used (approximately 4.5 hrs for a single AVIRIS scene). It is noted though that the 4.5 hrs is the time taken to estimate water vapour plus atmospherically correct the entire scene from radiance to surface reflectance .

In conclusion, the TSR is a robust method of estimating atmospheric water vapour from remotely sensed hyperspectral radiances. It provides substantial improvement on current band ratio methods and includes features that may benefit current band ratio methods. The versatility of the TSR method demonstrates that alternative methods of retrieving column water vapour are still viable and that such methods have a traceable physical basis which leads its significant improvement of pixel-by-pixel estimated water vapour.

Appendix A

Principle Symbols

The principle symbols used are presented here. Not all symbols are shown due to the numerous perturbations of some symbols. **Some** symbols formed by the addition of subscripts and/or superscripts or primes to principle symbols are not listed. As well, **some** symbols that show functionality i.e. $L(\theta, W, \phi)$ are also not shown in this form. Notation that is considered as transient in nature is also not listed.

By omitting symbols that are formed by the addition of sub/superscripts, symbols such as $L_{r,1}$ may not listed. The principle symbol L is listed though. In this case the symbol $L_{r,1}$ is identifiable as spectral radiance based on the definition of the principle symbol L. The relevance of the subscripts r and 1 would, in this case, be found in the text at the first occurrence of the symbol $L_{r,1}$.

In the same way, the symbol $L(\theta, W, \phi)$ is also identifiable as spectral radiance from the principle symbol L. The variables θ, ϕ and W will, in almost all cases, appear in the following principle symbols lists. As such, this will define $L(\theta, W, \phi)$ if it is not apparent from the text. Again though, such symbols are defined as they occur in the text.

General	**Definition**	**units**
π	Pi: constant	3.1416
λ	Wavelength	nm
A,B,C,...	Equation coefficients	variable
A_k	Equation coefficients	variable
$a_{n,i \text{ or } k}$	Equation coefficients	variable
$b_{n \text{ or } k}$	Equation coefficients	variable
$c_{n \text{ or } k}$	Equation coefficients	variable
d_k	Equation coefficients	variable
F	Integrating factor	-
s	length	m
z	Distance normal	m

Irradiance/Radiance	**Definition**	**units**
E_0	Extraterrestrial solar irradiance	W/(m^2 nm)
$F^{\downarrow}$	Downward irradiance	W/(m^2 nm)
J	Source function	W/(m^2 sr nm)
J_d	Diffuse radiation field source function	W/(m^2 sr nm)
J_r	reduced radiation field source function	W/(m^2 sr nm)
L or L(λ)	Spectral radiance	W/(m^2 sr nm)
L_S	At-sensor radiance	W/(m^2 sr nm)
L_s	Surface radiance	W/(m^2 sr nm)
$L_{p \text{ or } path}$	Path scattered radiance	W/(m^2 sr nm)
L_{pm}	Modelled path scattered radiance	W/(m^2 sr nm)
$\overline{L}$	Weighted mean Radiance	W/(m^2 sr nm)

Transmission and Absorption and Reflection	**Definition**	**units**
j	Emission coefficient	W/(kg sr nm)
κ	Mass absorption coefficient	m^2/kg
$P(\theta,\phi;\theta',\phi')$ or $P(\Omega,\Omega')$	Rayleigh scattering phase function[1]	-
$R(\theta,\phi;\theta',\phi')$	Reflectance function[1]	-
$r(\mu_0)$	Planetary albedo	-
$\bar{r}$	Spherical albedo	-
$T(\theta,\phi;\theta',\phi')$	Transmission function[1]	-
$t(\mu_0)$, $t(\mu)$	Diffuse transmittance	-
τ	Normal optical thickness	-
τ_1	Normal total atmospheric optical thickness	-
W_1, W_2	Continuum interpolation weighting factors	-
X_1, X_2	Transmittance slope interpolation weighting factors	-
γ_{wv}	Total atmospheric transmittance	-
$\gamma(\mu)$, $\gamma(\mu_0)$	Total atmospheric transmittance[2]	-
$\rho(\lambda)$, ρ, ρ_s	Spectral surface reflectance	-
$\rho_m(\lambda)$, ρ_m, ρ_{sm}	Synthetic model spectral surface reflectance	-
ρ_b	Background surface reflectance	-

---

[1] The incoming radiation geometry is represented by θ' and ϕ' or alternatively, Ω' and the outgoing radiation is represented by θ and ϕ or alternatively Ω.

[2] The total atmospheric transmittance is defined as the sum of the direct plus diffuse transmittance.

Geometry	**Definition**	**Units**
θ	Zenith angle	radian
ϕ	Azimuth angle	radian
θ'	Incident zenith angle	radian
ϕ'	Incident azimuth angle	radian
θ_0	Solar zenith angle	radian
ϕ_0	Solar azimuth angle	radian
Ω	Solid angle	sr
Ω'	Incident solid angle	sr
μ	Path length, $\mu = \cos\theta$	
μ_0	Path length, $\mu_0 = \cos\theta_0$	
μ'	Incident path length, $\mu' = \cos\theta'$	

Meteorological	**Definition**	**Units**
β	Water vapour density	kg/(m^3)
PW, $PCWV$	Precipitable column water vapour	cm or kg/m^2
W	Atmospheric column water vapour[3]	kg/m^2 or cm

---

[3] If W is expressed in *cm* of water then strictly speaking it is the precipitable column water vapour

Appendix B

Acronyms

ACORN	Atmospheric Correction Now
APDA	Atmospheric Precorrection Differential Absorption
AVIRIS	Airborne Visible Infrared Imaging Spectrometer
CIBR	Continuum Interpolated Band Ratio
DEM	Digital Elevation Model
DISORT	Discreet Ordinates Transform
FOV	Field of View
FWHM	Full Width Half Maximum
GPS	Global Positioning System
HyMap	Hyperspectral Mapper
JPL	Jet Propulsion Laboratory
LUT	Look-up-Table
MLS	Mid-Latitude Summer
MLW	Mid-Latitude Winter
MODIS	Moderate Resolution Imaging Spectrometer
MODTRAN	Moderate Transmittance
NASA	National Aeronautics and Space Administration
NDVI	Normalised Difference Vegetation Index
NEDL	Noise Equivalent Radiance Difference
NIR	Near Infrared

PC	Percentage Change Scale Factor
PWV	Precipitable Column Water Vapour
RGB	Red-Green-Blue
ROI	Region of Interest
RTE	Radiative Transfer Equation
SAS	Sub-arctic Summer
SAW	Sub-arctic Winter
SNR	Signal-to-Noise Ratio
SWIR	Short Wave Infrared
TM	Thematic Mapper
TOA	Top-of-Atmosphere
TS	Transmittance Slope
TSR	Transmittance Slope Ratio
USS	United States Standard
UTC	Coordinated Universal Time
VMR	Vertical Mixing Ratio
VNIR	Visible Near Infrared

References

Adler-Golden, S. M., Bernstein, L. S., Richtsmeier, S., Acharya, P. K., Matthew, M. W., Anderson, G., Allred, C. L., Jeong, L. S., and Chetwynd, J. H. (1998). FLAASH, A MODTRAN4 Atmospheric Correction Package for Hyperspectral Data Retrievals and Simulations. In *Proceedings of the Seventh Airborne Visible/Infrared Imaging Spectrometer (AVIRIS) Workshop*, JPL Publ. 97-21, Vol. 1, Jet Propulsion Laboratory, Pasadena, CA, 9–14.

Adler-Golden, S. M., Matthew, M. W., Bernstein, L. S., Levine, R. Y., Berk, A., Richtsmeier, S. C., Acharya, P. K., Anderson, G., Felde, G., Gardner, J., Hoke, M., Jeong, L. S., Pukall, B., Mello, J., Ratkowski, A., and Burke, H. H. (1999). Atmospheric Correction for Short-wave Spectral Imagery Based on MODTRAN4. *Imaging Spectrometry V: SPIE*, **3753**.

Bagheri, S. and Dekker, A. (1999). Remote Sensing of Nearshore Water Quality Using Bio-Optical Modeling and Retrieval Techniques. In *Proceedings of the Eighth Airborne Visible/Infrared Imaging Spectrometer (AVIRIS) Workshop*, JPL Publ. 99-17, Jet Propulsion Laboratory, Pasadena, CA, 47–53.

Barnes, W. L., Pagano, T. S., and Salomonson, V. V. (1998). Prelaunch Characterisics of the Moderate Resolution Imaging Spectrometer (MODIS) on EOS-AM1. *IEEE Transactions on GeoScience and Remote Sensing*, **36**(4), 1088–1100.

Berk, A., Bernstein, L. S., Anderson, G. P., Acharya, P. K., Robertson, D. C., Chetwynd, J. H., and Adler-Golden, S. M. (1998). MODTRAN Cloud and Multiple Scattering Upgrades with Application to AVIRIS. *Remote Sens. Environ.*, **65**, 367–375.

Boardman, J. W. and Green, R. O. (2000). Exploring the Spectral Variability of the Earth as Measured by AVIRIS in 1999. In *Proceedings of the Ninth Airborne Visible/Infrared Imaging Spectrometer (AVIRIS) Workshop*, JPL Publ. 00-18, Jet Propulsion Laboratory, Pasadena, CA, 55–64.

Boas, M. L. (1966). *Mathematical Methods in the Physical Sciences*, chapter Integral Transforms, pages 615–621. John Wiley & Sons, Inc. New York.

Borel, C. C. and Schläpfer, D. (1996). Atmospheric Pre-Corrected Differential Absorption Techniques To Retrieve Columnar Water Vapor: Theory And Simulations. In *Proceedings of the Sixth Airborne Visible/Infrared Imaging Spectrometer (AVIRIS) Workshop*, JPL Publ. 96-4, Jet Propulsion Laboratory, Pasadena, CA, 13–21.

Bruegge, C. J., Conel, J. E., Margolis, J. S., Green, R. O., Toon, G., Carrère, V., Holm, R. G., and Hoover, G. (1990). In-Situ Atmospheric Water-Vapor Retrieval in Support of AVIRIS Validation. *Imaging Spectroscopy of the Terr. Environ: SPIE*, **1298**, 150–163.

Burke, H. H., Griffin, M. K., and Snow, J. W. (2000). Mitigation of Atmospheric Effects in Hyperspectral Data Analysis. *Algorithms for Multispectral, Hyperspectral, and Ultraspectral Imagery VI: SPIE*, **4049**, 433–443.

Carrére, V. and Conel, J. E. (1991). Comparison of two simple techniques to extract path precipitable water from AVIRIS radiance data: CIBR and "Narrow/Wide band ratio" - Sensitivity analysis and application to AVIRIS data. In *Proceedings of the Third Airborne Visible/Infrared Imaging Spectrometer (AVIRIS) Workshop*, JPL Publ. 91-28, Jet Propulsion Laboratory, Pasadena, CA, 96–98.

Carrére, V. and Conel, J. E. (1993). Recovery of Atmospheric Water Vapor Total Column Abundance from Imaging Spectrometer Data Around 940 nm - Sensitivity Analysis and Application to Airborne Visible/Infrared Imaging Spectrometer (AVIRIS) Data. *Remote Sens. Environ.*, **44**, 179–204.

Chabrillat, S. and Goetz, A. (1999). The Search for Swelling Clays Along the Colorado Front Range: The Role of AVIRIS Resolution in Detection.

In *Proceedings of the Eighth Airborne Visible/Infrared Imaging Spectrometer (AVIRIS) Workshop*, JPL Publ. 99-17, Jet Propulsion Laboratory, Pasadena, CA, 69–78.

Chandrasekhar, S. (1960). *Radiative Transfer.* Dover Publications, Inc. New York.

Conel, J. E., Bosh, J. V. D., and Grove, C. I. (1993a). Application of a Two-Stream Radiative Transfer Model for Leaf Lignin and Cellulose Concentrations from Spectral Reflectance Measurements (Part 1). In *Proceedings of the Third Airborne Visible/Infrared Imaging Spectrometer (AVIRIS) Workshop*, JPL Publ. 93-26, Jet Propulsion Laboratory, Pasadena, CA, 39–43.

Conel, J. E., Bosh, J. V. D., and Grove, C. I. (1993b). Application of a Two-Stream Radiative Transfer Model for Leaf Lignin and Cellulose Concentrations from Spectral Reflectance Measurements (Part 2). In *Proceedings of the Third Airborne Visible/Infrared Imaging Spectrometer (AVIRIS) Workshop*, JPL Publ. 93-26, Jet Propulsion Laboratory, Pasadena, CA, 45–51.

Davis, C. O. (1994). Processing and Analysis of AVIRIS Imagery of the Coastal Ocean. In *Proceedings of the International Symposium on Spectral Sensing Research*, 10-15 July, San Diego, CA, 661–672.

de Hann, J. F., Hovenier, J. W., Kokke, J. M. M., and van Stokkom, H. T. C. (1991). Removal of Atmospheric Influences on Satellite-Borne Imagery: A Radiative Transfer Approach. *Remote Sens. Environ*, **37**, 1–21.

Deschamps, P. Y., Herman, M., and Tanre, D. (1983). Definitions of atmospheric radiance and transmittance in remote sensing. *Remote Sens. Environ.*, **13**, 89–92.

Egorova, T., Jagovkina, S., and Rozanov, E. (1999). The simulation of atmospheric ozone distribution with a 2-d model and validation against uars and toms data. *Phys. Chem. Earth (C)*, **24**(5), 465–471.

Frouin, R., Deschamps, P. Y., and Lecomte, P. (1990). Determination from Space of Atmospheric Total Water Vapor Amounts by Differential Absorption

Near 940 nm: Theory and Airborne Verification. *Journal of Applied Meteorology*, **29**, 448–459.

Gao, B. C. and Goetz, A. F. H. (1990). Column Atmospheric Water Vapor and Vegetation Liquid Water Retrievals From Airborne Imaging Spectrometer Data. *Journal of Geophysical Research*, **95**(D4), 3549–3564.

Gao, B. C. and Goetz, A. F. H. (1995). Retrival of Equivalent Water Thickness and Information Related to Biochemical Components of Vegetation Canopies from AVIRIS Data. *Remote Sens. Environ.*, **52**, 155–162.

Gao, B. C. and Kaufman, Y. J. (1998). The MODIS Near-IR Water Vapor Algorithm. MODIS Algorithm Theoretical Basis Document: ATBD-MOD-03, NASA/GSFC.

Gao, B. C., Kierein-Young, K. S., Goetz, A. F. H., Westwater, E. R., Stankov, B. B., and Birkenheuer, D. (1991a). Case Studies of Water Vapor and Surface Liquid Water from AVIRIS Data MEasured Over Denver, CO and Death Valley, CA. In *Proceedings of the Third Airborne Visible/Infrared Imaging Spectrometer (AVIRIS) Workshop*, JPL Publ. 91-28, Jet Propulsion Laboratory, Pasadena, CA, 222–231.

Gao, B. C., Goetz, A. F. H., and Zamudio, J. A. (1991b). Removing Atmospheric Effects From AVIRIS Data For Surface Reflectance Retrievals. In *Proceedings of the Third Airborne Visible/Infrared Imaging Spectrometer (AVIRIS) Workshop*, JPL Publ. 91-28, Jet Propulsion Laboratory, Pasadena, CA, 80–86.

Gao, B. C., Heidbrecht, K. B., and Goetz, A. F. H. (1993). Derivation of Scaled Surface Reflectances from AVIRIS Data. *Remote Sens. Environ.*, **44**, 165–178.

Goetz, A. F. H., Heidbrecht, K. B., Kindel, B., and Boardman, J. (1998). Using Ground Spectral Irradiance for Model Correction. In *Proceedings of the Seventh Airborne Visible/Infrared Imaging Spectrometer (AVIRIS) Workshop*, JPL Publ. 97-21, Jet Propulsion Laboratory, Pasadena, CA, 159–168.

Green, R. O. (1990). Retrieval of Reflectance from Calibrated Radiance Imagery Measured by the Airborne Visible/Infrared Imaging Spectrometer

(AVIRIS) for Lithological Mapping of the Clark Mountains, California. In *Proceedings of the Second Airborne Visible/Infrared Imaging Spectrometer (AVIRIS) Workshop*, JPL Publ. 90-54, Jet Propulsion Laboratory, Pasadena, CA, 167–175.

Green, R. O. (1991). Retrieval of Reflectance From AVIRIS-Measured Radiance Using a Radiative Transfer Code. In *Proceedings of the Third Airborne Visible/Infrared Imaging Spectrometer (AVIRIS) Workshop*, JPL Publ. 91-28, Jet Propulsion Laboratory, Pasadena, CA, 200–210.

Green, R. O. (1998). Apparent Surface Reflectance of the DOE ARM SGP CART Central Site Derived from AVIRIS Spectral Images. In *Proceedings of the Seventh Airborne Visible/Infrared Imaging Spectrometer (AVIRIS) Workshop*, JPL Publ. 97-21, Jet Propulsion Laboratory, Pasadena, CA, 175–184.

Green, R. O. (2000). AVIRIS 1999 NEDL Data. Personal Communication.

Green, R. O. and Boardman, J. (2000). Exploration of the Relationship between Information Content and Signal-to-Noise Ratio and Spatial Resolution in AVIRIS Spectral Data. In *Proceedings of the Ninth Airborne Visible/Infrared Imaging Spectrometer (AVIRIS) Workshop*, JPL Publ. 00-18, Jet Propulsion Laboratory, Pasadena, CA, 195–206.

Green, R. O. and Pavri, B. (2000). AVIRIS In-Flight Calibration Experiment, Sensitivity Analysis and Intraflight Stability. In *Proceedings of the Ninth Airborne Visible/Infrared Imaging Spectrometer (AVIRIS) Workshop*, JPL Publ. 00-18, Jet Propulsion Laboratory, Pasadena, CA, 207–221.

Green, R. O. and Roberts, D. A. (1995). Vegetation Species Composition and Canopy Architecture Information Expressed in Leaf Water Absorption Measured in the 1000 nm and 2200 nm Spectral Region by an Imaging Spectrometer. In *Proceedings of the Fith Airborne Visible/Infrared Imaging Spectrometer (AVIRIS) Workshop*, JPL Publ. 95-1, Jet Propulsion Laboratory, Pasadena, CA, 95–98.

Green, R. O., Conel, J. E., Margolis, J. S., Bruegge, C. J., and Hoover, G. L. (1991). An Inversion Algorithm for Retrieval of Atmospheric and Leaf Water Absorption From AVIRIS Radiance With Compensation for Atmospheric Scattering. In *Proceedings of the Third Airborne Visible/Infrared Imaging Spectrometer (AVIRIS) Workshop*, JPL Publ. 91-28, Jet Propulsion Laboratory, Pasadena, CA, 51–61.

Green, R. O., Conel, J. E., and Roberts, D. A. (1993). Estimation of Aerosol Optical Depth and Additional Atmospheric Parameters for the Calculation of Apparent Reflectance from Radiance Measured by the Airborne Visible/Infrared Imaging Spectrometer. In *Proceedings of the Third Airborne Visible/Infrared Imaging Spectrometer (AVIRIS) Workshop*, JPL Publ. 93-26, Jet Propulsion Laboratory, Pasadena, CA, 73–76.

Green, R. O., Conel, J. E., and Roberts, D. A. (1995). Measurement of Atmospheric Water Vapor, Leaf Liquid Water and Reflectance with AVIRIS in the Boreal Ecosystem-Atmosphere Study: Initial Results. In *Proceedings of the Fith Airborne Visible/Infrared Imaging Spectrometer (AVIRIS) Workshop*, JPL Publ. 95-1, Jet Propulsion Laboratory, Pasadena, CA, 87–90.

Green, R. O., Eastwood, M. L., Sature, C. M., Chrien, T. G., Aronsson, M., Chipendale, B. J., Faust, J. A., Pavri, B. E., Chovit, C. J., Solis, M., Olah, M. R., and Wiliiams, O. (1998). Imaging Spectroscopy and the Airborne Visible/Imaging Spectrometer (AVIRIS). *Remote Sens. Environ.*, **65**, 227–248.

Hirsch, K. L., Balick, L., Borel, C., and McLachlan, P. (2001). A Comparison of Four Methods for Determining Precipitable Water Vapor Content from Multi-Spectral Data. *Proc. SPIE*, **4381**, in press.

Jacob, D. (2001). The Role of Water Vapor in the Atmosphere. A Short Overview from a Climate Modeller's point of View. *Phys. Chem. Earth (A)*, **26**(6–8), 523–527.

Kaufman, Y. J. (1984). Atmospheric effects on remote sensing of surface reflectance. *Critical Reviews of Technology: SPIE*, **475**(6), 20 – 33.

Kaufman, Y. J. (1989). *Theory and Applications of Optical Remote Sensing*, chapter The Atmospheric Effect On Remote Sensing and Its Correction, pages 336 – 428. John Wiley and Sons.

Kaufman, Y. J. and Gao, B. C. (1992). Remote Sensing of Water Vapor in the Near IR from EOS/MODIS. *IEEE Trans. on Geosc. and R. S*, **30**(5), 871 – 884.

Kaufman, Y. J., Brakke, T. W., and Eloranta, E. (1986). Field experiment for measurement of the radiative characteristics of a hazy atmosphere. *Journal of the Atmospheric Sciences*, **43**(11), 1135–1151.

Khalil, M. A. K. and Rasmussen, R. A. (1994). Global emmisions of methane during the last ceveral centuries. *Chemosphere*, **29**(5), 833–842.

Kindel, B., Qu, Z., and Goetz, A. F. H. (2000). Hyperspectral Solar Radiometry for Surface Reflectance Retrieval. In *Proceedings of the Ninth Airborne Visible/Infrared Imaging Spectrometer (AVIRIS) Workshop*, JPL Publ. 00-18, Jet Propulsion Laboratory, Pasadena, CA, 243–249.

Kruse, F. A., Boardman, J. W., Lefkoff, A. B., Young, J. M., Keirein-Young, K. S., Cocks, T. D., Jenssen, R., and Cocks, P. A. (2000). The 1999 AIG/HyVista HyMap Group Shoot: Commercial Hyperspectral Sensing is Here. *Algorithms for Multispectral, Hyperspectral, and Ultraspectral Imagery VI: SPIE*, **4049**, 210–217.

Latorre, M. L. and Dias, L. A. V. (2000). Atmospheric Correction Method for AVIRIS Data in Tropical Regions. In *Proceedings of the Ninth Airborne Visible/Infrared Imaging Spectrometer (AVIRIS) Workshop*, JPL Publ. 00-18, Jet Propulsion Laboratory, Pasadena, CA, 283–288.

Liou, K. (1980). *An Introduction to Atmospheric Radiation.* Academic Press, Inc. New York.

Matthew, M. W., Adler-Golden, S. M., Berk, A., Richtsmeir, S. C., Levine, R. Y., Bernstein, L. S., Acharya, P. K., Anderson, G. P., Felde, G. W., Hoke, M. P., Ratkowski, A., Burke, H. H., Kaiser, R. D., and Miller, D. P. (2000). Status of atmospheric correction using a MODTRAN4-based algorithm. *Algorithms for Multispectral, Hyperspectral, and Ultraspectral Imagery VI: SPIE*, **4049**, 199–207.

Meidunas, E., Acharya, P. K., Adler-Golden, S. M., Anderson, G. P., Armstrong, P. S., Berk, A., Bernstein, L. S., Felde, G. W., Gardner, J. A., Hoke, M. P., Matthew, M. W., and Ratkowski, A. J. (2000). Atmospheric Correction of Spectral Imagery Data. *Algorithms for Multispectral, Hyperspectral, and Ultraspectral Imagery VI: SPIE*, **4049**, 184–189.

Moreno, J. F. and Green, R. O. (1996). Measurement of Atmospheric Water Vapor, Leaf Liquid Water and Reflectance with AVIRIS in the Boreal Ecosystem-Atmosphere Study: Initial Results. In *Proceedings of the Sixth Airborne Visible/Infrared Imaging Spectrometer (AVIRIS) Workshop*, JPL Publ. 96-4, Jet Propulsion Laboratory, Pasadena, CA, 175–184.

Roberts, D. A., Green, R. O., Sabol, D. E., and Adams, J. B. (1993). Temporal Changes in Endmemeber Abundances, Liquid Water and Water Vapor Over Vegetation at Jasper Ridge. In *Proceedings of the Third Airborne Visible/Infrared Imaging Spectrometer (AVIRIS) Workshop*, JPL Publ. 93-26, Jet Propulsion Laboratory, Pasadena, CA, 153–156.

Roberts, D. A., Green, R. O., and Adams, J. B. (1997). Temporal and Spatial Patterns in Vegetation and Atmospheric Properties from AVIRIS. *Remote Sens. Environ.*, **62**, 223–240.

Schläpfer, D., Borel, C. C., Keller, J., and Itten, K. I. (1996). Atmospheric Pre-Corrected Differential Absorption Techniques To Retrieve Columnar Water Vapor: Application To AVIRIS 91/95 Data. In *Proceedings of the Sixth Airborne Visible/Infrared Imaging Spectrometer (AVIRIS) Workshop*, JPL Publ. 96-4, Jet Propulsion Laboratory, Pasadena, CA, 209–217.

Schläpfer, D., Borel, C. C., Keller, J., and Itten, K. I. (1998). Atmospheric Pre-Corrected Differential Absorption Technique To Retrieve Columnar Water Vapor. *Remote Sens. Environ*, **65: 353–366**.

Schläpfer, D. R. (1998). *Differential Absorption Methodology for Imaging Spectroscopy of Atmospheric Water Vapor.* Doctoral dissertation, University of Zűrich.

Sommese, T., Essel, M., Weiss, D., Mertz, F., and Westmoreland, S. (2000). Atmospheric Correction Using Imbedded Models (ACUIM). *Algorithms for Multispectral, Hyperspectral, and Ultraspectral Imagery VI: SPIE*, **4049**, 411–422.

Stewart, A. and Kaiser, R. (2000). Performance assesment of Atmospheric Correction Algorithms for VIS-SWIR Hypersepctral Data. *Algorithms for Multispectral, Hyperspectral, and Ultraspectral Imagery VI: SPIE*, **4049**, 423–432.

Tahl, S. and v. Shőnermark, M. (1998). Determination of the Column Water Vapor of the Atmosphere Using Backscattered Solar Radiation Measured by the Modular Optoelectronic Scanner (MOS). *Int. J. Remote Sensing*, **19**(17), 3223–3236.

Tanre, D., Deroo, C., Duhaut, P., Herman, M., Mocrette, J. J., Perbos, J., and Deschamps, P. Y. (1986). Simulation of the Satellite Signal in the Solar Spectrum (5S). User Guide, Laboratoire d'Optique Atmosphérique, Université des Sciences et Techniques de Lille, France.

Taylor, J. A. and Orr, J. C. (2000). The natural latitudinal distribution of atmospheric co$_2$. *Global and Planatery Change*, **26**, 375–386.

Thomas, G. B. and Finney, R. L. (1992). *Calculus and Analytic Geometry*, chapter Infinite Series, pages 586 – 592. Addison-Wesley Publishing Company, 8 edition.

van den Bosch, J. M. and Alley, R. E. (1991). Quantitative Analysis of Three Atmospheric Correction Models for Airborne Visible/Infrared Imaging Spectrometer (AVIRIS)Data. In *Proceedings of the Third Airborne Visible/Infrared Imaging Spectrometer (AVIRIS) Workshop*, JPL Publ. 91-28, Jet Propulsion Laboratory, Pasadena, CA, 87–95.

Wang, W. C., Liang, X. Z., Dudek, M. P., and Pollard, D. (1995). Atmospheric ozone as a climate gas. *Atmospheric Research*, **37**, 247–256.